

Use of SRPK1 inhibitors for the treatment of Diabetic Retinopathy



**University of
Nottingham**

UK | CHINA | MALAYSIA

Naseeb Kaur Malhi

**A thesis submitted to the University of Nottingham for
the degree of Doctor of Philosophy (PhD)**

**Supervisors: Prof. David Bates & Dr.
Kenton Arkill**

July 2020

Abstract

Microvascular damage results from ischaemia-driven production of pro-angiogenic vascular endothelial growth factor (VEGF). Proximally spliced VEGF is upregulated in the ischemic diabetic retina and has been implicated as the principal driver of the pathological growth and leakage of blood vessels during diabetic retinopathy (DR). Serine-Arginine Rich protein kinase-1 (SRPK1) regulates splicing of VEGF, and inhibition of this kinase with small molecular weight inhibitors has been shown to inhibit choroidal neovascularization (CNV) in mice by decreasing pro-angiogenic and increasing anti-angiogenic VEGF isoforms. These isoforms have previously been described to inhibit increased vascular permeability with protective effects against DR-induced pathology. SRPK1 inhibitors such as SPHINX31 may therefore switch splicing in DR and prevent increased vascular permeability.

Retinal pigment epithelial cells were exposed to hyperglycaemia (HG) and hypoxia (Hx) and treated with SPHINX31. SRSF1 localisation in the nuclear speckles, SRPK1 activity and monolayer permeability were assessed by immunofluorescence and Electrical Cell Impedance Sensing. In a rodent model of type 1 diabetes fluorescein fundus angiography (FFA) and optical coherence tomography (OCT) was performed weekly from day 0 to 28. Animals received twice daily topical eye drops with eye formulation control buffer or SPHINX31. On day 1 animals received a single dose of streptozotocin to induce type I diabetes. FFA was quantified using ImageJ; the intensity of sodium fluorescein in the retinal interstitial area and the retinal vessels were measured and the permeability assessed from this relationship. An FFA and OCT time course was used to determine an estimate of permeability and retinal thickness. Retina petals were stained with IB4 and for junctional proteins to deduce vascular density.

HG and Hx induced a significant increase ($p < 0.05$) in SRSF1 nuclear localisation, which was blocked by SPHINX31. HG induced a release of SRSF1 from the nuclear speckles ($p = 0.002$). Inhibition of SRPK1 decreased RPE monolayer permeability ($p < 0.05$). The increase in retinal permeability on days 14-28 seen in the diabetic eye formulation only control cohort ($n = 8$) was stabilised following topical treatment of diabetic animals with SPHINX31 ($n = 9$) for 28 days ($p < 0.0001$). Mean retinal thickness increased in diabetes ($p < 0.05$) and this increase appeared to be blocked following SPHINX31 treatment.

SPHINX31 protected the retinal barrier from hyperglycaemia-associated loss of integrity in RPE cells *in vitro* and in diabetic rats *in vivo*. SPHINX31 may therefore be a potential topical therapeutic for DR.

Publications, Abstracts and Awards

Publications

Boardman R, Pang V, **Malhi N**, Lynch AP, Leach L, Benest AV, Bates DO, Machado MJ. (2019). *Activation of Notch signaling by soluble Dll4 decreases vascular permeability via a cAMP/PKA-dependent pathway*. American Journal of Physiology Heart and Circulatory Physiology; 316 (5): H1065-H1075

Allen, CL., **Malhi, NK.**, Whatmore, JD., Bates, DO., & Arkill, KP. (2020). *Non-invasive measurement of retinal permeability in a diabetic rat model*. Microcirculation, micc.12623. <https://doi.org/10.1111/micc.12623>

Abstracts

23rd Annual Nottingham Eye and Research Symposium, UK, 2019 – Oral presentation. The SRPK1 inhibitor SPHINX31 stabilises retinal permeability in vitro and in vivo models of diabetes.

6th UK RNA Splicing Workshop, Lake District, UK, 2019 – Oral presentation. The SRPK1 inhibitor SPHINX31 stabilises retinal permeability in vitro and in vivo models of diabetes.

British Microcirculation Society 69th Annual Meeting, Exeter, 2019 – Poster presentation. The SRPK1 inhibitor SPHINX31 stabilises retinal permeability in vitro and in vivo models of diabetes.

Vasculata, Milwaukee, USA, 2019 – Poster presentation. The SRPK1 inhibitor SPHINX31 stabilises retinal permeability in vitro and in vivo models of diabetes.

Cancer and Stem Cells Divisional Meeting, University of Nottingham, UK – Poster presentation. The SRPK1 inhibitor SPHINX31 stabilises retinal permeability in vitro and in vivo models of diabetes.

Divisional Cancer Meeting, University of Nottingham UK, 2018 – Oral presentation. The SRPK1 inhibitor SPHINX31 stabilises retinal permeability in vitro and in vivo models of diabetes.

International Society for Eye Research Meeting, Belfast, 2018 – Poster presentation. The SRPK1 inhibitor SPHINX31 stabilises retinal permeability in vitro and in vivo models of diabetes.

2nd Annual Splicing Meeting, Caparica, Portugal, 2018 – Oral shotgun presentation with poster. The SRPK1 inhibitor SPHINX31 stabilises retinal permeability in vitro and in vivo models of diabetes.

British Microcirculation Society 68th Annual Meeting, Nottingham, UK, 2018 – Oral presentation. The SRPK1 inhibitor SPHINX31 stabilises retinal permeability in a rodent model of diabetes.

European Vision and Eye Research (EVER) Conference Nice, France, 2017 – Poster presentation. The SRPK1 inhibitor SPHINX31 stabilises retinal permeability in a rodent model of diabetes.

Awards

Travel Award, Vasculata. 2019.

Laboratory Visit Grant, British Microcirculation Society. 2019.

Travel Award, British Microcirculation Society, 2019.

‘Best third year poster’ at Cancer and Stem Cells Divisional Meeting, 2019.

Travel Fellowship, Biennial International Symposium on Eye Research, 2018.

‘Excellent Shotgun Communication Award’ for oral presentation at 2nd Annual Splicing Meeting, 2018.

Travel Award, University of Nottingham School of Medicine Doctoral Programmes Committee, 2018

First prize for oral presentation at NC3Rs summer school, 2017.

‘Best poster in retinal section’ at European Vision and Eye Research (EVER) Conference, 2017.

Travel Grant, National Eye Research Centre, 2017.

Acknowledgments

I would like to thank my supervisors, Prof. David Bates and Dr. Kenton Arkill for giving me the opportunity to work on this exciting project and their guidance along the way. Dave – your intelligence and passion for science serve as a constant source of inspiration for me, thank you for pushing me and giving me the confidence to travel/collaborate/present all over the world. Kenton – thank you for giving me opportunities to work outside my comfort zone and believing in my abilities. Also thanks for the office chats. I would also like to thank the National Eye Research Centre for funding this research.

Dr. Claire Allen, thank you for teaching me everything I know, being my role model and dealing with my emotions! You brightened the most difficult days, and I will always be grateful for your mentorship and even more grateful for your friendship.

Special thanks have to go to Dr. Heidrun Deißler for the wonderful experience at the University of Ulm, I miss our academic and political discussions!

This PhD experience has been the most enjoyable 3-years of my life due to the brilliant people I have worked with, who I am lucky to call my friends. I am indebted to them for their kindness, support and tea-breaks helping to maintain my sanity! There are too many people to thank individually but I want to mention: Roaa, thank you for being my quarantine queen and giving me strength; Amany, TJ, Eduardo, Mireia, Mussarat, thank you for the adventures; Liz, thank you for all the help in the lab.

Thank you to Andrea, my rock over my whole scientific career never letting me give up – it means more than you know.

This thesis is dedicated to my parents, for continuously inspiring me with their hard work, dedication and unending love. Thank you to Mum for supporting my passion to move into this field, despite it not being the easiest path. Although Dad, Harbhajan Singh, can't be around to see the fruit of his labour, his memory gave me strength throughout this PhD. I am incredibly grateful to be supported by my amazing family: my sister Gurj for letting me move in to her brand new

house, her continuous cheerleading, gourmet meals and unbelievable patience dealing with me writing this thesis during a pandemic!; my sister Amardeesh for the banter, generosity and the 5am lifts to give rats eye-drops!; my brother-in-law Ranbir for his kind nature, german translations for lab equipment and travel tips; and finally my brother Manveer for his unending encouragement and belief in me, even when I didn't believe in myself. Words do little to portray my gratitude – I would not be where I am without them.

Author's Declaration

I, Naseeb Kaur Malhi, confirm that the work presented in this thesis was carried out in accordance with the requirements of the University's Regulations and Code of Practice for Research Degree Programs and that it has not been submitted for any other academic award. I confirm that the work and views demonstrated in this thesis are my own. Where information has been derived from other sources, I confirm this has been indicated in the thesis.

SIGNED  DATE....03/08/2020.....

List of Abbreviations

AGE	Advanced Glycation End products
AMD	Age-related Macular Degeneration
ANGPTL4	Angiopoietin-like Protein-4
ATP	Adenosine Triphosphate
AUC	Area Under the Curve
BIM	Bisindolylmaleimide
BRB	Blood Retinal Barrier
BRET	Bioluminescence Resonance Energy Transfer
BSA	Bovine Serum Albumin
CD31	Cluster of Differentiation 31
CI	Cell Index
CLK	Cdc2-Like Kinase
CNV	Choroidal Neovascularisation
Co-L	Co-localisation
DAG	Diacylglycerol
DAPI	4',6-diamidino-2-phenylindole
Db	Diabetic
dH ₂ O	distilled H ₂ O
DMEM	Dulbecco's Modified Eagle Medium
DMO	Diabetic Macula Oedema
DMSO	Dimethyl Sulfoxide
DNA	Deoxyribonucleic Acid
DR	Diabetic Retinopathy
EB	Evan's Blue
ECIS	Electrical Cell Impedance Sensing
EGF	Epidermal Growth Factor

ELISA	Enzyme-Linked Immunosorbent Assay
FAK	Focal Adhesion Kinase
FBS	Foetal Bovine Serum
FFA	Fundus Fluorescein Angiography
FIJI	Fiji Is Just ImageJ
FITC	Fluorescein isothiocyanate
GCL	Ganglion Cell Layer
GFAP	Glial fibrillary acidic protein
GLUT	Glucose Transporter
GUK	Guanylate Kinase
HbA _{1c}	Glycated Haemoglobin
HEK293	Hamster Embryonic Kidney
HG	Hyperglycaemia
HIF	Hypoxia Inducible Factor
hpRPE	human primary Retinal Pigment Epithelium
HRE	Hypoxia Response Element
Hsp	Heat-shock protein
hTERT	human Telomerase Reverse Transcriptase
Hx	Hypoxia
i.p.	Intraperitoneal
IB4	Isolectin B4
iBREC	immortalised Bovine Retinal Endothelial Cell
IC ₅₀	Concentration required for 50% Inhibition
ICAM-1	Intracellular Adhesion Molecule-1
IGF	Insulin-like Growth Factor
IgG	Immunoglobulin G
INL	Inner Nuclear Layer

JAM	Junctional Adhesion Molecule
LB	Lysogeny Broth
MAP	Mitogen-Activated Protein
MEM	Modified Eagle Medium
miR	microRNA
MMP	Matrix Metalloproteinase
MRI	Magnetic Resonance Imaging
mRNA	messenger Ribonucleic Acid
NaF	Sodium Fluorescein
NDb	Non-Diabetic
NF- κ B	Nuclear Factor kappa-B
NG	Normoglycaemia
NOD	Nonobese Diabetic
NP40	Nonionic Polyoxyethylene 40
NPDR	Non-Proliferative Diabetic Retinopathy
NRP	Neuropilin
ns	Not significant
Nx	Normoxia
O-GlcNAc	O-linked N-acetylglucosamine glycosylation
OCT	Optical Coherence Tomography
ONL	Outer Nuclear Layer
P-SR	Phosphorylated SR
PBS	Phosphate Buffered Saline
PBS-T	Phosphate Buffered Saline 1% Tween
PBSd	PBS without Ca ²⁺ /Mg ²⁺
PCR	Polymerase Chain Reaction
PDR	Proliferative Diabetic Retinopathy

PDZ	Post-synaptic Density/discs-large/ZO-1
PFA	Paraformaldehyde
PIGF	Placental Growth Factor
PKC	Protein Kinase C
PLC	Phospholipase C
PMSF	Phenylmethylsulfonylfluoride
PRP	Pan-retinal Photocoagulation
PTP	Protein Tyrosine Phosphatases
PVDF	Polyvinylidene Fluoride
RAGE	Advanced Glycation End product Receptors
RBP	RNA Binding Protein
REC	Retinal Endothelial Cell
RLU	Relative Light Unit
RNA	Ribonucleic Acid
ROS	Reactive Oxygen Species
RPE	Retinal Pigment Epithelium
RS	Arginine and Serine alternating residues
SH3	Src Homology-3
snRNP	small nuclear Ribonucleo-Protein
SR	Serine-rich
SRPK	Serine/Arginine Protein Kinase
SRSF	Serine/Arginine Rich Splicing Factor
STAT	Signal Transducer and Activator of Transcription
STZ	Streptozotocin
TBS	Tris Buffered Saline
TBS-T	Tris Buffered Saline 1% Tween
TCA	Tricarboxylic Acid

TGF	Transforming Growth Factor
TNF	Tumour Necrosis Factor
UPW	Ultrapure Water
UTR	Untranslated Region
VE-Cadherin	Vascular Endothelial Cadherin
VEGF	Vascular Endothelial Growth Factor
VEGFR	Vascular Endothelial Growth Factor receptor
Veh	Vehicle
WCL	Water Control
WPI	World Precision Instruments
X31	SPHINX31
ZO-1	Zonula Occludin-1

Table of Contents

1	CHAPTER 1.....	21
1.1	Diabetic retinopathy	22
1.1.1	Epidemiology of diabetic retinopathy.....	22
1.1.2	Physiopathogenesis of diabetic retinopathy	23
1.1.3	Mechanisms associated with DR	26
1.1.4	Current therapies.....	30
1.2	Blood-Retina Barrier	32
1.2.1	Inner Blood-Retina Barrier	34
1.2.2	Outer Blood-Retina Barrier	34
1.3	VEGF and Diabetic Retinopathy.....	37
1.3.1	VEGF expression in the diabetic retina	37
1.3.2	VEGF and permeability.....	38
1.3.3	VEGF-A _{165b}	41
1.4	SRPK1.....	42
1.4.1	SR Proteins.....	42
1.4.2	SRPK1	43
1.4.3	SPHINX31.....	46
1.5	Hypothesis and Aims.....	47
2	CHAPTER 2.....	49
2.1	Cell culture	50
2.1.1	Routine cell culture.....	50
2.1.2	Primary retinal pigment epithelial cell culture.....	50
2.1.3	iBREC Culture	51
2.1.4	Cell storage	52
2.1.5	Cell counting	52
2.2	Isolation of primary cells.....	53
2.3	Protein extraction	54
2.3.1	RPE Cell lysis.....	54
2.3.2	Tissue lysis.....	55
2.3.3	iBREC lysis	55
2.3.4	Protein quantification	55
2.4	Western Blot.....	56
2.4.1	RPE	56
2.4.2	iBREC	57
2.5	Immunoprecipitation.....	58
2.6	Immunofluorescence	59
2.6.1	Immunocytochemistry.....	59
2.6.2	Immunohistochemistry.....	60
2.7	ELISA.....	61
2.8	NanoBRET	63
2.8.1	Plasmid Preparation	63
2.8.2	NanoBRET assay.....	64
2.8.3	NanoBRET Imaging.....	65
2.9	Electric Cell-substance Impedance Sensing.....	66
2.10	XCelligence	68
2.11	<i>In vivo</i> work.....	69
2.11.1	Topical administration of SPHINX31	70

2.11.2	Streptozocin-induced Type I Diabetic Model	70
2.11.3	Optical Coherence Tomography	71
2.11.4	Fundus Fluorescein Angiography	72
2.12	Data Analysis	73
2.12.1	SRSF1 localisation	74
2.12.2	Integrity of tight junction as determined by ZO-1	74
2.12.3	Quantification of SRSF1:SRSF2 co-localisation	77
2.12.4	Measurement of vascular parameters	78
2.12.5	Acellular capillary number	79
3	CHAPTER 3.....	81
3.1	Introduction	82
3.2	Methodology	85
3.3	Results.....	86
3.3.1	VEGF-A ₁₆₅ isoform expression in response to hyperglycaemia and hypoxia in RPEs	86
3.3.2	Changes to permeability of the outer blood-retinal barrier in hyperglycaemia and hypoxia	88
3.3.3	SRSF1 expression in HG and Hx hpRPEs	93
3.4	Discussion.....	106
3.4.1	hpRPEs provide a better model of <i>in vitro</i> outer blood-retinal barrier in comparison with ARPE-19s.....	106
3.4.2	Hyperglycaemia and hypoxia upregulates VEGF-A _{165a} expression and disrupts RPE monolayer properties	106
3.4.3	SRPK1 activity increases in response to hyperglycaemia and hypoxia	107
3.5	Summary	110
4	CHAPTER 4.....	111
4.1	Introduction	112
4.2	Methodology	115
4.3	Results.....	116
4.3.1	Changes in VEGF-A ₁₆₅ isoform expression in response to SRPK1 inhibition in hyperglycaemia and hypoxia	116
4.3.2	Impact of SRPK1 inhibition on integrity of RPE monolayer	118
4.3.3	SRPK1 activity in HG and Hx RPEs in response to SPHINX31	122
4.3.4	Determining the impact of PKC on SRPK1 activity in hyperglycaemia	127
4.4	Discussion.....	130
4.4.1	SRPK1 inhibition attenuates differential VEGF-A ₁₆₅ isoform expression in response to hyperglycaemia and hypoxia restoring barrier properties of RPE monolayer	130
4.4.2	SPHINX31 abrogates nuclear shuttling of SRSF1 and release from nuclear speckles potentially through restoration of SRPK1:SRSF1 complexes in diabetic-mimicking conditions	131
4.4.3	Pan-PKC inhibition blocks HG-induced increases in SRPK1 activity and SRSF1 nuclear shuttling.....	132
4.5	Summary	134
5	CHAPTER 5.....	135
5.1	Introduction.....	136
5.2	Methodology	140
5.3	Results.....	142

5.3.1	Impact of topical administration of SPHINX31 on retinal permeability in an <i>in vivo</i> model of DR.....	142
5.3.2	Impact of inhibiting SRPK1 on retinal thickness in a type-I diabetic model.....	146
5.3.3	Assessment of vascular parameters in response to STZ-induced diabetes and SRPK1 inhibition.....	150
5.3.4	Effects of hyperglycaemia, VEGF-A _{165b} and SRPK1 inhibition on retinal endothelial cell permeability	156
5.4	Discussion.....	166
5.4.1	Retinal permeability can be deduced non-invasively through fundus fluorescein angiography.....	166
5.4.2	SRPK1 inhibition ameliorates DR-induced increase in retinal permeability in an <i>in vivo</i> model of Type-I diabetes.....	168
5.4.3	STZ-induced increase in retinal thickening is localised to the RPE-Choroid layer and ameliorated by SPHINX31.....	172
5.4.4	STZ and SPHINX31 induces slight, but not significant changes in vessel parameters after 28-days	173
5.4.5	SRPK1 inhibition protects against diabetes-induced acellular capillary formation	175
5.4.6	VEGF-A _{165b} ameliorates VEGF-A _{165a} -induced disruption in iBREC monolayer permeability in normo- and hyperglycaemia.....	176
6	Chapter 6	179
6.1	COVID-19 Impact Statement.....	180
6.2	SRPK1 and hyperglycaemia.....	180
6.3	Dual effects of hypoxia and hyperglycaemia on RPEs	182
6.4	Targeting the outer BRB for DR therapy	182
6.5	SPHINX31 mechanism of action	187
6.6	Summary	189
7	REFERENCES	192
8	Appendix	224

Table of Figures

Figure 1.1.1	Pathogenesis of Diabetic Retinopathy	25
Figure 1.1.2	Schematic of pathways contributing to DR	26
Figure 1.2	Schematic of blood-retinal barriers	33
Figure 1.3	Schematic of intracellular pathways contributing to permeability	40
Figure 1.4	Schematic of SRPK1-SRSF1 axis	45
Figure 1.5	Chemical structure of SPHINX31	47
Figure 2.1	Formula for calculating cell number	53
Figure 2.2	Schematic summarising primary cell isolation	54
Figure 2.8	Schematic of Nano-BRET principle	63
Figure 2.9	Schematic of ECIS principle	67
Figure 2.11	Analysis of retinal permeability through FFA	73
Figure 2.12.2	Optimisation of ZO-1 staining analysis protocol	76
Figure 2.12.3	Summary of image analysis to determine Co-L	78
Figure 2.12.4	Calculation of vessel parameters using Imaris software	79
Figure 3.3.1	HG and Hx significantly increase VEGF-A _{165a} expression and reduce VEGF-A _{165b} expression relative to VEGF-A _{165a}	87
Figure 3.3.2-1	Barrier localisation of tight junction protein ZO-1 is reduced in HG and Hx in hpRPE monolayers but not ARPE-19s	89
Figure 3.3.2-2	Expression of tight junction protein ZO-1 is reduced in Hx but not HG in hpRPEs	91
Figure 3.3.2-3	Monolayer permeability is increased due to HG in hpRPEs but not ARPE-19s	92

Figure 3.3.3-1	Hx but not HG reduces SRSF1 expression in hpRPEs	93
Figure 3.3.3-2	HG induces increased nuclear SRSF1 localisation, reversed by removal of glycaemic stimulus	95
Figure 3.3.3-3	SRSF1 phosphorylation is unchanged in HG and Hx in hpRPEs	96
Figure 3.3.3-4	HG induces an increase in SRPK1 activity which causes a disassociation of the SRPK1-SRSF1 complex	98
Figure 3.3.3-5	HG appears to induce translocation of SRSF1:SRPK1 complexes to RPE nuclei	100
Figure 3.3.3-6	Hx induces nuclear localisation of SRSF1	102
Figure 3.3.3-7	Optimisation of SRSF1 and SRSF2 staining and analysis	104
Figure 3.3.3-8	SRSF1 is released from nuclear speckles in HG RPEs	105
Figure 4.3.1	SRPK1 inhibition ameliorates hyperglycaemia- and hypoxia-induced changes in VEGF-A ₁₆₅ isoform expression	117
Figure 4.3.2-1	Loss of barrier localisation of ZO-1 in HG and Hx is ameliorated by SRPK1 inhibition	119
Figure 4.3.2-2	SPHINX31 blocks HG-induced increases in RPE monolayer permeability potentially through a VEGF-A _{165b} mediated manner	121
Figure 4.3.3-1	SRPK1 inhibition blocks nuclear localisation of SRSF1 in hyperglycaemia and hypoxia but not normoglycaemia	123
Figure 4.3.3-2	SPHINX31 ameliorates HG-induced SRSF1 release from nuclear speckles	125
Figure 4.3.3-3	HG induces an increase in SRPK1 activity which causes a disassociation of the SRPK1-SRSF1 complex and increase in BRET ratio	126
Figure 4.3.4-1	Blocking PKC α - ϵ isoforms increases cytoplasmic SRSF1 localisation in normo- and hyperglycaemia	128

Figure 4.3.4-2	Inhibition of PKC α - ϵ isoforms blocks HG-induced increases in SRPK1 activity	129
Figure 5.3.1-1	SRPK1 inhibition increased VEGF-A _{165b} isoform expression in diabetic retiniae	143
Figure 5.3.1-2	SPHINX31 blocks increases in retinal permeability in diabetic Norway-Browns	145
Figure 5.3.2-1	Retinal thickness is increased in STZ-induced type-I diabetic rats which is ameliorated by SPHINX31	147
Figure 5.3.2-2	RPE and Bruch's membrane retinal layer thickness is increased in STZ-induced type-I diabetic rats and blocked by SPHINX31	149
Figure 5.3.3-1	STZ-induced diabetes or SPHINX31 does not change total vessel density and mean diameter in the upper and lower plexuses of the retina after 28-days	152
Figure 5.3.3-2	The number of dendrite branches, vascular diameter and volume of retinal vasculature are unaffected by STZ-induced diabetes or SPHINX31 after 28-days	154
Figure 5.3.3-3	SPHINX31 inhibits diabetes induced increase in acellular capillary formation	156
Figure 5.3.4-1	Permeability increases in response to glucose in a dose-dependent manner	158
Figure 5.3.4-2	Claudin-5 expression is decreased in iBRECs exposed to 30mM and 40mM glucose	159
Figure 5.3.4-3	SPHINX31 induces a reduction in iBREC monolayer impedance in both basal media and HG conditions	160
Figure 5.3.4-4	SRPK1 inhibition, osmotic and hyperglycaemic insult has no significant effect on ZO-1, Claudin-1 and VE-Cadherin in iBRECs	162
Figure 5.3.4-5	VEGF-A _{165b} ameliorates VEGF-A _{165a} -induced disruption in iBREC monolayer permeability in normo- and hyperglycaemia	164
Figure 6	Proposed mechanism of SPHINX31 in DR	190
Figure 8	The impact of HG coupled with Hx	225

Table of Figures

Table 1	VMnHC culture medium	52
Table 2	Antibodies used for western blots on RPE lysate	56
Table 3	Antibodies used for western blots on REC lysate	58
Table 4	Antibodies used for immunocytochemistry	60
Table 5	Antibodies used for immunohistochemistry	61
Table 6	Antibodies used for ELISA	62
Table 7	Settings used for XCelligence measurements	69

CHAPTER 1

Introduction

1.1 Diabetic retinopathy

1.1.1 Epidemiology of diabetic retinopathy

Diabetes mellitus is recognised as a major global epidemic, with the number of diagnosed cases increasing in all countries, most discernibly in middle income countries. Adult diabetic patients made up 8.5% of the global population in 2014, a number projected to increase to 9.9% in 2045, reflecting the rise in the number of obese or overweight people worldwide. Diabetes, and its associated complications, has a marked impact on the economy of most countries directly, due to the costs incurred by patients and healthcare organisations to treat the chronic illness, and also indirectly, due to the impact of time away from work (Ezzati, 2016). Thus, there is a major requirement for novel treatment strategies to combat this chronic disease.

The disease can be divided into either type I or type II diabetes. Type I diabetes is typically characterised as an immune or autoimmune-mediated condition (Atkinson, 2014); loss of pancreatic β -cells incapable of regeneration as a consequence of T-cell destruction results in a lack of insulin secretion and thus an impaired ability to control blood glucose levels (Devendra et al., 2004). Type II diabetes, formerly known as adult-onset diabetes due to its association obesity and aging, results from both a lack of insulin production and an insulin resistance (Donath & Shoelson, 2011). To compensate for this loss, there is an increase in β -cell number to enhance insulin secretion. However, over time this mechanism is no longer sufficient resulting in an incapability of cells to uptake glucose in an insulin-mediated manner and thus persistent hyperglycaemia (Donath & Shoelson, 2011; Rydén et al., 2013). The disease has widespread clinical complications, primarily affecting the vascular systems. Patients experience a myriad of macrovascular complications, immune dysfunctions and microvascular complications, affecting multiple organs (DeFronzo et al., 2015). Those with long-term elevated glycated haemoglobin (HbA_{1c}), a marker for plasma glucose concentration are most at risk of developing microvascular complications (Cheung et al., 2010). One of the most devastating consequence of diabetes, with regards to the largest impact on a patient's quality of life, is diabetic retinopathy (DR). This ocular disorder arises as a secondary

microvascular complication of both type I and II diabetes mellitus, and remains the leading cause of blindness across the working population of the western world (Sivaprasad et al., 2012). DR has been estimated to be the cause of 2.6 million cases of visual impairment or blindness globally in 2015, a number projected to rise to 3.2 million in 2020 (Flaxman et al., 2017). In higher income countries, the incidence of vision threatening cases have been reduced, despite the high number of diabetes cases, which has been attributed to the improved therapies and diabetes management, however this is not the case for lower and middle income countries (Liew et al., 2017). Clinical retinopathy will be present at some level, in 90% of type I and 60% of type II diabetic patients after twenty years with the disease (Klein, 2007). DR occurs in approximately one third of diabetic patients (Cheung et al., 2010) and whilst the disease doesn't appear to discriminate between sexes, onset is affected by race and socioeconomic status (Olivares et al., 2017).

Despite being classically described as a disease of the microvasculature, DR manifests itself with both a number of neuroglial and microvascular abnormalities. The pathologies have a synergistic effect, exacerbating their damage to the eye, and ultimately leading to vision impairment. Loss of tight regulation of blood-glucose concentration in diabetes appears to be the major contributing factor to DR, and prevalence correlates with duration of diabetes (Nentwich, 2015). However, the exact molecular mechanisms with which hyperglycaemia and hypoxia induces its effect on the retinal tissue remain to be elucidated (Crawford et al., 2009).

1.1.2 Physiopathogenesis of diabetic retinopathy

DR can be classified as one of two forms, non-proliferative diabetic retinopathy (NPDR) and proliferative diabetic retinopathy (PDR). Type I diabetics are at greater risk of developing PDR compared to type II patients, however the converse is true for diabetic macular oedema (DMO) (Nentwich, 2015). DR diagnosis and grading can be assessed non-invasively through fundus examinations and can be subdivided according to PDR and DMO, the primary causes of vision loss (*Fig 1.1.1*). Haemodynamically, there is a loss of blood perfusion before the onset of DR (Curtis et al., 2009). NPDR, the earliest DR

stage, involves microvascular changes that are predominately asymptomatic, even at the more advanced state (Sivaprasad & Pearce, 2018).. DR initially manifests through weakening of vessel walls, small haemorrhages and microaneurysms. As the disease progresses, there is more extensive leakage as more vessels are prone to rupture and closure of capillaries. The lack of sufficient perfusion can result in areas of ischaemia within the retina (Gardner et al., 2011).

Figure 1.1.1 summarises the conventional microvascular-associated clinical assessments of DR progression, however pre-clinical studies have also described the role of the 'dis-integration' of the neurovascular unit in DR. This occurs prior to vasculopathy in both the inner and outer retina, and is reflected by disturbed neurotransmitter signalling, of both glutamate and dopamine (Aung et al., 2014). Neuroprotective peptides, somatostatin, pigment epithelium-derived factor and erythropoietin, are all reduced in the diabetic retina. Furthermore, dendritic fields are altered and there is a reduction in proteins associated with synapses. This includes connexin, which leads to astrocyte loss. Prolonged uncontrolled diabetes can lead to apoptosis of neurons and changes in activation of glial cells. This is evidenced by impaired interconversion of glutamate and glutamine, alterations in potassium channels followed by expression of glutamate-aspartate transporter, glial fibrillary acidic protein (GFAP) and other intermediary filament proteins (Ou et al., 2020).

Breakdown of the blood retinal barriers (BRB) due to the loss of tight junctions between the retinal endothelial or epithelial cells, allows extravasation of fluid into the extracellular space of the macula (Hosoya & Tachikawa., 2013). The result is a net change in hydrostatic and oncotic pressures, favouring further fluid extravasation, leading to the development of a DMO (Wenick & Bressler, 2012). Clinically, DMO often results in the presence of hard exudates; lipid and protein deposits accumulated from the fluid leakage of the vessels. Additionally, "cotton wool spots" are the result of damage to the nerve fibre layer (Antonetti et al., 2012).. PDR is characterised by angiogenesis on the surface of the retina. The newly formed blood vessels are tortuous, leaky and chaotic in nature, with weak vessels walls allowing fluid to leak out (Ved et al., 2017). Contrasting

NPDR, the adverse effects of PDR are not contained to the retina, but branch out through the surface of the retina to invade the surrounding space (Crawford et al., 2009). In the later stages of the disease, there is a laying down of fibrotic tissue from the retina to the vitreous cavity. This tissue can contract and cause the detachment of the retina, causing blindness (Caldwell et al., 2003).

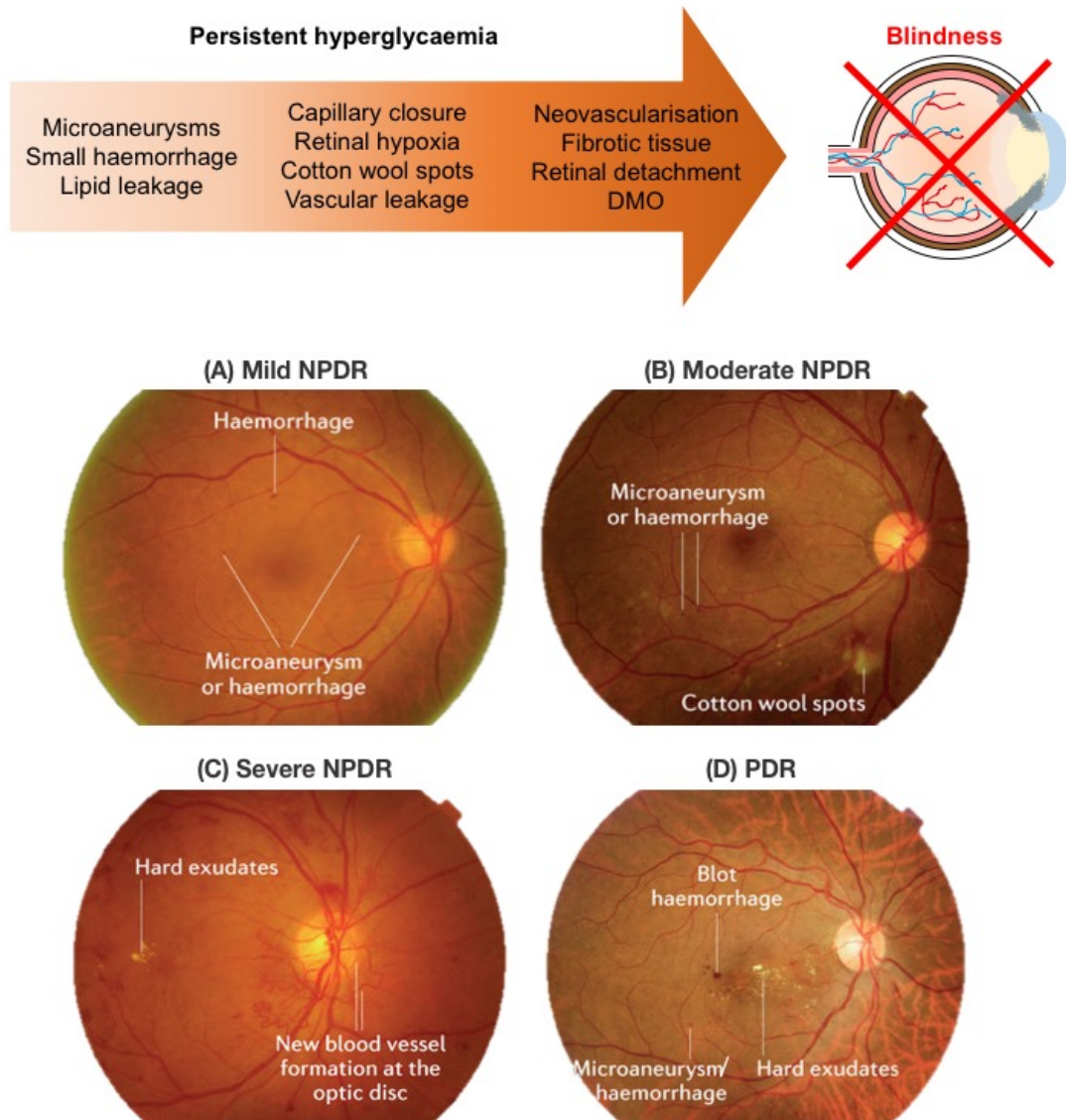


Figure 1.1.1: The pathogenesis of diabetic retinopathy can be described in four stages: mild, moderate (which can contribute to the formation of oedema), severe nonproliferative retinopathy and proliferative retinopathy. Hyperglycaemia induced ischaemia causes vessels to swell and break-down causing a leakage of fluids into the retina. As the condition advances, macula oedema can form and abnormal neovascularisation can occur on the surface of the retina, which can lead to scarring. Fibrotic tissue can contract, causing retinal detachment and ultimately blindness. Images adapted from the text in (Perrin et al., 2005). Clinical images from (Wong et al., 2016).

1.1.3 Mechanisms associated with DR

DR, in short, is a multi-stage disease progressing through the manifestation of multiple biochemical, morphological and functional changes in the retinal capillaries (Mandarino, 1992) and neurovascular unit. Morphological changes include the structural changes to retinal capillaries through the thickening of the basement membrane and loss of pericytes. The ratio of endothelial cells to pericytes is increased from approximately 1:1 to 4:1 due to this loss (Robison et al., 1985). Functional changes include an increase in vascular permeability and breakdown of BRBs. The biochemical effects occur as a result of multiple interconnecting pathways including those relevant in this thesis: poly-ol pathway; accumulation of advanced glycation end products (AGEs); increased activation of protein kinase C (PKC); hexosamine pathway (see Figure 1.1.2) (Gologorsky et al., 2012).

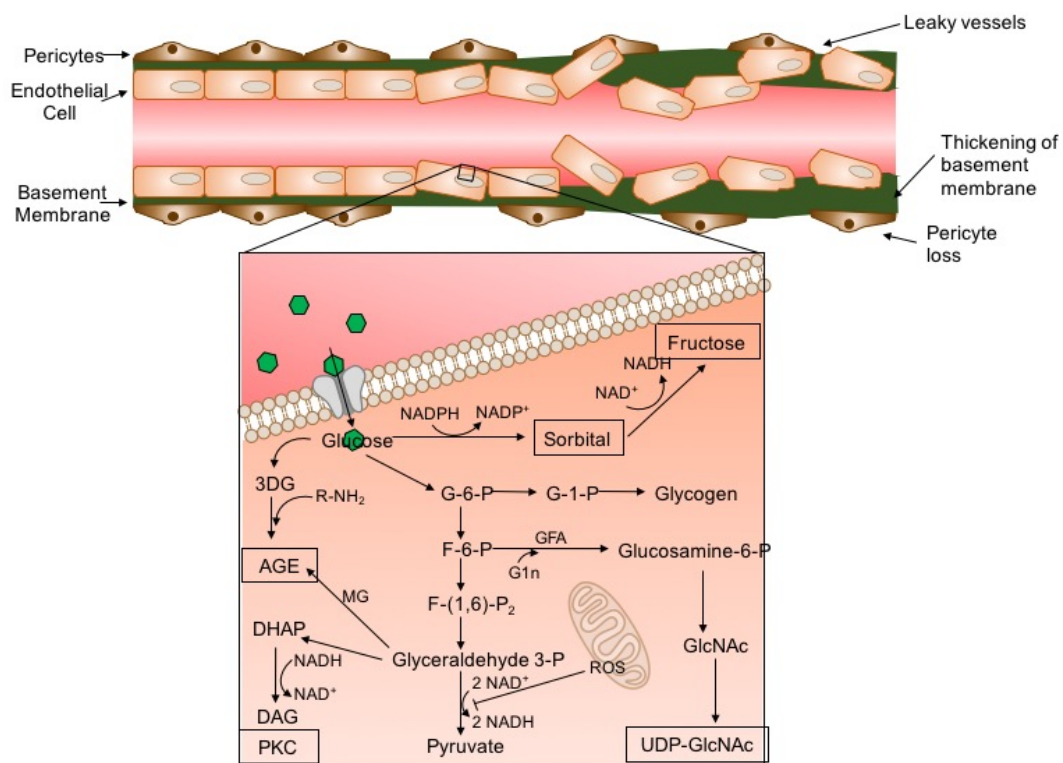


Figure 1.1.2: Schematic of pathways contributing to DR pathogenesis. Glucose is taken into cells via glucose transporters causing activation of poly-ol pathway, accumulation of AGEs and PKC activation. The net result is an increase in vessel permeability, thickening of basement membrane and pericyte loss. Image adapted from the text in (Abcouwer, 2013).

The retina is highly metabolically active and has the highest oxygen uptake and glucose oxidation relative to any other tissue. As such, this tissue is highly susceptible to hyperglycaemia-induced oxidative stress (Anderson et al., 1984). Due to uncontrolled glucose levels in diabetes, the extracellular environment is hyperglycaemic. Retinal cells are unable to effectively adapt glucose transport rates in this environment leading to increased intracellular glucose (Kaiser et al., 1993). Within the cell, glucose is metabolised through the tricarboxylic acid (TCA) cycle and electron transport chain resulting in the generation of oxygen-derived molecules: reactive oxygen species (ROS), including superoxide and hydrogen peroxide. Under physiological conditions, ROS production supports cell function and cell signalling, before undergoing detoxification through scavenging. The balance of production and removal of ROS is paramount for healthy cell function, however the diabetes-induced increase in intracellular glucose can cause hyperactivity of electron transport chain and overproduction of ROS. Cells are unable to compensate for this increase by clearing ROS at the same rate as it is produced, leading to a shift towards the pro-oxidative state known as oxidative stress (Farnoodian et al., 2016). Consequentially, biological macromolecules such as lipids, proteins, carbohydrates and DNA are damaged, cellular homeostasis is disrupted and further ROS is generated (Cutler, 2005). Additionally, oxidative stress activates metabolic pathways associated with DR pathogenesis which feedback and mediate oxidative stress creating an interrelated connection further amplifying tissue damage (Kowluru & Chan, 2007).

Intracellular glucose is reduced to sorbitol via the poly-ol pathway through aldose-reductase. In conjunction with this reaction, NADPH is converted to NADP⁺ (Obrosova & Kador, 2011). Sorbitol is impermeable to cell membranes and thus accumulates within the cell (Kinoshita, 1990). Pericytes are affected by the increased output of sorbitol, disabling their primary ability to regulate retinal capillaries and inhibit proliferation of endothelial cells in the retina. This loss of function leads to a weakness and protrusion of capillary walls known as saccular outpouching, or microaneurysm (Crawford et al., 2009). Sorbitol can be oxidised to fructose through the action of sorbitol dehydrogenase, which leads to NADH production (Obrosova & Kador, 2011). Hyperactivity of poly-ol

pathway in diabetes results in a depletion of NADPH, a molecule vital for the production of nitric oxide (NO) and the ROS scavenger, glutathione. As such, ROS is not cleared as efficiently and accumulates further, promoting oxidative stress (Kowluru & Chan, 2007). NO regulates ocular blood flow, vascular tone, and contributes to vasodilatation. Reduction of NO bioavailability causes haemodynamic alterations in an already poorly perfused retina, which may exacerbate microvascular tortuosity and enhance tissue injury (Toda & Nakanishi-Toda, 2007).

Non-enzymatic attachment of sugars to free proteins, lipids and nucleic acids to form AGEs occurs endogenously at a slow rate. In diabetes, due to the availability of glucose and various other sugars, including fructose from the poly-ol pathway, the production of AGEs is increased (Vlassara & Uribarri, 2014). AGE accumulation occurs gradually, resulting in the dysfunction of tubulin and proteins in the basement membrane of blood vessels, promoting breakdown of inner BRB (iBRB). Disruption of this barrier is further enhanced by AGE-induced breakdown of tight junction complexes between endothelial cells (Kandarakis et al., 2014). Additionally, AGEs interact with collagen to initiate cross-linking between the fibres, altering ocular blood flow (Brownlee, 2001). AGEs act on their appropriate receptors (RAGEs) to stimulate the release of tumour necrosis factor- α (TNF- α) and other proinflammatory cytokines from monocytes and macrophages (Shanmugam et al., 2003), as well as elevating ROS. Multiple cells of the retina express RAGEs including pericytes, retinal pigment epithelial cells (RPE) and retinal endothelial cells (REC), and thus are sensitive to AGE formation (Hammes et al., 1999). RAGE activation is associated with enhanced permeability of retinal vasculature, increased expression of vascular endothelial growth factor (VEGF) and postulated to induce breakdown of the outer BRB (oBRB) (Kandarakis et al., 2014).

PKC is activated due to the release of TNF- α and increased production of its endogenous activator diacylglycerol (DAG) because of hyperactivation of the glycolysis pathway. The kinase exists as one of 11 isoforms, subdivided into typical (α , β I, β II and γ), novel (δ , ϵ , η and θ) or atypical (ζ and λ). DAG is

capable of activating both typical and novel PKC isoforms, whilst Ca^{2+} only activates typical isoforms (Parekh et al., 2000). Atypical isoforms are unique in that they are not dependant on DAG or Ca^{2+} concentration and instead are activated by lipid components (Omri et al., 2013). DAG expression is increased in the retina due to elevated intracellular glucose (Koya & King, 1998), postulated to be formed *de novo* (Brownlee, 2001). Upregulation of DAG is additionally a result of aberrant hyperglycaemia-induced ROS expression, which triggers the formation of the DAG precursor, triose phosphate (Shiba et al., 1993). Activation of PKC results in a number of pathophysiological consequences, including leukocyte dysfunction and a release of pro-angiogenic factors (Kim et al., 2010). Leukocytes attach to vessel walls, in a process known as leukostasis, blocking the capillaries and therefore obstructing blood flow. This leukocyte adhesion appears to be mediated by intracellular adhesion molecule-1 (ICAM-1), upregulated because of the release of TNF- α activating the transcription factor nuclear factor kappa-B (NF- κ B), the expression of which is increased in response to PKC activation (Rahman et al., 2000). Furthermore, vascular occlusion occurs as a result of PKC-induced expression of transforming growth factor- β (TGF β), which increases collagen and fibronectin synthesis and activity (Brownlee, 2001). PKC activation has also been described to reduce expression of NO and endothelial nitric oxide synthase, further compromising retinal microvasculature (Toda & Nakanishi-Toda, 2007). PKC acts by phosphorylating proteins at the serine or threonine residue, however in diabetes this phosphorylation has been described to occur on tight junction proteins of cells of BRBs, resulting in a disruption of the tight junction complex and thus a reduction in barrier integrity (Harhaj et al., 2006). PKC β 1 and PKC β 2 are the most extensively characterised in DR, as they are hypothesised to be the most sensitive of all PKC isozymes to glucose concentration (Donnelly et al., 2004). PKC- α , - γ and - δ are also upregulated in the diabetic retina, though to a lesser extent (Idris et al., 2001). VEGF-induced mitogenic activity is predominately regulated through PKC β and PKC also increases VEGF expression in RPE in hyperglycaemic conditions (Poulaki et al., 2002). Moreover, use of PKC β inhibitors LY33531 and ruboxistaurin resulted in a reduction in both VEGF-induced retinal permeability (Aiello, 2002)

and endothelial cell activation (Xia et al., 1996) suggesting a PKC β mediation. Despite the emphasis placed on PKC β , other PKC isoforms are also impactful in DR. PKC δ is overexpressed in the diabetic retina and induces pericyte apoptosis and formation of acellular capillaries in a ROS and NF- κ B-mediated manner (Geraldes et al., 2009). Furthermore, PKC δ is evidenced to promote VEGF secretion in hypoxic RPE *in vitro* whilst PKC ζ triggers VEGF expression in hyperglycaemic RPE (Young et al., 2005).

Intracellular glucose is converted to glucose-6-phosphate and subsequently to fructose-6-phosphate. In diabetic conditions, there is an accumulation of intracellular fructose-6-phosphate due to increased cellular glucose uptake. Consequentially, the hexosamine biosynthesis pathway is highly activated in order to consume excess fructose-6-phosphate by converting it to N-acetylglucosamine-6-phosphate in a glutamine fructose-6-phosphate amidotransferase-mediated manner (Brownlee, 2001). The dominant end product of the pathway is uridine diphosphate N-acetylglucosamine, which acts to catalyse O-linked N-acetylglucosamine glycosylation (O-GlcNAc) of protein serine and threonine residues (Coucha et al., 2015). Levels of O-GlcNAc have been found to be increased in hyperglycaemic pericytes impairing their migration (Gurel et al., 2013) and promoting their apoptosis (Gurel et al., 2014).

1.1.4 Current therapies

Current therapies against DR are at both the systemic and local level. Systemic efforts aim to prevent or delay DR onset, or reverse early DR symptoms. The regulation of blood glucose and blood pressure have been confirmed by multiple studies to offer a protective role against DR (Amoaku et al., 2020). Intensive glycaemic control via extensive insulin therapy has been shown to reduce the risk for DR development and progression (Rajalakshmi et al., 2016), a 10% reduction in H1bAc resulted in a 43% reduction in the risk of retinopathy progression. Moreover, cells exhibit a metabolic memory which allows for long-term benefits of tight glucose control, even after glycaemic levels are not maintained (Nathan & DCCT/EDIC Research Group, 2014). Localised treatments focus on remedying the later stages of DR; DMO and PDR, and

include focal laser photocoagulation, intravitreal injections of anti-VEGF and steroidal agents and surgical intervention (Duh et al., 2017). Pan-retinal photocoagulation (PRP) involves inducing multiple burns of 500µm diameter across the retina by heating to 57-67°C with an argon laser. This is the treatment of choice for early stage PDR, targeting the ischaemic retina. The resultant ablation of ischaemic tissue reduces the metabolic demand of the outer retina, increasing oxygen availability to the inner retina from choroidal circulation (The Diabetic Retinopathy Study Research Group., 1981). Whilst this has been reported to decrease DR risk factors (Kozak & Luttrull, 2015), destroying retinal tissue induces a number of side effects, such as defects in peripheral vision, reduced night and colour vision and a decrease in the sensitivity of phase contrast (Royle et al., 2015). Despite this PRP remains a viable treatment option, as studies have shown it reduces the risk of blindness by at least 50% (The Diabetic Retinopathy Study Research Group., 1981). Depending on the localisation of the oedema, one therapy for DMO includes intravitreal injections of macromolecules targeting the potent mitogen pro-angiogenic VEGF, which are also found to be highly effective in regressing neovascularisation in PDR (Duh et al., 2017). They require monthly or 8-weekly intravitreal injections, for the rest of the patient's life (Shah et al., 2017) . Primary treatments include bevacizumab (Avastin, Genentech, San Francisco), a humanised, recombinant monoclonal pan-VEGF-A antibody, ranibizumab (Lucentis, Genentech, San Francisco), a fragment antibody against pan-VEGF-A and a soluble VEGF receptor fusion protein, aflibercept (Eyelea, Regeneron, NY, USA), which binds to all VEGF-A isoforms, VEGF-B and additionally a pleiotropic cytokine, placental growth factor. Intravitreal VEGF-binding activity 79-days post single 1.15mg Aflibercept injection has been found to be comparable to ranibizumab at 30 days, thus reducing the current frequency of injections (Stewart, 2012). Whilst an effective course of treatment for some patients, 50% of patients are non-responsive and affected by a number of side effects due to constant tissue damage from the needle leading to intraocular inflammation and potentially infectious endophthalmitis (Falavarjani & Nguyen, 2013). DR pathogenesis is also attributed to non-VEGF dependent inflammatory pathways, thus steroidal agents are considered (Bolinger & Antonetti, 2016). Steroids are administered through the intravitreal route, either

through peribulbar, intravitreal injection or intravitreal implant, and benefits include reduction in DMO and stabilisation of vision (Amoaku et al., 2020). Triamcinolone acetonide, dexamethasone (Stewart et al., 2016) and fluocinolone acetonide (Boyer et al., 2014; Campochiaro et al., 2012) are the agents currently recommended for use particularly for DMO cases where VEGF therapies offer no benefit, or have conditions contraindicated for anti-VEGFs, for example a recent myocardial event (Tabakci & Ünlü, 2017). Furthermore, recent studies have addressed disruption to the neurovascular unit alongside microvascular complications. Neuropeptide Y has been found to offer a potential protective role in DR, promoting vascular integrity whilst inhibiting glial cell apoptosis (Ou et al., 2020). Despite some success of these pharmacological interventions, the issue of non-responders remain, and multiple promising pre-clinical candidates have failed to translate clinically (Rodrigues et al., 2018). Thus, there is an urgent need to develop drugs against novel targets with different modes of entry, with multiple research groups have identified potential targets (Batson et al., 2017; Bolinger & Antonetti, 2016; Kern et al., 2010). Where pharmacological interference and PRP has failed, a vitrectomy is necessary to treat later stage PDR. This surgery can be performed with or without peeling of the internal limiting membrane of the retina to treat DMO. Although vitrectomies do effectively treat retinal thickening, only 30% of patients report visual improvements, and actually 20-30% of patients experience visual loss (Newman, 2010).

1.2 Blood-Retina Barrier

Retinal homeostasis is regulated by two BRBs: iBRB and oBRB. The inner barrier is formed through the cell-cell tight junctions of capillary endothelium. The formation of the outer barrier is also due to tight junctions, however these are formed between RPE cells across the outer edge of the retina, separating it from the choroid (*see Figure 1.2*) (Desjardins et al., 2016). These barriers protect the neural retina from retinal and choroidal circulation, controlling the flux of fluid and molecules across cells. DR results in the breakdown of both of these barriers, although emphasis in the literature has been placed on iBRB (Marreros et al., 2005). Additional support to the BRB is provided by astrocytes

and Müller cells, the primary site of nutrient storage. Müller cells support both the retinal blood vessels and neurons through uptake and recycling retinoic acid compounds, ions and neurotransmitters such as glutamate and γ -aminobutyric acid. Furthermore, they aid metabolism through supply of nutrients, help regulate blood flow through expression of vasodilators and vasoconstrictors and support BRB maintenance via secretion of anti-angiogenic factors including pigment epithelium-derived factor (PEDF) and thrombospondin-1 (Eichler et al., 2004). Astrocytes are also supportive, they provide nutrients and physical support for neurons, whilst their foot processes envelop endothelial cells to maintain BRB integrity. Their role as a secretome involves expression of growth factors such as TGF β , glial-derived neurotrophic factor, angiopoietin-1 and basic fibroblastic growth factor. Importantly for the BRB, astrocytes express sonic hedgehog, which enhances barrier properties whilst decreasing inflammation (Ly et al., 2011).

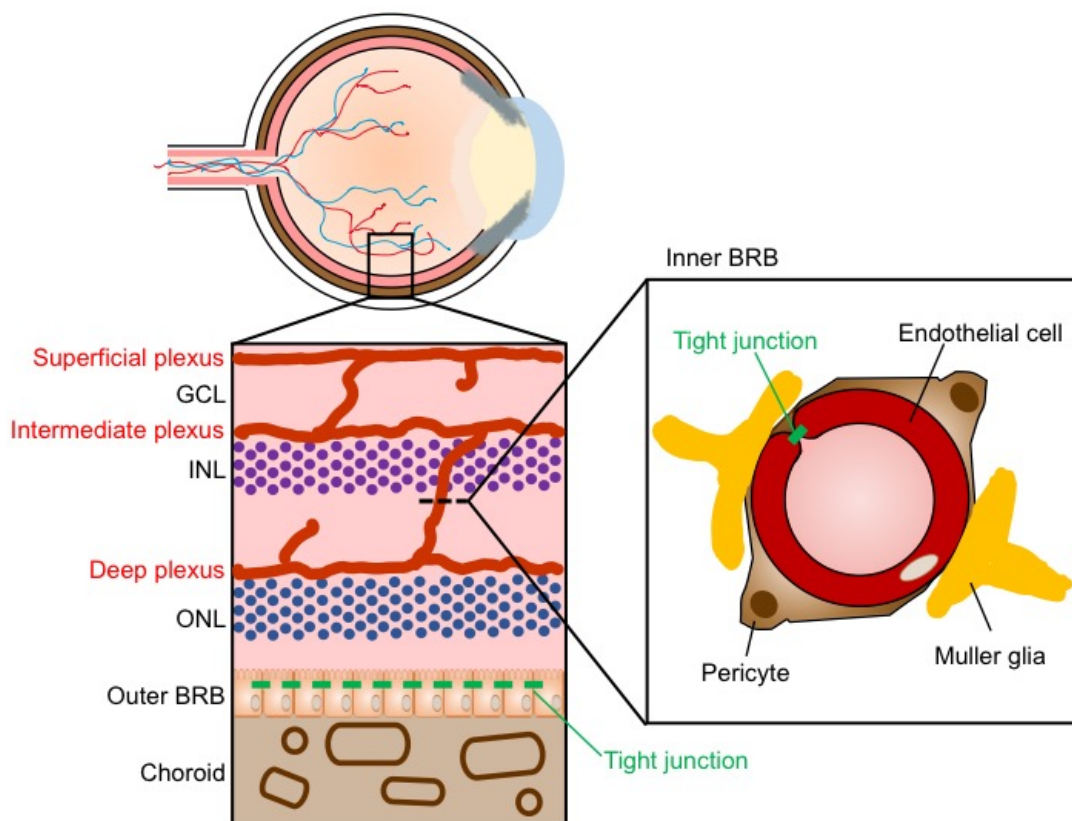


Figure 1.2: Schematic of blood-retinal barriers (BRBs). The retina is made up of a number of layers, including the ganglion cell layer (GCL), inner (INL) and outer nuclear layers (ONL), which are maintained by the inner and outer BRBs. The inner BRB surrounds the retinal circulation and is comprised of tight

junctions between endothelial cells of retinal vasculature, and supported by pericytes and glial cells. The outer BRB protects the neural retina from the highly vascularised and fenestrated choroidal circulation through tight junctions between retinal pigment epithelial cells.

1.2.1 Inner Blood-Retina Barrier

The retinal vasculature is divided into three plexuses, the superficial, intermediate and deep plexus which provide nourishment and removal of waste products to the inner two thirds of the retina to maintain a constant milieu (Morimoto, 1998). Junctional complexes, known as tight junctions, exist on the basal lamina of vessel RECs, regulating the selectively permeable barrier. The iBRB is also described as a glio-vascular unit due to the presence of glial cells (primarily Müller cells, but also astrocytes) supporting the endothelial cells alongside pericytes (Hosoya & Tachikawa, 2013). The tight junction unit consists of transmembrane, scaffolding and signalling proteins. Occludin, claudin and junctional adhesion molecule (JAM) are the predominant transmembrane proteins. Cytoplasmic tails of the former two are linked to the cytoskeleton via accessory proteins, such as ZO-1. Supporting tight junctions, adherens junctions composed of vascular endothelial-cadherin (VE-Cadherin) and catenins act to maintain barrier integrity (Shakib & Cunha-Vaz, 1966). Pericytes induce the expression of ZO-1 and occludin mRNA and protein in their associated REC in normoxic conditions to support junctional maintenance. Moreover, pericytes are able to partially ameliorate hypoxia-induced loss of ZO-1 and occludin (Wang et al., 2007). Exposure to NO, ROS and VEGF-A, such as that in DR, disrupts junctional complexes inducing an increase in vascular permeability. In particular relevance to this thesis, VEGF-A has been described to induce rapid phosphorylation of ZO-1 and occludin, increasing REC monolayer permeability (Antonetti et al., 1999). As such, ZO-1 is a useful marker for BRB permeability. VEGF secreted from Müller cells promotes iBRB breakdown (Wang et al., 2010), however RECs also secrete VEGF in hypoxic conditions to autonomously regulate the iBRB (Aiello et al., 1995).

1.2.2 Outer Blood-Retina Barrier

The oBRB is formed from the tight junctions between cells of the RPE monolayer, which separates the neural retina and fenestrated choroidal

capillaries. The barrier is responsible for the nourishment of only a third of the retina, primarily photoreceptors, from the blood supply of the choroid, despite supplying 80% of the blood circulation to the retina (Cunha-Vaz, 1979). Choroidal vessel fenestration allows the transport of larger molecules such as fatty acids and glucose from the circulation, a supply vital for neural activity. However, the large leaky blood supply risks the retina being exposed to potentially deleterious macromolecules, thus the integrity of oBRB is crucial for protection and maintenance of retinal function (Simó et al., 2010). RPEs manage the bi-directional flow of ions and nutrients to the highly metabolically active photoreceptors, removal of waste material and maintain an ionic gradient for phototransduction (Shakib & Cunha-Vaz, 1966). They transport glucose via GLUT1 and GLUT3 channels. Furthermore, these cells have a role in the absorption of light to protect against photooxidation, and regulate the visual cycle, through the exchange of 11-cis retinal and all-trans-retinol (Scoles et al., 1997). Polarity is an important property of RPEs, vital to their function, and is present due to tight junction localisation to the apical side of cells. In addition, the apical surface contains villi-like structures that intercalate with the lipid-rich outer segment disks of rod and cone photoreceptors. These structures facilitate the phagocytosis of photoreceptors, of which approximately 10% are renewed daily (Young & Bok, 1969). Polarisation of RPE defines their role as a secretome; they emit various cytokines and inflammatory mediators apically by the NaKATPase channel, or on the basal side through anion channels (Strauss, 2005). Pro- and anti-angiogenic factors are expressed from RPE, including VEGF, whose secretion occurs both apically and basolaterally in healthy cells, predominately on the basal side to maintain choroidal endothelium and fenestrae. (Kannan et al., 2006). Inflammatory cytokines and chemokines are also secreted, protecting against damage to the neural retina, (Ponnalagu et al., 2017). In addition to this, RPE protects against oxidative stress through antioxidant, including superoxide dismutase, production (Kowluru & Chan, 2007).

DR results in a switch in directionality of VEGF secretion, it is excessively secreted on the apical side of RPE (Kannan et al., 2006). Apical expression of VEGFR2 has been associated with diabetes-induced breakdown of tight junction complexes and increase in oBRB permeability (Desjardins et al.,

2016). oBRB barrier disruption occurs concomitantly with hyperglycaemia, even in early DR, as fluorescent dye leakage has been observed across RPE monolayer in a diabetic *in vivo* model. Furthermore, large breakpoints and intensive fluorescent dye flux across RPE was observed in an oxygen-induced retinopathy model, highlighting the impact of hypoxia on oBRB integrity (Xu et al., 2011). They have also been reported to secrete a pro-angiogenic protein: angiopoietin-like protein 4 (ANGPTL4) in response to hyperglycaemia (Yokouchi et al., 2013). With regards to DMO formation, breakdown of RPE monolayer has also been implicated, as RPE are unable to sufficiently clear fluid leakage from blood and excessive water. Whilst this view could be described as simplistic as DMO is not solely the result of protein and water leakage, the general consensus is that sufficient evidence exists to conclude RPE barrier breakdown is involved in oedema formation (Xia & Rizzolo, 2017). Non-angiogenic factors such as IL-6, IL-8 and MCP-1 are upregulated in the diabetic eye (Ponnalagu et al., 2017). These inflammatory markers have been proposed for use as biomarkers for DR progression, as they have a strong correlation with DR staging (Crane et al., 2000; Dong et al., 2012). This highlights the potential of therapeutically targeting RPE for DR and DMO treatment. In fact, proteomic studies have implicated multiple proteins involved in membrane dynamics, cell metabolism, cytoskeleton adhesion, junctional complex and cell survival secreted from RPE in DR progression (Decanini et al., 2008). The level of anti-oxidants are also reduced in hyperglycaemic RPE, leaving the retina susceptible to oxidative stress (Kowluru & Chan, 2007).

With regards to glial cells, Müller cells are sensitive to glucose concentration but able to withstand shifts in oxygen levels so long as the glucose concentration is maintained, which is indicative of their dependence on glycolysis rather than oxidative phosphorylation for ATP production (Winkler et al., 2000). DR results in a decrease in neurotransmitter and potassium uptake early on in the disease, contributing to glutamate toxicity within the retina. Hyperglycaemia also induces Müller cell activation, indicated through expression of GFAP, promoting the release of growth factors, cytokines and chemokines including VEGF, IL- β , IL-6 and tumour necrosis factor- α (TNF- α), driving BRB breakdown and DR progression (Coughlin et al., 2017). Astrocytes

however exhibit reduced GFAP, attributed to early cell loss, as well as a reduction in gap junction protein expression. These changes in DR have been linked to neuronal dysfunction of the retina, with astrocyte loss occurring prior to Müller cells (Ly et al., 2011).

1.3 VEGF and Diabetic Retinopathy

The retina has played a pivotal role in the discovery of vascular endothelial growth factors (VEGFs) characteristics and function. The idea of pathological angiogenesis being stimulated by a secreted factor was first proposed by Isaac Michaelson in 1948, who discovered a mystery angiogenic factor 'Factor X' in the ischaemic retina (Michaelson, 1948). Following his ground-breaking discovery and, after forty years of pioneering research from different groups, this mystery factor was named vascular endothelial growth factor or VEGF (Ferrara & Henzel, 1989). Over the ensuing thirty years, there have been a plethora of findings amassed, implicating VEGF with a multitude of roles in growth, development, cancer and diabetes, amongst others. The impact of this protein is to such an extent, that a Nature review published in 2017 described the gene encoding the VEGF protein as the fourth most researched gene of the human genome (Dolgin, 2017). VEGFs are part of a superfamily of growth factors whose members include VEGF-A (hereafter known as VEGF) VEGF-B, VEGF-C VEGF-D, and placenta growth factor (PGF). The family is unique in their additional role in vascular permeability alongside angiogenesis. VEGF acts upon its cell surface receptors: VEGFR1, VEGFR2, neuropilin-1 and neuropilin-2 to mediate many intracellular pathways (Ferrara et al., 2003).

1.3.1 VEGF expression in the diabetic retina

The principal pro-angiogenic factor in DR is VEGF, present at high concentrations in vitreous and aqueous fluids of patients due to the consistent upregulation in retinal neovasculature, predominately in retinal pigmented epithelial cells (Adamis et al., 1993), glial cells and intravitreal fibroblasts (Malecaze et al., 1994). Expression is correlated with glucose availability and has been shown in differing cell lines to increase in response to both hypo- and hyperglycaemia (Caprnda et al., 2017). *In vitro* studies have confirmed that high

glucose (18.5 or 30mM) increases VEGF secretion in retinal endothelial cells, retinal pigment epithelial cells and human retinal pericytes, although glucose deprived conditions induced a pro-angiogenic phenotype in retinal endothelial cells compared to high glucose (Caprnda et al., 2017). In Müller cells however, 30mM glucose reduced VEGF secretion compared to 5mM glucose. PKC activation induces VEGF release (Koya & King, 1998; Williams et al., 1997), which, through a positive feedback loop, causes further activation of PKC and mediates its pro-angiogenic effects (Xu et al., 2008). Vascular occlusion is suggested to be the primary reason for hypoxia, however this is still up for debate. Another hypothesis is that increased flux through the poly-ol pathway generates an imbalance between the levels of pyruvate and lactate, causing a pseudohypoxia (Williamson et al., 1993).

In the ischaemic retina, VEGF is upregulated due to the formation of hypoxia-inducible factor-1 (HIF-1), a heterodimer responsible for orchestrating the cellular response to oxygen saturation, consisting of alpha and beta subunits (Ozaki et al., 1999). HIF-1 α is ubiquitinated and degraded under normoxic conditions, due to dihydroxylation by a prolyl hydroxylase. During hypoxia, such as that seen in DR, there is an inactivation of prolyl hydroxylase causing an accumulation of HIF-1 α . This leads to the formation of HIF-1, as accumulating alpha subunits bind HIF-1 β . Newly formed HIF-1 translocates to the nucleus, binding hypoxia response element (HRE) based in the promoter region of the VEGF gene, transactivating it together with a multitude of other genes. Thus, VEGF, alongside the several other HIF-1 regulated gene products, produces the characteristic retinal neovascularisation phenotype seen in PDR (Campochiaro et al., 2016).

1.3.2 VEGF and permeability

Permeability of a vessel can be defined by the ability of a vessel wall to impede movement of solutes between the intravascular and extravascular spaces. However, flux of a solute is determined not just by the properties of the vessel wall, but by a number of physical variables, such as hydrostatic and osmotic pressures; electrical and chemical gradients; transport aids like vesicles and channels; and the properties of the fluid itself (Dejana, 2004). Angiogenesis,

the formation and growth of new blood vessels from pre-existing vessels, is often coupled with an increase in vascular permeability (Eliceiri et al., 1999). Vascular growth requires endothelial cells to migrate and proliferate, weakening junctional strength and causing an increase in vascular permeability (Corada et al., 2002). The mechanism of action with which VEGF mediates vascular permeability is complex and not completely understood, perhaps due to the contribution of other factors such as erythropoietin, angiotensin-1 (Abcouwer, 2013), and FAK (Chen et al., 2012). Activation of the PI3K-Akt pathway (*Fig 1.3*) in DR downregulates the expression of GLUT1, impeding nutrient uptake of photoreceptors (Kim et al., 2007). The fact that vascular permeability increase is a net result of the interplay between several signalling pathways (*see Fig 1.3*) makes it difficult to pinpoint one specific mechanism (Bates, 2010). However, it is clear that a major part of the permeability increase is due to phosphorylation and reorganisation of specific junctional proteins.

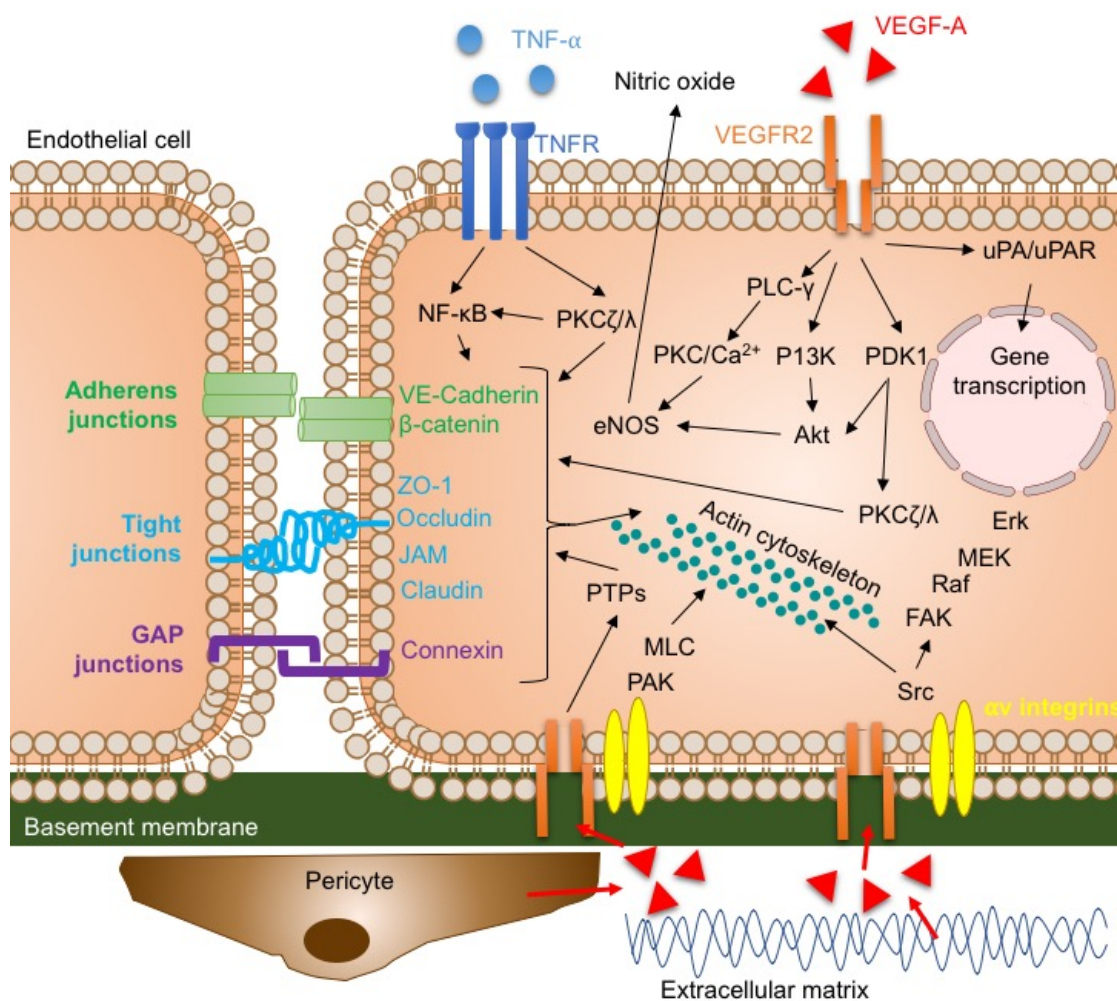


Figure 1.3: Schematic of some permeability-inducing intracellular signalling pathways. VEGFR2 activation in response to plasma or serum VEGF and inflammatory stimulation on cell-cell junctions. Additionally VEGF bound to extracellular matrix or secreted from pericytes and glia also initiate signalling pathways. VEGFR2 interacts with integrins, inducing signalling to cell-matrices and actin cytoskeleton with Adherens, tight and gap junctions are disrupted through activation of protein tyrosine phosphatases (PTPs) and Src. Protein kinase C (PKC) activation phosphorylates tight junction proteins disrupting complexes and weakening cell-cell junctions. Release of nitric oxide induces vasorelaxation. Image adapted from text in (Weis & Cheresh, 2005) and (Bolinger & Antonetti, 2016) .

VEGF is able to exert its action through tyrosine kinase receptors. Activation of VEGFR1, causes different effects, depending on the pathophysiological environment. In the diabetic retina, activation of VEGFR1 by placental growth factor (PIGF) promotes angiogenesis and survival of cells in the hypoxic environment (Shih et al., 2003). Inhibition of this receptor prevented vascular leakage, leukostasis and junctional breakdown in a rat model of diabetes, however the full extent of VEGFR1 involvement in DR are as yet unknown (He et al., 2015). Activation of VEGFR2 induces a cascade of a number of inter-linking downstream pathways (*summarised in Fig 1.2.1*). The primary effects are phosphorylation of junctional proteins, cell proliferation through the activation of mitogen-activated protein (MAP) (Unemori et al., 1992) and cell migration by matrix metalloproteinase (MMP)-mediated degradation of basement membrane. Interestingly, HIF-1 upregulates gene expression for VEGFR1, the higher affinity VEGF receptor, but not VEGFR-2, perhaps as a protective measure against the toxic hypoxic environment (Gerber et al., 1997).

Reports of solute permeation across a tight junction are still highly varied, but the general consensus is that movement occurs via two pathways, distinct by their selectivity to electrostatic characteristics and size (Itallie & Anderson, 2006). Solutes with a diameter below 8-9Å pass through claudin pores, with the ability to discriminate by charge, along an electrochemical gradient. The second pathway is speculated to involve a breakage and subsequent sealing of tight junctions to allow larger solutes through (Itallie et al., 2009). Tight junctions are primarily comprised of two types of transmembrane proteins, occludins and claudins, which span the membrane four times. The proteins are cross-linked with zonula occludin-1 (ZO-1) on the cytoplasmic surface of the plasma

membrane (Itoh et al., 1999). ZO-1 is a 210kDa membrane-associated guanylate kinase required for the assembly of tight and adherens junctions (Stevenson et al., 1986). It is the founding member of the TJ-MAGUK family, alongside ZO-2 and ZO-3, all with roles associated with tight junctions. The family is defined by the presence of an actin binding region, acidic domain and a region homologous to guanylate kinase (GUK), a Src homology-3 (SH3) domain and three post-synaptic density/discs-large/ZO-1 (PDZ) domains (Beatch et al., 1996). ZO-1 is essential for growth, development and morphogenesis, as knockout of the gene is embryonically lethal (Katsuno et al., 2008), the expression of ZO-1 in endothelial cells is inversely proportional to blood-retinal barrier permeability (Choi et al., 2007). VEGF-induced PKC pathway results in the phosphorylation of ZO-1 and another tight junction protein, occludin. Phosphorylation leads to the formation of abnormal relationships with other proteins of the junctional complex and therefore a weakness in cell-cell contacts, increasing vascular permeability (Antonetti et al., 1999; Pedram et al., 2002).

1.3.3 VEGF-A_{165b}

The human *vegf* gene is 14kb long containing eight exons alongside seven introns. Exons are alternatively spliced at exons six and seven from pre-RNA to produce at least seven isoforms: the major VEGF₁₈₉, VEGF₁₂₁ and VEGF₂₀₆ and the minor VEGF₁₈₃, only found in the iris; VEGF₁₄₅ VEGF₁₄₈ and VEGF₁₆₅ (Ferrara et al., 2003). In 2002, an additional event of alternative splicing of VEGF pre-mRNA was discovered, resulting in an anti-angiogenic phenotype due to the expressed protein (Bates et al., 2002). An alternative splice site coding for 6 different amino acids (CDKPRR to SLTRKD) at the distal end of VEGF gene results in two families of isoforms with opposing functionality, VEGF_{xxx}a and VEGF_{xxx}b respectively. The 'a' isoforms, henceforth named VEGF_{xxx}a, are spliced at the proximal end and have proangiogenic properties, with the ability to increase vascular permeability. Conversely, the 'b' isoforms, henceforth named VEGF_{xxx}b, are the result of distal splicing and are antiangiogenic and protective against vascular leakage (Perrin et al., 2005). In 1998, Koya and King identified a C-G polymorphism at the 5' untranslated region (UTR) of VEGF gene as a DR risk factor, emphasising the importance

of transcriptional regulation or splicing events in DR (Koya & King, 1998). VEGF_{xxx}b isoforms retain receptor binding and dimerisation domains, thus are able to bind to receptors, competing with VEGF_{xxx}a isoforms at a one-to-one ratio (Varey et al., 2008). However, binding to the receptor does not stimulate its activation, conversely, it inhibits the downstream cascade usually triggered by VEGF_{xxx}a isoforms. The effect is predicted to be due to the loss of net positive charge between 'a' and 'b' isoforms, as positively charged arginine is replaced by neutral leucine and aspartic acid. Currently, only four VEGF_{xxx}b variants have been described in further detail: VEGF₁₁₁b VEGF₁₂₁b, VEGF₁₆₅b and VEGF₁₈₉b. VEGF₁₂₁b has been found to inhibit tumour neovascularisation and tumour growth in an *in vivo* tumour mouse model, but requires further investigation to elucidate its properties (Rennel et al., 2009). VEGF₁₆₅b is the most investigated of the 'b' family and has been shown to decrease migration and proliferation of cultured endothelial cells through its action on VEGFR2. VEGF₁₆₅b is unable to bind to heparan sulphate or neuropilin-1, a VEGFR2 co-receptor (Suarez et al., 2006). In addition, VEGF₁₆₅b has been shown to modulate VEGFR1-STAT3 signalling, decreasing perfusion in peripheral arterial disease (Ganta et al., 2017). However, VEGF₁₆₅b has also been hypothesised to induce transient increases in vessel permeability in pre-eclampsia which can be reversed with neutralising antibodies targeted against the isoform (Bills et al., 2011). Expression of VEGF₁₆₅b is decreased in the diabetic retina, whilst being preferentially expressed over VEGF₁₆₅a in non-diabetics. Thus, this apparent 'switch' in splicing from anti- to pro- angiogenic isoforms of VEGF could be a contributing factor to the development of DR (Perrin et al., 2005). Furthermore, VEGF₁₆₅b appears to prevent diabetes-induced and thus VEGF₁₆₅a-induced breakdown of tight junctions, vascular permeability and growth within the retina, and thus provides a potential target for DR therapy (Ved et al., 2017).

1.4 SRPK1

1.4.1 SR Proteins

The role of splicing: the removal of introns from precursor mRNA, in gene expression, cellular differentiation and our overall biological complexity is

paramount. Splicing of pre-mRNA occurs during transcription and is regulated by the spliceosome, a macromolecular complex consisting of five small nuclear ribonucleo-proteins (snRNPs): U₁, U₂, U₅ and base-paired U₄/U₆, and over 100 auxiliary proteins (Yang et al., 2007). The complex is important for recognition of 5' and 3' splice sites and catalyses exonic binding and intron removal thorough transesterification. Cis-acting RNA sequence elements and trans-acting RNA binding proteins (RBPs) are essential for pre-mRNA recruitment to the spliceosome. Serine-rich (SR) proteins are a family of RBPs, that interact with the spliceosome (Naro & Sette, 2013). They modulate the binding of exonic and intronic splicing enhancers and silencers, selecting splice sites. The importance of phosphorylation (and de-phosphorylation) of SR proteins is paramount for the efficient assembly of the spliceosome and catalysis of splicing reactions. Their structure is characterised by the inclusion of one or two RNA binding domains and an RS domain within the C-terminus. The RS domain functions as a nuclear localisation signal stimulating transport of the splicing factors into the nucleus and nuclear speckles to induce their effect (Kataoka et al., 1999). In addition, the phosphorylation of this domain is vital for binding to the C-terminus of RNA polymerase II, thus co-ordinating splicing (Gonçalves & Jordan, 2015). Within the nucleus, SR proteins tend to accumulate within the nuclear speckles, however they require release in order to form their action in transcriptional regulation. Their release is modulated through phosphorylation (Kim et al., 2016).

1.4.2 SRPK1

The Serine-rich protein kinase (SRPK) family of enzymes, are responsible for the modulation of a highly conserved family of splicing factors, SR proteins. Their primary role, along with Cdc-like 2 kinases (CLKs), is to phosphorylate dipeptide Arginine-Serine (RS) repeats thus inducing structural changes within proteins. The inclusion of an RS domain within different proteins vary in location and number of repeats, and modifications to this domain could induce changes in interactions with other proteins or RNA molecules (Voukkalis et al., 2016). Whilst CLKs have additional phosphorylation targets, such as lysine, SPRKs retain a remarkable specificity to RS (Aubol et al., 2013). Their structure is characterised by the inclusion of a unique spacer sequence splitting the

catalytic domain in two. This spacer has no effect on the functionality of the protein but instead its cellular location due to the inclusion of a cytoplasmic retention signal (Zhong et al., 2009). SRPK1, the prototypical member of the SRPK family, is a ubiquitous and has been proposed to be constitutively active kinase. SRPK1 binds centrally to RS domains and then proceeds phosphorylating in the direction of the N-terminus (Aubol et al., 2013). The protein is regulated via its cellular localisation mediated by the spacer rather than activity (Gonçalves & Jordan, 2015). Within the cytoplasm, SRPK1 interacts with heat-shock proteins (Hsp) Hsp70/Hsp90 via their co-chaperones Aha1/Hsp40. This complex assists with folding of SRPK1 to its active state and protects against degradation. Stress signalling can abrogate binding of the complex and induce nuclear shuttling of SRPK1. CLK-1 assists movement of SRPK1 across the nuclear pores by reversibly binding to SRPK1. Phosphorylation of SRPK1, causes hyperphosphorylation of SR proteins during cellular stress induced by sorbitol, like that seen in DR (Aubol et al., 2013).

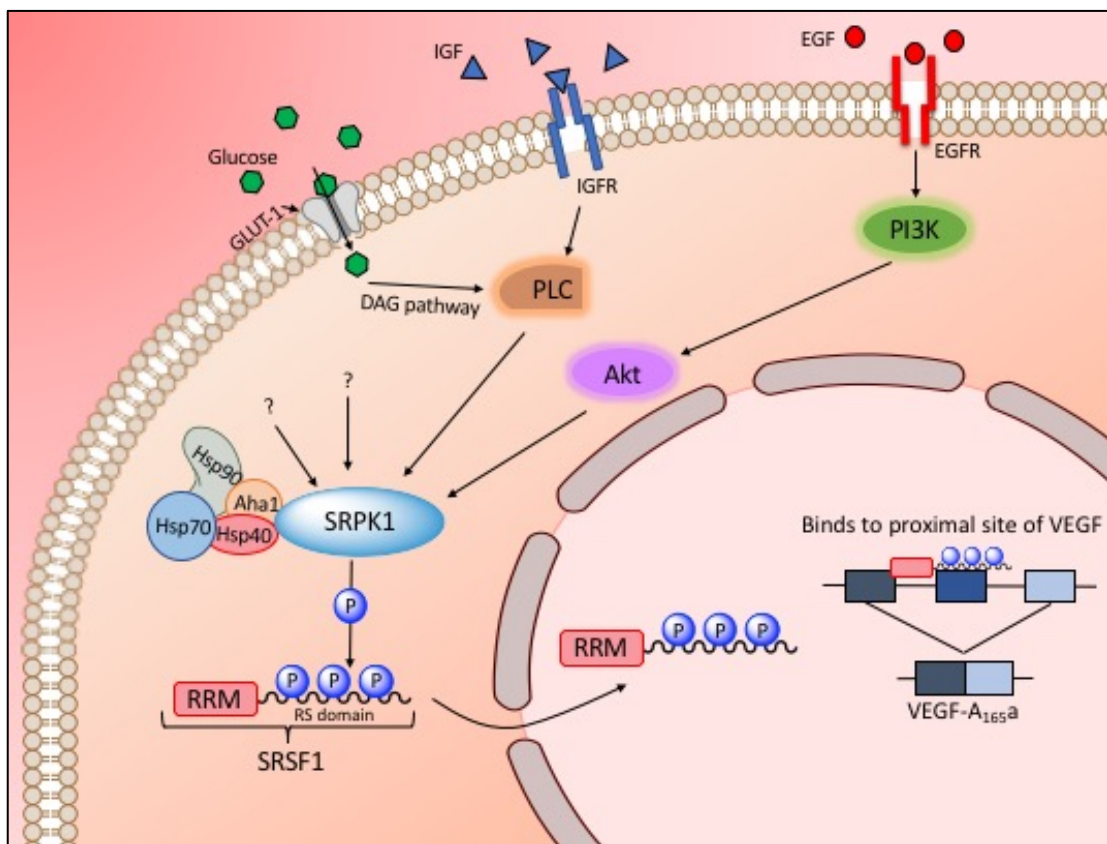


Figure 1.4: Schematic of what is currently known of the mechanism of SRPK1-SRSF1 axis in VEGF alternative splicing. Image adapted from the text in

(Batson et al., 2017; Manetti et al., 2011; Mavrou et al., 2015; Nowak et al., 2008; Nowak et al., 2010; Wang et al., 2016; Zhou et al., 2012).

Role in VEGF splicing

There is still much to be discovered about alternative slicing of VEGF, especially with regards to VEGF_{xxx}b isoforms, however, SR proteins: SRSF6 (SRp55), SRSF1, SRSF2 and perhaps SRSF5, have been recognised to play a role (Biselli-Chicote et al., 2017). Nowak et al found SRSF1 and SRSF5 potential binding sites next to the proximal splice site on the 3' end of the VEGF gene. Despite the putative binding site, SRSF5 had no effect on VEGF expression. Distal splice site selection could be attributed to SRSF6, due to the discovery of cluster of SRSF6 binding sites near the distal site (Nowak et al., 2008). A striking positive correlation between VEGF₁₆₅b expression and SRSF6 expression was discovered in skin cells. In addition, this correlation was also observed between VEGF₁₆₅b and cytokine, transforming growth factor- β (TGF β), thus acting as a contributing factor to VEGF₁₆₅b expression. The two together could be the cause of an increased expression of VEGF₁₆₅b in these cells (Manetti et al., 2011). As mentioned previously in section 1.1.3, there is activation of PKC and increased TNF- α levels in the diabetic retina, both of which have been attributed to proximal splice site selection (Nowak et al., 2008; Nowak et al., 2010). SRSF2 has been described to have a unique role in transcriptional activation and elongation and is the only SR protein to be constantly present within the nucleus. SRPK1 has no interaction with SRSF2, whose phosphorylation is mediated by SRPK2 (Wang et al., 1998). SRPK1 phosphorylates the first 12 serine residues within SRSF1 RS domain, enabling the SR protein to bind to transportin-SR2, a nuclear import factor. Thus, SRSF1 is shuttled to the nucleus where it is phosphorylated further by SRPK1 or CLK-1 in the distal RS domain. The complete phosphorylation of the RS domain instigates a dispersion of SRSF1 where it accumulates in the nuclear speckles, associating with the spliceosome via RNA polymerase II (Gonçalves & Jordan, 2015). Here, it stimulates the selection of the proximal splice site of VEGF pre-mRNA, leading to the production of the VEGF_{xxx}a isoform. Stimulation of HEK293 cells by IGF-1 induces an increase in pro-angiogenic VEGF isoforms, which could be impeded by blocking PKC or SRPK1, providing clear evidence

for the role of this SRPK1 in VEGF gene splicing (Nowak et al., 2010). Furthermore, knockdown of SRPK1 induced an increase in VEGF_{165b} expression in melanoma and colon cancer cell lines (Mavrou et al., 2015). Thus, inhibition of the SRPK1-SRSF1 axis may be a useful treatment option for DR.

1.4.3 SPHINX31

Small molecule SRPK1 inhibitors are currently in development from multiple groups (Fukuhara et al., 2006; Morooka et al., 2015; Székelyhidi et al., 2005). Whilst they successfully inhibit SRPK1, some also target SRPK2 and other closely related kinases, and lack potency. The 3-(trifluoromethyl)anilide scaffold SPHINX31 has excellent potency and selectivity for SRPK1. The group utilised the crystal structure of SRPK1 to develop an inhibitor to target unique structural features of SRPK1, resulting in a highly potent and selective inhibitor. The compound has an IC₅₀ of 5.9nM, and occupies the binding pocket of SRPK1 exploiting an unusual helical insert close to the kinase hinge region inducing a backbone flip. Differential scanning fluorimetry to screen SPHINX31 against SRPK1 and 50 other closely related kinases revealed high interaction with SRPK1. SRPK2 affinity to SPHINX31 was approximately 50-fold less than SRPK1, same as CLK-1, whilst CLK-4 had 100-fold less binding affinity. The inhibitor is ATP-competitive and has been described to induce a switch in splicing in RPE cells from VEGF-A_{xxx}a to VEGF-A_{xxx}b. Excitingly, the compound reaches the back of the eye through topical administration (Batson et al., 2017). SPHINX31 will be used over the course of this study to inhibit SRPK1 kinase activity.

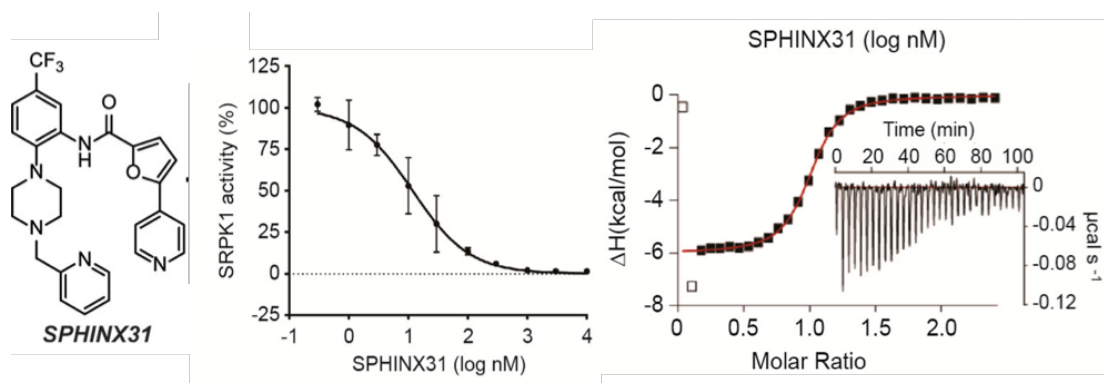


Figure 1.5: Chemical structure of SPHINX31. Left graph is radioactive SRPK1 kinase assay dose response with SPHINX31. Right graph is isothermal calorimetry of SPHINX31 binding to SRPK1 (Batson et al., 2017).

1.5 Hypothesis and Aims

Pro-angiogenic, permeability inducing VEGF-A has been clearly implicated in the progression of DR. The alternative VEGF-A_{xxx}b isoform family offers protection against DR-induced pathologies *in vitro* and in animal models as this restores of VEGF-A_{xxx}a: VEGF-A_{xxx}b ratio. I will test the hypothesis that SRPK1 inhibition may be a novel, more advantageous approach of restoring isoform balance because it may induce a cellular 'switch' in splicing of VEGF-A from the pro- to anti-angiogenic isoform to physiological levels. Topical administration of ocular drugs offer benefits against the more popular intravitreal route as it results in fewer inflammatory side-effects, thus I also hypothesise that topical SPHINX31 therapy is a novel approach to treating DR. Furthermore, I hypothesise that the oBRB is involved in DR progression and targeting this barrier will successfully treat diabetes-induced pathology.

I will test these hypotheses with a number of experiments aiming to:

1. Develop a reproducible model of RPE monolayer of the oBRB *in vitro* and determine the effects of diabetic-mimicking conditions on VEGF-A isoform expression and monolayer permeability.
2. Establish the role of SRPK1 in response to hyperglycaemic and hypoxic conditions in this *in vitro* model.
3. Inhibit SRPK1 in this *in vitro* model and determine changes in VEGF-A expression, SRPK1 activity and monolayer permeability.
4. Assess whether a four-week *in vivo* model of type-1 diabetes will induce changes in retinal permeability and thickness and, if so, evaluate the response to topical administration of an SRPK1 inhibitor.

5. Determine changes in vascular parameters and acellular capillary formation in this *in vivo* model, if any, and assess the response to SRPK1 inhibition.
6. Compare the impact of SRPK1 inhibition in each BRB via use of a REC monolayer to establish how *in vivo* retinal changes, if any, are occurring.

CHAPTER 2

Materials and Methods

2.1 Cell culture

2.1.1 Routine cell culture

All cell culture was performed in sterile conditions using a class II microbiological safety cabinet (Walker, Glossop) and incubated at 37°C, 5% CO₂ (MCO-5AC-UV-PE, Panasonic). All solutions were heated to 37°C before use on cells using a water bath. The immortalised cell line, ARPE-19s, were purchased from ATCC and cultured in a 1:1 mixture of Dulbecco's modified Eagle Medium (DMEM) low glucose (Sigma Aldrich) and Ham's F12 nutrient mixture (Gibco Life Technologies) supplemented with 10% (v/v) fetal bovine serum (FBS) (Sigma Aldrich). The medium contained 7.5mM glucose, this was the basal level of exposure for cells. All cells were routinely grown in T175 or T225 cell culture flasks (Costar) depending on the cell number required. The plasticware was not coated with any attachment aiding solutions as this provides a better representation of the native retinal pigmented epithelia (Tian et al., 2004). Cells were routinely passaged once they had reached approximately 80% confluency within the flask. The media was removed and cells were initially washed with Dulbecco's phosphate buffered saline (PBS) (Sigma Aldrich). The PBS was removed and replaced with 5mL or 8mL of 1x trypsin (Sigma Aldrich) for T175 and T225 flasks respectively. The flasks were incubated at 5% CO₂, 37°C for approximately 5-7 minutes to allow the cells to detach from the flask. Flasks were agitated by gently hitting the sides to aid cell dissociation which was confirmed by observing the cells under a microscope. The reaction was quenched by the addition of 200% (v/v) of media to trypsin and one fifth of the total volume of solution in the flask was added to a fresh flask containing 10mL or 23mL of media (for T175 or T225 flasks respectively).

2.1.2 Primary retinal pigment epithelial cell culture

The primary cell lines, human primary retinal pigment epithelial cells (hpRPEs) were cultured in a separate, primary culture specific hood. hRPEs were cultured using DMEM:F12 media with GlutaMAX™ supplement (Gibco Life Technologies, UK) with the addition of 10% (v/v) FBS and 1% (v/v) penicillin streptomycin (Sigma Aldrich) containing 17.5mM glucose. Flasks were coated

with neat attachment factor (Sigma Aldrich), incubated at 37°C for 30 min and then removed before adding cells. One week prior to experimental study, hpRPEs were transferred to the 7.5mM glucose medium used for ARPE-19s to ensure they were not hyperglycaemic.

2.1.3 iBREC Culture

All experiments involving iBRECs were performed in Dr Heidrun Deißler's laboratory in the University of Ulm. These cells had previously been isolated from a bovine source and immortalised using hTERT (Deissler et al., 2005) Monthly proteomic profiling was performed from the Deißler lab on these cells to ensure the cell line remained endothelial. As with experiments performed in Nottingham, all cell culture was performed under sterile conditions using a Class II microbiological safety cabinet. To ensure sterility, cabinets were exposed to UV radiation for 1h prior and post use. Solutions were warmed to 37°C in a water bath before being exposed to cells. Flasks (Greiner) were washed with 5mL PBSd (PBS minus Ca^{2+}/Mg^{2+}), coated with 3mL 0.1mg/mL (w/v) fibronectin (Corning) and incubated for 1h at 37°C 5%CO₂ to allow the fibronectin to bind. Fibronectin solution was collected and stored at 20°C (reused 3 times before disposing) and replaced with VMnHC media, consisting of the solutions stated in the table below. Inclusion of gentamycin in media was paramount to guarantee activity of hTERT. Flasks were incubated again for 1h at 37°C 5% CO₂ to allow the media to equilibrate before cells were added, this was confirmed by the media turning from pink to orange. Whilst media was equilibrating, cells were detached from flasks after they achieved at least 70% confluence across a surface area. This was achieved through removal of culture medium, and washing cells twice with PBSd. Accutase (Sigma) was warmed to 37°C for 5 min, but not longer to avoid denaturing the enzyme, and 1mL was added to flasks. Cells were incubated for 5 min at 37°C 5%CO₂ followed by physical agitation of the flasks to promote cell detachment, this was confirmed through observation of detached cells under the microscope. Protease reaction was quenched through the addition of at least 3mL of pre-warmed VMnHC, and culture surface was washed with cell suspension to yield any remaining attached cells. Cell suspension was transferred to a 15mL falcon tube which was placed in a Multifuge X1R, Heraeus and span at 1,200rpm for

7 min at room temperature to pellet the cells. Supernatant was carefully removed and pellets were resuspended in 6mL VMnHC, pipetting up and down multiple times to ensure single cell suspension. Fibronectin-coated flasks containing equilibrated culture medium were removed from the incubator, and 1mL of cell suspension was added to each flask. The following day, cells were observed through microscopy to confirm attachment and medium was replaced.

Table 1

VMnHC		
Volume (v/v)	Solution	Source
500mL	Endothelial Cell Growth Medium	Promocell
3mL	Geneticin (50mg/mL)	Invitrogen
25mL	FBS	Promocell
2mL	Endothelial Cell Growth Supplement	Promocell
500µL	Humanised endothelial growth factor (0.1µg/mL)	Promocell
500µL	Hydrocortison (1mg/mL)	Promocell

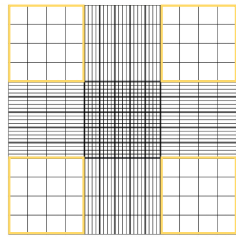
2.1.4 Cell storage

Cells were stored for future use at -150°C in FBS with 10% (v/v) dimethyl sulfoxide (DMSO). This was achieved by detaching the cells from a T175 flask as described in 2.1.1. and spinning the cell suspension in a 15mL falcon at 12,000rpm for 5 minutes. The resultant pellet was resuspended in 3mL FBS 10% DMSO and aliquoted into three cryovials. The vials were stored in Mr. Frosty™ freezing container at -80°C overnight before transferring to -150°C for long term storage. Upon use, one cryovial was rapidly thawed followed by the swift addition of 5mL of media to dilute out the remaining DMSO. The suspension was decanted into a T25 flask (Costar) and incubated at 5% CO₂, 37°C to allow cell-cell adhesion to occur.

2.1.5 Cell counting

Cell detachment as described in 2.1.1. was performed and the resulting suspension was spun at 12,000 rpm for 5 minutes in a 15mL falcon. The pellet was resuspended in 1mL of media, mixing thoroughly by pipette to ensure a single cell suspension. A glass coverslip was moistened by breath and fixed to

a haemocytometer. The presence of Newton refraction rings under the microscope was observed to confirm coverslip adhesion. 10uL of cell suspension was added to the haemocytometer by capillary action and the cells sixteen squares of each of the four corner squares (yellow boxes in the figure below) are counted, avoiding those that cross the top and right lines. The concentration of cells is calculated using the formula below:



Counting chamber of haemocytometer

Number of cells/mL

$$= \text{average cell count per mm}^2 \times 10^4 \times \text{dilution factor}$$

Figure 2.1: Formula for calculating cell number

2.2 Isolation of primary cells

Posterior segments of human eyes were received from the Manchester Eye Bank under appropriate ethics. All dissection equipment was sterilised with 70% (v/v) denatured ethanol. Firstly, there was a severing of remaining optic nerve. Pupil and lens was removed and discarded. The thick, gel-like vitreous humour was gathered using forceps and any attached retinal tissue was scraped from the surface in order to be harvested. Once completely free of retina, the vitreous was discarded. The retina remained attached to the choroid in the centre of the petals, thus a small incision was used to separate the two layers and retina was harvested in a 6-well plate containing sterile PBS. The choroid was peeled away from the sclera and placed in a separate well containing sterile PBS. Tissue was cut into small sections, decanted into a 15mL falcon and centrifuged at 2,000rpm for 5 minutes. This was followed by disposal of supernatant, and the tissue was washed by resuspending in 3mL PBS, mixing through gentle agitation and centrifuging at 2,000rpm for 5 minutes. These steps were repeated twice. After removal of supernatant, tissue was resuspended in 0.1% (w/v) collagenase (Sigma Aldrich) and incubated at 37°C for 1 hour, agitating every 10 minutes. At this stage, 500µL FBS was

added to choroid suspension and decanted into a T25 flask containing DMEM:F12 with GlutaMAX™ supplement coated with attachment factor (Thermo Fisher).

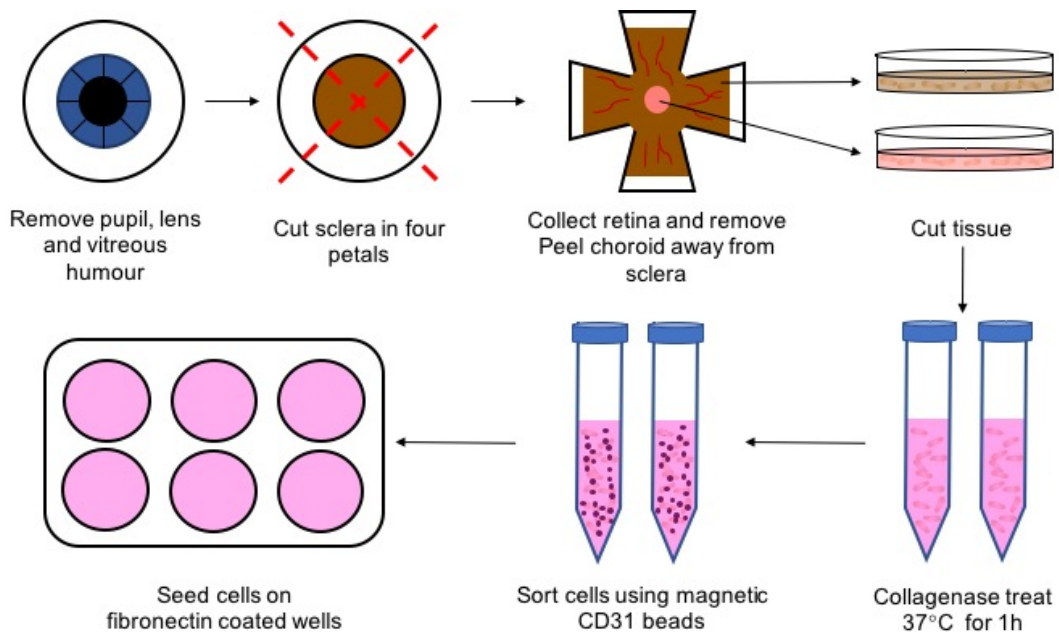


Figure 2.2: Schematic summarising the steps to isolate primary cells

2.3 Protein extraction

2.3.1 RPE Cell lysis

Cells were washed with ice-cold PBS and kept on ice. NP40, consisting of 150mM NaCl, 50mM Tris (pH 8.0) and 1% TritonX100 (Sigma Aldrich) with protease and phosphatase inhibitors PMSF (1mM), NaVO₃ (1mM), NaF (50mM) and 2% (v/v) Roche protease inhibitor cocktail (Sigma Aldrich) was made up, and 100uL was added to each plate. Plates were left to incubate on ice for 10 minutes with the complete lysis buffer. Cells were detached using cell scrapers (Greiner) and aspirated into 1.5mL eppendorfs. Cells suspensions were vortexed and mixed via pipetting, to ensure all protein had been detached, and then centrifuged at 14,800rpm for 15 minutes to pellet the cell debris. Supernatant was transferred to a fresh eppendorf and stored at -80°C until required.

2.3.2 Tissue lysis

Retinae excised from eyecups (isolation method described in section 2.6.2) were collected into 2mL screw cap Beadbug™ tubes filled with 3 acid washed stainless steel beads. 300µL ice-cold NP40 (recipe in 2.3.1) were added and tissue was mechanically homogenised for 3 min at speed 300 using the Beadbug™. Samples were then centrifuged at 12,000g for 10 min and the supernatant collected and transferred to a fresh Eppendorf tube.

2.3.3 iBREC lysis

Flasks were removed from the incubator and placed on a freeze board, cells were washed twice with ice-cold PBSd 1M MgCl₂, followed by addition of 5mL PBSd 1M MgCl₂. Cell scrapers were used across flasks to detach cells and the suspension collected into a 15mL falcon. A final wash of the flask with PBSd 1M MgCl₂ allowed collection of remaining cell suspension, which was pooled with the initial suspension. Centrifugation at 3,200rpm for 7min at 4°C in Multifuge X1R, Heraeus followed, with disposal of supernatant and re-centrifugation of the pellet under the same conditions as previous. Remaining supernatant was carefully removed via pipetting and the pellet was left to dry on ice for 10min. Pellets were resuspended thoroughly in 300µL commercial lysis buffer (Bio-Techne, R&D) supplemented with 0.1% 5mg/mL (v/v) Aprotinin pH 7.4 (Biorad), 0.4% 2.5mg/mL (v/v) Pepstatin (Sigma), 0.2% 5mg/mL (v/v) Leupeptin (Sigma), 0.5% Phosphatase-inhibitor cocktail (Sigma). Cell lysate was transferred into a 1.5mL pre-cooled Eppendorf and incubated on ice for 30min on a rotator before being centrifuged at 14,800 rpm for 30min at 4°C in Eppendorf-Centrifuge, Fresco 21. Supernatants were stored at -80°C before use.

2.3.4 Protein quantification

A Bradford assay was used to determine the protein concentration of samples. Bovine serum albumin (BSA) was diluted in PBS to a concentration of 1mg/mL and then serially diluted 1:1 with PBS to obtain concentrations of 500µg/mL, 250µg/mL, 125µg/mL, 62.5µg/mL, 31.25µg/mL and 15.625µg/mL. Samples were diluted 1:10 in PBS and loaded into a 96 well plate alongside the BSA

standards (10 μ L/well). Wells containing just PBS were included to use as blanks. Bio-Rad protein assay dye was diluted 1:5 with distilled H₂O (dH₂O) and 200 μ L was loaded per well. The plate was agitated for 10 seconds before the absorbance was read at 620nm using a plate reader. The BSA standards produced a standard curve of which the sample protein concentrations could be calculated from on Microsoft Excel™.

2.4 Western Blot

2.4.1 RPE

Cell lysates diluted with dH₂O and 1X Laemmli (BioRad) were heated to 95°C for 5 minutes and loaded onto 4-20% or 10% Mini-PROTEAN® TGX™ Precast Protein gels alongside 4 μ L molecular weight marker (PrecisionPlus dual colour standard, BioRad). A current of 180V was imposed onto gels submerged in running buffer (25mM Tris 192mM Glycine 0.1% SDS pH 8.3) using the 'Mini-PROTEAN Tetra Cell 1-D vertical gel electrophoresis' system in order to separate out the proteins within the sample by their molecular weight. Proteins were transferred onto methanol activated polyvinylidene fluoride (PVDF) membrane using the Trans-Blot® Turbo™ Transfer system (BioRad) and Transfer buffer (Biorad) 10% methanol. Membranes sub-sequentially blocked in blocking buffer; 5% (w/v) BSA tris-buffered saline (TBS) 1% Tween20 0.22 μ m filtered, for 2 hours at room temperature on a roller. Primary antibody was diluted to the appropriate concentration (*see table below*) in blocking buffer and incubated at 4°C with the membranes overnight on a roller.

Table 2

	Antibody	Dilution (1/x)	Source
Primary antibodies	Rabbit anti-ZO-1	1,000	Invitrogen
	Mouse anti-actin	400	Invitrogen
	Rabbit anti-SRSF1	2,000	Abcam
	Mouse anti-phosphoSR	500	Merck millipore
Secondary antibodies	IRDye® 800CW Donkey anti-Mouse IgG	5,000	Licor
	IRDye® 680RD Donkey anti-Rabbit IgG	5,000	Licor

Post incubation, membranes were washed three times in quick succession with TBS 1% Tween20 (TBS-T) followed by three, longer, 15 min washes with TBS-T at room temperature on a roller. Secondary antibodies were diluted to the appropriate concentration (*see table above*) in blocking buffer same as the primaries and incubated in the dark with the membranes for 1 hour with gentle agitation. The membranes were washed again same as previously and imaged using Licor system. The results were analysed using ImageJ software with FIJI update.

2.4.2 iBREC

Cell lysates were thawed, and spiked with 4x Laemmli sample buffer (Biorad) 1M DTT to 1x concentration. Solutions were heated to 100°C for 5min to reduce protein followed by centrifugation for 5min at 13,000rpm at room temperature. Mini Protean TGX 4-20% gels (Biorad) were rinsed with running buffer and each individual well was washed by pipetting. Samples were loaded into wells, alongside a protein ladder and proteins were separated by gel electrophoresis (200V, 0.4A) for approximately 45min. Proteins were transferred to methanol activated PVDF membranes using Trans-Blot® Semi-Dry system (Biorad) and Transfer Buffer (Biorad) 10% methanol. To promote protein transfer, both membrane and gel were submerged in transfer buffer before running at 20V, 0.16A for 90min. Following transfer, membranes were rapidly immersed in PBS-T to avoid the membrane drying out and washed twice in the buffer. Blocking steps were achieved using a polymer based blocking buffer (1:100 ROTI®Block (Carl Roth) PBST), incubating on a rotator for 15min at room temperature followed by a further 15min at room temperature or overnight at 4°C. Membranes were washed twice for 3min with PBS-T and exposed to 7.5mL primary antibody for 90min at room temperature. Another two 3min washes in PBS-T followed, and membranes were immersed in 7.5mL secondary antibody for 30min. A final wash step of four 3min washes in PBS-T occurred prior to developing blots using ECLPlus Western Blotting Detection Kit (Pierce). Membranes were exposed in the dark at room temperature for 5min to ECLPlus reagent and imaged at various exposure times using FUSION Pulse TS system (Vilber). Blots were exported into ImageJ for analysis.

Table 3

	Antibody	Dilution (1/x)	Source
Primary antibodies	Rabbit anti-ZO-1	400	Invitrogen
	Mouse anti-Actin	5,000	Novus
	Rabbit anti-Claudin-1	3,000	Invitrogen
	Rabbit anti-Claudin-5	1,250	Invitrogen
	Rabbit anti-VECadherin	1,000	Cell Signalling
Secondary antibodies	Goat anti-Mouse-HRP	30,000	Biorad
	Goat anti-Rabbit-HRP	30,000	Biorad

2.5 Immunoprecipitation

Proteins were isolated and precipitated out of solution with the use of a specific antibody bound to magnetic protein A/G beads (PureProteome, Merck, UK). A magnetic rack was used to immobilise the beads at each step whilst the supernatant was removed. All steps were performed on ice. Initially, the magnetic beads were washed three times with TBS-T. The beads were blocked by incubating with 0.1% (w/v) BSA TBS-T, rotating for 1 hour at 4°C. Cell lysates were diluted in 500µL NP40 buffer (recipe in 2.3.1) to the appropriate protein concentration and pre-cleared with the blocked beads on a rotator for an hour at 4°C and washed as previously. This step was required to reduce non-specific binding thus decreasing the background signal and improving the signal to noise ratio. Pre-cleared lysate was incubated with 1µg mouse anti-SRSF1 antibody and blocked magnetic beads overnight at 4°C on a rotator. A control set of beads and lysate was incubated with mouse anti-IgG2 antibody in order to detect any non-specific binding to IgG. The following day, the lysate was removed and the beads washed as previously. The protein was disassociated from the antibody-bound beads by heating to 95°C with 10µL 2x laemmli buffer for 5 minutes. The supernatant was loaded onto a gel and a western blot was performed as described in 2.4.1. with the only deviation being the gel was run at 4°C. An additional western blot was performed alongside the precipitated protein samples of the input lysate with 10% of the protein used in the immunoprecipitation.

2.6 Immunofluorescence

2.6.1 Immunocytochemistry

RPE cells were stained with specific fluorescent antibodies in order to find the expression and localisation of particular proteins. Cells were seeded in a 96 well imaging plate (Sigma Aldrich) and allowed to adhere to the surface overnight. The following day, they were exposed to a particular condition for a set amount of time. The density at which cells were seeded was as such that they achieved a monolayer but would not become over-confluent and grow on top of one another. The media was changed every other day in order to maintain the treatment concentration. Post-treatment, the media was removed and cells were washed with PBS, making sure at this step and going forward to pipette down the side of the plate so as not to disturb the cell monolayer. At no point during the staining procedure were the cells exposed to air for a prolonged period of time and allowed to dry out. The fixative, paraformaldehyde (PFA) was diluted in PBS to 4% (v/v) and added to each well for 10 minutes at room temperature. This was then washed out with PBS-T for 3 minutes, repeating a further two times to ensure all the PFA was removed. Cells were then permeabilised with 0.2% (v/v) TritonX100 for a period of 5 minutes at room temperature before washing again as previously. In order to ensure specific binding of the antibodies, cells were incubated with a blocking buffer; 1% (w/v) BSA 0.1% (v/v) TritonX100 PBS, 0.22 μ m filtered to avoid albumin aggregation, for 1 hour at room temperature. The cells were washed again in PBS-T before being incubated overnight at 4°C with primary antibody diluted to the appropriate concentration (*see table below*) with blocking buffer.

Table 4

	Antibody	Dilution (1/x)	Source
Primary antibodies	Rabbit anti-ZO-1	400	Invitrogen
	Mouse anti-SRSF1	100	Clone 96; Santa Cruz
	Rabbit anti-SRSF2	500	Abcam
	IgG control	2,500	21903; Pierce
Secondary antibodies	Goat anti-mouse 555	400	Invitrogen
	Goat anti-rabbit 488	400	Invitrogen
	Goat anti-rabbit 555	400	Invitrogen
Stain	Hoechst	10,000	Thermo Fisher

Secondary antibodies and Hoechst were diluted in blocking buffer to the appropriate concentration (*see table above*). The cells were washed as stated previously and incubated with the secondary antibody mixture for one hour at room temperature in the dark. This was followed by an additional wash step and cells were stored in PBS. In order to get a 3-D image of the emitted fluorescence across the entire cell monolayer, 2-D images of slices were taken using a confocal microscope. Nuclear staining was used in order to find the top of the cell, and images were captured at 2µm depths through the cell until there was no further staining. The images were collated together to form a Z-stack, and analysed using FIJI software.

2.6.2 Immunohistochemistry

Rats were culled using Schedule 1 inhalation of carbon dioxide followed by a cardiac puncture. Upon euthanasia confirmation, eyes were extracted from Norway-Browns using Dumont curved forceps (World Precision Instruments (WPI)) and immediately placed in 4% PFA for 30min. Eyes were transferred to PBS and stored at 4°C until ready for dissection. A petri dish was filled halfway with PBS, an eye was placed in the solution and visualised under a dissection microscope. Remaining attached connective tissue surrounding the eyes was removed using scissors and an incision was made anterior to the ora serrata with a microsurgical knife (WPI). Microdissection vannas scissors were inserted into the incision and cut along the ora serrata around the circumference of the eye to remove the iris, lens and cornea. The optic nerve was dissected away and four cuts were made in the eye cup, approximately 70% deep at 90° angles to each other. Tissue was carefully pulled back to reveal the retina and choroid

and vitreous was gently removed. One quartile of retina was lifted and fine curved tip scissors were inserted underneath to detach the retina away from the choroid. This was repeated across all four quartiles until retinae were successfully isolated and transferred to 0.5% PBLEC (PBS (pH 6.8), 0.1mM MgCl₂, 0.1mM CaCl₂, 0.01mM MnCl₂, 0.1% TritonX100). Retinae were blocked in 500µL 1% BSA PBLEC for 1h at room temperature followed by 500µL primary antibody for a further hour on a rocker. Antibody was washed away with 10min washes in triplicate of PBLEC before addition of 500µL secondary antibody. Retinae were incubated with secondary antibody for 1h in room temperature on a rocker prior to being washed three times with PBLEC for 10min. The tissue was removed from solution, placed on a microscopic slide (Fisher) and a single drop of Vectashield mounting medium containing DAPI (Vectorlabs) was administered. A coverslip was carefully placed on top of the retina under the dissection microscope to remove tissue folds. Fluorescence was captured using a 20x objective on Leica SPE confocal microscope; IB₄ staining was used to determine the lowermost point of retinal vasculature, and a Z-stack of images were produced from this point, upwards in steps of 10µm, until staining was no longer detected. Stacks were exported to Imaris or Image J software for analysis.

Table 5

	Antibody	Dilution (1/x)	Source
Primary antibodies	Isolectin B4 (biotin conjugated) from <i>Bandeiraea simplicifolia</i>	400	Sigma
	Mouse anti-collagen	100	Abcam
Secondary antibodies	Streptavidin 488	400	Invitrogen
	Goat anti-mouse 555	400	Invitrogen

2.7 ELISA

Cells were lysed and protein concentration measured as per section 2.3.1 and 2.3.4 respectively. Tissue was lysed as per section 2.3.2. Due to the high-sensitivity of the assay, all buffers and solutions were made with ultra-pure water (UPW) thereby reducing background signal. In addition, all steps were

performed at room temperature. High-binding 96 well clear microplates were coated with 100 μ L capture antibody (see table 6), sealed with parafilm and incubated with agitation overnight. The following day, wells were washed three times with a wash buffer consisting of 0.05% (v/v) Tween20 PBS. After each wash, plates were inverted and firmly tapped onto blotting paper to ensure removal of all buffer and reduce carry-over. Plates were blocked with blocking buffer; 100 μ L/well 1% (w/v) BSA PBS 0.22 μ m filtered, and incubated for 2 hours on a shaker. VEGF-A_{165a} and VEGF-A_{165b} recombinant protein was diluted in blocking buffer to 500pg/mL followed by 1:1 serial dilution to obtain a 10-point standard curve down to 3.9pg/mL. Samples were to be loaded in duplicate wells with 250 μ g protein per well, and thus diluted in blocking buffer accordingly. A single sample of VEGF-A_{165a} and VEGF-A_{165b} was also made up to 500pg/mL. Post blocking, the wash step was repeated as stated previously and 100 μ L of VEGF-A_{165a} and VEGF-A_{165b} standards and samples were loaded into the corresponding wells in duplicate. The inclusion of a VEGF-A_{165a} and VEGF-A_{165b} standard was in order to detect any inappropriate binding of the capture antibody to the splice variant. As previously, plates were sealed in parafilm and incubated with agitation for 2 hours.

Table 6

	Antibody	Conc	Source
Capture Antibody	anti-human VEGF-A _{165a}	0.25 μ g/mL	DY293B DuoSet ELISA kit, R&D systems
	VEGFxxx _b 56/8	10 μ g/ml	In house
Detection Antibody	anti-human pan-VEGF	100ng/mL	DY293B DuoSet ELISA kit, R&D systems
	Streptavidin-horseradish peroxidase	1:200	Thermo Fisher

Detection antibody (see table 6) diluted in blocking buffer was added to each well (100 μ L) following another wash. The plates were incubated, sealed, for another 2 hours on the shaker. Plates were washed again and 100 μ L of streptavidin conjugated to horseradish peroxidase (see table 6) diluted in blocking buffer was added to each well. For this step, plates were sealed and incubated for only 30 minutes away from direct contact with light. Post-incubation, plates were washed a final time and 100 μ L substrate solution

(DY999, DuoSet ELISA kit, R&D systems) was loaded into each well initiating a colour change. The plates were incubated in the dark until the colour change reached an appropriate intensity, before saturation and precipitation of proteins. The reaction was quenched by the addition of 50µL per well 1M HCl and shaken for 10 seconds to ensure thorough mixing. A spectrophotometer was used to determine the relative optical densities at 450nm. The data was exported onto Microsoft Excel and analysed using GraphPad Prism software.

2.8 NanoBRET

Nano-BRET (bioluminescence resonance energy transfer) is a proximity based assay that allows the quantitative characterisation of protein-protein interactions in real-time. ARPE-19 cells were transfected with two fusion proteins: SRPK1 conjugated to Nanoluc; a bright luciferase, and SRSF1 tagged with HaloTag. If both proteins come to close proximity to one another, energy will be transferred from the Nanoluc donor to the HaloTag acceptor causing it to fluoresce (*Fig 2.8*).

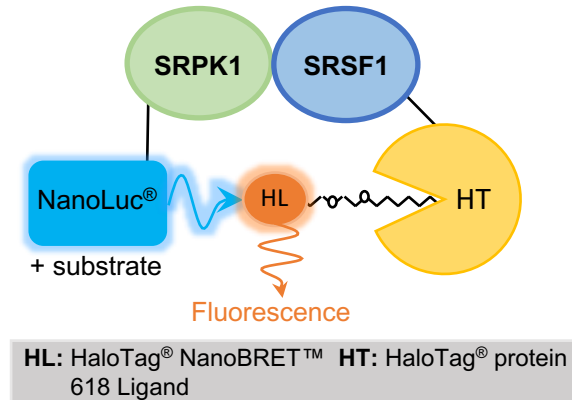


Figure 2.8: Schematic of Nano-BRET principle

2.8.1 Plasmid Preparation

Bacterial clones expressing plasmids were amplified from glycerol stocks, SRPK1-Nanoluc has chloramphenicol resistance whilst SRSF1-halotag has kanamycin. Lysogeny broth (LB)(Sigma) was prepared (20g in 1L dH₂O) and autoclaved for 15min at 121°C. A sterile pipette tip was used to scrape glycerol stocks to inoculate 10mL LB at 37°C, and the solution was transferred to a

shaker where it was incubated for 4h at 37°C. Starter culture was decanted into 200mL LB at 37°C containing the appropriate antibiotic, 50µg/mL kanamycin (Sigma) or 25µg/mL chloramphenicol (Sigma). Solutions were again incubated at 37°C in a shaker for at least 16h. Bacterial cultures were aliquoted into 50mL falcons and centrifuged for 10min at 5,000g at 4°C. Supernatants were discarded and pellets were resuspended in 12mL Suspension Buffer plus RNase (Genopure Maxiprep Kit, Roche) followed by an addition of 12mL Lysis Buffer (Genopure Maxiprep Kit, Roche). Falcons were gently inverted 6-8 times to ensure solutions were mixed and incubated at room temperature for 3min. This was followed by addition of 12mL pre-chilled Neutralisation Buffer (Genopure Maxiprep Kit, Roche) and another gentle mixture via inverting until a homogeneous suspension was formed. Falcons were incubated on ice for 5min as the solutions became cloudy and a flocculent precipitate formed. Lysates were cleared through filtration with 6mL Equilibration Buffer (Genopure Maxiprep Kit, Roche) and plasmids eluted in 15mL Elution buffer (50°C), columns emptied via gravity flow. 11mL isopropanol was added to the flowthrough to precipitate the eluted plasmid DNA and immediately centrifuged for 90min at 10,000g, 4°C. Plasmid DNA was washed with 4mL 70% (v/v) ethanol at 4°C followed by centrifugation for 30min at 10,000g at 4°C. Ethanol was removed carefully so as not to disturb the pellet, and air-dried for 10min at room temperature. Pellet was resuspended in 200µL dH₂O and concentrations and quality of DNA was measured using a Nanodrop 2000 spectrophotometer (ThermoFisher Scientific).

2.8.2 NanoBRET assay

ARPE-19s were seeded onto 10cm dishes at a density of 3×10^6 cells in DMEM:F12 plus Glutamax® and incubated overnight at 37°C, 5% CO₂ to allow cells to recover and adhere to dish. The following day, cells were washed with PBS and media exchanged for Opti-MEM™ I Reduced Serum Medium, no phenol red (Sigma). Transfection mixtures consisting of 6µg SRSF1-Halotag plasmid; 0.06µg SRPK1-Nanoluc; 300µL Opti-MEM™ and 24µL FuGENE® HD transfection reagent (Promega) were incubated for 10min at room temperature before 300µL was administered to each 10cm dish, mixed via gently swirling plates. Plates were incubated overnight at 37°C, 5% CO₂ to allow proteins to

be expressed, alongside Corning® 96 Well White Polystyrene Microplates (Sigma), coated with 50µL/well poly-L-lysine (Sigma). Transfected cells were removed from dishes through addition of 1mL Trypsin and incubation at 37°C, 5% CO₂ for 5min. Reactions were quenched with 2mL Opti-MEM™ and transferred to a 15mL falcon, centrifuged at 1,700g for 7min. Media was poured away and pellets resuspended in 2mL Opti-MEM™. Cell density was calculated as in section 2.1.5 and adjusted to 4.4x10⁵ cells/mL. Cells were divided into two stocks; a 'no-ligand' stock consisting of 3.2mL cells with 3.2µL 100% DMSO (Sigma) and a 'ligand' stock with 6.4mL cells with 6.4µL 618-ligand (NanoBRET™ Nano-Glo® Detection System 1000 Assays, Promega). Poly-L-lysine solution was removed from wells and replaced with 90µL cells, one column of no-ligand stock was followed by two columns of ligand stock. Treatments were made up to 10x the required concentration and 10µL was added to each well. Plates were incubated at 37°C, 5% CO₂ for as long as the treatment was necessary. NanoBRET™ Nano-Glo® Substrate in Opti-MEM® I Reduced Serum Medium, no phenol red was made up at a 5x concentration in 2.5mL and 25µL was loaded into each well. Within 10min of substrate addition, plates were shaken for 30secs and emission at 460nm and 660nm were measured using CLARIOstar Microplate Reader (*BMG Labtech*) to determine donor and acceptor signals respectively. Results were exported to Microsoft Excel™ and the BRET ratio was calculated using the equation below:

$$\frac{618nm_{EM}}{460nm_{EM}} = \text{Raw NanoBRET}^{\text{TM}} \text{Ratio} = BU \quad BU \times 1,000 = mBU$$

$$\begin{aligned} & \text{Mean experimental } mBU - \text{Mean no ligand control } mBU \\ & = \text{Mean corrected } mBU \end{aligned}$$

2.8.3 NanoBRET Imaging

ARPE-19s were transfected with nano-BRET constructs as per section 2.8.2. The following day, cells were detached using Trypsin and resuspended in phenol-free DMEM:F12. 7x10⁵ cells were seeded into each quartile of a 4-well glass-bottomed imaging dishes. Halotag-618 ligand (1:1,000 (v/v)) was added to 3 quartiles, whilst an equivalent volume of 100% DMSO was added to the 4th quartile, acting as the no-ligand control. Media was supplemented with either +30mM D-mannitol or +30mM D-glucose and incubated at 37°C, 5% CO₂ for

three days. The Olympus LV200 inverted microscope was used for imaging; with a double-layered chamber type incubator for 35 mm dish to maintain the environment at 37°C, 5% CO₂. Initially a brightfield image was taken of the cell monolayer so as to establish the optimal focus. 5µL Nanoluc substrate was added to a quartile and the resulting luminescence imaged. Brightness, contrast, positioning and focus was adjusted within 10min after addition of furimazine. A 30min video was taken of bioluminescence and fluorescence under BRET Cy5 filter (663 - 739nm) at one frame per second, with exposure fixed at 60s and gain at 400 in order to localise the SRSF1:SRPK1 interaction within the cell. Videos were exported into Image J for analysis.

2.9 Electric Cell-substance Impedance Sensing

The permeability across a monolayer of cells in response to hyperglycaemia was measured over real-time using electrical cell-substance impedance sensing, or ECIS. This system can be used to measure cytoskeleton mediated changes in the cell, such as cell morphology and migration (Wegener et al., 2000). Cells were grown directly onto gold-coated ECIS microarrays (8W10, Applied BioPhysics) and stimulated with a small alternating current at a range of frequencies from the bottom of the well. The short distance between the gold-coated electrodes and the cells means that this system is capable of measuring cellular changes from the micrometer down to the sub-nanometer range (*Applied BioPhysics | Quantifying Cell Behavior*, 2017). The application of the current results in a measurable change in potential across the electrodes. Ohm's law can be expanded when dealing with alternating current so that impedance (Z) = potential (V) / current (I), thus the impedance can be calculated by the ECIS software. At lower frequencies, below 40kHz, cells act as insulators prohibiting current movement across the cell, forcing the flow around and between cells through paracellular pathways. At higher frequencies, above 40kHz, current is able to flow capacitatively across the cell along transcellular pathways (see *Figure 2.9*)(Benson et al., 2013).

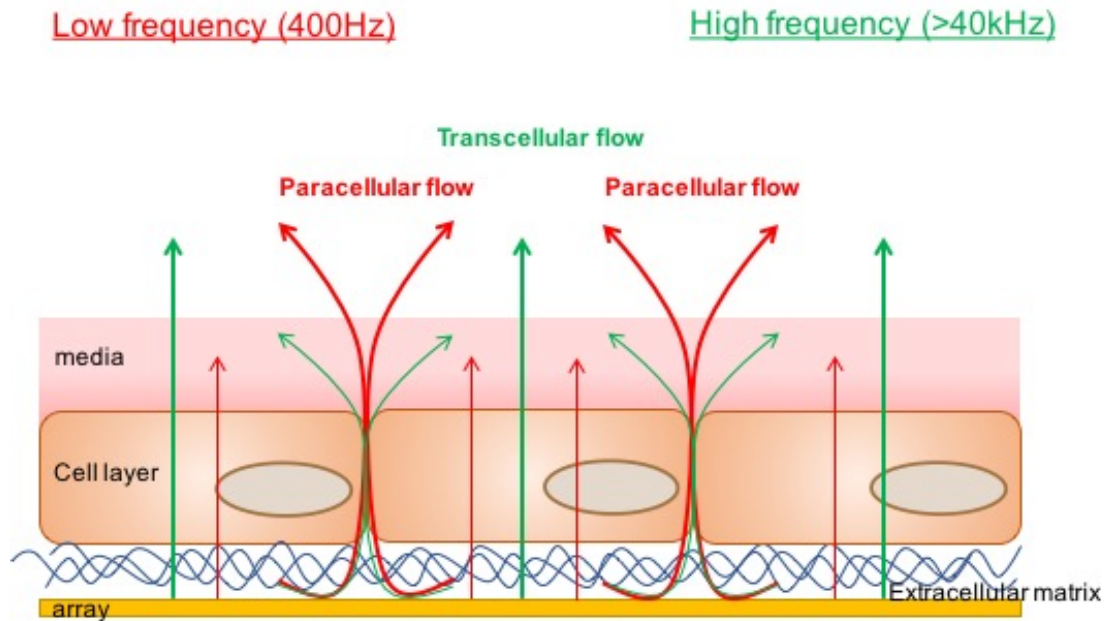


Figure 2.9: Current flow at low and high frequencies. At lower frequencies (red arrows), cells act as an insulating barrier and the majority of flow moves around the cells around tight junctions through the paracellular pathway. Thus, impedance measured is primarily a result of the surrounding elements of the cells. At higher frequencies, current is able to pass through the cells via the transcellular pathway across cell membranes (image adapted from (Applied BioPhysics | Quantifying Cell Behavior, 2017)).

All steps were performed in a microbiological safety cabinet with great care to ensure everything remained sterile. ECIS arrays were initially washed in 10mM cysteine followed by three washes with dH₂O. The wells were then coated with sterile 0.1% (v/v) gelatine and incubated for 90 minutes at 37°C. A second wash with dH₂O was performed and the array allowed to air dry for 15 minutes. Wells were filled with 300µL of cell medium, the array slotted into the ECIS adaptor and the stabilisation program on ECIS software was performed. The array was removed from the adaptor and cells were seeded at the appropriate density in a volume of 450µL into each well. The array was placed at 37°C for 20 minutes to allow the cells to settle before placing it back into the adaptor. Current was applied at multiple frequencies and the resultant impedance was measured every ten minutes and monitored. Once the impedance reached approximately 1,500Ω and appeared to stabilise over at least six hours, the system was paused, as cells were concluded to be confluent. The appropriate treatment was made up at 8x the required concentration and 50µL was added slowly to

the side of each well, to not disturb the cell monolayer, under the hood before continuing with the experiment. Media was changed every other day carefully to not disrupt monolayers, to ensure the cells were exposed to the correct concentration of treatment. Data was exported onto Microsoft Excel™ and analysed using GraphPad Prism software.

2.10 XCelligence

The XCelligence system follows the same principles as ECIS: application of an electrical current causes movement of electrons through an electrical conductive solution (cell media) from the negative to positive electrode that can be impeded by presence of adhered cells. Electronic microtiter plates (E-Plates®) (ACEA Biosciences Inc., San Diego) contain interdigitating strand electrodes which cover 70-80% of surface area of the well. An E-plate® contains two columns of eight wells, and 3 plates can be run simultaneously. Impedance is presented as unitless parameter, cell index (CI) calculated using the formula below. CI can fluctuate in response to changes in cell number, morphology, cell-cell attachment quality and cell-substrate attachment quality. By ensuring cell confluence and reducing physical disruption to monolayer, this method can be used to determine changes in monolayer permeability.

$$CI = \frac{\textit{impedance at time point } n - \textit{impedance in the absence of cells}}{\textit{nominal impedance value}}$$

E-plates® are highly sensitive to physical disruption and the electrodes can be easily contaminated by environmental particles such as dust. As such, great care was taken whilst handling the plates, and a specific aluminium platform was used to place to the E-plates on whilst adding or removing solutions. iBRECs were detached from a confluent T25 flask using 500µL Accutase™ (STEMCELL Technologies) following two washes with PBSd (Invitrogen). The solution was suspended in 2.5mL VMnHC media. 150µL VMnHC supplemented with 2% fibronectin was added to each well of an E-plate under the hood with the exception of one control well where 200µL was added instead. E-plates were docked into the xCELLigence® RTCA DP instrument at 37°C 5% CO₂ and an initial background reading was taken which would be

subsequently subtracted from later measurements. 50µL of cell suspension was added to each well except for the control well under the hood before E-plates were again placed in the instrument. CI was recorded over 72h as cells reached confluence within the wells. Once confluence was confirmed (Table 7: Step 4), 195µL was removed from each well, taking care not to touch the bottom of the well with the pipette tip and replaced with 180µL of SHMnHC (VMnHC with no FBS) with 1% fibronectin. 20µL of appropriate conditioned media was added to wells, at least 3 wells per condition. Wells were assessed visually for bubbles before re-docking in the instrument and continuing CI measurements (Table 7: Step 5). Following completion of the study, CI's were normalised to the point prior to treatment addition and averaged between wells of the same condition. Data was exported to Microsoft Excel™ and further analysed using GraphPad Prism software. The table below summarises the settings used for CI measurements.

Table 7

Step 1:	Pre-installed background reading	<i>*System paused, cell suspension added</i>
Step 2:	Sweep every 15min (100x)	
Step 3:	Sweep every 30min (100x)	
Step 4:	Sweep every 1h (100x)	<i>*System paused, treatment added</i>
Step 5:	Sweep every 15min (250x)	
Step 6:	Sweep every 2min (90x)	
Step 7:	Sweep every 5min (750x)	
Step 8:	Sweep every 15min (250x)	
Step 9:	Sweep every 1h (100x)	

2.11 *In vivo* work

Rats were housed and maintained at University of Nottingham Biological Services Unit (BSU). All procedures were performed in accordance to the ARVO statement for Use of Animals in Ophthalmic and Vision Research, and under a UK Home Office licence (PPL 30/3184). An initial pilot study was conducted with 3 animals before the larger study with 24 animals. Data was collated together from both studies.

2.11.1 Topical administration of SPHINX31

Male Brown Norway rats were purchased from Charles River and housed until they reached at least 250g in weight. Eighteen animals received twice-daily eye drops, approximately 6h apart, of 20 μ L 200 μ g/mL SPHINX31 in both eyes from day 0 until termination of the study. A control cohort of 9 animals received 20 μ L eye formulation control buffer in both eyes at the same frequency as SPHINX31 group.

2.11.2 Streptozocin-induced Type I Diabetic Model

Due to potential carcinogenic, mutagenic and teratogenic properties of streptozocin (STZ), Tyvek® (DuPont) suits were worn until STZ was completely excreted alongside double gloves and shoe covers. Housing rooms were bleached in the morning and evening of study days, STZ treated animals were isolated and cages were cleaned with bleach upon diabetic confirmation. All procedures and cleaning were performed by myself to avoid exposure to BSU staff. Some protocols require an overnight fast before diabetic-induction as it minimises competition between STZ and dietary glucose for low-affinity GLUT2 transporters on β -cells of pancreas. However, previous work from other members of our group have found evidence of acute toxicity to STZ, animals display a rapid drop in weight, occasionally above the threshold stipulated in the licence (>20%), alongside polyuria and dehydration. On the other hand, lack of fasting risked animals not becoming diabetic (~10%) but avoided acute toxicity symptoms. As such, 18 animals (9 from SPHINX31 cohort, 9 from control cohort) were not fasted, weighed and 50mg/kg STZ (Sigma) was administered by intraperitoneal (i.p.) injection. To ensure STZ activity, the solution was freshly made up in 0.1M citrate buffer in a foil-wrapped bijoux and injected within 30min. Nine control rats who were treated with SPHINX31 were given equivalent volumes of saline via i.p. Animals were closely monitored across three days for weight fluctuations and overall health before blood glucose was measured from a bolous of blood extracted from the tail vein and assayed using an Accu-Chek monitor. The nape of those animals with >15mmol/L blood glucose were shaved, sterilised with chlorohexidine and one third of an insulin pellet (LinShin) was implanted subcutaneously using a 16

gauge trocar (LinShin) approximately 1.5cm along neck midline under isoflurane anaesthesia (3-5%). The 7mm by 2mm implant undergoes gradual erosion upon implantation to slowly release a set basal dose of insulin hourly, the effects of which can be measured within an hour. As such, animals do not experience glucosuria or ketonuria. Animals with $<15\text{mmol/L}$ blood glucose were re-injected with 50mg/kg STZ i.p. as previously and assessed for blood glucose after three days. At this point, 1 rat was not diabetic and as such was removed from the study.

2.11.3 Optical Coherence Tomography

Once a week, rats were anaesthetised with an i.p. of ketamine (30mg/kg, Ketaset, Zoetis) and medetomidine hydrochloride (0.25mg/kg, Sedastart, Animalcare Group). Rats were placed on an image cradle fitted with a heat mat. Topical applications of 5% phenylephrine (Bausch & Lomb) and 0.8% tropicamide (Bausch & Lomb) were administered to dilate the pupil followed by a carbomer 980 gel (Viscotears, Bausch & Lomb) to prevent corneal dehydration. Reveal Optical Coherence Tomography (OCT)[™] software was opened and a white paper was placed in front of the Micron[™] IV ophthalmoscope with Image-guided OCT2 attachment (Phoenix Research Labs) lens to adjust white balance. The ophthalmoscope was advanced towards the left eye at a right angle, orientation and focus was adjusted until the optic disk was visualised and centred in the field of view. The reference arm was adjusted to position the retinal scan to the top third of the frame. At this point, focus and polarisation were fine-tuned to obtain the crispest, brightest image possible. A circular scan around the optic nerve at a rate of 13,000 A-scans per second was captured, followed by a line scan through the optic nerve.

Scans were exported into Insight[™] software for analysis. The automatic segmentation tool was used to isolate the retinal layers. However, whilst this proved accurate for choroidal and ganglion cell layers, the algorithm was unable to accurately segment between inner and outer nuclear layers, and differentiate RPE/Bruch's membrane layers from photoreceptor layers. As such, the manual tool was utilised which involved placing markers at short intervals along the layer border. Following this, the software drew a line along

the retinal layer which could be adjusted if the line appeared to deviate from the border. Upon visual confirmation of accuracy of segmentation, the software measured the thickness of each layer every 3 μ m along and expressed this as a mean.

2.11.4 Fundus Fluorescein Angiography

The Image-guided OCT2 laser attachment was unplugged from the Micron™ IV and Discover software was opened. With animals still under anaesthesia, adjustments to brightness and contrast were made to display a sharp image of retinal vessels. A brightfield image was captured to assess for any abnormalities. The green filter was selected, brightness increased to maximum and an i.p. of sodium fluorescein (NaFl) was administered to the right peritoneal cavity by carefully lifting the right leg, so as to not disturb the alignment of the ophthalmoscope. Immediately, a 3min video was captured with a gain of 11 at 15 frames per second to monitor perfusion of the small molecular fluorescent tracer across the retina. Animals were recovered with an i.p. of atipamezole hydrochloride (1mg/mL, Sedastop, Animalcare), transferred into a heated recovery cage with absorbance pads and monitored until righting reflex was restored. To aid recovery, animals were fed mash the following day before restoration of their normal diet.

Angiograms were imported as avi files into Fiji software. A box was drawn in a major retinal vessel (Box 1) and a secondary in nearby tissue (which includes unresolved capillaries – Box 2) (*Fig 2.11.A*). Boxes were checked to make sure they remained within the region of interest for the whole video, as there was small movement of the eye during video capture. Once this was confirmed, the mean intensity within each box was measured every frame up to 2400 frames. A time course was plotted (*Fig 2.11.B*) and only the region where there was detectable tissue fluorescence but no major vessel saturation was used for analysis. In addition, tissue intensity over vessel intensity was calculated and plotted over time (*Fig 2.11.B black trace*). The gradient of the curve at the steepest point (*Fig 2.11.B green section*) was calculated and used as permeability coefficient. Before the large *in vivo* study assessing retinal permeability in diabetic rats was conducted, a smaller study on three non-

diabetic rats was completed in order to optimise the methodology (Fig 2.11.C). There is a variability between different rats, even when permeabilities were normalised to day 0 (Fig 2.11.D), therefore an n=9 was decided for the larger study.

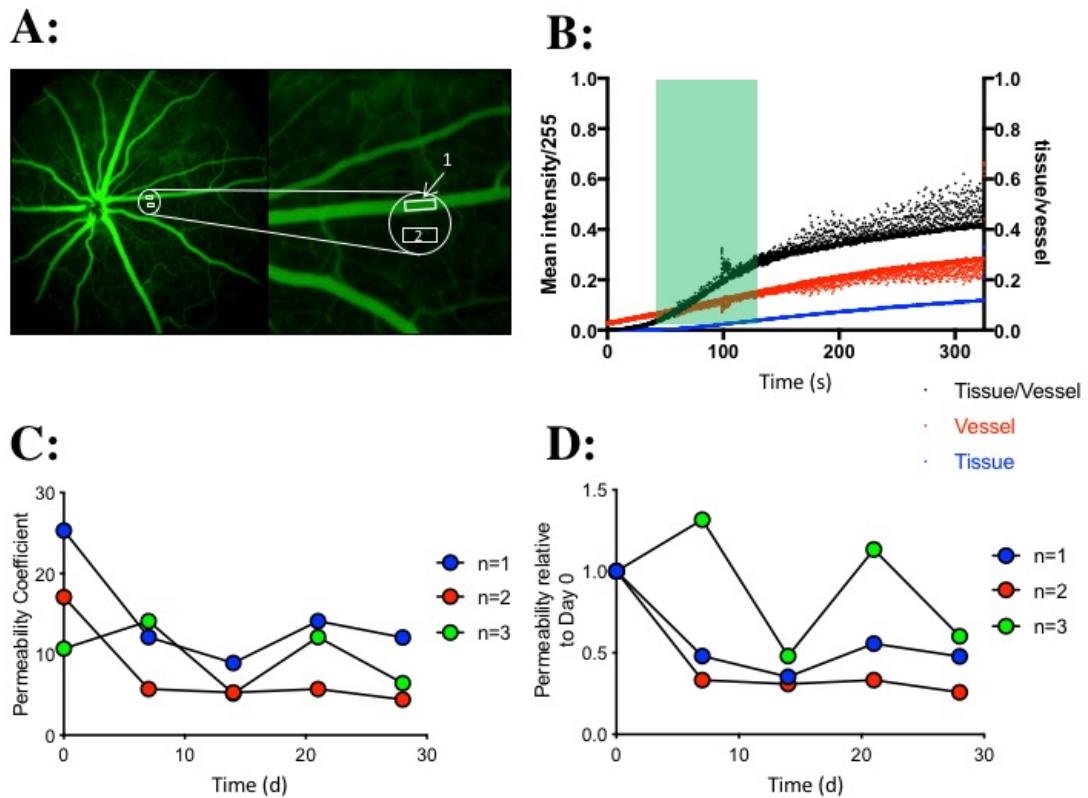


Figure 2.11: Analysis of retinal permeability through FFA.

Fundus angiograms were analysed to determine retinal permeability by measuring the fluorescence intensity over time in a box drawn in a retinal vessel and a secondary box drawn over nearby tissue (A). B: Mean intensities within these boxes were plotted over time, alongside the tissue/vessel intensity. The gradient of the steepest point of the curve (green box) determined the permeability co-efficient. C: Changes in permeability in 3 non-diabetic Norway browns over 28 days. D: Data from (C) normalised to day 0.

2.12 Data Analysis

All *in vitro* data was analysed using a mixture of Microsoft Excel™ and GraphPad Prism with the exception of western blots and immunofluorescence, where FIJI or Imaris software was used. The former had the intensity of the bands quantified using gel analysis tools within the software. The latter was analysed as detailed below:

2.12.1 SRSF1 localisation

Images of SRSF1 staining were analysed using FIJI software in order to quantify the cytoplasmic to nuclear stain. The total staining of SRSF1 was measured from the image. The channel containing DAPI staining was thresholded using the automatic function, and the background adjusted to black. This was followed by converting the image to a mask and an inversion of look up table. The plug in: 'Analyze Particles; size: 25.00' was run in order to determine the number of nuclei and size of each. This mask was selected and pasted onto the image containing SRSF1 stain. Thus, the intensity and volume of staining within the nuclei could be measured, expressed as average staining per nuclei. This number was subtracted from the total staining in order to find the level of SRSF1 within the cytoplasm, which was divided by the total number of cells (determined by the number of nuclei), in order to find the average per cell. The final value was expressed as a ratio of nuclear to cytoplasmic staining.

2.12.2 Integrity of tight junction as determined by ZO-1

Prior to determining the changes in integrity of tight junctions in response to hyperglycaemia and hypoxia, the analysis methods used in order to produce quantitative data from the staining required optimisation. ZO-1 intensity across a tight junction was quantified using FIJI software. Although images were taken using confocal microscopy, a single plane was chosen that displayed cell-cell junctions. A particular cell at random was chosen and zoomed towards. Intensity of staining within the cell was measured. The value of mean staining plus three standard deviations was subtracted from the image. A freehand line, with a width of 5 pixels, was drawn around the cell, along the staining of ZO-1 and the profile of this line was plot to give the frequency of staining along the line. Counting, either manually or using an Excel™ array formula ensued of the number of peaks within the profile to calculate the number of gaps within the staining. In addition, the total staining along the line could be calculated from this profile. Both these values were divided by distance of line. To ensure the results were representative of the staining, three cells from each image were analysed, and three images were taken per well, with three wells per condition, thus for one condition a total of 27 cells were analysed. This was time

consuming and unsuitable for a high throughput assay, therefore the range and distribution of the results per image and well were assessed.

Each well represents a different condition, so the distribution is determined by the error bars. Peak number/distance variability between each well (Fig 2.12.2-A) is quite small, however the results for intensity fluctuates. Figure 2.12.2-B shows that the results within each well remain quite close together, for both peak number and intensity. Thus, it was decided that one image per well would be analysed, but there would be three wells per condition, hence a total of nine analyses. With regards to the optimal median filter to use, the values given with background included decrease steadily as the filter number increases (Fig 2.12.2-C). However, when background is removed, the results drop quite dramatically after 2-3 pixel filter and then appear to level off. Figure 2.12.2-D is a 5-day NG timecourse analysed both with and without subtracting the background. Without subtracting the background, the peak number hardly changes with each treatment, possibly due to the fluctuations in the profile of background staining. On the other hand, there is no difference in intensity with and without background, except for the exact values. Thus, due to the combined results of Figure 2.12.2-C & -D, a median filter of 2 pixels was imposed with background subtraction for one cell per well and three wells per condition.

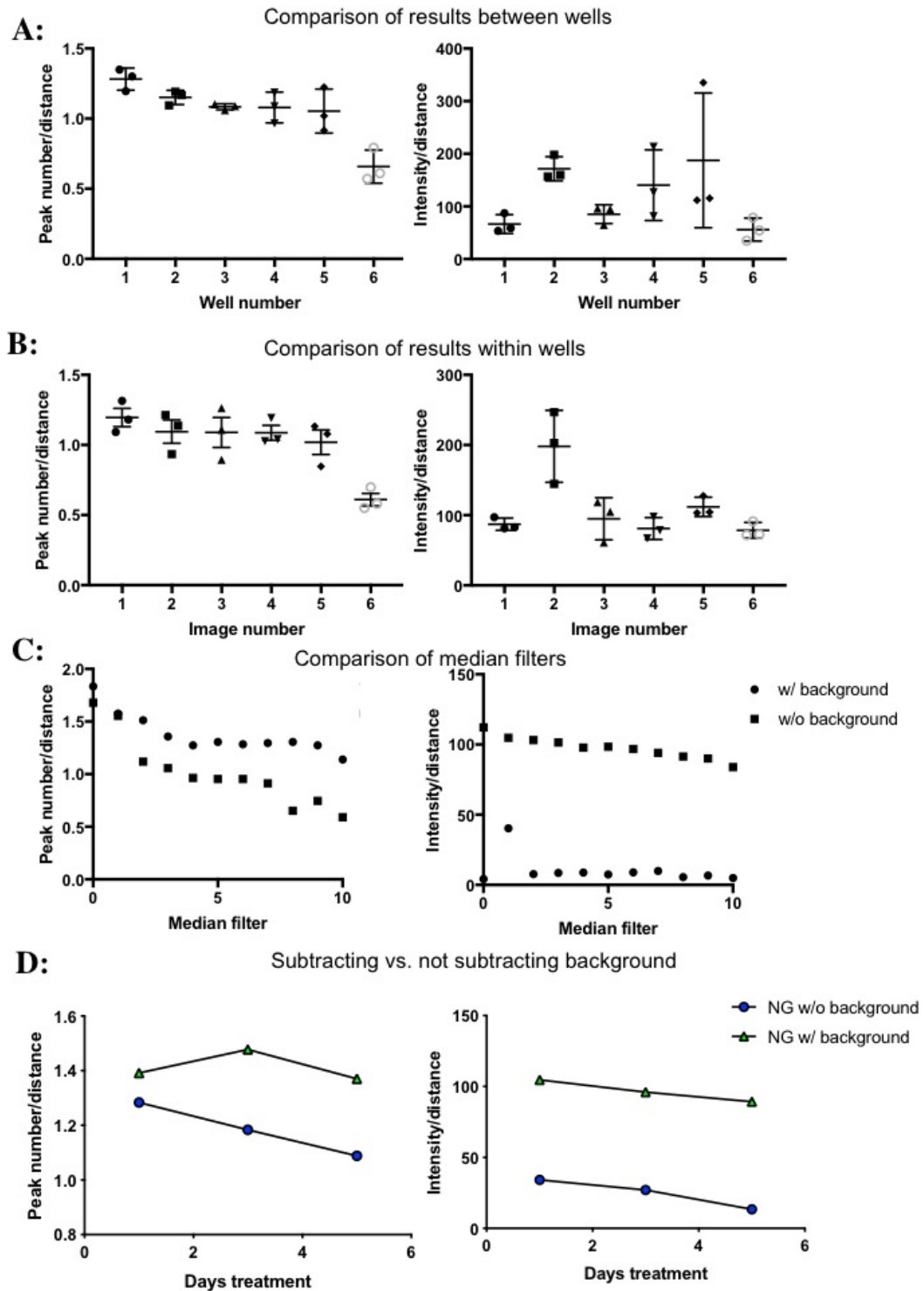
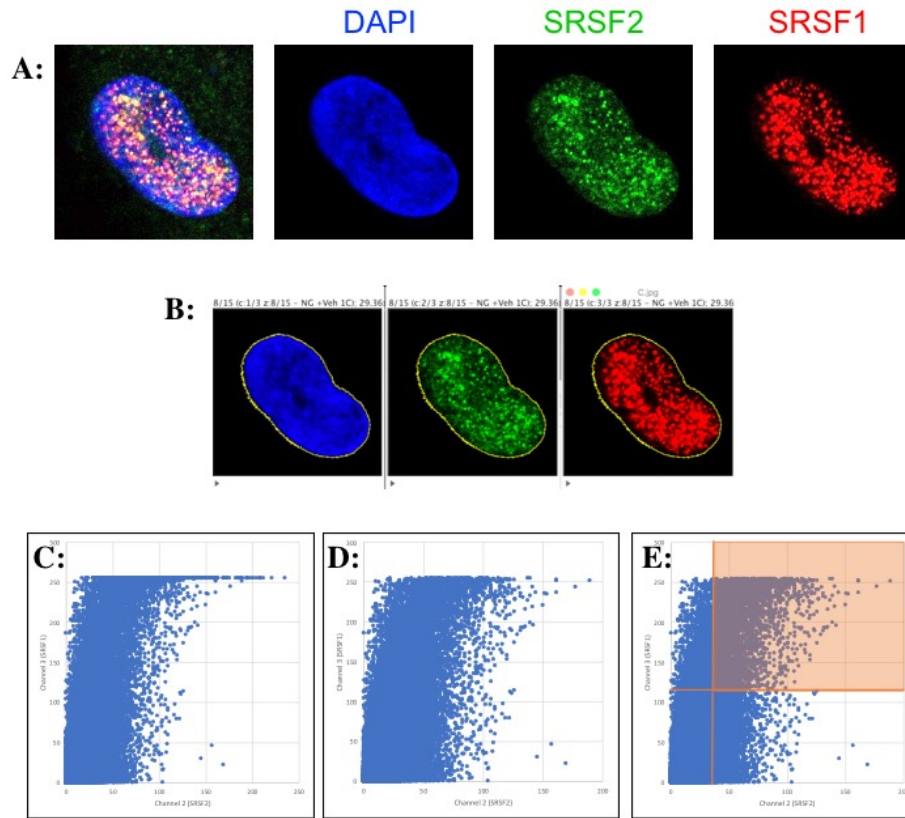


Figure 2.12.2: Optimisation of ZO-1 staining analysis protocol

A: ZO-1 analysis of peak number and fluorescence intensities over distance in 3 RPE cells across different wells. **B:** ZO-1 analysis as previous in 6 RPE within one well. **C:** ZO-1 analysis as previous comparing median filters from 0-10 with and without background. **D:** ZO-1 analysis as previous of background vs. no background at 1, 3 and 5 days 30mM D-Mannitol treatment.

2.12.3 Quantification of SRSF1:SRSF2 co-localisation

RPE cells were stained for DAPI to visualise the nucleus, SRSF2 to demarcate nuclear speckles and SRSF1. A Leica SPS confocal microscope was used with 63x magnification (oil-immersed) to take Z-stack images of cell nuclei (Gain: DAPI: 600; SRSF2: 700; SRSF1: 650). Z-stacks were imported into FIJI for image analysis. Initially, channels were split (*Fig 2.12.3-A*), the wand tool used on the DAPI channel to delineate the nucleus. This tracing was exported as a region of interest and imposed on both SRSF2 and SRSF1 channels (*Fig 2.12.3-B*). XY co-ordinates of staining within the mask were recorded and exported into Microsoft Excel™. Intensities of both channels at each pixel were plotted against one another (*Fig 2.12.3-C*), any points equating to 255 (saturated pixels) were deleted (*Fig 2.12.3-D*). Interquartile ranges of each channel was calculated and the number of pixels within the upper quartile of both channels was counted (*Orange box of Fig 2.12.3-E*). The number of pixels in the upper quartile of both channels was taken as a percentage of total number of pixels to determine the percentage co-localisation (Co-L) (*Fig 2.12.3-F*).



$$F: Co - L = \frac{\sum_{top\ 25\%} Channel\ 1 \& \sum_{top\ 25\%} Channel\ 2}{\sum_{top\ 25\%} Channel\ 1 \sum_{top\ 25\%} Channel\ 2} \cdot 100$$

Figure 2.12.3: Summary of image analysis to determine Co-Localisation

A: Staining of RPE nuclei with nuclear marker DAPI, anti-SRSF2 and anti-SRSF1. **B:** Singular channel images post nuclear tracing and removal of staining outside the nucleus. **C:** Intensity in each pixel of both channels plotted against each other. **D:** Intensity plot after removal of saturated pixels. **E:** Number of pixels within orange quartile determines Co-L. **F:** Formula for Co-L.

2.12.4 Measurement of vascular parameters

Retinae isolated from the eyedrop study were stained for IB₄ and imaged using a Leica SPS confocal. A 20x objective was used to generate z-stacks of retinal vasculature staining. Z-stacks were exported into Image J with FIJI plugin for analysis. A singular plane was chosen that appeared to showcase the middle of each plexus was chosen, and the freehand line tool was utilised to trace along all retinal vessels within that plane. This tracing was measured in order to determine total vessel length; and divided by the image area to calculate total vessel density per image. A grid was applied to the image, and within a particular square, chosen from a number generated randomly by a tool,

diameter of vessels was measured using the straight line tool. Diameters were measured within 10 squares of the image, and averaged to determine the mean diameter.

Z-stacks of IB₄ staining were also imported into Imaris software, and a 3-D rendering of retinal vasculature across 3 plexuses were generated. The filament tracer tool was repurposed to determine vascular parameters. The fully automatic tool was used to trace vessels, with diameter of vessels set at 3µm. To threshold the image, the 'no-loops' algorithm was utilised, and the threshold adjusted until the trace filled the vessels, fill cavities was checked. The number of dendrite seed points were adjusted, and seed points around starting points were removed. Upon visual confirmation that the trace accurately represents the retinal vasculature (*Fig 2.12.4*), the minimal ratio of branch radius to trunk radius was set at 1.5. Finally, the function was performed to determine the number of dendrite branches, vascular diameter and volume.

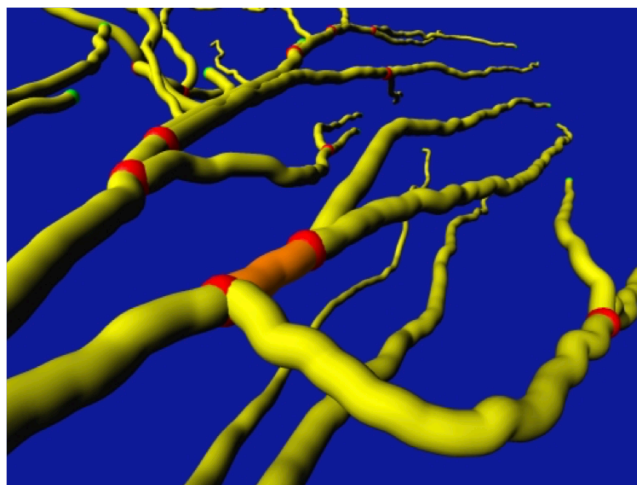


Figure 2.12.4: Calculation of vessel parameters using Imaris software (www.bitplane.com)

Frame of Imaris analysis software after addition of trace over vessels.

2.12.5 Acellular capillary number

Following termination of the SPHINX31 eyedrop study, retinae were isolated, whole-mounted and stained for IB₄, collagen IV and DAPI. Fluorescence was captured using confocal microscopy as described in section 2.6.2. Z-stacks were imported into Image J software with FIJI plug-in. An acellular capillary was

defined as a capillary positively stained for collagenIV but lacking IB4. This was manually counted through the retinal section across three planes, leaving enough space between each plane to ensure a capillary was not counted twice and placing a grid on top of the image to ensure no area was missed. The number was expressed per mm². This was repeated for 10 images per retina and the average number was expressed.

CHAPTER 3

SRPK1 activity in an *in vitro* model of the RPE monolayer of the outer blood retinal barrier

3.1 Introduction

The retina is the most metabolically active tissue in the eye, with glucose being the primary source of energy for these cells. *In vivo* glucose is supplied to the inner retina; consisting of retinal ganglion, Müller glial and amacrine cells, via a branched microvascular network derived from the central retinal artery. The endothelial lining of these vessels, termed inner blood retinal barrier (iBRB), exert a protective role to the ocular cells, preventing passive diffusion of cytokines, glucose and inflammatory factors from the blood (Duke-Elder, 1956). Glucose transport to outer retinal cells, including photoreceptors and retinal pigment epithelial cells (RPEs), is provided by a dense fenestrated vessel network in the choroid; termed choriocapillaries (Shakib & Cunha-Vaz, 1966). The tortuous, leaky nature of this capillary bed allows passive diffusion to the surrounding tissue, across the thin acellular lamina of the Bruch's membrane to the RPEs. However, at this point, movement is restricted due to interepithelial junctional complexes, including tight junctions, known as the outer blood retinal barrier (oBRB). Emphasis in literature has been placed on disruption of the iBRB with regards to the development of DR and DMO, as the majority of their pathological features; such as acellular capillary and exudate formation, arise due to a loss of iBRB integrity (Harhaj & Antonetti, 2004). However, changes to the oBRB are observed in DR, even in early stage disease (Xu & Le, 2011).

The selectivity and permeability of the oBRB is defined by RPEs. Through the action of tight junction and transporter proteins, RPEs are able to nourish the photoreceptors with metabolic products such as glucose and remove waste material (Ponnalagu et al., 2017). These cells are highly polarised, a feature important for their function, and is present due to tight junctional complexes consisting of claudins, occudin and zonula occludens (ZO) protein families. Cellular stress, imposed by hyperglycaemia or hypoxia for example, can induce breakdown of RPE barrier (Weinberger et al., 1995), through intracellular trafficking of tight junction proteins away from cell membrane complexes (Farnoodian et al., 2016). Once internalised, the junctional complex is disrupted, increasing paracellular flux which can potentially accumulate in the sub-retinal space, leading to oedema formation if unimpeded.

RPEs also act as a secretome, supplying VEGF-A, which prevents endothelial cell apoptosis, maintains the neural retina and stabilises the high permeability of choriocapillary fenestrations (Marneros et al., 2005). VEGF-A expression is non-polarised, but predominantly secreted by the basolateral membrane. However, under diabetic conditions, the reverse occurs and VEGF expression is dominantly on the apical side (Kannan et al., 2006). Although the mechanism for this is not known. DR can lead to areas of ischaemia, which can be due to leaky vasculature failing to provide adequate perfusion to retinal tissue. Resultant hypoxia promotes an overexpression of proximately spliced VEGF-A, which negatively feedbacks by enhancing retinal permeability across both iBRB and oBRB (Aiello et al., 1995). SRPK1 regulates alternative splicing of VEGF, via phosphorylation of a splicing factor SRSF1. Inhibition of this kinase has been shown to inhibit choroidal neovascularization in mice by decreasing proximately spliced VEGF-A whilst increasing distally spliced VEGF-A isoforms (Gammons et al., 2013). The distally spliced isoform, VEGF-A_{165b} has also previously been described to inhibit diabetes-induced vascular permeability *in vivo* (Ved et al., 2017), and thus may offer therapeutic potential for DR.

Hyperglycaemia alone is sufficient to initiate diabetic-like retinopathies in rodents and canines (Engerman & Kern, 1984; Kador et al., 1990). and numerous studies have demonstrated that therapies reducing hyperglycaemic exposure to the eye can inhibit retinopathy development (Engerman et al., 1977; Nathan et al., 1993). Thus multiple pathways associated with hyperglycaemia have been implicated with the pathogenesis of DR. The retina receives 60-80% of glucose through the transport system provided by RPEs, and the percentage of glucose entering the retina in diabetes has been found to be larger across the RPE barrier than the retinal vasculature, highlighting the importance of RPEs in responding to the high glucose retinal requirements (Decanini et al., 2008). Despite this, the direct action of glucose on RPEs remains elusive. There have been a plethora of studies attempting to understand the impact of hyperglycaemia and VEGF-A on *in vitro* RPE barrier integrity and function, however they have produced conflicting results (Ablonczy et al., 2011; Kim et al., 2014; Villarroel et al., 2009). Contradictory data in this field are due to a number of factors; differences in RPE cultures,

passage number, lack of cell polarisation, amongst others (Xia & Rizzolo, 2017). This highlights the need for a robust, reliable, representative *in vitro* model of the oBRB to delineate the impact of diabetic conditions and VEGF-A alternative splicing.

Dysfunction of the oBRB has been implicated in DR, and especially in DMO formation. I aim to establish an *in vitro* model of the RPE, which is representative of the RPE monolayer in the *in vivo* oBRB. I will impose diabetes-mimicking conditions (hyperglycaemia and hypoxia) to my model, and determine the impact, if any, on VEGF-A isoform expression and barrier integrity, in particular ZO-1. In this way, not only will I further understand the impact of DR on the RPE barrier but I will also be able to validate my model against published literature. Furthermore, I aim to elucidate changes to SRPK1 activity in these conditions, indirectly, through observing the effects on SRSF1 expression and localisation, and directly with the use of a nano-BRET.

3.2 Methodology

The following experiments were carried out in ARPE-19 cells or human primary retinal pigment epithelial cells (hpRPE) isolated from human donor eyes. Cells were cultured in media with a basal concentration of 7.5mM glucose. In order to mimic normoglycaemia and hyperglycaemia, media was supplemented with 30mM D-mannitol or D-glucose respectively. These concentrations were chosen because RPE cells cultured with no glucose were difficult to maintain and produced a non-representative phenotype. Cells used in hypoxic experiments were also subjected to 1% pO₂ by being placed in a sealed hypoxia chamber. VEGF-A isoform expression was determined in RPE in each condition via an ELISA. In order to determine changes to RPE monolayer integrity, expression and distribution of ZO-1 was visualised using immunofluorescence. Furthermore, impedance measurements were taken across the monolayer using electrical cell impedance sensing. Cells were assayed for SRSF1 protein expression, phosphorylation and localisation using western blot, immunoprecipitation and immunofluorescence. All replicates are technical repeats, unless otherwise stated. All methods are described in more detail in Chapter 2.

3.3 Results

3.3.1 VEGF-A₁₆₅ isoform expression in response to hyperglycaemia and hypoxia in RPEs

To assess the effects of hyperglycaemia (HG) and hypoxia (Hx) on the oBRB, human primary RPEs (hpRPEs) were subjected to five days exposure to +30mM D-mannitol (NG) or +30mM D-glucose (HG) or three days exposure to 1% pO₂ (Hx) as a positive control. The cell lysate was assayed for expression of VEGF-A₁₆₅ alternative isoforms using an ELISA (See Chapter 2: Materials and Methods for further detail). To validate the specificity of the assay, recombinant VEGF-A_{165a} protein was probed against α VEGF-A_{165b} antibody and vice versa (*Fig 3.3.1.C*). Each antibody was found to have high specificity for their target, producing no signal for the alternative isoform. VEGF-A_{165a} expression was increased in response to both HG and Hx (*Fig 3.3.1.D*) despite having no effect on VEGF-A_{165b} expression (*Fig 3.3.1.E*). However, when assessed as a ratio of VEGF-A_{165b}/VEGF-A_{165a} expression, I found that both HG and Hx reduced this ratio by approximately four-fold.

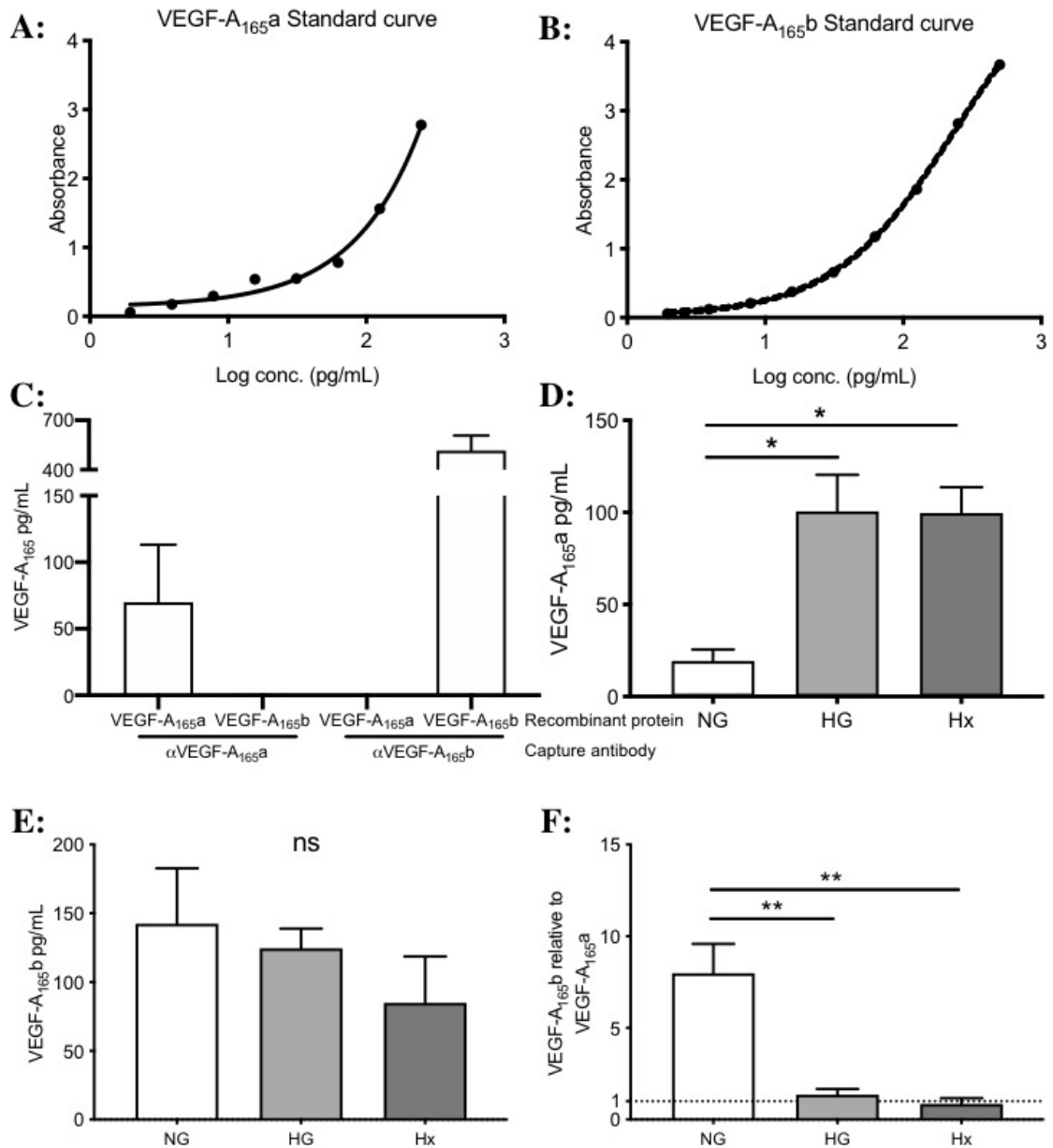


Figure 3.3.1: HG and Hx significantly increase VEGF-A_{165a} expression and reduce VEGF-A_{165b} expression relative to VEGF-A_{165a}

A+B: Standard curves of VEGF-A_{165a} and VEGF-A_{165b} respectively. **C:** Assessment of antibody isoform specificity using 50pg/mL recombinant VEGF-A_{165a} and 500pg/mL VEGF-A_{165b} proteins. Both antibodies were highly specific for their target isoform. **D:** VEGF-A_{165a} expression is increased ($p < 0.05$) by HG and Hx whilst VEGF-A_{165b} levels (**E**) do not significantly change in these conditions. **F:** The ratio of VEGF-A_{165b} to VEGF-A_{165a} expression significantly reduced ($p < 0.01$) in response to HG and Hx. Error bars represent mean plus standard error. Statistical analysis via one-way analysis of variance, Bonferroni post-hoc. ($n=5$) ns=not significant, * $p < 0.05$, ** $p < 0.01$.

3.3.2 Changes to permeability of the outer blood-retinal barrier in hyperglycaemia and hypoxia.

It is well documented that increased VEGF-A expression results in a disruption in tight-junction integrity in retinal endothelial cells (Antonetti et al., 1999) and epithelial cells (Ved et al., 2017). Thus in order to evaluate whether this is the case in my model of the oBRB, ZO-1 localisation was determined using immunofluorescence and optimised Image J analysis (explained in further detail in Chapter 2: Materials and Methods). In short, a profile of ZO-1 staining along the cell membrane was plotted (*Fig 3.3.2-1A*) after images were subjected to a median filter of 2 and the background staining was subtracted. The number of peaks in the plotted profile were counted in order to determine the 'gaps' in the staining, and the total cumulative sum of the plot gave the staining intensity. The immortalised RPE cell line, ARPE-19 is commonly used as an alternative to hpRPEs, as they are dependable and easier to culture and maintain (Samuel et al., 2017). However, use of ARPE-19s as a model for barrier function is controversial as the cells have been found to form an inferior monolayer compared to the primary equivalent (Ablonczy et al., 2011). Nevertheless, I compared ZO-1 staining in HG and Hx for both ARPE-19s and hpRPEs (*Fig 3.3.2-1B*). With regards to the peak number (*Fig 3.3.2-1C-D*), there was no difference between NG and HG in both cell lines, but a reduction in number of peaks in hypoxia in hpRPE. Surprisingly, ZO-1 staining increased in HG compared to NG in ARPE-19s but not in Hx (*Fig 3.3.2-1E*). Thus, moving forward, this analysis method will not be used as a measure of ZO-1 integrity. The intensity of staining over distance was found to significantly decrease in HG and Hx in hpRPEs (*Fig 3.3.2-1F*).

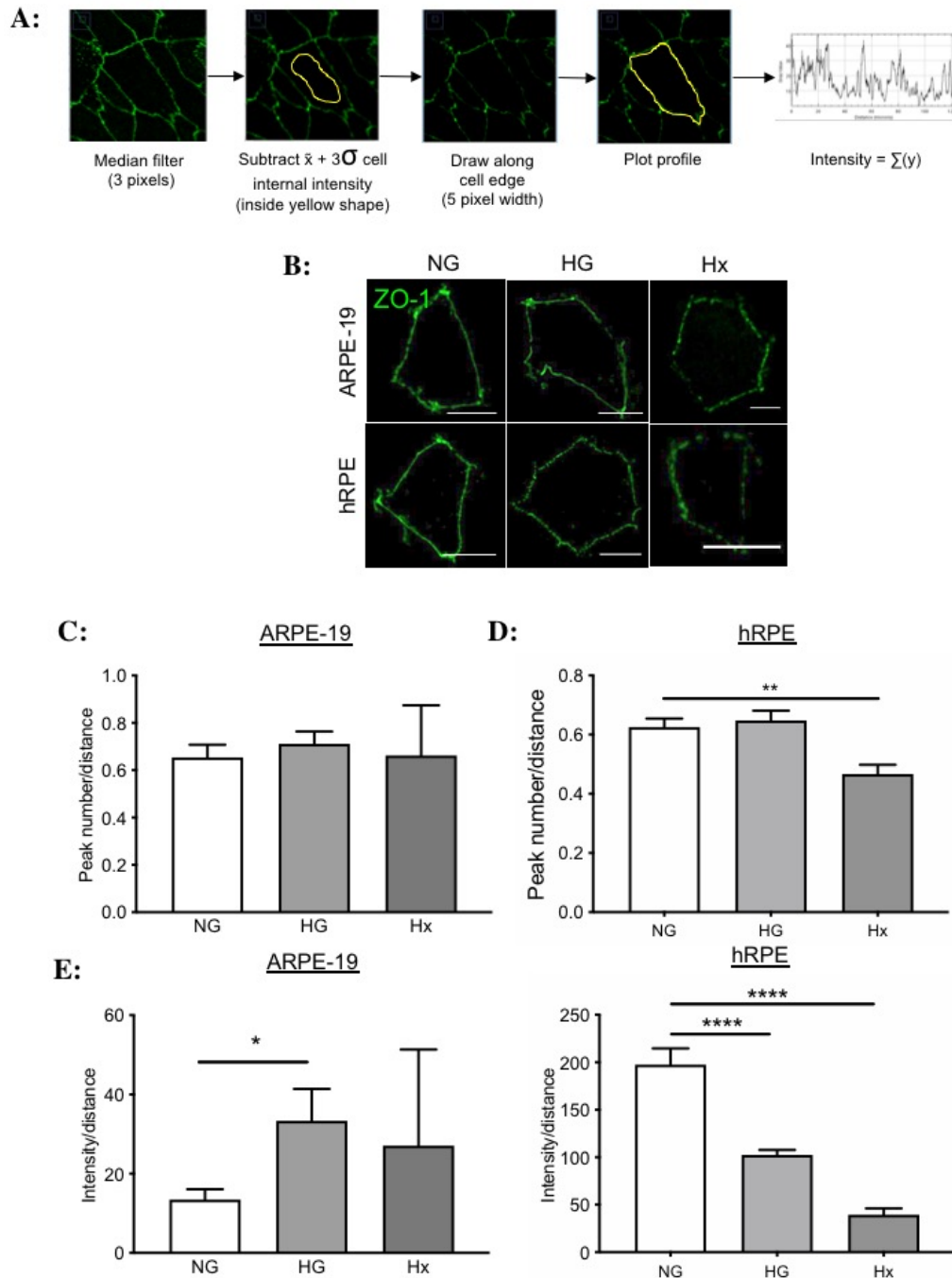


Figure 3.3.2-1: Barrier localisation of tight junction protein ZO-1 is reduced in HG and Hx in hRPE monolayers but not ARPE-19s.

A: Analysis method to determine ZO-1 peak number and intensity along a cell membrane. **B:** ZO-1 staining of an individual ARPE-19 cell in NG, HG and Hx and an individual hRPE cell in NG, HG and Hx. Scale bar = 10 μ m. **C:** Peak number did not change in ARPE-19s in response to HG and Hx compared to the NG control. **D:** HG produced no change in peak number in hRPEs, however Hx significantly reduced the number of peaks ($p < 0.01$). **E:** Intensity of ZO-1 staining significantly increased in HG ($p < 0.05$) compared to NG but not Hx. **F:** HG and Hx induced a significant reduction in ZO-1 staining intensity ($p < 0.0001$) in hRPEs. Confocal images taken with 40x lens. Error bars

*indicate mean + standard error. Statistical analyses performed using a one-way analysis of variance, post-hoc Tukey's test. * $p < 0.05$, ** $p < 0.01$, **** $p < 0.0001$ ($n=9$).*

The observed changes in the junctional expression of ZO-1 in hpRPEs could be due to degradation or an internalisation of the protein. To determine changes to ZO-1 total protein in the oBRB, HG hpRPE cell lysate were immunoblotted for ZO-1 (*Fig. 3.3.2-2A*) and the loading control actin. HG over the course of five days caused no changes in ZO-1 expression compared to the osmotic control (NG) or basal media alone (*Fig. 3.3.2-2B*). Thus, potentially this could mean that the HG results of *Fig. 3.3.2.1F* are due to an internalisation of ZO-1 away from the cell membrane, rather than a degradation. ZO-1 expression decreased in response to Hx (*Fig. 3.3.2-2C-D*) over the course of three days, corroborating with what was observed in *Fig. 3.3.2-1F*. Due to this result, I decided that 3 days in Hx would be the optimal time point for future experiments.

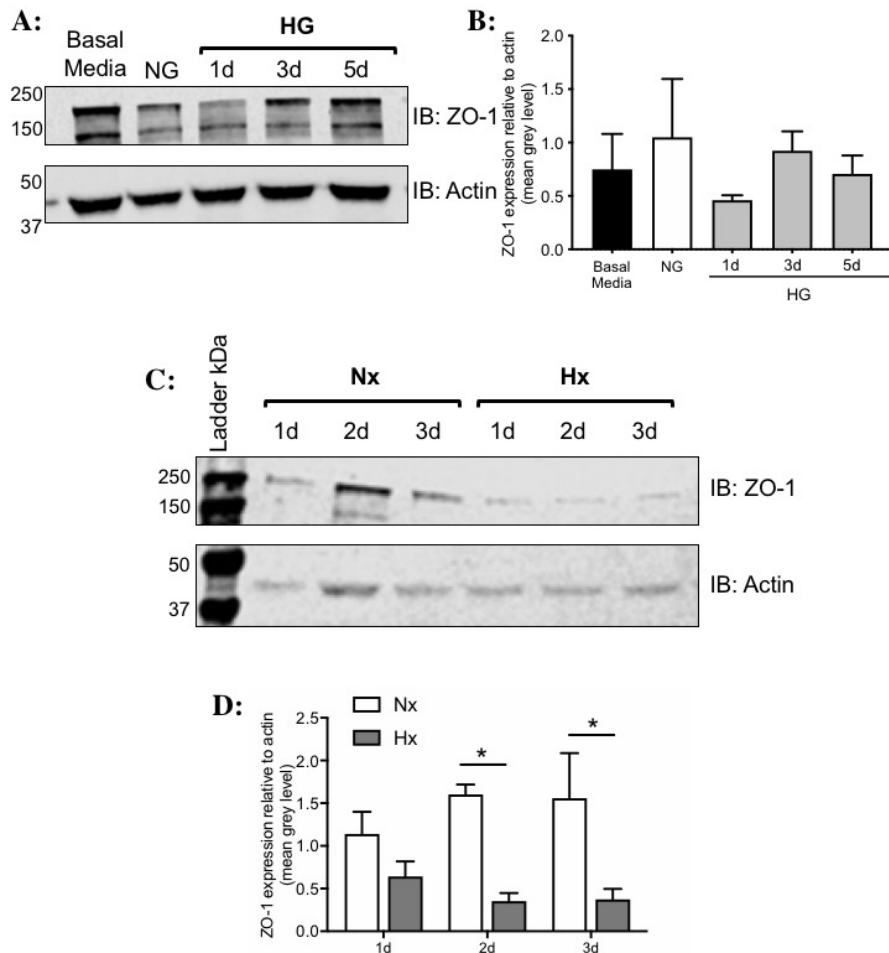


Figure 3.3.2-2: Expression of tight junction protein ZO-1 is reduced in Hx but not HG in hpRPEs.

A: Immunoblot for ZO-1 and actin of hpRPE lysates treated with basal media only, 5d D-mannitol (NG) or 1, 3 or 5d D-glucose (HG) **B:** ZO-1 expression relative to actin is unchanged in HG conditions compared to basal media and NG. **C:** Immunoblot of hpRPE lysate treated with $\approx 20\%pO_2$ (Nx) or $1\%pO_2$ (Hx) for ZO-1 and actin **D:** Hx induced a reduction in ZO-1 expression after two days exposure ($p < 0.05$). Error bars indicate mean + standard error. Statistical analyses performed using a one-way analysis of variance, post-hoc Tukey's test. * $p < 0.05$, ($n = 5$).

A loss of tight junction proteins *in vivo* is indicative of increased barrier permeability. To deduce whether this translates to my *in vitro* model of the RPE monolayer, RPEs were grown to confluence on gold-coated ECIS array plates and impedance measurements across the monolayer were taken continuously. A permeability co-efficient was gained by plotting $1/\text{impedance}$ over the course of 15 hours post treatment artefact (see Chapter 2: "Material and Methods"). The use of ARPE-19s were again evaluated for their use as a permeability

model of the oBRB. In agreement with Fig. 3.3.2-1C, HG induced no change to monolayer permeability compared with NG (Fig. 3.3.2-3A-B). Consequently, moving forward I decided to not use ARPE-19s as a model for the RPE layer. Use of the primary cells proved to be a better model, as HG was found to increase monolayer permeability as evidenced by the higher trace for HG (Fig. 3.3.2-3C) and also the larger area under the curve value. These results confirm those of Fig. 3.3.2-1 and also agree with published literature (Yokouchi et al., 2013).

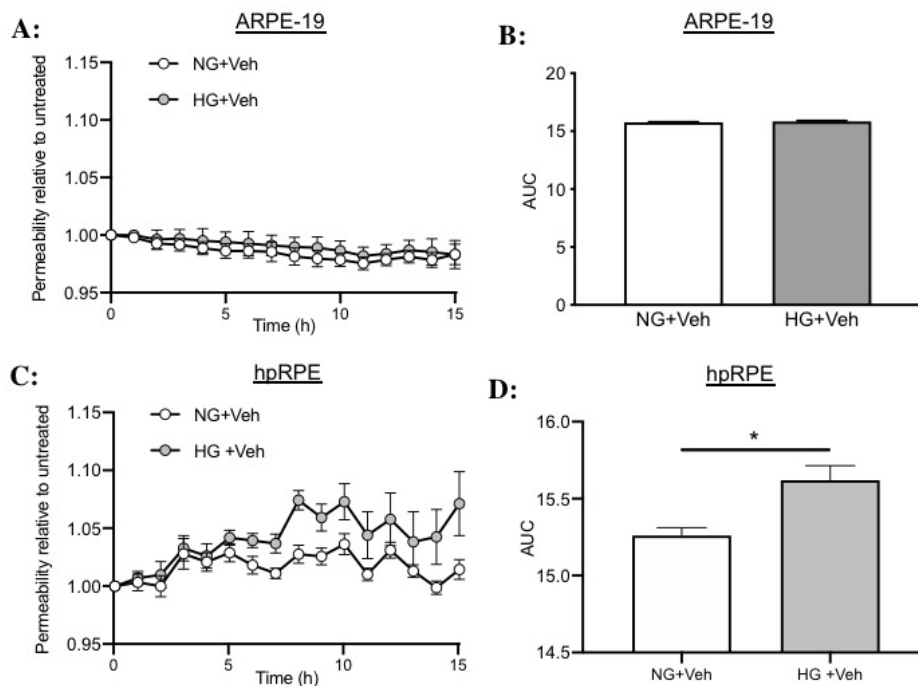


Figure 3.3.2-3: Monolayer permeability is increased due to HG in hpRPEs but not ARPE-19s

A: ARPE-19s were grown to monolayer and impedance was measured over time using ECIS. $1/\text{impedance}$ was plotted to give a measure of monolayer permeability. **B:** HG had no effect on ARPE-19 monolayer permeability ($n=4$) **C:** Permeability values of hpRPE monolayers subjected to NG or HG treatment over the course of 15 hours post addition of treatment and resulting artefact. **D:** HG monolayers have increased permeability (AUC: 15.6 ± 0.089) compared to that of NG monolayers (AUC: 15.3 ± 0.056) ($n=9$). Error bars of **A** and **C** indicate mean \pm standard error, **B** and **D** indicate mean + standard error. Statistical analyses of area under the curves performed using a t-test. * $p < 0.05$.

3.3.3 SRSF1 expression in HG and Hx hpRPEs

Alternative splicing of VEGF-A has been attributed to the action of SR proteins, in particular SRSF1, which has been found to have a binding site next to the proximal splice site of the 3' end of VEGF-A exon 8 (Nowak et al., 2010). Therefore, I assumed that the expression of SRSF1 would be increased in response to HG and Hx in hpRPEs, due to their differential VEGF-A isoform expression (see Fig. 3.3.1). To test this hypothesis, HG and Hx hpRPE lysate was immunoblotted against SRSF1 and a loading control, actin (Fig 3.3.3-1A). The expression of SRSF1 in HG remained unchanged compared to that of NG, however Hx cells had significantly reduced expression ($p < 0.05$) (Fig 3.3.3-1B).

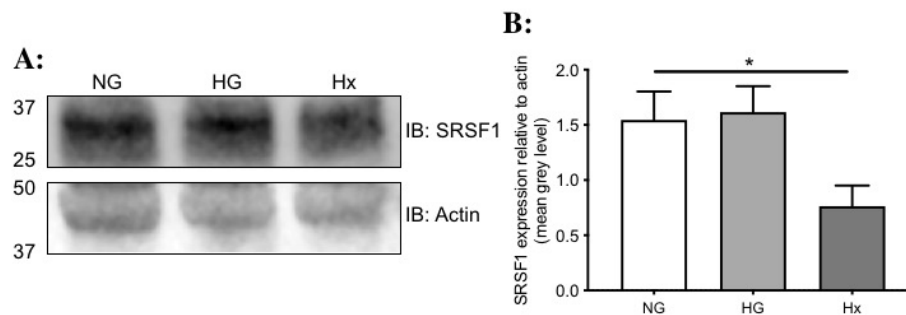


Figure 3.3.3-1: Hx but not HG reduces SRSF1 expression in hpRPEs

A: Western blot of NG, HG and Hx hpRPE cell lysate probed for SRSF1 and actin. **B:** SRSF1 expression relative to actin was unaffected by 5 days in HG but significantly reduced in response to 3 days in Hx (0.76 ± 0.67) compared to NG (1.62 ± 0.53) Error bars indicate mean + standard error. Statistical analysis performed using a one-way analysis of variance with Bonferonni post-hoc. * $p < 0.05$, ($n=3$).

The results of Fig 3.3.3-1 were surprising, as it went against the hypothesis that SRSF1 expression would be increased to mediate VEGF-A_{165a} expression. However, the function of SRSF1 is highly dependent on the localisation within the cell. SRSF1 is a shuttling protein, that moves from the cytoplasm to the nucleus depending on its phosphorylation state (Gonçalves & Jordan, 2015). Within the nucleus, it is then free to bind VEGF-A pre-mRNA and promote proximal splice site selection (Nowak et al., 2010). Therefore, it is perhaps more important to evaluate the localisation of SRSF1 within the cell as a property of its function, rather than expression. To assess changes in SRSF1 localisation in response to HG, hpRPEs were cultured to between passage 4-6, in order to

remove the autofluorescing pigments, and grown to confluent monolayers on imaging plates. Cells were stained for ZO-1, to visualise cellular edges, DAPI, to see the nucleus and SRSF1. Image J analysis was performed in order to obtain the ratio of nuclear to cytoplasmic expression of SRSF1 (see Chapter 2: Materials and Methods for full detail). Cells treated with HG showed a steady increase in nuclear localisation of SRSF1 to 3.3 over the five-day treatment, whilst the values for NG and basal media remained between 1.8 and 2.3 (*Figure 3.3.3-2B*). This correlates with what was visualised under the microscope; the red signal in the nucleus intensified the longer the cells were exposed to glucose, highlighted by the red arrows in *Figure 3.3.3-2A*. This difference between HG and the two controls at 5 days was determined as statistically significant. Cells that were initially HG, but exposed to NG media for 5 days exhibited a statistically significant decrease in the nuclear to cytoplasmic ratio of SRSF1 expression from 3.3 to 2.3, matching that of the controls. This is represented by the white arrows in *Figure 3.3.3-2A*, displaying areas of cytoplasmic SRSF1 localisation. Thus, the changes in the cell were due to the presence of the glycaemic stimulus. Additionally, this could suggest that the effects of hyperglycaemia on SRSF1 may be reversible.

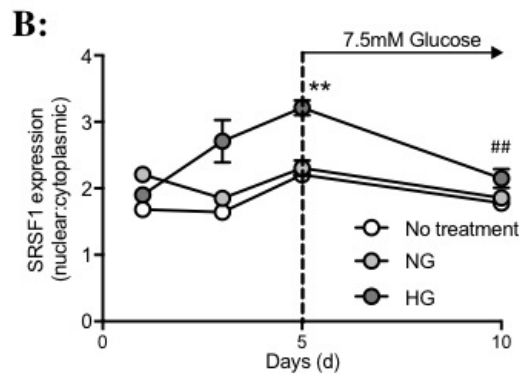
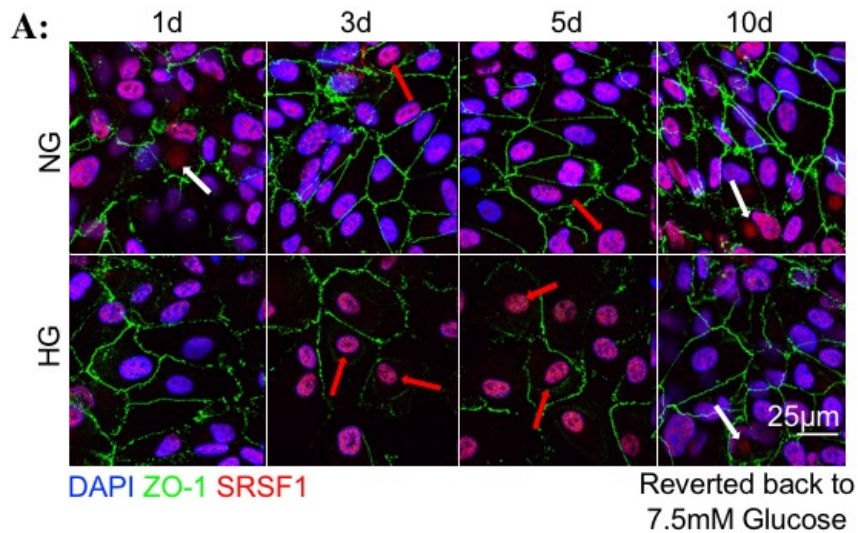


Figure 3.3.3-2: HG induces increased nuclear SRSF1 localisation, reversed by removal of glycaemic stimulus.

A: Overlay images of **DAPI**, **ZO-1** and **SRSF1** staining in response to the different conditions. White arrows highlight cytoplasmic SRSF1 staining, red arrows highlight nuclear SRSF1 staining. Scale bar = 25µm. **B:** SRSF1 localisation expressed as a ratio of nuclear to cytoplasmic. Nuclear SRSF1 expression increased in response to prolonged HG exposure compared to NG or untreated cells. Removal of HG back to 7.5mM glucose after 5 days resulted in a reversal in nuclear expression similar to that seen in NG and untreated cells. Confocal images taken with 40x objective. Error bars indicate mean \pm standard error. Data was analysed by a two-way analysis of variance corrected by Bonferroni, ** $p=0.0048$ ($n=3$)

The phosphorylation state of SRSF1 is the primary determinate of its localisation within the cell. SRPK1 phosphorylates the first 12 serine residues within the SRSF1 RS domain, enabling the SR protein to bind to transportin-SR2, a nuclear import factor (Gonçalves & Jordan, 2015). This allows SRSF1 to shuttle to the nucleus where it is able to regulate VEGF-A alternative splicing. Due to the increased expression of VEGF-A_{165a} in HG and Hx hRPEs (Fig

3.3.1), I hypothesised that HG and Hx would result in increased SRSF1 phosphorylation. Thus, SRSF1 was immunoprecipitated out of NG, HG and Hx hpRPE lysate and immunoblotted against SRSF1 and phosphoSR (P-SR). This was run alongside the total lysate which was probed for the same as the precipitate (*Fig. 3.3.3-3A*). Bands for phosphorylated SR developed as a smear, perhaps due to the presence of various splice isoforms or post-translational modifications. To gain a measure of phosphorylation, the intensity of P-SR band at approximately 33kDa was taken as a percentage of the SRSF1 band. No difference was found in phosphorylation between NG and HG or Hx for the immunoprecipitation (*Fig 3.3.3-3B*). However, HG induced elevated SRSF1 phosphorylation (12.6 ± 0.46) compared to NG (9.21 ± 0.95) in the lysate. No change in phosphorylation occurred in response to Hx (6.89 ± 0.71).

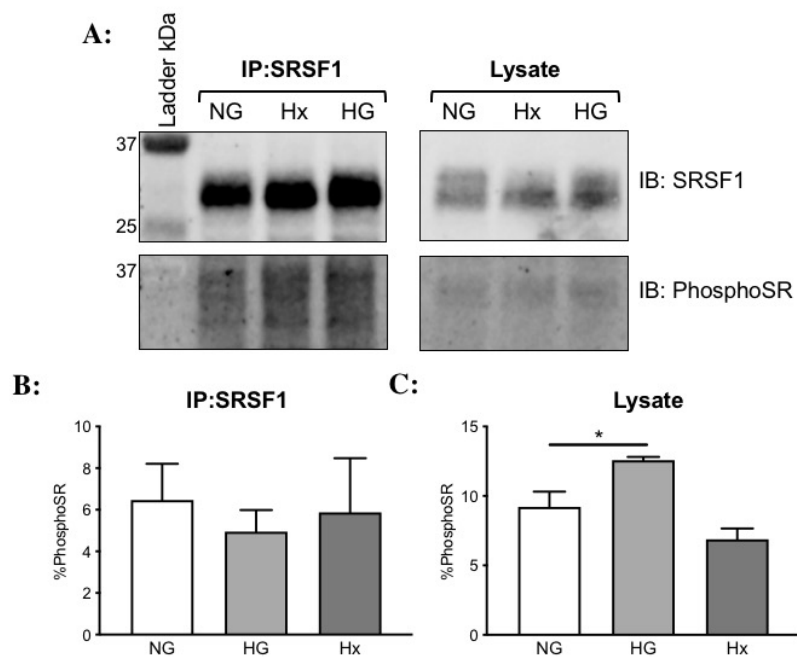


Figure 3.3.3-3: SRSF1 phosphorylation is unchanged in HG and Hx in hpRPEs.

A: Immunoblot (IB) of SRSF1 and P-SR of hpRPE lysate immunoprecipitated (IP) against SRSF1 and lysate alone. **B:** P-SR bands expressed as a percentage of SRSF1 pull-down. No change was observed in the extent of SRSF1 phosphorylation in response to HG or Hx. **C:** Percentage phosphorylation of SR proteins was increased in HG but not Hx when evaluated through total lysate. Error bars indicate mean + standard error. Data was analysed by a one-way analysis of variance corrected by Bonferroni, * $p < 0.05$ ($n=6$)

The impact of SPHINX31 on SRPK1 activity in diabetic mimicking conditions has been assessed in RPE indirectly through SRSF1 cellular localisation. However, several protein kinases have been described to be capable of phosphorylating SR proteins on serine residues, such as SRPK2 (Gui et al., 1994), CLK (Colwill et al., 1996) and DNA topoisomerase I (Rossi et al., 1996). Therefore, to confirm that the spatial differences in SRSF1 are due to the activity of SRPK1, I performed a nano-BRET to determine SRSF1:SRPK1 complex formation in response to HG. For these experiments, ARPE-19 cell line was utilised due to the increased transfection efficiency compared to a primary line. Dr Elizabeth Stewart performed a pull-down of SRSF1 and found that SRPK1 exists in a complex with SRSF1 (*Fig 3.3.3-4A*) in unstimulated ARPE-19s. Stimulating the cells with 100nM IGF caused a disassociation of SRPK1:SRSF1 complex reversed with the addition 10 μ M SPHINX31. This was confirmed by densitometry analysis (*Fig 3.3.3-4B*). Following her result, I co-transfected ARPE-19 cells with SRPK1-NanoLuc® and SRSF1-Halotag® constructs and cultured them with Opti-MEM™ supplemented with +30mM D-glucose or +30mM D-mannitol for three days. The reasoning for reduced exposure time compared to previous experiments in this chapter was due to using Opti-MEM™ media instead of DMEM:F12. Opti-MEM™ was required for successful transfection and fluorescence measurements but contains less additives than DMEM:F12, thus cells were beginning to die after 3 days exposure, hence the shorter exposure time. In order to determine the assay is working correctly, the signal at 450nm (*Fig 3.3.3-4C*) and 600nm (*Fig 3.3.3-4D*) was measured with and without ligand. The BRET ratio was calculated from these values (*Fig 3.3.3-4E*) and found to be 25% larger with ligand than without. The addition of mannitol appeared to have no effect on the BRET ratio when compared to media alone, however hyperglycaemia induced a reduction in BRET ratio, indicating an increase in SRPK1 activity (*Fig 3.3.3-4F*).

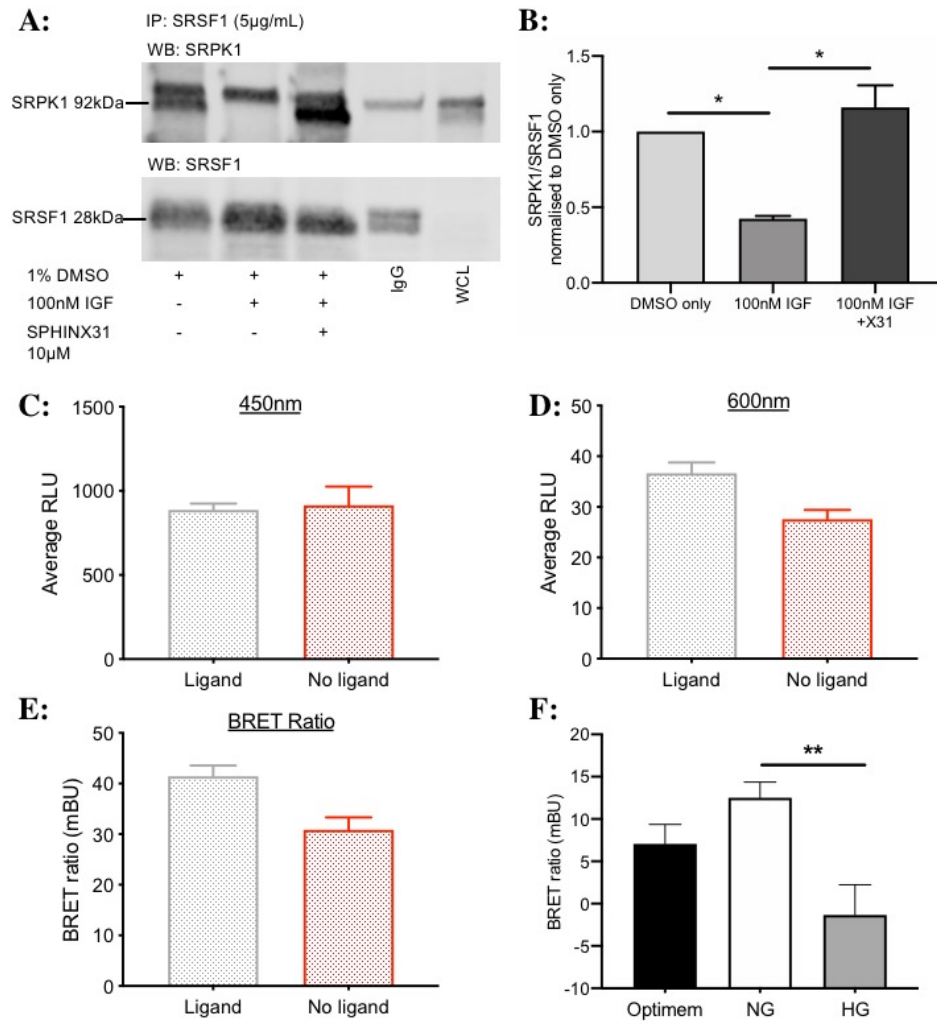


Figure 3.3.3-4: HG induces an increase in SRPK1 activity which causes a disassociation of the SRPK1-SRSF1 complex.

A: SRPK1 co-precipitates with SRSF1 in unstimulated RPEs. Stimulation of SRPK1 activity with 100nM IGF caused a loss of the SRPK1 band. 10µM SPHINX31 restored co-immunoprecipitation. **B:** Quantification of mean grey levels of immunoprecipitation (n=2). **C:** Average RLU is unchanged with the presence of ligand at 450nm. **D:** Average RLU is increased with halotag-618 ligand compared to no-ligand at 600nm. **E:** Calculated BRET ratio is increased with halotag-618 ligand. **F:** Mannitol induces no change in BRET ratio compared to basal media alone, however HG triggers a decrease in mean BRET ratio. Error bars indicate mean + standard error. Statistical analyses were performed using a one-way analysis of variance. *p<0.05, **p<0.01 (n=6).

Whilst Figure 3.3.2 shows that SRSF1 translocates to the nucleus in response to glycaemic insult, cellular stress has also been found trigger the movement of SRPK1 into the nucleus (Aubol et al., 2013). In order to determine where SRPK1 complexes with SRSF1, ARPE-19s were transfected with nano-BRET

constructs as previously. Opti-MEM™ media was exchanged for phenol-free DMEM:F12 as cells were plated onto 4-well imaging dishes. The change in media was due to the fact that cells would not adhere to imaging dishes in opti-MEM™, despite trailing different attachment factors. Cells were treated in NG or HG for three days. Nanoluc substrate was administered to cells, and a brightfield image on the Olympus LV200 was taken to assess cell morphology. Microscope parameters were adjusted to ensure optimal imaging within 10 min of addition of substrate and a 30min video was taken of bioluminescence and fluorescence (663-739nm) (see Chapter 2: Materials and Methods – 2.8.3 for full detail). NG cells appeared to have SRSF1:SRPK1 complexes across the whole cell (*Fig 3.3.3-5A*) whilst HG cells only appeared to have these complexes within the nucleus (*Fig 3.3.3-5B*). Videos were exported to FIJI for analysis, and fluorescent intensity within a cell was measured in all frames. This value was plotted over time. HG cells appeared to have higher BRET signal across 30min compared to that of NG.

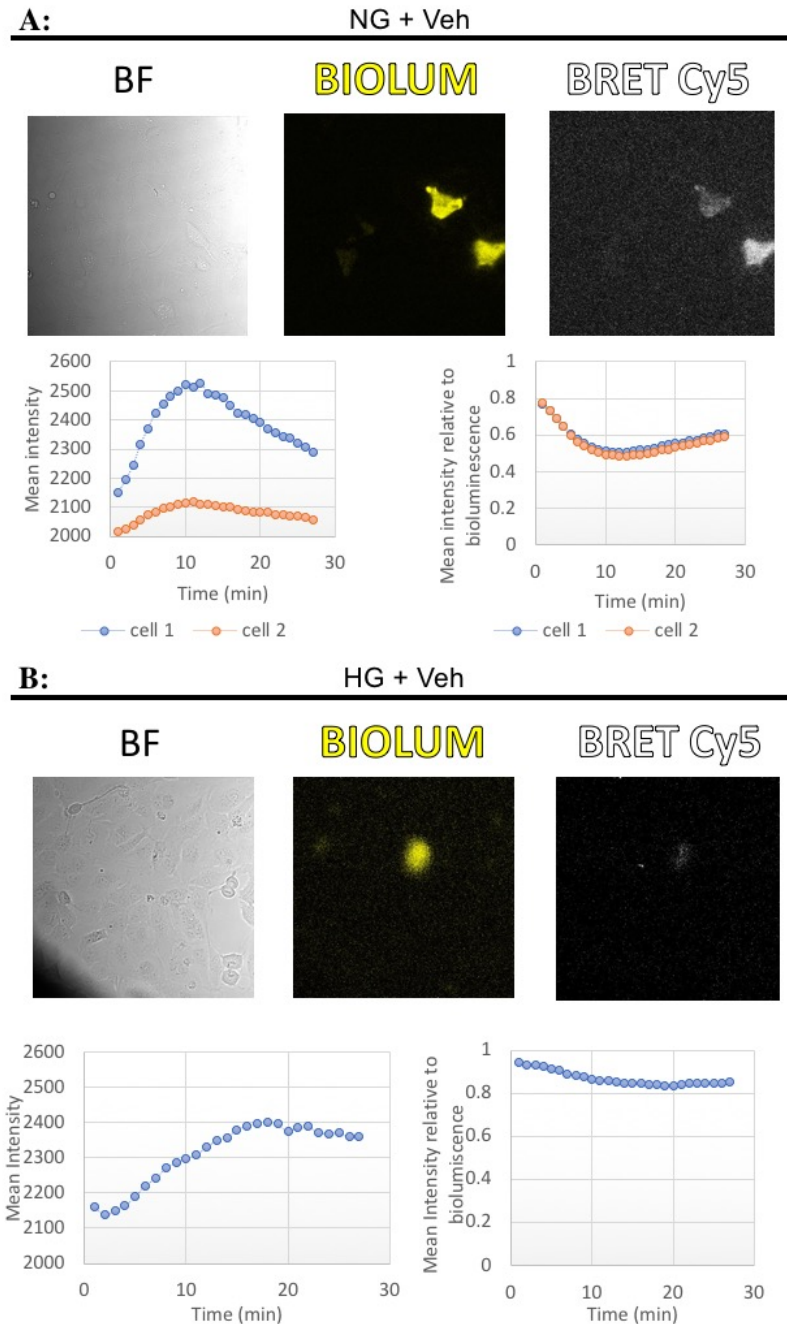


Figure 3.3.3-5: HG appears to induce translocation of SRSF1:SRPK1 complexes to RPE nuclei

A: RPE monolayers transfected with nano-BRET constructs. Brightfield image shows a healthy cell monolayer. In NG, bioluminescence imaging displays nanoluc construct across entire cell. BRET-Cy5 signal; fluorescence emitted from halotag-618 ligand due to excitation of luciferase, appears across entire cell. Mean intensity of bioluminescence within a cell plotted over time. BRET-Cy5 fluorescent intensity within a cell was normalised to bioluminescence and plotted over time. **B:** In HG, cell monolayers appear healthy when assessed through brightfield imagery. Bioluminescence and fluorescence appeared to the

localised within cell nuclei. Fluorescence intensity appeared to be higher in HG than NG (n=1).

Yoon *et. al.*, 2014 found that the hypoxic environment decreases expression of post-transcriptional regulator microRNA miR-9, which led to an increase in SRPK1 transcription and thus a shift in alternative splicing to the proangiogenic isoform of VEGF (Yoon *et al.*, 2014). Cells exposed to hypoxic conditions express significantly higher VEGF-A_{165a} protein compared to normoxic cells (*see Fig 3.3.1*). Thus, I hypothesised that these cells will also have an increase in SRSF1 nuclear expression, similar to that which is seen in Fig 3.3.3-2. Cells were grown to a confluent monolayer and treated with 1% pO₂ between one and five days. In addition, a subset of hpRPEs were exposed to +30mM D-glucose and hypoxia. Cells were stained for SRSF1, a nuclear stain DAPI and ZO-1 to visualise cell edges (*Fig 3.3.3-6A*). The ratio of nuclear to cytoplasmic SRSF1 expression was plotted over the course of five days (*Fig 3.3.3-6B*) and found to increase in response to HG as previously. Corroborating with previous experiments, nuclear SRSF1 expression in NG remains static across five days. Interestingly, Hx caused SRSF1 nuclear localisation to increase even further to that seen in HG conditions (*Fig 3.3.3-6C*). The timecourse was extended further to 10 days, to elucidate the effects of long-term HG, keeping Hx exposure to 72h as hpRPEs began to die if exposed for longer. The cells were seeded at a density to ensure they formed a monolayer with tight cell junctions and not grow on top of one another (*Fig 3.3.3-6D*). After ten days of glucose treatment, HG cells exhibited an increase in nuclear SRSF1 localisation which was not statistically significant despite the extended exposure time (*Fig 3.3.3-6E*). Hx was able to induce a statistically significant rise ($p=0.0335$) in nuclear localisation, similar to that seen at the 5-day point (*Fig 3.3.3-6F*). However, after ten days in culture, the cell morphology looked altered and inconsistent with previous RPE monolayers in normoxia. There were areas of cell death and areas of overconfluence. In addition, after 10 days, the dynamic range between treated and control cells was much lower than that of 5 days, which will have an impact for later experiments where I will try to manipulate splicing. Thus, I decided that for future experiments, HG treatment would be concluded after 5 days.

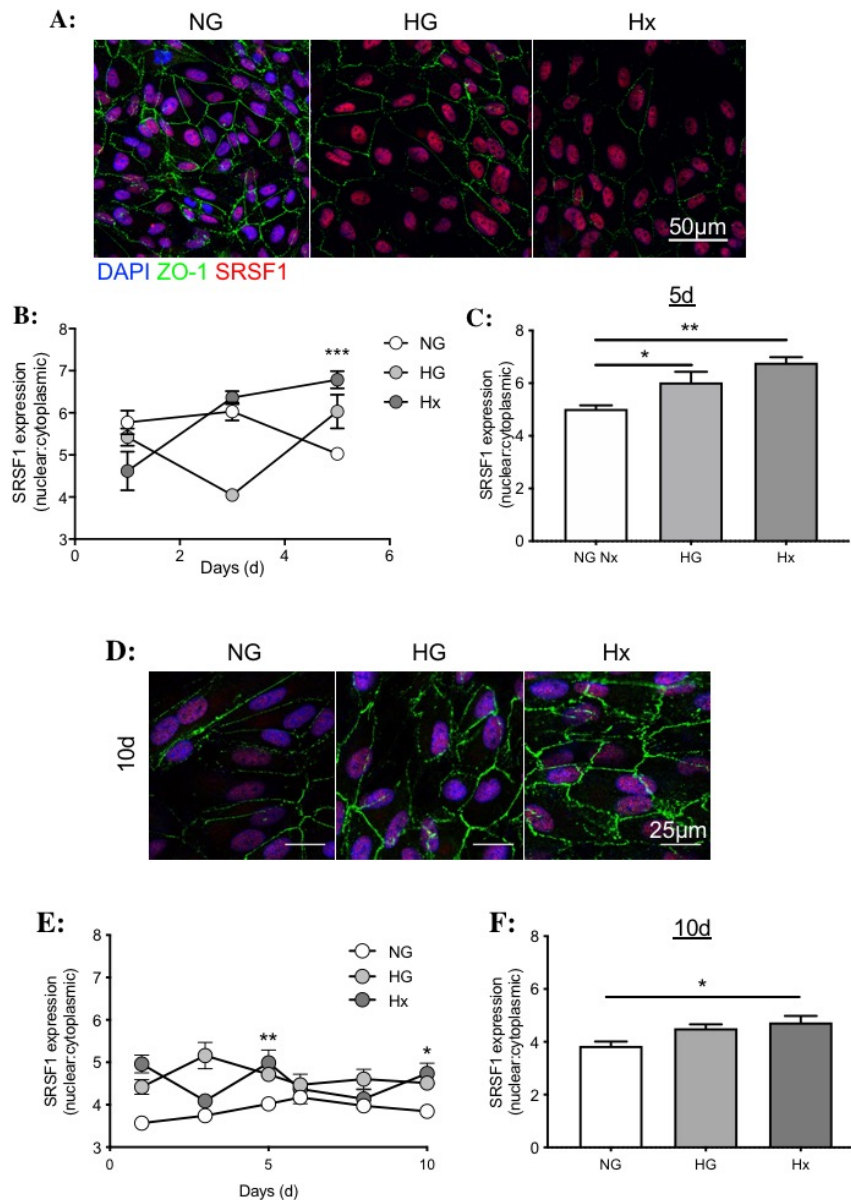


Figure 3.3.3-6: Hx induces nuclear localisation of SRSF1

A: Overlay images of **DAPI**, **ZO-1** and **SRSF1** staining in response NG, HG and Hx. Scale bar = 50µm. **B:** Five day timecourse of SRSF1 localisation expressed as a ratio of nuclear to cytoplasmic. **C:** After 5 days, nuclear SRSF1 expression increased in response to prolonged HG and Hx exposure compared to NG. **D:** Representative images of hPRPEs cultured for 10 days and stained with **DAPI**, **ZO-1** and **SRSF1** overlaid. 25µm scale bar. **E:** Ten day timecourse of ratio of nuclear to cytoplasmic SRSF1 expression **F:** Nuclear localisation appears greatest in Hx cells, whereas the prolonged exposure to HG has no effect. Confocal images taken with 40x lens. Data analysed using a two-way analysis of variance. Error bars of **B** and **E** indicate mean \pm standard error, **C** and **F** represent mean + standard error. Data was analysed by a two-way analysis of variance corrected by Bonferroni, *p<0.05, **p<0.01, ***p<0.001. (n=3).

Previous experiments of this chapter have established that cellular stress through HG or Hx induces nuclear localisation of SRSF1, and the literature confirms that function of SRSF1 is spatially regulated (Gonçalves et al., 2014). However, functions of splicing factors can be further understood through realising their sub-nuclear localisation. The mammalian nucleus is organised into multiple domains with various functionalities generally characterised by their protein and RNA content. Nuclear speckles are dynamic structures concentrated with transcription and pre-mRNA factors, and splicing factors appear to accumulate within these speckles when inactive (Tripathi et al., 2012). Complete phosphorylation of the RS domain of SRSF1 instigates a dispersion of the splicing factor out of the nuclear speckles where it is able to interact with the spliceosome via RNA polymerase II (Gonçalves & Jordan, 2015). The splicing factor SRSF2 (SC35) accumulates within the nuclear speckles, thus can be used as a nuclear speckle marker.

To determine the localisation of SRSF1 within the nucleus, initially it was necessary to optimise staining. To validate the antibody, ARPE-19 cells were fixed and stained with an antibody against SRSF2 alongside two cancer cell lines for comparison. Confocal microscopy using a 63x oil immersed objective was used to image the nuclei (*Fig 3.3.3-7A*). Whilst the staining in the cancer cell nuclei was quite widespread and diffuse, with no apparent specific localisation of SRSF1 or SRSF2, the RPE staining, although less intense, was of a more speckled nature, especially apparent with SRSF1. There was also some evidence of staining within the cytoplasm, not seen in the cancerous cells. To gain a quantitative measure of SRSF1, SRSF2 co-localisation, Image J analysis was performed (*Fig 3.3.3-7B*). Both SRSF1 and SRSF2 are dispersed across the z-plane of the nucleus, as evidenced in a zoomed in image of an RPE cell. DAPI staining generated a mask of the nucleus. Within the mask, the intensity of the SRSF1 stain and SRSF2 stain was plotted against each other. (See Chapter 2: "Materials and Methods").

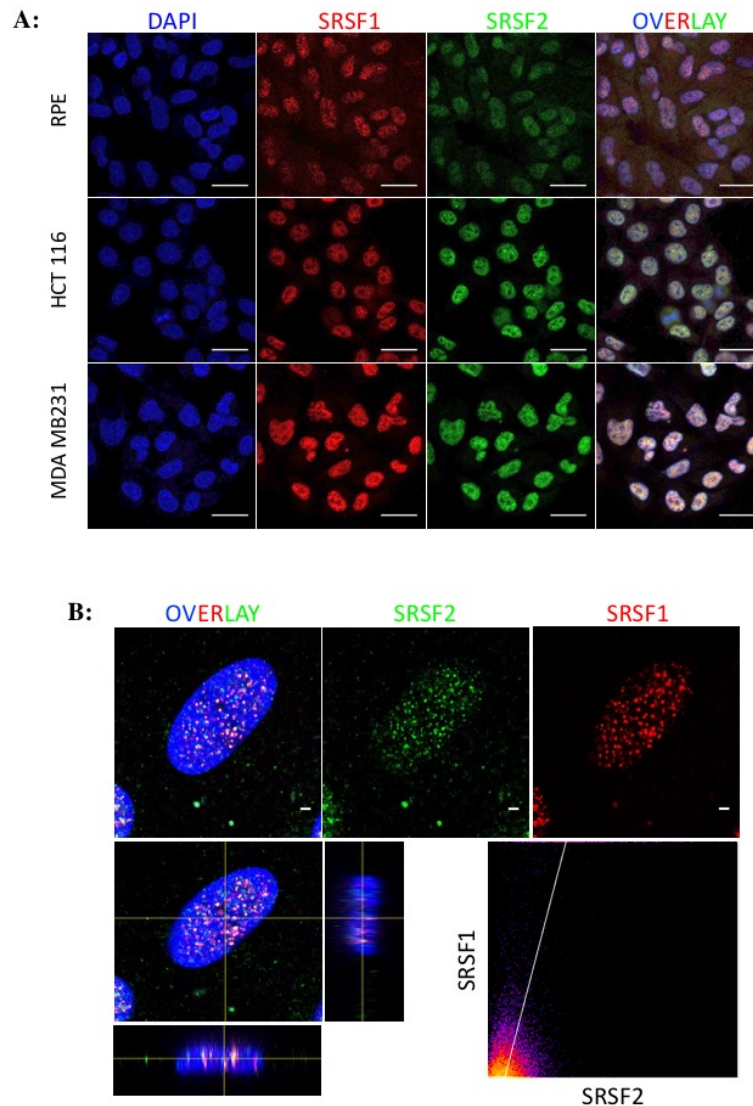


Figure 3.3.3-7: Optimisation of SRSF1 and SRSF2 staining and analysis

A: 63x oil-immersed lens images of **DAPI**, **SRSF2** and **SRSF1** staining in RPE, HCT 116 and MDA MB231 cell lines. Scale bar = 25µm. **B:** Confocal imaging of a zoomed in RPE cell. Z-plane images find SRSF1 and SRSF2 located throughout the whole nucleus in a speckle formation. Co-localisation plot generated by FIJI showing intensity of SRSF1 stain against SRSF2.

This methodology was used on hpRPE cells treated for five days with +30mM D-mannitol or D-glucose in order to elucidate the impact of HG on subnuclear localisation of SRSF1. HG exposure produced nuclei that appeared more red in colour compared to the ‘yellow’ nuclei in NG cells (Fig 3.3.3-8A). The yellow colour is a result of an overlay of the red SRSF1 and green SRSF2 channels, thus this could potentially mean that SRSF1 localisation against SRSF2 is reduced by HG compared to NG. Analyses confirmed this observation (Fig

3.3.3-8B), which could mean that SRSF1 is released from the nuclear speckles in response to HG.

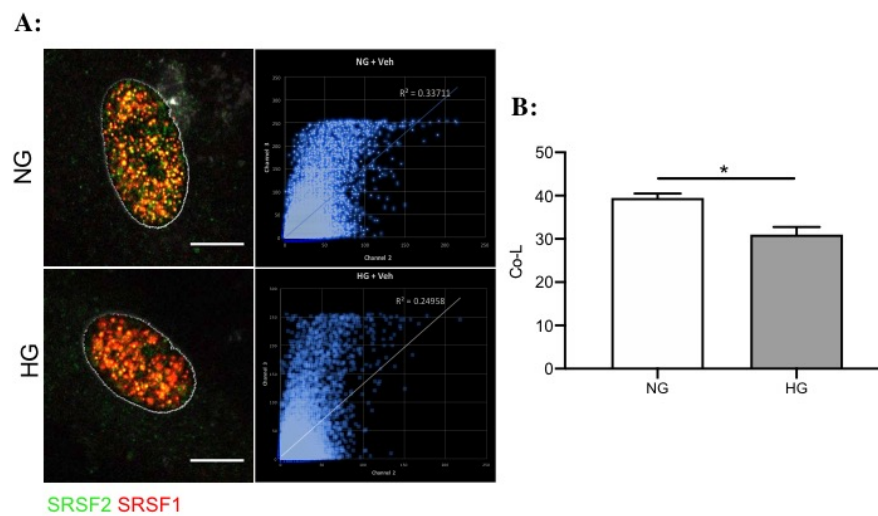


Figure 3.3.3-8: SRSF1 is released from nuclear speckles in HG RPEs

A: 63x oil-immersed lens images of SRSF2 and SRSF1 staining in hpRPE. Scale bar = 10µm. Intensity of SRSF1 and SRSF2 staining in each pixel was plotted against each other to determine the correlation of staining. **B:** HG induces a reduction in SRSF1:SRSF2 co-localisation co-efficient (Co-L) after 5 days. * $p < 0.05$, $n = 4$, statistical analysis performed using t-test.

3.4 Discussion

3.4.1 hpRPEs provide a better model of *in vitro* outer blood-retinal barrier in comparison with ARPE-19s

A lot of the research surrounding DR focuses on the iBRB, and the impact of VEGF-A on the retinal endothelial cells has been widely accepted. However, the RPE cell layer that contributes to the oBRB are not only disrupted in DR and DMO, but also act as a VEGF-A secretome and could potentially be manipulated in order to treat this disease (Ponnalagu et al., 2017). I generated an *in vitro* model of the oBRB RPE cell layer to study this, trialling the immortalised ARPE-19 cell line and hpRPEs isolated from donor eyes. With regards to barrier integrity, ARPE-19s were found to be a poor model. ZO-1 intensity on cell membranes in ARPE-19s appeared to increase in response to HG (*Fig 3.3.2-1*), although this did not translate functionally as there was no difference in permeability across the monolayer (*Fig 3.3.2-3*). Increase in membrane ZO-1 expression would suggest tighter cell-junctions, thus reduction in permeability and so these results contradict one another. Occludin was initially used as the marker of tight junctions when optimising experiments performed in section 3.3.2, but staining was weak in ARPE-19s, highly dispersed and did not appear to be localised to the tight junctional area. This result was also seen in the Ablonczy *et. al.* paper, and furthermore TER values were lower suggesting that ARPE-19 cells form weaker tight junctions compared to human primary cell lines (Ablonczy et al., 2011). Despite the issues described with ARPE-19s as a model for barrier integrity, trends in VEGF-A isoform expression and SRSF1 nuclear localisation remained the same as hpRPEs, just to a smaller extent. Thus, the cell line was useful for optimising experiments whilst waiting for primary cell lines.

3.4.2 Hyperglycaemia and hypoxia upregulates VEGF-A_{165a} expression and disrupts RPE monolayer properties

hpRPEs exhibited increased VEGF-A_{165a} expression in response to hyperglycaemia and hypoxia, and although VEGF-A_{165b} levels remained unchanged, the ratio of VEGF-A_{165b}/VEGF-A_{165a} was reduced (*Fig 3.3.1*)

consistent with published data in diabetic human vitreous (Perrin et al., 2005). In addition, *Kim et. al.* found that the hyperglycaemic environment is stimulatory for VEGF-A expression, however this expression did not cause angiogenesis (Kim et al., 2002). Barrier integrity was measured in multiple ways, one being ZO-1 membrane localisation (*Fig 3.3.2-1*). Two methods of analysis were tested, total intensity and 'peak' number. The number of peaks in the staining profile represents the number of 'gaps' in tight junctions, thus the higher the peak number, the weaker the barrier. This method proved to be unrepresentative as no change was seen in response to HG despite reduction in TER (*Fig 3.3.2-3*). Total intensity values were concluded to be the optimal measurement of membrane ZO-1 expression as this decreased in response to hyperglycaemia and hypoxia, corroborating with that observed *in vivo* (Xu & Le, 2011). ZO-1 protein expression remained static in hyperglycaemic conditions (*Fig 3.3.2-2*), which could suggest intracellular trafficking, but not degradation of ZO-1. However in hypoxia, ZO-1 levels were significantly reduced, an observation also seen in endothelial cells in response to HIF-1 α (Hu et al., 2019).

3.4.3 SRPK1 activity increases in response to hyperglycaemia and hypoxia

The SRPK1-SRSF1 axis has been implicated in regulating VEGF-A isoform expression. SRPK1 phosphorylates SRSF1 causing it to translocate from the cytoplasm to the nucleus where it is able to interact with VEGF-A pre-mRNA (Nowak et al., 2010). Thus, the activity of SRPK1 can be indirectly monitored through determining the localisation of SRSF1 within the cell. Hyperglycaemia induced an increase in nuclear SRSF1 over the course of five days compared to media only and an osmotic control. Reversion of glucose concentration back to 7.5mM post 5 days 37.5mM treatment restored SRSF1 localisation, highlighting the dependence of SRSF1 translocation on a glycaemic stimulus (*Fig 3.3.3-2*). After 10 days, the ratio of nuclear to cytoplasmic SRSF1 was also increased, but not to a statistically significant effect, (*Fig 3.3.3-6*) perhaps due to over-confluency of the cells and improper formation of the monolayer. Despite differential nuclear localisation, there was no difference in overall SRSF1 expression (*Fig 3.3.3-1*). The amplified SRSF1 nuclear shuttling

suggests an increase in its phosphorylation by SRPK1. However this wasn't reflected in the immunoprecipitation results (*Fig 3.3.3-3*), which could potentially be due to the P-SR band developed as a smear. An increase in P-SR was seen in the immunoblot of total lysate, suggesting that there is an increase in phosphorylation of SR proteins in HG, just not specifically in SRSF1. Rather than indirectly measuring SRPK1 activity through SRSF1 localisation and phosphorylation, a proximity based assay, nano-BRET was performed. Aubol et al found that SRPK1 affinity for SRSF1 increases five-fold when the splicing factor is unphosphorylated, which potentially explains why SRPK1 was found to exist in a complex with SRSF1 in unstimulated cells (*Fig 3.3.3-4*) (Aubol et al., 2016). Treatment with IGF-1, a known SRPK1 stimulator, causes a disassociation of this complex. Glycaemic and not osmotic shock was found to decrease SRSF1:SRPK1 complex formation in RPEs thus suggesting an increase in SRPK1 activity. At the time of writing this thesis, this appears to be the first time SRPK1 activity has been described to increase in HG through a direct assay. Osmotic stress has been found to trigger SRPK1 movement into the nucleus, but SRPK1:SRSF1 complexes were found across the entire cell when treated with mannitol (Ma et al., 2009). It is only after glycaemic insult, where SRPK1:SRSF1 appeared to translocate to the nucleus. This result, although exciting, requires further work to robustly conclude the translocation. The brightfield image was faint due to limitations of this microscope, but did show a monolayer of ARPE-19 cells. Despite this, only one or two cells appeared to be successfully transfected with the nano-BRET constructs. Transfection efficiency has been described to be greater in dividing cells compared to non-dividing, due to the repeated breakdown of nuclear membrane during cell division (Bettinger et al., 2001; Maury et al., 2014), and RPEs within a monolayer will display contact inhibition thus not be actively dividing (Stern & Temple, 2015). Had I decreased the seeding density, I may have achieved a higher transfection efficiency. The apparent poor transfection efficiency did not appear to be an issue for the nanoBRET assay as measurements were taken across the entire cell monolayer with a spectrophotometer. Furthermore, although the BRET-Cy5 signal in HG cells appears more rounded, however this is not conclusive proof that the complex is existing with the nucleus. Live cells could have been stained with the nuclear

marker, Hoechst, to confirm localisation of the nucleus and deduce whether the BRET-Cy5 signal overlays the stain. Another interesting experiment would have been to administer glucose to cells already expressing the nano-BRET constructs, and imaging the BRET-Cy5 signal. Through this, it would be possible to solve the time it takes for the complex to translocate to the nucleus.

HG mobilises SRSF1 to move into the nucleus, however, in order to further understand its function, it is necessary to visualise SRSF1 within subnuclear domains. Pre-mRNA splicing machinery are known to assemble into nuclear speckles and thus proteins which localise within the subnuclear storage sites are implicated in pre-mRNA processing (Kim et al., 2016). Transcriptionally active genes are commonly localised adjacent to these speckles, previously termed SC35 domains due to the high concentration of SRSF2 within them (Hall et al., 2006). Thus, immunofluorescence was performed to determine whether SRSF1 co-localises with SRSF2 within the nucleus. SRSF1 staining produces punctate foci within the nucleus (*Fig 3.3.3-8*). SRSF1 appears to be released out of the nuclear speckles in hyperglycaemic conditions.

Generally, hypoxia produced similar results to that of hyperglycaemia, just to a larger extent. An exception was SRSF1 expression, that reduced in hypoxic conditions but not in hyperglycaemia (*Fig 3.3.3-1*). This was surprising as elevated SRSF1 expression has been found in PC3 prostate cancer cells (Bowler et al., 2018). As mentioned previously, the function of SRSF1 is spatially regulated, and cells exposed to hypoxia for three days exhibited increased nuclear SRSF1 compared to normoxic cells (*Fig 3.3.3-6*). This suggests an elevation in SRPK1 activity, thus we would assume this would correspond with more SRSF1 phosphorylation. However, the immunoprecipitation and immunoblots did not support this hypothesis (*Fig 3.3.3-3*), which could potentially be due to the antibody used to detect P-SR or another assay error. This experiment underwent several rounds of optimisation, but the results remained inconclusive, thus I decided that this assay would not be used moving forwards to assess SRPK1 activity.

3.5 Summary

An optimal *in vitro* model of the oBRB in diabetes was generated, requiring hRPEs grown to form a monolayer and then treated with +30mM D-glucose for five days to represent hyperglycaemic conditions or 1% pO₂ for three days to represent hypoxia. A control of +30mM D-mannitol will always be included alongside to determine the impact of osmotic shock.

The evidence suggests that hyperglycaemia exhibits increased nuclear localisation of SRSF1 and SRSF1:SRPK1 complex, an increase in SRPK1 activity, where it is released from the nuclear speckles and able to bind to VEGF-A pre-mRNA. Thus, VEGF-A_{165a} levels are amplified resulting in a decrease in barrier integrity and overall increase in monolayer permeability.

Hypoxia also induced increased SRSF1 nuclear localisation, despite a reduction in overall expression, which corresponded with upregulated VEGF-A_{165a} expression. There was a loss of cell membrane localisation of tight junction protein ZO-1 alongside a complete reduction in overall protein expression.

CHAPTER 4

Elucidating the effects of inhibiting SRPK1 in a diabetic *in vitro* model of the RPE monolayer of outer blood retinal barrier

4.1 Introduction

Differential inclusion of VEGF-A terminal exon 8a or 8b results in production of alternative VEGF-A isoforms, VEGF-A_{xxx}a or VEGF-A_{xxx}b. Both isoforms bind to their cognate receptor VEGFR2 with equal affinity, and VEGF-A₁₆₅a can additionally bind to VEGFR2 co-receptor, NP-1 (Kawamura et al., 2008). Binding of VEGF-A₁₆₅a to VEGFR2 and NP-1, results in a conformational change in VEGFR2, inducing receptor dimerization and an internal rotation of the intracellular domain. The resulting tyrosine autophosphorylation is followed by VEGFR2 internalisation where downstream pathways enhancing permeability and promoting cell survival, amongst others, are activated (Ford et al., 2011; Harper & Bates, 2008). VEGF-A₁₆₅b is distinct from its sister isoform as it is unable to fully stabilise NP-1 binding and does not completely activate VEGFR2 when bound. VEGFR2 is only partially phosphorylated, and thus elicits weaker downstream effects (Harper & Bates, 2008). Perrin et al. discovered the existence of both families of isoforms in the adult vitreous, confirming their requirement for ocular function. Diabetes elicits a switch in splicing which results in an abundance of VEGF-A₁₆₅a such that VEGF-A₁₆₅b percentage in the vitreous decreases approximately five-fold compared with healthy eyes (Perrin et al., 2005). Thus, in the diabetic eye, there is an increased activation of VEGFR2 resulting in increased angiogenesis and permeability. Recombinant VEGF-A₁₆₅b ameliorates pathologies *in vivo* in experimental models of choroidal neovascularisation (Hua et al., 2010) and DR (Ved et al., 2017). In addition, this isoform is also protective *in vitro* against VEGF-A₁₆₅a- and hyperglycaemia induced breakdown of the RPE monolayer (Ved et al., 2017). Thus, VEGF-A₁₆₅b may offer therapeutic potential in the treatment of DR.

The splicing factor SRSF1 and its kinase SRPK1 regulates alternative splicing of VEGF-A (Nowak et al., 2008). When activated, SRPK1 phosphorylates the first twelve serine residues within the N-terminal portion RS domain (RS1) of SRSF1 (Aubol et al., 2013), enabling the SR protein to bind to a nuclear transport factor, transportin-SR2 (Kataoka et al., 1999). This complex shuttles into the nucleus where SRSF1 is stored as nuclear speckles, its release

facilitated by CLK-1 through a hyperphosphorylation of the remaining serine residues. Here, SRSF1 can mediate splicing reactions through interacting with splicing regulatory elements on pre-mRNA (Naro & Sette, 2013) including promoting proximal splice site selection of VEGF-A exon 8 and thus upregulating VEGF-A_{xxx}a expression (Nowak et al., 2010). Within the cytoplasm, SRPK1 exists in a complex with heat-shock proteins and their co-chaperones. Cellular stress can disrupt this complex and induce nuclear shuttling of SRPK1 (Aubol et al., 2013). Within the nucleus, SRPK1 is able to complex with CLK-1, an interaction that enhances CLK-1 ability to hyperphosphorylate SRSF1, promoting release from the nuclear speckles (Aubol et al., 2016). SRPK1 has an additional role in the nucleus, where it mediates disassociation of phospho-SRSF1 and CLK-1. Binding of SRPK1 increases five-fold to unphosphorylated SRSF1 in comparison to phospho-SRSF1, in addition, after phosphorylation of the first eight residues of RS1, SRPK1 affinity for SRSF1 decreases (Aubol et al., 2016). Inhibition of SRPK1 promotes VEGF-A_{165b}/reduces VEGF-A_{165a} expression in multiple tissues, particularly within the eye, without harming cell function (Batson et al., 2017).

PKC involvement is both upstream and downstream of VEGF-A. Diabetes induces increases in DAG levels and PKC activity in many vascularised tissues including the retina (Shiba et al., 1993). Multiple pathways have been implicated in PKC activation in response to diabetes. Hyperglycaemia stimulates synthesis of DAG *de novo* from glycolytic intermediates, and also an increase in oxidants such as H₂O₂. Oxidants are able to activate PKC activity directly (Konishi et al., 1997) and indirectly through increasing DAG production (Nishikawa et al., 2000). Diabetic induced changes in PKC activity is also isoform specific, PKC isoenzymes - α , - β I, - β II and - ε are all reported to increase in the retina membrane and cytosol of diabetic rats (Konishi et al., 1997). The mechanisms as to why there is selectivity to diabetes-induced changes to PKC isoform activity remains unclear, however it is hypothesised to be due to subcellular location (das Evcimen & King, 2007). PKC isozymes - α , - β I, - β II and - γ are characterised as conventional isozymes possessing tandem C1A and C1B domains capable of binding to DAG. Isozymes PKC δ , - ε , - θ , - η are described as novel, and also contain DAG-binding C1A and C1B domains, but

the affinity of C1B domain for DAG is 100-fold higher than that of conventional PKC isozymes (Wu-Zhang & Newton, 2013). SRPK1 can be activated via PKC, thus promoting expression of VEGF-A_{xxx}a isoforms (Nowak et al., 2010). It is through this process that PKC is able to feedback on itself, as VEGFR2 activation by VEGF-A stimulates PKC activation via PLC γ mediated manner (Xia et al., 1996). Notably, PKC activation in response to hyperglycaemia has been found to increase VEGF-A levels in RPE (Poulaki et al., 2002).

Small molecular weight inhibitors of SRPK1 have been developed. The 3-(trifluoromethyl)anilide scaffold SPHINX31 has excellent potency and selectivity for SRPK1. The compound has an IC₅₀ of 5.9nM, and occupies the binding pocket of SRPK1 inducing a backbone flip in the hinge region of the pocket (Batson et al., 2017). SPHINX31 will be used over the course of this study to inhibit SRPK1 kinase activity.

SRPK1 inhibitors are touted to have the potential to act as a therapeutic agent for a number of ocular diseases (Batson et al., 2017). In this chapter I aim to elucidate the impact of inhibiting SRPK1 in diabetes-mimicking conditions: hyperglycaemia and hypoxia, in a model of the RPE monolayer of the oBRB. SRPK1-SRSF1 axis has been implicated in VEGF-A terminal exon 8a or 8b selection (Gammons et al., 2014; Nowak et al., 2010), thus I will deduce how inhibiting this axis influences VEGF-A isoform expression. I also aim to evaluate the potential of SRPK1 inhibition as a blocking agent against increases in RPE monolayer permeability caused by diabetes mimicking conditions. Furthermore, the direct effect of topical agent SPHINX31 on SRPK1 activity will be determined through a nano-BRET assay, and indirectly through establishing its impact on SRSF1 localisation. Finally, to further understand differential SRPK1 activity in diabetes, PKC inhibitors will be utilised in assays of SRPK1 activity.

4.2 Methodology

The work described in this chapter was performed using human primary retinal pigmented epithelial (hpRPE) cells isolated from human donors or in the immortalised ARPE-19 cell line. Hyperglycaemia (HG) assays required the use of DMEM:F12 media, with a basal concentration of 7.5mM, supplemented with 30mM D-glucose. All experiments were carried out alongside a normoglycaemic (NG) control, where cells were exposed to DMEM:F12 supplemented with 30mM D-mannitol; a non-reactive sugar with the same osmolarity as D-glucose. Hypoxic conditions of 1%pO₂ was achieved using a sealed hypoxia incubator. SRPK1 inhibitor, SPHINX31, and PKC inhibitors BIM-1 and Go6976 were initially dissolved in 100% DMSO before diluted in media to a final concentration of 1% DMSO to treat cells. These experiments were performed alongside a vehicle only (1% DMSO) control. An ELISA determined VEGF-A₁₆₅ isoform expression in treated cells. To elucidate changes in RPE monolayer barrier properties, ZO-1 localisation was established using immunofluorescence. This was supported by impedance measurements across the monolayer via electrical cell impedance sensing. SRSF1 localisation studies were performed using immunofluorescence and confocal microscopy. Protein expression was determined using western blot. Cells were assayed for SRPK1 activity using nano-BRET in different conditions. Unless otherwise stated, all repeats are technical repeats. All methods are described in detail in Chapter 2: “Materials and Methods”.

4.3 Results

4.3.1 Changes in VEGF-A₁₆₅ isoform expression in response to SRPK1 inhibition in hyperglycaemia and hypoxia

The RPE monolayer restricts the movement of fluid across the oBRB, however, these cells are also a major contributor to VEGF-A expression within the eye (Marneros et al., 2005). Administering recombinant VEGF-A_{165b} has been found to have protective effects in models of diabetic retinopathy *in vivo* (Ved et al., 2017), thus it is postulated that switching VEGF-A splicing in RPE holds therapeutic potential for DR. The impact of inhibiting SRPK1 in RPE in VEGF-A isoform expression in diabetes-mimicking conditions was measured. An ELISA (previously validated in Chapter 3.3.1) was performed on cell lysate of RPEs treated with +30mM D-glucose (HG) for 5 days or 1%pO₂ for 3 days (Hx), with +30mM D-mannitol (NG) included as an osmotic control (see Chapter 2: Materials and Methods for further detail). Concentrations of VEGF-A_{165a} was determined using the standard curve (*Fig 4.3.1.A*) and as previously in Chapter 3.3.1, HG and Hx induced an increase in VEGF-A_{165a} expression but not NG (*Fig 4.3.1.B*). 3µM SPHINX31 blocked this increase ($p < 0.05$) in both conditions whilst having no effect in NG. VEGF-A_{165b} concentrations measured from a standard curve (*Fig 4.3.1.C*) did not significantly change in response to either condition or SRPK1 inhibition (*Fig 4.3.1.D*). When VEGF-A expression was assessed as a ratio, SPHINX31 restored VEGF-A_{165b}/VEGF-A_{165a} ratios in HG and Hx to NG levels (*Fig 4.3.1.E*).

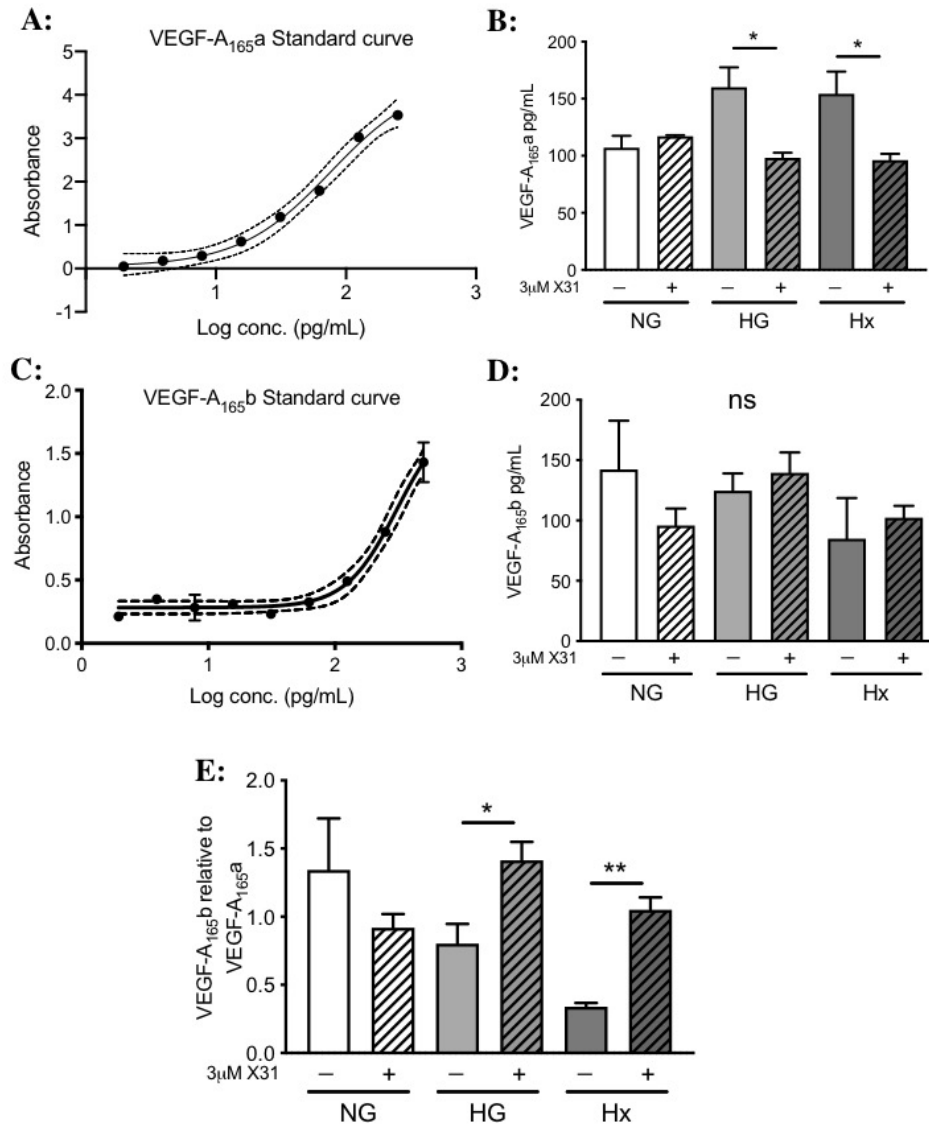


Figure 4.3.1: SRPK1 inhibition ameliorates hyperglycaemia- and hypoxia-induced changes in VEGF-A₁₆₅ isoform expression

A+C: Standard curves of VEGF-A_{165a} and VEGF-A_{165b} respectively. **B:** 3µM SPHINX31 (X31) had no impact in VEGF-A_{165a} levels in NG but reduced VEGF-A_{165a} in both HG (from 160±16.81pg/mL to 98.3±3.5pg/mL) and Hx (from 154.4±19.4pg/mL to 96.1±5.5pg/mL). **D:** VEGF-A_{165b} expression was not significantly impacted in response to X31 in any condition. **E:** VEGF-A_{165b} relative to VEGF-A_{165a} was increased in HG (from 0.80±0.14pg/mL to 1.41±0.12pg/mL) and Hx (from 0.34±0.02pg/mL to 1.05±0.09pg/mL) in response to X31. (n=3) ns=not significant, *p<0.05, **p<0.01. Statistical analyses performed using one-way analysis of variance with Bonferroni post hoc. Error bars represent mean plus standard error.

4.3.2 Impact of SRPK1 inhibition on integrity of RPE monolayer

Work from the previous chapter resulted in a reliable model of the RPE monolayer of the oBRB which was disrupted in response to the diabetes-mimicking conditions, HG and Hx. Loss in barrier integrity in these conditions is potentially due to the shift in VEGF-A₁₆₅ isoform expression where VEGF-A_{165a} levels overwhelm VEGF-A_{165b}. SRPK1 inhibition has been found to block this shift, returning VEGF-A₁₆₅ ratio to NG levels. Thus, in order to elucidate how this affects tight junction complexes within the RPE monolayer, hpRPEs were treated as 4.3.1 and ZO-1 expression was visualised using immunofluorescence and confocal microscopy (*Fig 4.3.2-1A*). FIJI analysis determined the intensity of ZO-1 expression along the cell membranes (for further detail of analysis method, see Chapter 2: “Materials and Methods”). As previously in Chapter 3, HG and Hx reduced ZO-1 intensity compared to NG. Excitingly, 3 μ M SPHINX31 increased ZO-1 intensity in both of these conditions compared to a vehicle only (1% DMSO) control (*Fig 4.3.2-1B*). An interesting observation was that Hx cells appeared to be larger in size than NG and HG, and this was not changed by SPHINX31 treatment (*Fig. 4.3.2-1A*).

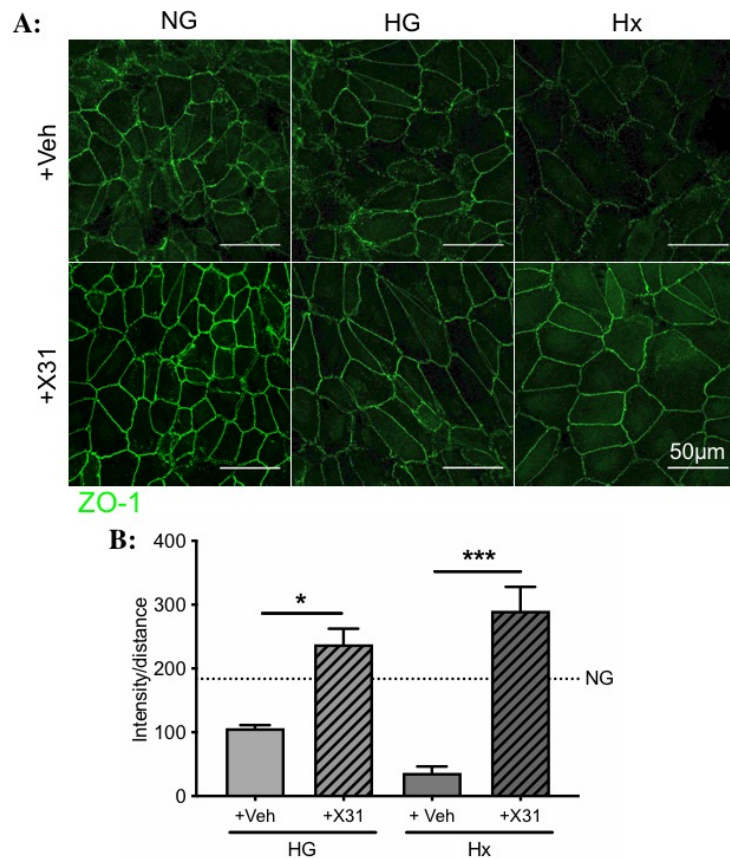


Figure 4.3.2-1: Loss of barrier localisation of ZO-1 in HG and Hx is ameliorated by SRPK1 inhibition.

A: 40x images of ZO-1 staining of hprPE monolayers imaged using confocal microscopy. **B:** Fiji analysis of staining to determine ZO-1 intensity over membrane distance. Dotted line represents ZO-1 intensity in NG. Both HG and Hx reduced ZO-1 intensity compared to NG. 3µM SPHINX31 significantly increased ZO-1 intensity in HG (from 106.4±3.4 to 238.1±23.1) and also Hx (from 36.5±8.0 to 290.6±35.3) compared to vehicle only control. (n=3) *p<0.05, ***p<0.001. Statistical analyses performed using one-way analysis of variance with Bonferroni post hoc. Error bars represent mean plus standard error.

Differential ZO-1 expression across cell-cell contacts in hprPEs suggested an overall change in total monolayer permeability. In order to test this hypothesis, hprPEs were grown to confluence on gold coated ECIS microarrays and impedance measurements in response to an electrical potential were taken non-invasively. Curves were plotted 1/impedance to gain a measure of permeability. Cells were treated with HG or an equivalent concentration of NG and co-treated with 3µM SPHINX31 or 1% DMSO control. Additionally, to deduce whether any changes in impedance in response to SRPK1 inhibition is due to VEGF-A₁₆₅ isoform expression, cells were exposed to 5nM αVEGF-A₁₆₅b

antibody. This concentration was chosen as it has been previously published as an optimal concentration for RPE cells to neutralise VEGF-A_{165b} effects (Kataoka et al., 1999). Finally, an IgG control was included to eliminate the non-targeting effects of an antibody (Chapter 2: “Materials and Methods” for full protocol). In NG (*Fig 4.3.2-2A*), SPHINX31 had no effect on monolayer permeability, whilst α VEGF-A_{165b} caused a slight increase in permeability, although not to a significant extent. Non-targeting IgG did not influence monolayer permeability (*Fig 4.3.2-2B*). In HG the effects of SPHINX31 were more impactful than in NG, inhibiting SRPK1 blocked the HG -induced increase in monolayer permeability. Notably, this change appeared to be mediated through VEGF-A_{165b} expression, as co-treatment with α VEGF-A_{165b} and SPHINX31 nullified the effects of SPHINX31 alone, evidenced by the curve overlaying the NG curve (*Fig 4.3.2-2C*) and similar area under the curve values (*Fig 4.3.2-2D*).

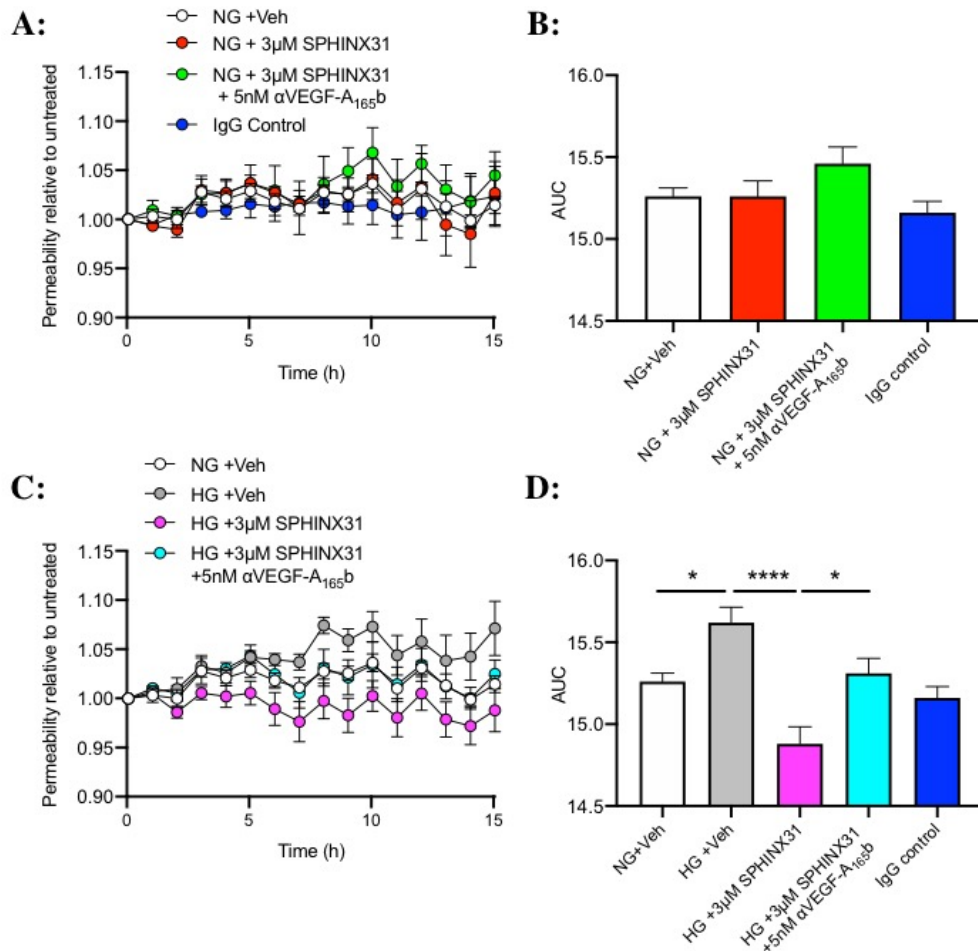


Figure 4.3.2-2: SPHINX31 blocks HG-induced increases in RPE monolayer permeability potentially through a VEGF-A_{165b} mediated manner

A: 1/impedance curves plotted over 15h in NG hprPE monolayers treated with 1% DMSO (+Veh) or 5nM α VEGF-A_{165b} and/or 3 μ M SPHINX31 or 5nM IgG. **B:** Area under the curves (AUC) for each treatment. Co-treatment with SPHINX31 and α VEGF-A_{165b} induced a slight (not significant) increase in permeability but no other treatment induced any changes. **C:** 1/impedance curves for HG hprPEs. **D:** AUC values for each treatment. HG increased permeability of RPE monolayer which was blocked by SPHINX31. Addition of α VEGF-A_{165b} antibody reversed effects of SPHINX31 alone. (n=9) * p <0.05, **** p <0.0001. Statistical analyses performed using one-way analysis of variance with Tukeys post hoc. Error bars of **A** & **C** represent mean \pm standard error. **B** & **D** represent mean + standard error.

4.3.3 SRPK1 activity in HG and Hx RPEs in response to SPHINX31

Chapter 3.3.3 describes how SRPK1 activity increases in response to HG and Hx, and results in the nuclear shuttling of its associated splicing factor SRSF1. Once within the nucleus, HG is able to induce the release of SRSF1 from the nuclear speckles, allowing it to mediate splicing activities. I have established that inhibiting SRPK1 resulted in a shift in VEGF-A₁₆₅ isoform expression in favour of VEGF-A_{165b}, and hypothesised that this effect is due to spatial changes of SRSF1. Thus, to elucidate how inhibiting SRPK1 would affect the cellular localisation of SRSF1, hpRPEs were treated with HG and Hx and co-treated with 1 μ M or 3 μ M SPHINX31 or 1% DMSO. Cells were stained with a nuclear stain DAPI, SRSF1 and additionally ZO-1 to delimit the cell membrane (*Fig 4.3.3-1A*). Ratio of nuclear to cytoplasmic SRSF1 was calculated using FIJI analysis and plotted as the difference from day 1 (See Chapter 2: Materials & Methods). SPHINX31 treatment in NG had no effect on nuclear localisation SRSF1 (*Fig 4.3.3-1B*), however it blocked the HG-induced increase with both concentrations (*Fig 4.3.3-1C*). Hx also increases nuclear shuttling of SRSF1 and inhibition of SRPK1 activity in these conditions (*Fig 4.3.3-1D*).

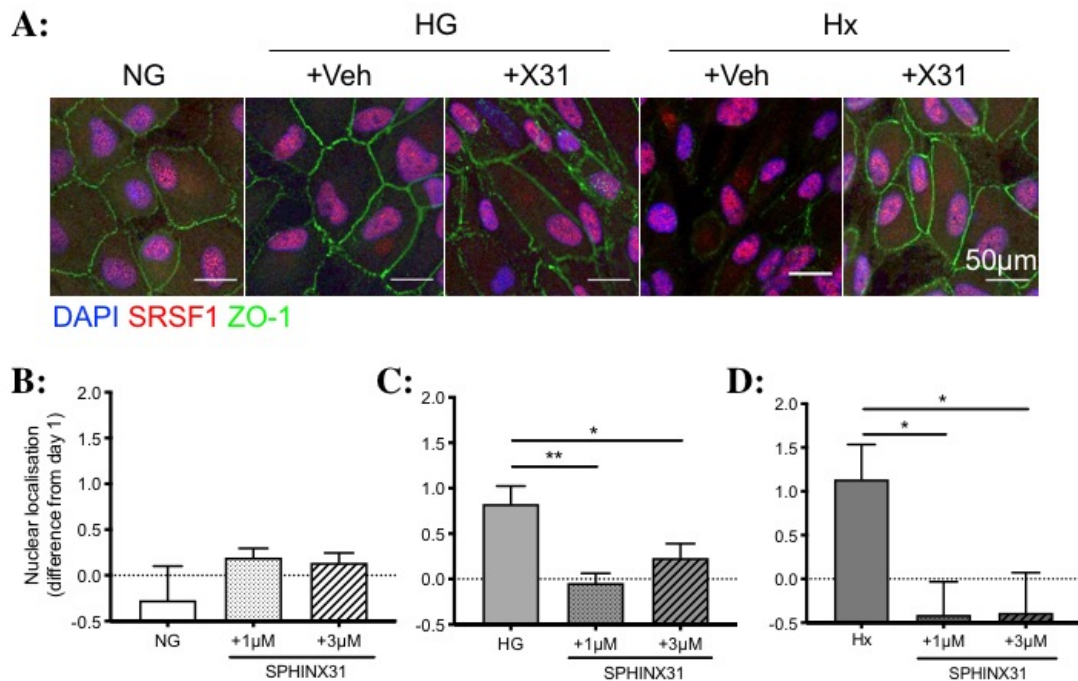


Figure 4.3.3-1: SRPK1 inhibition blocks nuclear localisation of SRSF1 in hyperglycaemia and hypoxia but not normoglycaemia.

A: Representative images of DAPI, ZO-1 and SRSF1 staining overlaid imaged via confocal microscopy with 40x objective. Scale bar 50µm. **B:** Ratio of nuclear to cytoplasmic SRSF1 in NG expressed as the difference from the ratio in day 1 NG cells (dotted line). Nuclear localisation is unchanged by SPHINX31. **C:** HG elevates nuclear localisation of SRSF1 which is blocked by 1µM and 3µM SPHINX31. **D:** Both concentrations of SPHINX31 also blocked Hx-induced increase in SRSF1 nuclear localisation. Error bars represent mean + standard error. A two-way analysis of variance with Bonferonni adjustment was performed for statistical analysis. NG&HG n=6 Hx n=3 *p<0.05 **p<0.01.

Partial phosphorylation of SRSF1 by SRPK1 is known to trigger cytoplasmic to nuclear shuttling of SRSF1 (Kataoka et al., 1999) where it compartmentalises within nuclear speckles in an inactive state. SRPK1 has additionally been implicated in facilitating the release of SRSF1 from the speckles through complexes with CLK-1 and promoting its activity (Aubol et al., 2016). Thus, I hypothesised that inhibiting SRPK1 activity would not only decrease nuclear SRSF1 concentration, but would also reduce SRSF1 release from the speckles. To elucidate whether this was the case, hPRPEs were treated with +30mM D-glucose or +30mM D-mannitol and co-treated with 3µM SPHINX31 or 1% DMSO. Cells were stained with DAPI to generate a nuclear mask, for SRSF1 and a nuclear speckle marker SRSF2 and high power images were obtained

using confocal microscopy with a 63x oil-immersed objective (*Fig 4.3.3-2A*). Analysis was performed using FIJI to obtain measure of co-localisation (Co-L) (for further detail about analysis method, see Chapter 2: ‘Materials and Methods’). Co-L significantly reduced in response to HG, corroborating with data from Chapter 3, thus we can assume SRSF1 is being released from the nuclear speckles. SPHINX31 had no effect on Co-L in NG, however reversed the reduction in Co-L in HG (*Fig 4.3.3-2B*), therefore suggesting that SRSF1 remains inactive within the speckles in this condition. To clarify whether the difference in Co-L is due to a change in localisation or differential expression of SRSF1 and SRSF2, a western blot was performed on the cell lysate (*Fig 4.3.3-2C*). No condition had any effect in SRSF1 or SRSF2 expression relative to the loading control actin (*Fig 4.3.3-2D-E*).

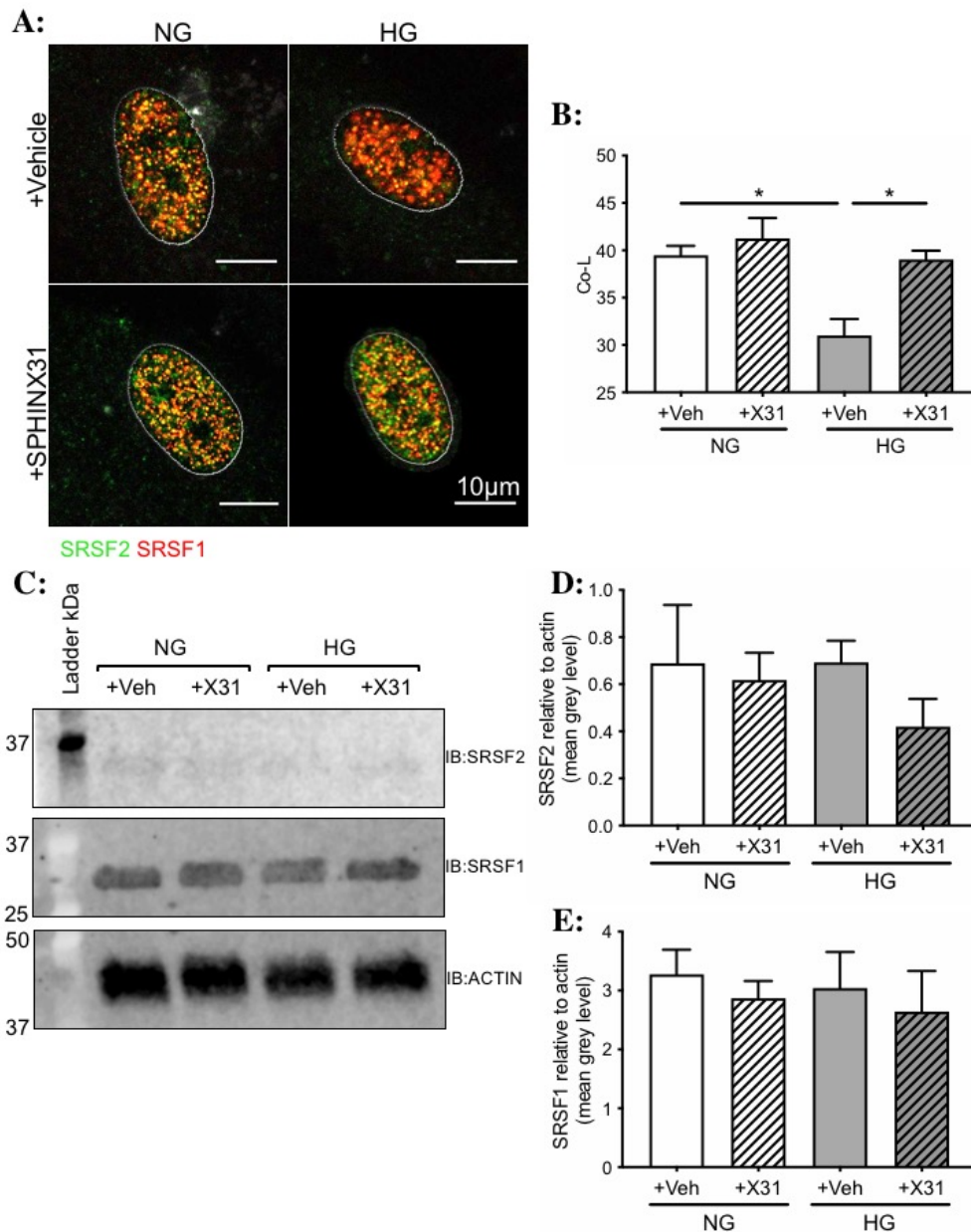


Figure 4.3.3-2: SPHINX31 ameliorates HG-induced SRSF1 release from nuclear speckles.

A: 63x oil-immersion objective images of SRSF1 and SRSF2 staining overlaid images. DAPI staining was used to create mask of nuclei (grey outline). Scale bar 10µm. **B:** FIJI analysis determined co-localisation (Co-L) extent of SRSF1 and SRSF2. In NG, Co-L value was not affected by SPHINX31. HG induced an decrease in Co-L **C:** Immunoblots against SRSF1, SRSF2 and actin of cell lysate from NG or HG hpRPEs co-treated with SPHINX31 or 1% DMSO (Veh). **D:** Density analysis from bands determined that SRSF2 expression did not differ in response to any condition. **E:** SRSF1 expression across all conditions did not significantly vary. Error bars represent mean + standard error. A two-way analysis of variance with Tukey post hoc was performed for statistical analysis. (n=3) *p<0.05.

In addition, cells were exposed to 3 μ M SPHINX31 or 1% DMSO control for three days. Following addition of Nano-Luc® substrate, if the two constructs are in close proximity with each other, energy will be transferred from luciferase to Halotag-618 ligand causing it to fluoresce (Fig 4.3.3-3C). Resultant emission can be converted to a BRET ratio (see Chapter 2: Materials and Methods for full detail) to gain a measure of SRPK1 complexing with SRSF1. SPHINX31 induced no change in BRET ratio in NG, however increased BRET ratio in HG (Fig 4.3.3-3D). Thus, it can be assumed that SRSF1:SRPK1 complexes are increased in response to SPHINX31 reflecting a reduction in SRPK1 activity in HG.

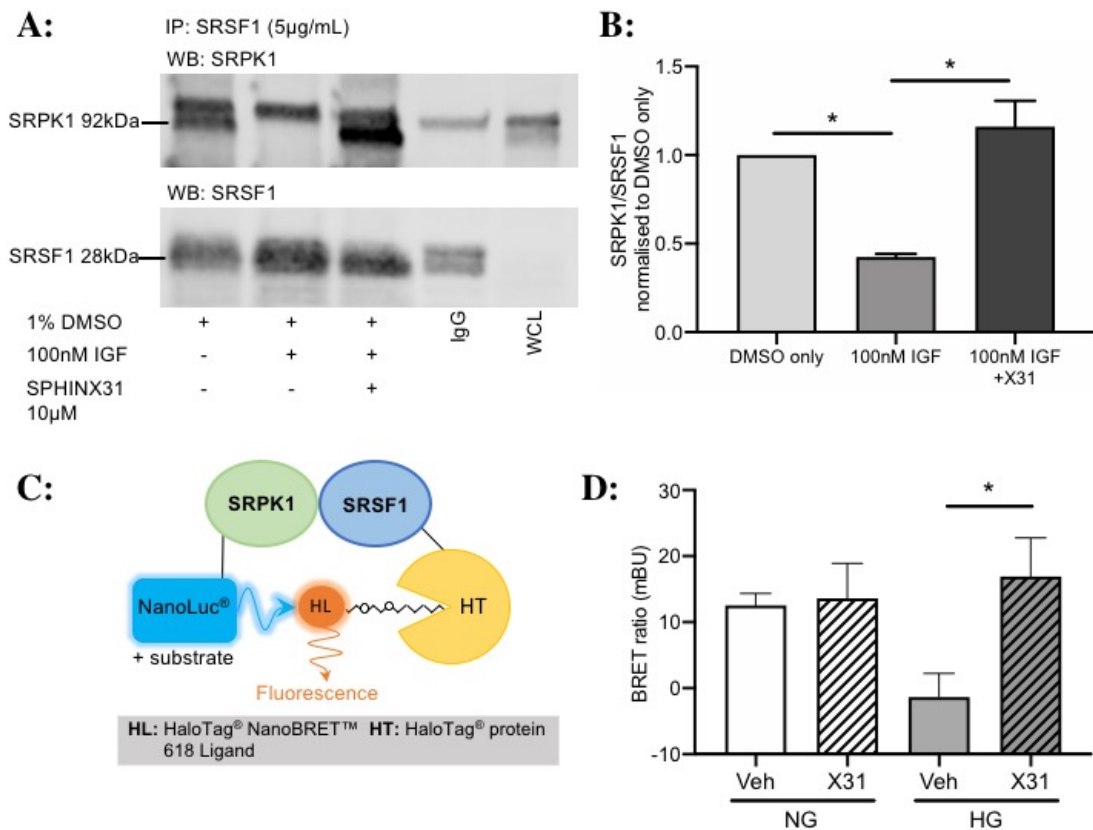


Figure 4.3.3-3: HG induces an increase in SRPK1 activity which causes a disassociation of the SRPK1-SRSF1 complex and increase in BRET ratio.

A: SRPK1 co-precipitates with SRSF1 in unstimulated RPEs. Stimulation of SRPK1 activity with 100nM IGF causes a loss of the SRPK1 band thus a disassociation of SRSF1/SRPK1 complex. 10 μ M SPHINX31 restores this complex as the SRPK1 band remains **B:** Quantification of mean grey levels of immunoprecipitation (n=2). **C:** Schematic of principle underlying NanoBRET assay. SRPK1 is conjugated to NanoLuc® whilst SRSF1 is attached to a Halotag associated to 618 ligand. **D:** HG induces a decrease in mean bret ratio which is blocked by SPHINX31. Error bars indicate mean + standard error (n=6)

Statistical analyses were performed using a two-way analysis of variance. * $p < 0.05$ **A&B**: data courtesy of Dr. Elizabeth Stewart.

4.3.4 Determining the impact of PKC on SRPK1 activity in hyperglycaemia

PKC has been shown to be both activated by HG (Omri et al., 2013) and also to stimulate SRPK1 activity (Harper & Bates, 2008). To elucidate how HG is activating SRPK1, I performed a SRSF1 nuclear localisation assay in the presence of a PKC inhibitor that inhibits the α , $\beta 1$, $\beta 2$, γ , δ , ϵ isoforms: bisindolylmaleimide I (10 μ M BIM-1). Due to the presence of a dye in BIM-1 which was captured by remaining pigment in hpRPE cells (*Fig 4.3.4-1A*) interfering with immunofluorescence, I had to use ARPE-19 cells for this experiment. ARPE-19s were grown to confluence and treated with NG or HG and SPHINX31 or a vehicle control as previously. In addition, a dose response of BIM-1 was imposed on cells (*Fig 4.3.4-1B*). In HG, as previously discussed, there is an evident increase in SRSF1 nuclear shuttling. However blocking PKC α - ϵ abrogated this increase to the same level as SPHINX31 (*Fig 4.3.4-1C*). In NG, inhibiting SRPK1 with SPHINX31 induced no change in SRSF1 localisation. Interestingly, we discovered that pan-PKC inhibition blocked nuclear localisation of SRSF1 without a glycaemic stimulus, suggesting SRPK1-independent PKC-mediated nuclear shuttling of SRSF1. The co-inhibition of PKC α - ϵ and SRPK1 in HG conditions produced an insignificant reduction in SRSF1 nuclear localisation. (*Fig 4.3.4-1D*).

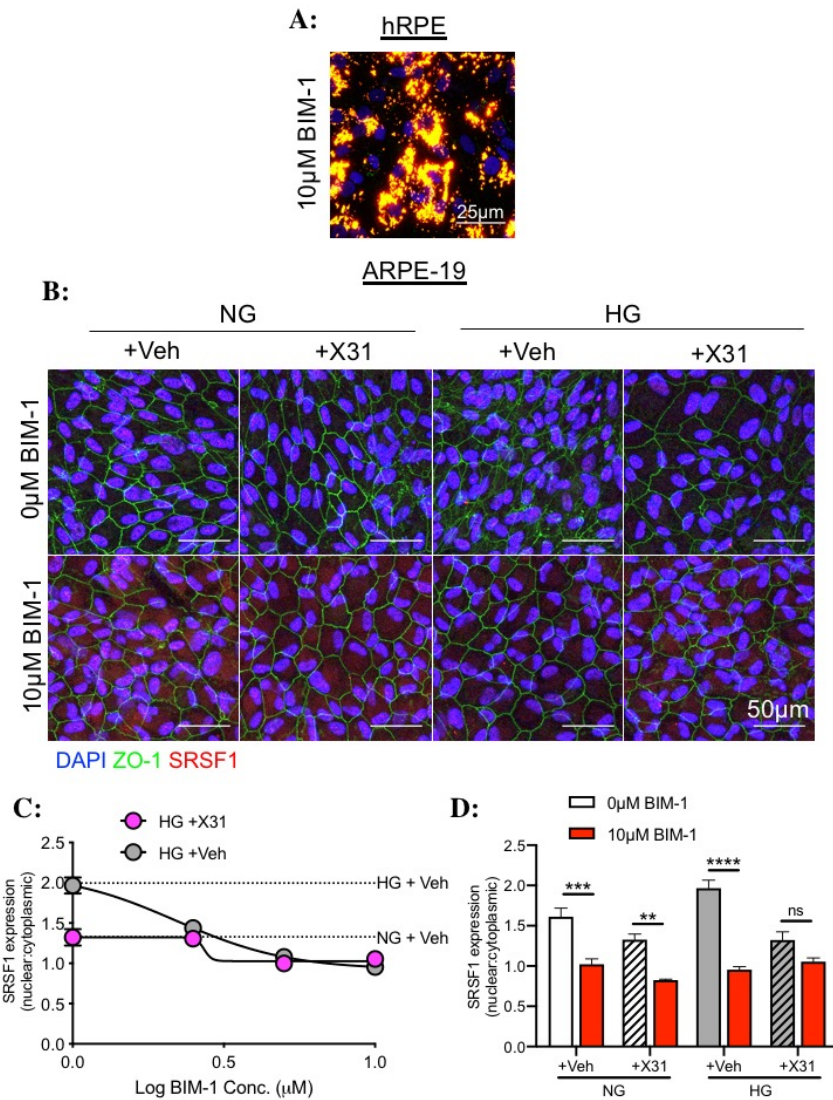


Figure 4.3.4-1: Blocking PKC α - ϵ isoforms increases cytoplasmic SRSF1 localisation in normo- and hyperglycaemia

A: *hpRPEs* treated with 10µM BIM-1 imaged with confocal microscopy. Drug colouring is captured by remaining pigment in cells and so primary cells were determined to be inappropriate for use. Scale bar = 25µm **B:** ARPE-19 cells were treated with either 30mM D-mannitol (NG) or 30mM D-glucose (HG) with and without 3µM SPHINX31 (X31) for 5 days. In addition a dose-response with PKC inhibitor BIM-1 was performed. Cells stained for DAPI, SRSF1 and ZO-1 and imaged using confocal microscopy with 40x objective. Scale bar = 50µm. **C:** BIM-1 dose response curves. FIJI analysis was performed to determine the ratio of nuclear to cytoplasmic expression of SRSF1. Dotted line denotes value at 0µM BIM-1. Error bars indicate mean \pm standard error. **D:** SRSF1 nuclear:cytoplasmic ratios at 10µM BIM-1. Nuclear localisation significantly reduced in all conditions except HG+X31. Error bars indicate mean + standard error. Statistical analysis performed with two-way analysis of variance with Tukeys post-hoc. ns=non-significant, **p<0.01, ***p<0.001, ****p<0.0001 (n=3).

To determine the impact of PKC inhibition on SRPK1 activity, ARPE-19 cells were treated with either +30mM D-mannitol (NG) or +30mM D-glucose (HG) for two days following a co-transfection with SRPK1-Nanoluc® and SRSF1-Halotag® constructs. Alongside this, cells were treated for 24h with a 10µM of an inhibitor specific for α , β 1, β 2, γ , δ , ϵ isoforms of PKC, BIM-1, or an inhibitor specific for only α , β 1, β 2 PKC isoforms, Go6976 with and without 3µM SPHINX31 (X31). The nano-BRET assay was performed as stated in Chapter 2: Materials and Methods. Pan-PKC inhibition completely abrogated the change in BRET ratio under HG conditions, producing results similar to SPHINX31. This is evidenced by the similar mean corrected BRET ratios (Fig 4.3.4-2A) and when the data is expressed as a difference in BRET ratio in response to HG (Fig 4.3.4-2B). However, blocking only PKC α - β 2 specific isoforms failed to attenuate the HG-induced increase in BRET ratio, thus did not have any impact on SRPK1 activity. Furthermore, the co-treatment of SPHINX31 and PKC α - β 2 inhibitor completely reversed the change in BRET ratio under HG conditions. These results indicate that HG stimulates SRPK1 activation through activation of PKC γ , δ and/or ϵ isoforms.

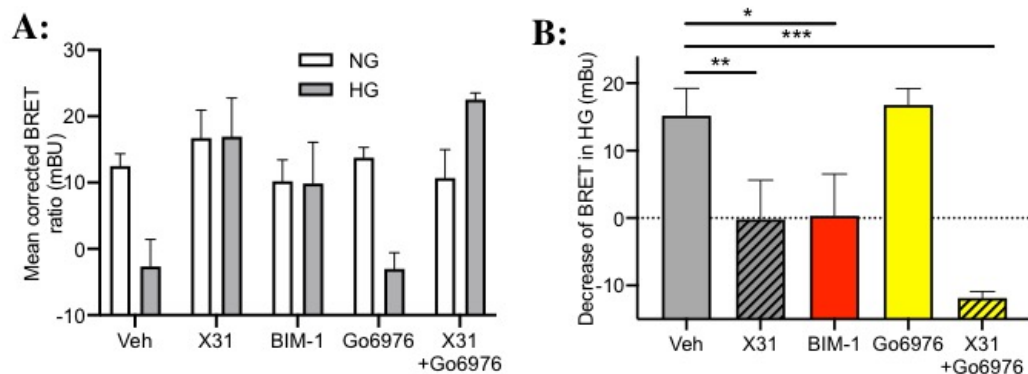


Figure 4.3.4-2: Inhibition of PKC α - ϵ isoforms blocks HG-induced increases in SRPK1 activity

A: Mean corrected BRET values. **B:** Difference in BRET ratio in HG as compared to NG. HG induced an increase in BRET signal which was blocked by 3µM SPHINX31 and 10µM BIM-1 but not 10µM Go6976. Co-treatment of cells with SPHINX31 and Go6976 resulted in a reduction of the BRET signal. Dotted line shows no change. Error bars indicate mean + standard error. Statistical analyses were performed using a two-way or one-way analysis of variance. *p<0.05, **p<0.01, ***p<0.001 (n=6).

4.4 Discussion

4.4.1 SRPK1 inhibition attenuates differential VEGF-A₁₆₅ isoform expression in response to hyperglycaemia and hypoxia restoring barrier properties of RPE monolayer

VEGF-A has been described to act as a survival factor for both vascular and non-vascular tissues, as such its blockade contributes to the treatment of many pathologies, particularly those of the eye (Ford et al., 2011). However, the majority of these therapeutics fail to discriminate between alternatively spliced VEGF-A isoforms, which is hypothesised to be one reason why some patients are non-responders, as well as the fact that they do not target non-VEGF pathways which contribute to DR (Stitt et al., 2016). Consistent with work from Chapter 3 and published literature (*Fig 3.3.1*), VEGF-A_{165a} expression increased in response to diabetic mimicking conditions in hpRPEs (*Fig 4.3.1-1B*) (Brownlee, 2001). Use of type I kinase inhibitor of SRPK1, SPHINX31 ameliorated this increase whilst having no effect on VEGF-A_{165b} expression, but reducing VEGF-A_{165a} expression. This was surprising as inhibition of SRPK1 has been previously shown to promote VEGF-A distal splice site selection in colorectal cancer (Walter et al., 2018), prostate cancer (Ferguson & Gray, 2018) and notably neovascular eye disease (Yang et al., 2018). However, when expressed as a ratio, VEGF-A_{165b} expression almost doubled in response to SPHINX31 in HG and tripled in Hx. This is encouraging, as Perrin et al found that VEGF-A_{xxx}b isoforms makes up two-thirds of total VEGF-A in normal vitreous, thus we are potentially seeing a restoration of healthy VEGF-A levels due to SPHINX31 (Perrin et al., 2005).

It is widely accepted that HG insult is followed by a reduction in tight junction expression and increase in permeability. I have found this in my model of the RPE monolayer of the oBRB in Chapter 3, through both loss of ZO-1 expression and reductions in cellular impedance. However, it is relatively unknown what the impact of SRPK1 inhibition will be on RPE permeability. Excitingly, I found that SPHINX31 increased ZO-1 expression in hpRPEs with a diabetic insult (*Fig 4.3.2-1*) which also was seen functionally as the monolayer permeability did not change relative to NG hpRPEs (*Fig 4.3.2-2*). I also describe for the first time how the effect of SRPK1 inhibition with regards to RPE monolayer

permeability is mediated by VEGF-A_{165b} expression, as co-inhibition of SRPK1 and endogenous VEGF-A_{165b} negated the effects of SRPK1 alone. This is supported by recombinant VEGF-A_{165b} preventing tight junction disruption triggered by VEGF-A_{165a} or HG in RPEs (Ved et al., 2017).

4.4.2 SPHINX31 abrogates nuclear shuttling of SRSF1 and release from nuclear speckles potentially through restoration of SRPK1:SRSF1 complexes in diabetic-mimicking conditions

SRPK1 is inextricably linked to the nuclear shuttling of SRSF1. Depletion of SRPK1 from HT29 cells were found to have increase cytoplasmic concentrations of SRSF1 (Gonçalves & Jordan, 2015). SRPIN40, another selective SRPK1 inhibitor prevents IGF-1 stimulated nuclear localisation of SRSF1 in podocytes (Nowak et al., 2010). Specifically in the RPE, SRPIN40 was found to reduce EGF induction of SR-protein phosphorylation (Gammons et al., 2013). My results corroborate with that of existing literature, as in hpRPEs HG-induced nuclear shuttling of SRSF1 was abrogated by both 1 μ M and 3 μ M SPHINX31 (*Fig 4.3.3-1C*). SPHINX31 also reduced release of its cognate splicing factor from nuclear speckles in response to HG insult (*Fig 4.3.3-2*). As described in section 4.1, cytoplasmic SRPK1 hypo-phosphorylates SRSF1 causing it to translocate to the nucleus and compartmentalise within the nuclear speckles (Kataoka et al., 1999). It is only after the remaining SR residues are phosphorylated by CLK-1 that SRSF1 is released from the speckles and able to bind pre-mRNA. SRPK1 facilitates this hyper-phosphorylation through complexing with CLK-1 (Aubol et al., 2016). This is potentially explain the results of Fig 4.3.3-2, as SPHINX31 blocks formation of SRPK1:CLK-1 complexes and thus reduces the efficiency of SRSF1 hyperphosphorylation. Unlike its complexing with CLK-1, SPHINX31 actually promotes SRPK1:SRSF1 complexes within the cytoplasm in HG as SRSF1 is unable to be phosphorylated and released from SRPK1 (*Fig 4.3.3-3*). Thus SPHINX31 was able to prevent SRPK1 hyperactivity whilst not affecting basal kinase activity. This is in line with the nuclear localisation assay results: a higher cytoplasmic concentration of SRSF1 due to SPHINX31. Furthermore, an increased sequestering of SRSF1 in the nuclear speckles offers an explanation as to why

VEGF-A_{165a} expression is decreased in response to SPHINX31 these conditions, as the splicing factor is unable to bind to VEGF pre-mRNA whilst sequestered.

With regards to hypoxia, SPHINX31 ameliorated the increase in nuclear localised SRSF1 at both 1 μ M and 3 μ M (*Fig 4.3.3-1D*). Another SRPK1 inhibitor SRPIN340 is evidenced to have protective effects in an oxygen-induced retinopathy model, inhibiting pre-retinal neovascularisation and reducing VEGF-A_{165a} isoforms (Gammons et al., 2013). This could potentially be due to a loss of nuclear SRSF1 localisation in hypoxia, such as that which is seen in *Fig 4.3.3-1D*.

NG cells, those that had been treated with 30mM mannitol, were not responsive to SPHINX31 with respect to SRSF1 subcellular localisation (*Fig 4.3.3-1&2*) or SRPK1 activity (*Fig 4.3.3-3*). Mannitol has been included as a control in all experiments to account for the effects of osmotic change, and it has been described SRSF1 can be spatially regulated by changes in osmolarity, as an osmotic shock can cause the factor to migrate into stress granules in the cytoplasm (Twyffels et al., 2011). However, in our experiments, mannitol appears to have no effect, thus suggesting that observed changes in HG experiments are specifically due to glycaemic stimulus. In addition, the fact that SPHINX31 has no effect in NG conditions attests to its potential power as a therapeutic for DR, as it suggests that it will exclusively act on cells with HG-insult without affecting 'healthy' cells.

4.4.3 Pan-PKC inhibition blocks HG-induced increases in SRPK1 activity and SRSF1 nuclear shuttling

Diabetes stimulates PKC activity in the retina through a number of pathways (Shiba et al., 1993) where it phosphorylates serine or threonine residues of intracellular proteins (Harhaj & Antonetti, 2004). PKC can indirectly regulate VEGF-A isoform expression through its activation of SRPK1. Therapeutically inhibiting PKC has been found to block IGF-stimulated VEGF-A_{xxx}a expression in podocytes but has no effect in unstimulated cells (Nowak et al., 2010). Activation of IGF receptor stimulates SRPK1 activity which in turn mediates

VEGF-A isoform expression (Amin et al., 2011), highlighting PKC involvement in SRPK1 activity. I found that blocking PKC α - ϵ isozymes ameliorated HG-induced increase in SRSF1 nuclear localisation, a potential explanation for the increase in VEGF-A_{165a} expression reported in Nowak et al., 2010. The reduction in SRSF1 nuclear:cytoplasmic ratio was actually below that of direct inhibition of SRPK1 with SPHINX31 (0.96 ± 0.03 vs 1.32 ± 0.09) (Fig 4.3.4-1D) which was surprising as I hypothesised that the effect of PKC on SRSF1 was through SRPK1 activation. However, in NG conditions, which I have previously found not to stimulate SRPK1 activity, PKC α - ϵ isozyme blockade also induced a reduction in nuclear localisation of SRSF1 to approximately the same extent as in HG. This suggests that there is an SRPK1-independent action of PKC on SRSF1. Furthermore, inhibition of PKC α - ϵ isozymes blocked SRPK1 activity in HG but induced no change in NG (Fig 4.3.4-2A) supporting the hypothesis that although PKC modulates SRSF1 cellular localisation through SRPK1 activity, there is an additional pathway independent of SRPK1 involvement. The literature surrounding this hypothesis is lacking, but a recent paper has found that SRSF1 does feedback on PKC in chronic myeloid leukaemic cells as the kinase activity is reduced in SRSF1-depleted cells (Sinnakannu et al., 2020). In addition, PKC β 2 promotes expression of transcription factor c-myc in HG pancreatic β cells (Kaneto et al., 2002) which could trigger upregulation of SRSF1 expression (Das et al., 2012). This could potentially explain how PKC affects SRSF1 outside the SRPK1-SRSF1 axis but it is clear that more research would need to be done in order to confirm these ideas. However, PKC actions are isoform specific. The role of PKC β 1 and PKC β 2 are perhaps the most well described in DR, as they are hypothesised to be the most sensitive to glucose concentration (Donnelly et al., 2004). PKC- α , - γ and - δ are also upregulated, albeit to a lesser extent (Idris et al., 2001). The impact of PKC β in DR is so significant, that a number of therapeutics are in development to block its action (Poulaki et al., 2002). Consequentially, it was surprising that specifically inhibiting PKC isozymes α , β 1 and β 2 did not change SRPK1 activity (Fig 4.3.4-2), rather implying that it is through PKC γ , PKC δ or potentially PKC ϵ that SRPK1 hyperactivity in response to HG is mediated.

4.5 Summary

This chapter focused on the impact and activity of SRPK1 in a diabetic *in vitro* model of the RPE monolayer and evaluated the therapeutic potential of SRPK1 inhibitor, SPHINX31.

SPHINX31 blocked HG- and Hx-induced increases in VEGF-A_{165a} expression, and restored VEGF-A_{165a}: VEGF-A_{165b} levels to that which is seen in NG. With regards to RPE monolayer integrity, SPHINX31 ameliorated barrier disruption caused by both HG and Hx insult by elevating ZO-1 localisation along cell-cell junctions. Moreover, SPHINX31 restored HG-induced increases in total RPE monolayer permeability perhaps through a VEGF-A_{165b}-mediated manner.

SRSF1, the associated splicing factor of SRPK1, exhibits a reduction in nuclear shuttling in response to SPHINX31 in both HG and Hx conditions. Furthermore, its release from the nuclear speckles in response to HG is also reduced. Thus, not only is nuclear SRSF1 expression reduced due to SPHINX31, but that which is within the nucleus is less able to mediate VEGF-A alternative splicing events.

Complexing of SRSF1 with SRPK1 in response to HG was also assessed in this chapter. SPHINX31 caused an increase in SRPK1:SRSF1 complex formation, a direct reduction in SRPK1 activity as SRSF1 is not phosphorylated and released from SRPK1, in HG.

To understand why SRPK1 activity is increased in response to diabetic insult, the impact of PKC activity was also determined. Pan-PKC inhibition induced a reduction in SRSF1 localisation in the nucleus in both NG and HG conditions. HG-induced PKC action on SRPK1 was established to be isozyme specific, with PKC γ , PKC δ and PKC ϵ implicated as potential targets.

Excitingly, all SPHINX31 effects were either HG or Hx specific and had no impact on NG cells. This is encouraging, as suggests less side-effects associated with the drug because the only responders are those with SRPK1 hyperactivity.

CHAPTER 5

Inhibiting SRPK1 activity in an *in vivo* model of Type I diabetes

5.1 Introduction

In the UK, guidelines currently stipulate no ocular treatment for background retinopathy, and recommend management of diabetes to reduce the risk of advancement of retinopathy (The Royal College of Ophthalmologists Diabetic Retinopathy Guidelines, 2012). For the later, proliferative stage of DR, clinicians are recommended to use pan retinal laser photocoagulation (PRP), which focuses light on RPE and underlying choroid to produce thermal burns and localised retinal cell death. This ameliorates retinal hypoxia and restores oxygen levels, but results in a loss of photoreceptors, formation of scar tissue and the benefits to visual acuity are highly variable between patients (Royle et al., 2015).

Prolonged HG triggers multiple signalling pathways resulting in areas of ischaemia within retinal tissue. Expression of HIF-1 α has been found to correlate temporally and spatially with VEGF-A expression (Ozaki et al., 1999). As such, anti-VEGF-A therapies are a widely investigated area of research for treating DR. However, anti-VEGF-As are limited with their effectiveness, only 50% of patients respond positively (Duh et al., 2017). They are administered through intravitreal injection, a process that necessitates a trained professional, requires continuous repetition over monthly or 8-weekly periods and is associated with inflammatory side effects (Falavarjani & Nguyen, 2013). Aberrant VEGF-A expression is targeted to treat DMO and another ocular visually-impairing disorder, wet-AMD, much more successfully than in DR. Despite the positivity surrounding anti-VEGF-As, the issue of non-responders remain. One hypothesis is that this is due to the fact that the current drugs on the market are not able to discriminate between VEGF-A alternative isoforms. As such, they block global VEGF-A action, including the protective effects offered by VEGF-A_{xxx}b isoforms. Furthermore, these drugs only target the VEGF-mediated effects of DR. The benefits of VEGF-A₁₆₅b exposure in reducing DR pathologies in animal models have been previously described (Ved et al., 2017), however a potentially more advantageous approach would be to restore cellular expression of VEGF-A alternative isoforms to physiological levels. SRPK1 inhibitors are currently in development, and whilst some lack the required specificity and potency, a kinome screen has found

SPHINX31 is highly specific for SRPK1 (Batson et al., 2017) and thus is a promising candidate for the treatment of DR.

To confidently and robustly evaluate a novel therapeutic agent against DR, a reproducible and representative model is required. Diabetes (type I and II) can be induced in rodents in a number of different ways; by induction or genetic insult. Generation of a genetic model tends to be more time-consuming and expensive than environmental induction (Lai & Lo, 2013). Streptozotocin (STZ)-induced model is the most commonly used model of type I diabetes, due to its fast rate of disease development and heavily characterised disease phenotype. STZ, synthesised from *Streptomyces achromogenes* is a broad-spectrum antibiotic with a particular selective toxicity to insulin-producing β -cells of the pancreas (Junod et al., 1967). Following uptake via GLUT2 low-affinity glucose transporters, STZ causes cell necrosis through alkylation and fragmentation of DNA. HG is observed two hours after injection, followed by hypoglycaemia 6 hours later due to a sharp rise in blood insulin. Eventually, blood insulin levels reduce and HG is achieved (Szkudelski, 2001). HG (>15mmol/L glucose) can be transient, thus requires monitoring, but can remain for 20 weeks (Rungger-Brändle et al., 2000). Rats are much more susceptible to STZ toxicity compared to mice, thus require a lower dose and have a higher success rate of diabetic induction. Crucially for this present study, BRB breakdown is observed in STZ rats two weeks after diabetes onset (Rungger-Brändle et al., 2000; Zhang et al., 2008). However, acute toxicity is a major side effect of STZ exposure potentially leading to animal death (Wang-Fischer & Garyantes, 2018). To counteract this, animals can be chronically exposed to low-dose insulin to avoid ketoacidosis whilst maintaining HG (Luippold et al., 2016). Unfortunately, there is no animal model of DR that can completely encompass the entire pathophysiological progressions observed in humans, however the STZ model does address the early stage symptoms such as increased BRB permeability (Olivares et al., 2017).

Breakdown of both BRBs has been implicated in the pathogenesis of DR (Gillies et al., 1997). The iBRB is maintained by tight junction complexes between retinal endothelial cells (RECs), who restrict diffusional permeability to

the order of $0.14 \times 10^{-5} \text{ cm s}^{-1}$ for sodium fluorescein (Cunha-Vaz & Maurice, 1969). HG damages the iBRB through disruption of these complexes (Vitale et al., 1995) similar to the oBRB. PKC isoform activation; overactivity of hexosamine and poly-ol pathway; increased advanced glycation products (AGEs) formation and increased expression of AGE receptors (RAGEs) results in the generation of reactive oxygen species (ROS) (Brownlee, 2005). Retinal vascular changes in DR are described to be caused and aggravated by VEGF-A and non-VEGF-A inflammatory mediators (Gupta, 2013). Thus, anti-VEGF-As and anti-inflammatory agents are a widely researched area for the treatment of DR. Whilst Müller cells, astrocytes and RPE produce the bulk of VEGF-A in the eye, RECs also express VEGF-A which can feedback and alter REC phenotype (Aiello et al., 1995). There are difficulties associated with isolating and propagating primary RECs from human donor eyes: they have a limited life-span; may potentially be contaminated with pericytes or other ocular cells; have a low yield and each isolation is not always successful. In addition, due to the low yield, tissues tend to be pooled together, and thus there is higher heterogeneity in the isolated cells. A well-established model of retinal endothelial cells is telomerase-immortalised bovine RECs (iBRECs) (Deissler et al., 2005). The ribonucleoprotein telomerase is expressed in germline not somatic cells and synthesises TTAGG/CCTAA repeats at 3' end of telomeres. These repeats are shortened with each cell division, pushing cells into senescence (Zvereva et al., 2010). The core enzyme of telomerase, telomerase reverse transcriptase (TERT), can immortalise a variety of cell types whilst maintaining cell cycle control, contact inhibition, anchorage dependence, possess a normal karyotype and still require growth factors for cell proliferation (Ouellette et al., 2000). Ectopic expression of human TERT in bovine cells show no significant change to cellular processes, but have an extended life-span (up to 90 passages) and are free of contaminating cells (Deissler et al., 2005). Moreover, endothelial marker proteins are highly conserved between human and bovine homologues and are sensitive to VEGF-A isoforms (Deissler et al., 2013), thus iBRECs can be used to model human RECs.

Previous work in this thesis has established that inhibition of SRPK1, through SPHINX31, is protective against diabetic insult on the RPE monolayer of oBRB.

In view of these findings, I hypothesised that inhibition of this kinase could impact retinal barrier *in vivo*. To investigate this, and understand the therapeutic potential of SRPK1 inhibition in DR further, in this chapter I will topically administer SPHINX31 on a streptozotocin-induced type-I diabetic model. Changes in retinal permeability can be monitored non-invasively in the same animal over time (Allen et al., 2020), thus this technique will be used to elucidate the impact of SPHINX31 on retinal permeability. DR induces thickening of the retina, which could be an early clinical sign of oedema (Hee et al., 1998). I will determine whether my *in vivo* model of DR is sufficient to observe this clinical symptom, and establish the effect, if any, of SPHINX31. Changes in retinal vasculature are a characteristic pathology associated with DR, thus I will determine changes in retinal vasculature *in vivo* and with an *in vitro* model of RECs, the cells lining retinal blood vessels.

5.2 Methodology

Twenty-seven male Norway-Brown rats (220-300g) received twice-daily topical eye drops (20 μ L) of eye formulation control buffer or 200 μ g/mL SPHINX31 in both eyes. FFA and OCT was performed in order to determine baseline levels of permeability and retinal thickness. Eighteen rats were given an intraperitoneal (i.p.) injection of 50mg/kg streptozotocin (STZ) in citrate buffer pH 4.5. Nine control rats were given an equivalent volume of saline i.p. Following three days of close monitoring, glucose levels were measured using an Accucheck blood glucose monitor and a tail vein blood sample. Those with levels >15mmol/L were deemed hyperglycaemic. Hyperglycaemic animals were anaesthetised with 2-5% isoflurane, hair removed from the back of the neck and sterilised with chlorhexidine solution. The animal was scruffed at the back of the neck and a 16-gauge needle was inserted subcutaneously approximately 1.5cm along the midline of the neck. The needle was subsequently removed and replaced with a trocar containing one-third of a sustained release insulin implant. A plunger was used to deposit the pellet into the neck cavity and the animals were recovered. Rats injected with STZ that were not hyperglycaemic on day 4 were re-injected with 50mg/kg STZ and the above process repeated. Those that were not hyperglycaemic at this point were excluded from the study. Animals were monitored weekly for retinal permeability and thickness with FFA and OCT. FFA avi files were imported to FIJI for analysis (Allen et al., 2020). OCT files were analysed using Insight™ software. Following a four-week period, animals were culled, enucleated and retinae mounted and stained for endothelial cell markers. Imaris software was used to examine vascular parameters in each treatment group. VEGF-A_{165b} expression in the corresponding eye was assayed using an ELISA.

iBRECs were grown to confluence on gold microelectrodes and exposed to HG or an equivalent concentration of mannitol as an osmotic control for 3d. Cells were co-treated with 50ng/mL recombinant VEGF-A₁₆₅ isoforms for 24h. Furthermore, cells were subjected to different concentrations of SPHINX31. The impedance of the monolayer in response to an electrical potential was measured using xCelligence system. Western blots were performed in order to deduce changes in junctional proteins in these conditions.

Unless otherwise stated, all repeats are technical repeats. All methods are described in further detail in Chapter 2: “Materials and Methods”.

5.3 Results

5.3.1 Impact of topical administration of SPHINX31 on retinal permeability in an *in vivo* model of DR

Before a large *in vivo* study assessing retinal permeability in diabetic rats was conducted, a smaller study was completed in order to optimise the methodology and determine the variability. FFA was performed on three non-diabetic Norway Brown rats treated twice daily with SPHINX31 eye drops (200µg/mL). FFA and OCT was performed weekly over the course of 28 days (*Results detailed in Chapter 2: Materials and Methods*). Following completion of the primary study, type I diabetes was successfully induced in Norway Brown rats following a single dose of 50mg/kg STZ, confirmed by glucose measurements three days post STZ injection (NDb+X31: 5.67 ± 0.20 ; Db+Veh: 27.6 ± 1.27 ; Db+X31: 25.6 ± 1.39) (*Fig 5.3.1-1A*). To maintain animal health for a long term study, an insulin bolus was implanted subcutaneously. Due to the severity of the model, animal health was monitored and weights were continuously taken over the course of the study. Diabetic animals untreated with SPHINX31 had significantly lower weights compared to non-diabetic (Db+Veh : $+32 \pm 7.30$ g; NDb+X31: $+67.5 \pm 2.45$ g). Although diabetics treated with SPHINX31 trended with lower weights than non-diabetics, the difference was not significant ($+38.06 \pm 7.44$ g) (*Fig 5.3.1-1B*). Following final FFA and OCT measurements at 28 days, glucose measurements were taken again to confirm HG (NDb+X31: 6.57 ± 0.23 ; Db+Veh: 22.5 ± 1.52 ; Db+X31: 21.1 ± 2.25) (*Fig 5.3.1-1A*). Animals that maintained >15 mmol/L glucose were enucleated for further analysis. Retinae were isolated from eyes using a dissection microscope and homogenised with lysis beads. VEGF-A_{165b} isoform expression was assayed using an ELISA (previously validated in Chapter 3.3.1) and found to significantly decrease in response to diabetes. Topical SPHINX31 treatment increased VEGF-A_{165b} expression although not to a statistically significant extent (*Fig 5.3.1-1C*).

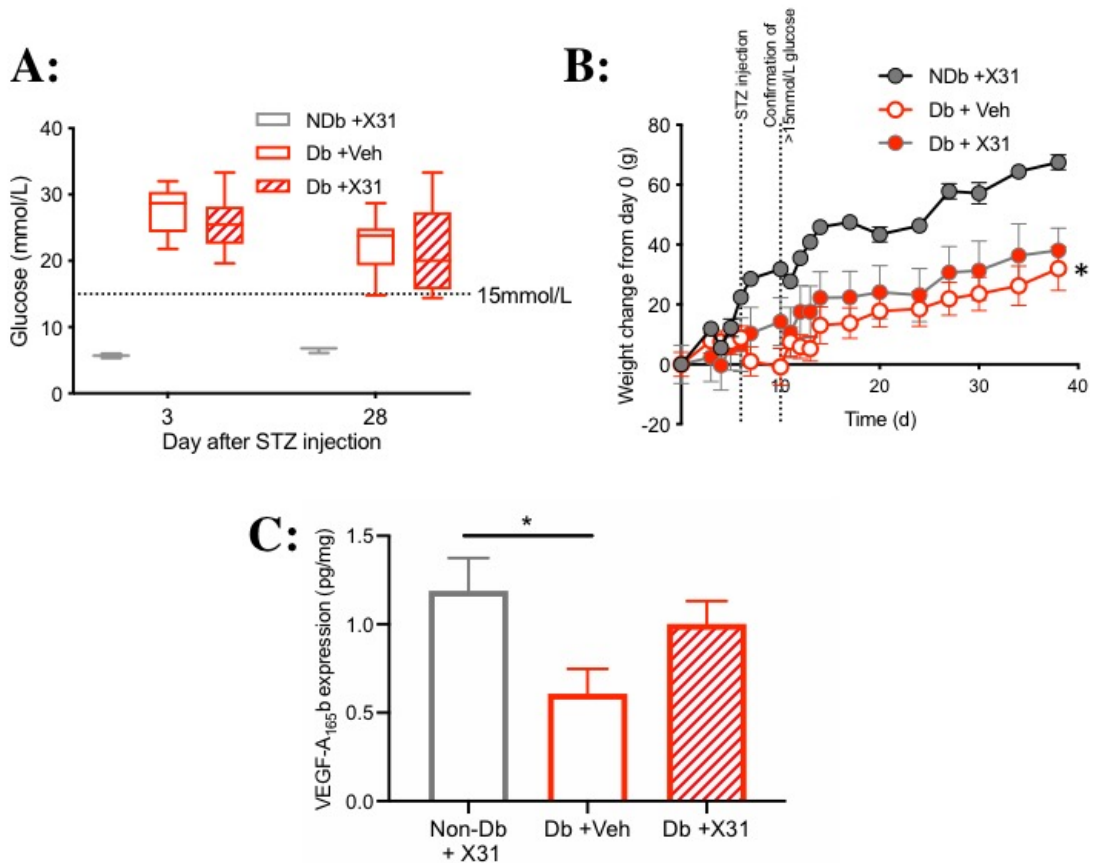


Figure 5.3.1-1: SRPK1 inhibition increased VEGF-A_{165b} isoform expression in diabetic retinae

A: STZ increased in blood glucose above 15mmol/L three days post injection. Equivalent dosing with saline did not induce HG. This STZ-induced increase in blood glucose was maintained until day 28 whilst saline-injected animals retained NG. **B:** Animal weights taken over the course of the study. All cohorts increased weights across the study. NDb animal weights increased significantly over the increase in Db+Veh animals. Db+X31 weights increased although not significantly different from the other two cohorts. **C:** VEGF-A_{165b} expression was significantly reduced in the diabetic retina (measured by ELISA). Twice-daily SPHINX31 eye-drops slightly increased VEGF-A_{165b} expression. NDb: n=9; Db+Veh: n=8; Db+X31: n=9. *p<0.05. Statistical analysis of **B** performed using two-way analysis of variance with Tukey's post hoc; statistical analysis of **C** performed using a one-way analysis of variance with Tukey's post hoc. Error bars of **A** highlight min to max; **B** represent mean ± standard error; **C**: mean plus standard error.

The results from previous chapters indicate that inhibiting SRPK1 ameliorates the HG-induced changes in the oBRB. In view of these findings, we hypothesised that inhibiting this kinase could impact retinal barrier integrity *in vivo*. To test this hypothesis, FFA was performed on the left eyes of Norway-Brown rats in each treatment group weekly. Rats were intra-peritoneally injected with small molecular tracer, NaFl, pupils were dilated using topical applications of 5% phenylephrine and 0.8% tropicamide and the Phoenix Micron IV retinal imaging microscope using a green filter was used to take videos of NaFl perfusion across the retina (*Fig 5.3.1-2A*). Angiograms were imported as avi files into Fiji software and mean fluorescence intensity was measured individually in major retinal vessel and a region of nearby tissue every 200 frames from the point of detectable fluorescence to just prior to saturation. These were plotted over time course alongside tissue over vessel ratios (*Fig 5.3.1-2B*). The region of detectable fluorescence to just prior to saturation (*green highlighted area of Fig 5.3.1-2B*) was used to calculate the permeability coefficient (*further detail of this experiment in Chapter 2: Materials and Methods*). Permeability coefficients were plotted over time to map the changes in permeability in response to diabetes and twice-daily topical administration of SPHINX31 (*Fig 5.3.1-2C*). To account for biological variability between each animal, permeability values were normalised to day 0. STZ-induced diabetes caused a significant increase in retinal vascular permeability from days 14 (3.19 ± 1.19) -28 (3.54 ± 1.19) compared to non-diabetic control animals (day 14: 0.65 ± 0.17 ; day 28: 0.69 ± 0.16). Excitingly, this increase was ameliorated through twice-daily topical administrations of $200 \mu\text{g/mL}$ SPHINX31 after day 14 and continued to day 28 (day 14: 0.53 ± 0.21 ; day 28: 0.66 ± 0.18) (*Fig 5.3.1-2D*).

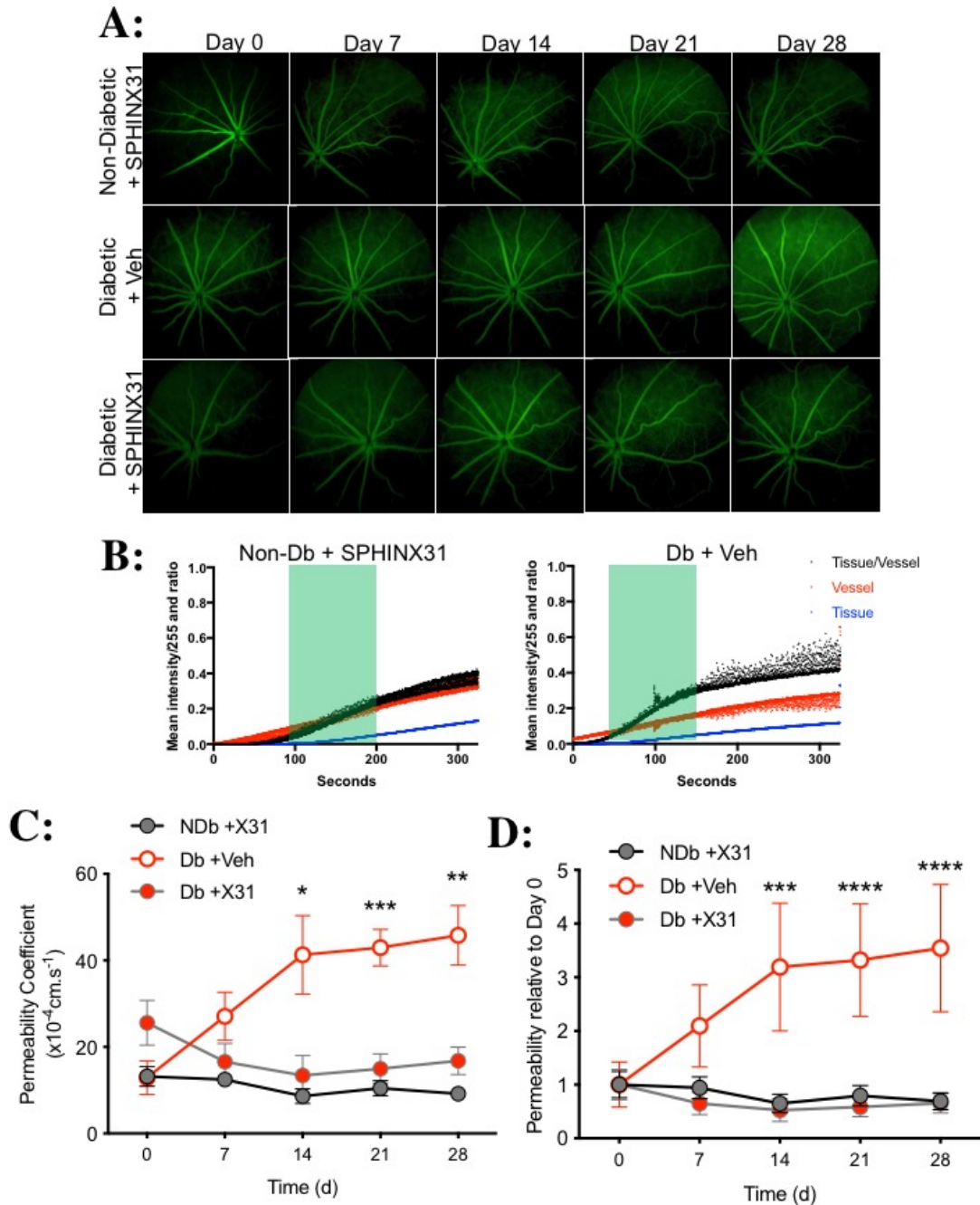


Figure 5.3.1-2: SPHINX31 blocks increases in retinal permeability in diabetic Norway-Browns.

A: In a streptozotocin-induced rodent model of type 1 diabetes or non-diabetic control group, fluorescein fundus angiography (FFA) was performed over 28 days. Animals received twice daily topical eye drops with eye formulation control buffer or 200 μ g/mL SPHINX31. **B:** FFA was quantified using the ratio of interstitial to vascular fluorescence. The shaded green area indicates the section of the slope that was used to calculate the permeability coefficient. **C:** Permeability coefficient plotted over time for three cohorts. **D:** Diabetes induced an increase in retinal permeability from day 14 through day 28 compared to non-diabetic animals. SPHINX31 blocked the diabetic-induced increase. Error

bars indicate mean \pm standard error. NDb: n=9; Db+Veh: n=8; Db+X31: n=9. Statistical analysis performed using two-way analysis of variance plus Dunnett's post-hoc. *** $p < 0.001$, **** $p < 0.0001$.

5.3.2 Impact of inhibiting SRPK1 on retinal thickness in a type-I diabetic model

Clinically, retinal thickening can be an early sign of a macula oedema, which is a primary cause of vision loss in diabetic patients. Although not all patients with increased retinal thickness will progress to form oedema, it is recommended that these patients are monitored closely and follow up tests are performed (Sánchez-Tocino et al., 2002). Typically a longer term study (16 weeks) is used to study DMO, however electron micrographs have shown that RPE microstructure drastically changes only three-weeks after STZ-induction of diabetes (Blair et al., 1984; Grimes & Laties, 1980). Thus, I was interested to learn whether I would observe any changes in my model. Alongside FFA, OCT was performed using Phoenix Micron™ Image-guided OCT2 system to measure retinal thickness (see *Chapter 2: Materials and Methods for full detail*). A fundus image was taken in order to assess ocular health and align the eye to take a circular scan around the optic nerve (*Fig 5.3.2-1A*). A high resolution image of the retinal layers was obtained, exported into Insight™ software and total retinal thickness was measured (*highlighted by black arrow in Fig 5.3.2-1A*). An interesting observation was in some, but not all, diabetic plus vehicle animal images, there appeared to be evidence of potential oedema (choroidal separation from the retina), which was surprising as this is a relatively short term model (*Fig 5.3.2-1B red arrow*). In contrast, no signs of choroidal separation was observed in non-diabetic or diabetic plus SPHINX31 treated animals (*Fig 5.3.2-1B*). Diabetes induced a significant increase in mean total retinal thickness 28-days after STZ injection (NDb+X31: $176 \pm 1.65 \mu\text{m}$; Db+Veh: $192 \pm 4.89 \mu\text{m}$). SPHINX31 topical administration blocked this increase to a significant extent ($178 \pm 4.9 \mu\text{m}$) (*Fig 5.3.2-1C*).

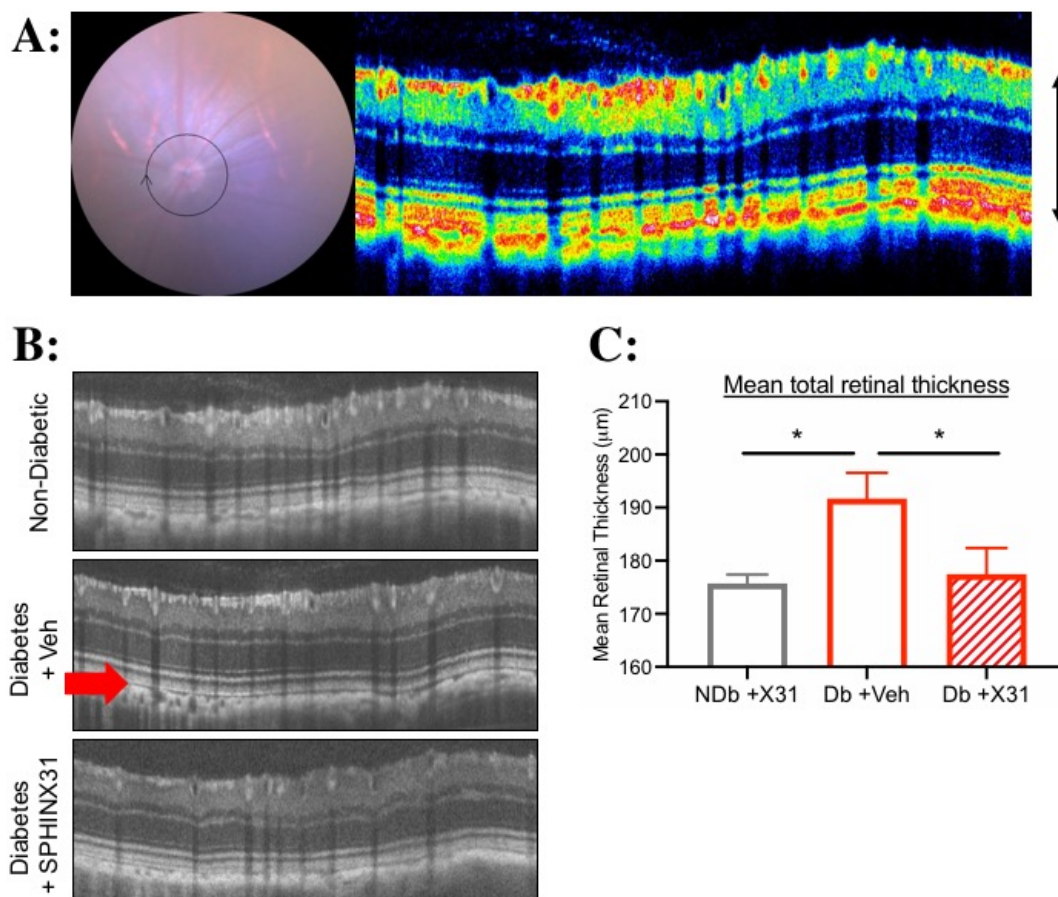


Figure 5.3.2-1: Retinal thickness is increased in STZ-induced type-I diabetic rats which is ameliorated by SPHINX31.

A: Alongside a non-diabetic group, type I diabetes was successfully induced in Norway Brown rats and topical treatment of 200µg/mL SPHINX31 or control eye formulation buffer was administered twice-daily. Optical coherence tomography was performed using the Phoenix OCT2. Images were assessed for retinal thickness by measuring the distance between the black arrows **B:** Representative OCT scan of each treatment. Red arrow indicates potential formation of oedema. **C:** Mean retinal thickness, measured every 3µm across the image automatically using InSight software, was found to increase in diabetic plus vehicle rats compared to non-diabetic rats but was blocked by SPHINX31 treatment after 28 days. Error bars indicate mean + standard error. NDb: n=9; Db+Veh: n=8; Db+X31: n=9. Data was analysed via a one-way analysis of variance with Bonferroni adjustment (*p<0.05).

To disseminate where the increase in retinal thickness is localised, segmentation of retinal layers were characterised manually using InSight™ software (Fig 5.3.2-2A). Initially, the automatic segmentation tool was utilised but the manual tool was found to be more accurate. Fig 5.3.2-2B highlights the detail in a slice of an OCT image and how each of the layers was segmented.

There was no difference in thickness in response to diabetes or SPHINX31 in ganglion cell (*Fig 5.3.2-2C*); inner nuclear (*Fig 5.3.2-2D*); outer nuclear (*Fig 5.3.2-2E*) and photoreceptor layers (*Fig 5.3.2-2F*). In contrast, the RPE and Bruch's membrane layer was thickened in response to diabetes plus vehicle (NDb+X31: $14.4 \pm 1.08 \mu\text{m}$; Db+Veh: $20.09 \pm 0.70 \mu\text{m}$) but not in the diabetes plus SPHINX31 treatment group ($13.04 \pm 0.80 \mu\text{m}$) (*Fig 5.3.2-2G*).

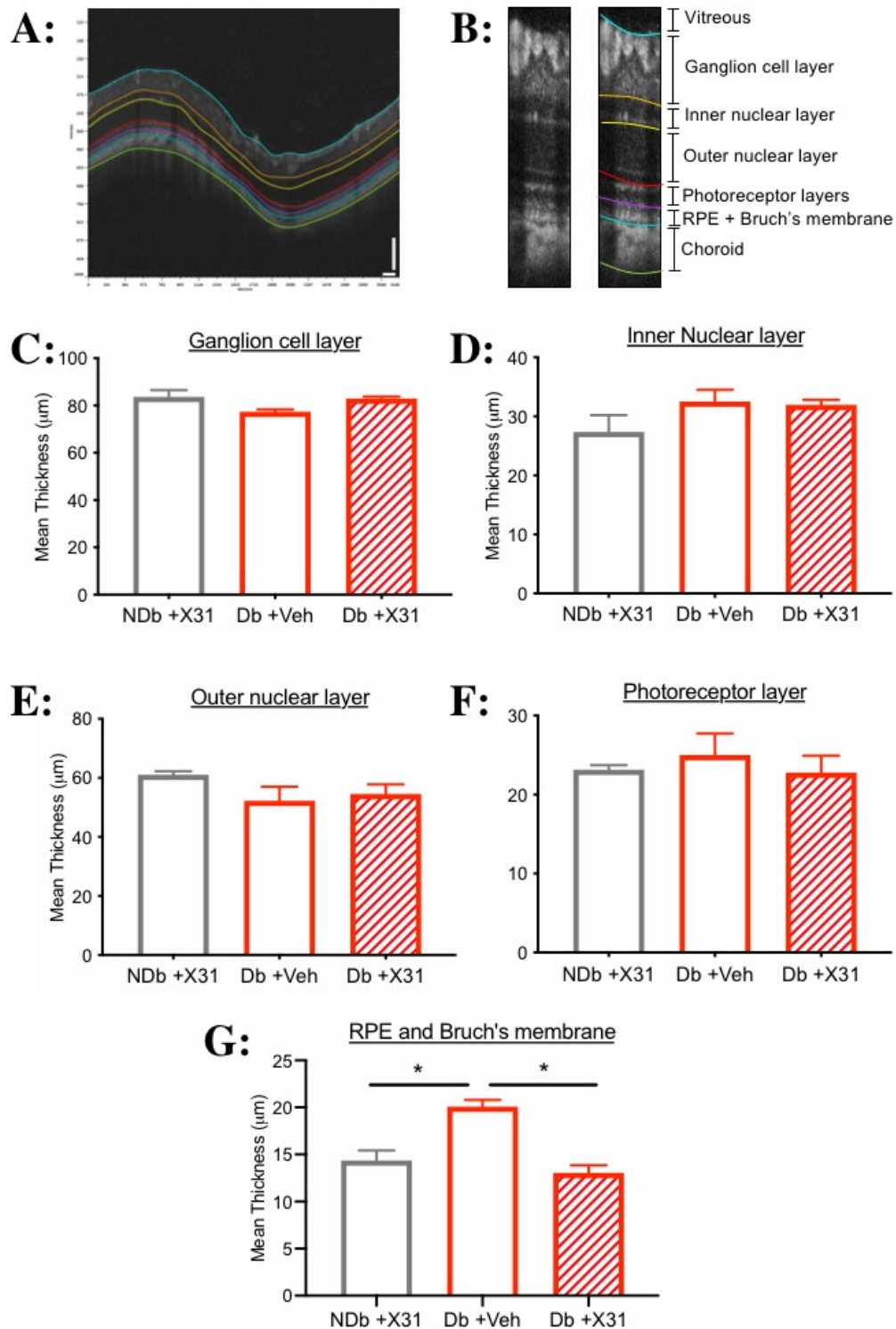


Figure 5.3.2-2: RPE and Bruch's membrane retinal layer thickness is increased in STZ-induced type-I diabetic rats and blocked by SPHINX31.

A: Optical coherence tomography was performed using the Phoenix OCT2 28-days post control saline injection or STZ-injection to induce type I diabetes. Animals received twice daily topical treatment of 200µg/mL SPHINX31 or control eye formulation buffer. **B:** Retinal layers were measured every 3µm between each of the segments highlighted in the figure. Diabetes nor

SPHINX31 induced any difference in mean thickness in the ganglion cell layer (C), inner nuclear layer (D), outer nuclear layer (E) or photoreceptor layer (F). G: RPE and Bruch's membrane thickness increased in diabetic rats compared to non-diabetic rats. SPHINX31 treatment blocked this increase in thickness in diabetic animals. NDb: n=9; Db+Veh: n=8; Db+X31: n=9. Error bars indicate mean + standard error. Data was analysed via a one-way analysis of variance with Bonferroni adjustment (*p<0.05).

5.3.3 Assessment of vascular parameters in response to STZ-induced diabetes and SRPK1 inhibition

DR can be characterised as a major microvascular complication of both type-I and II diabetes. Prolonged hyperglycaemia can lead to a multitude of vagaries to retinal microvessels, such as impaired perfusion, increased vascular permeability and endothelial cell-mediated leukostasis (Cheung et al., 2010). Vasculature within the retina exists as three plexuses: superficial (upper); intermediate; deep (lower) capillary plexus and visualising morphological changes could help further understand the pathogenesis of the disease (Morimoto, 1998). Following completion of the eye-drop study, eyes were enucleated, retinae excised and stained with a specific endothelial cell marker, isolectin B₄ (IB₄). Retinae were whole-mounted and imaged with a 10x objective on a confocal microscope to obtain z-stacks (Fig 5.3.3-1A). This technique allowed for segmentation of both the upper and lower capillary plexus, however the middle plexus was not distinct from other plexuses. As such, I decided to only measure properties from the upper and lower plexuses. Z-stacks were exported into FIJI and total vessel density was measured manually across one plane using a tracer tool. Diabetes slightly reduced vessel density in the upper plexus although not to a significant extent (NDb+X31: 2653±247µm; Db+Veh: 1925±203µm). Vessel density in diabetic animals was unchanged by SPHINX31 treatment (2088±72.9µm) (Fig 5.3.3-1B). In the lower plexus, diabetes nor SPHINX31 had any effect on the total vessel density (Fig 5.3.3-1C). These observations were not only interesting for determining disease pathology, but also supported our method of non-invasively measuring retinal permeability *in vivo* (section 5.3.1). To reiterate, mean intensity of NaFl was measured over time in one primary retinal vessel and also in an area of surrounding tissue. The associated formula used the assumption that there would be no significant differences in vascular density, as the area of

surrounding tissue would also include capillaries unable to be resolved by the imaging system. The lack of significant differences supports the idea that mean intensity measured in the surrounding tissue is due to dye leakage out of retinal vessels, and not increased number of unresolved capillaries in this area. Venous beading is a clinical sign of DR severity, and widening of the retinal vessels can be a potential sign of disease progression to the vision threatening proliferative stage (Wong, 2011). To determine this parameter in my model of DR, retinal vessel diameter was measured using the freehand tool of FIJI on a singular plane of IB₄ stained retina. There was no significant difference in retinal diameter in the upper plexus in response to diabetes or SPHINX31 treatment (*Fig 5.3.3-1D*) nor in the lower plexus (*Fig 5.3.3-1E*).

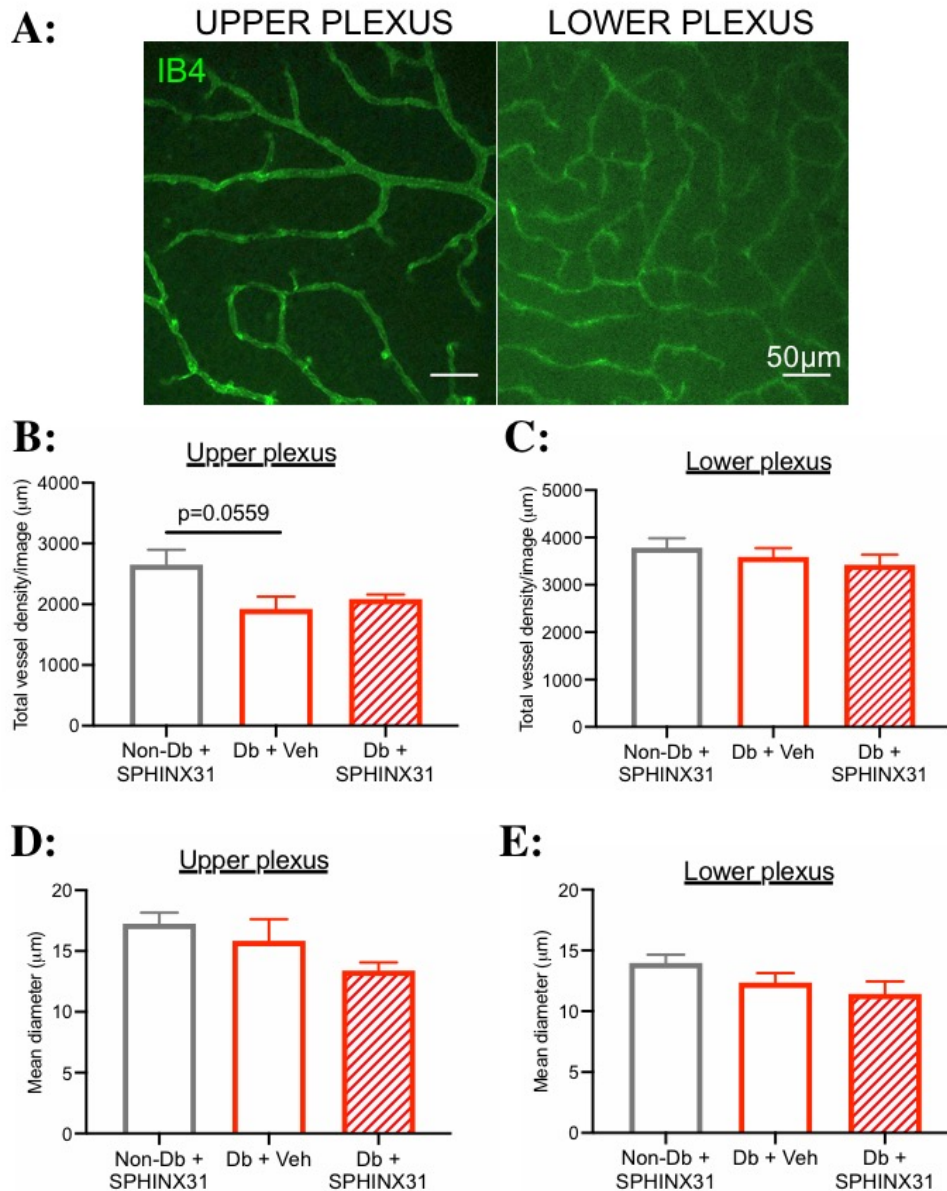


Figure 5.3.3-1: STZ-induced diabetes or SPHINX31 does not change total vessel density and mean diameter in the upper and lower plexuses of the retina after 28-days.

A: Retinae excised from scleral/choroidal cups of non-diabetic or type-I diabetic rats treated with SPHINX31 or control eye formulation buffer were whole-mounted and stained with endothelial cell marker IB₄ followed by Alexafluor-488-streptavidin. Confocal microscopy was performed to obtain z-stacks of retinal vasculature with defined upper and lower retinal plexuses. Scale bar = 50µm **B:** Fiji analysis determined total vessel density in the upper plexus and was slightly decreased in diabetic+veh group compared to the non-diabetic group. SPHINX31 induced no change in total vessel density. **C:** No changes were observed in total vessel density in the lower plexus. Mean diameter was unchanged in all conditions in both upper (**D**) and lower (**E**) plexuses. NDb: n=9; Db+Veh: n=8; Db+X31: n=9. Error bars indicate mean + standard error. Data was analysed via a one-way analysis of variance with Tukey's post hoc.

Analysing the confocal stacks using FIJI software meant that I was able to measure vascular parameters in each individual plexus by choosing the plane which appeared to optimally resolve each plexus. The filament tracer tool from Imaris can be repurposed to measure properties from a complete 3-D rendering of the z-stack (*Fig 5.3.3-2A*). The number of dendrite branches may be indicative of new vessel formation to increase vascular surface area (Geraldes et al., 2009). I hypothesised that there would be no difference in the number of branch points, as a 4-week model is not long enough to see evidence of neovascularisation. There was a very slight increase in the number of dendrite branches in response to diabetes treated with and without SPHINX31, but this difference was not statistically significant (*Fig 5.3.3-2B*). Vascular diameter measured using the Imaris tool rather than FIJI did appear to show a trend. Diabetes appeared to induce an increase in vascular diameter (NDb+X31: $6.86 \pm 0.59 \mu\text{m}$; Db+Veh: $9.62 \pm 1.34 \mu\text{m}$) which was blocked by SPHINX31 ($6.99 \pm 0.28 \mu\text{m}$). Although these changes were not statistically significant, the numbers suggest that it may have been if the n numbers were increased (*Fig 5.3.3-2C*). Another interesting point to note is that vessels measured using Imaris have a vascular diameter of between 5-11 μm , whilst FIJI analysis determined vascular diameter to be between 10-18 μm (*Fig 5.3.3-1D&E*). Vascular volume appeared to have a similar trend to changes in vascular diameter, increasing in response to diabetes, and decreasing with the administration of SPHINX31 (NDb+X31: $19.7 \pm 2.38 \mu\text{m}^3 \times 10^5$; Db+Veh: $54.3 \pm 15.5 \mu\text{m}^3 \times 10^5$; Db+X31: $26.75 \pm 4.31 \mu\text{m}^3 \times 10^5$) (*Fig 5.3.3-2D*). However again, these differences were not statistically significant but were perhaps unsurprising as vascular volume is calculated from vascular diameter.

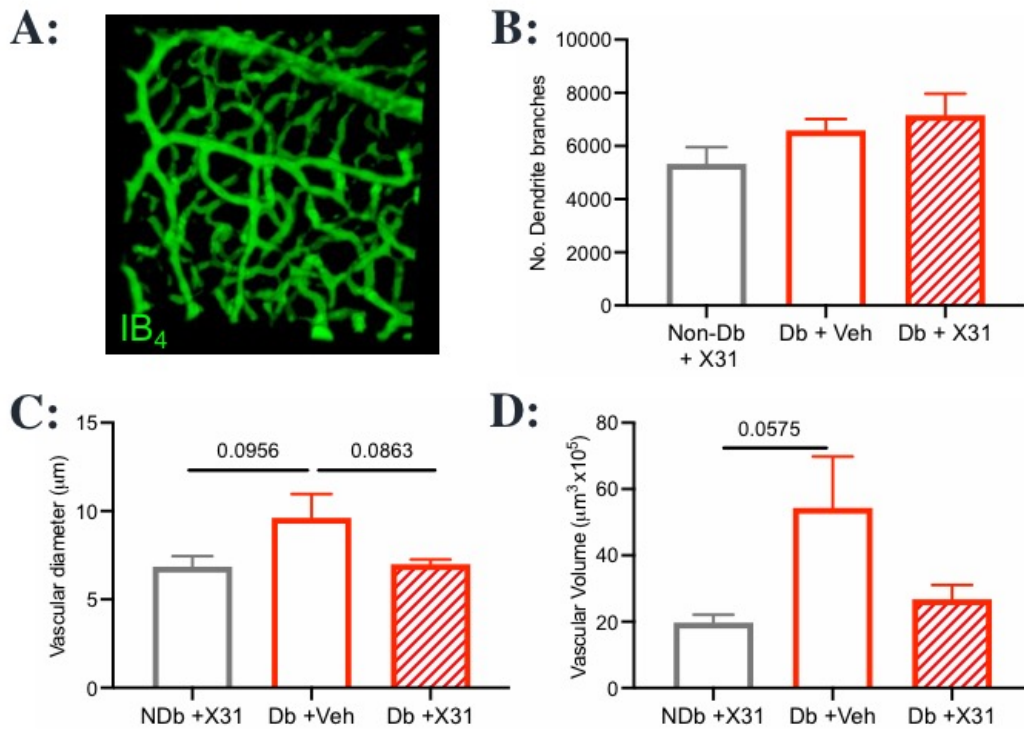


Figure 5.3.3-2: The number of dendrite branches, vascular diameter and volume of retinal vasculature are unaffected by STZ-induced diabetes or SPHINX31 after 28-days.

A: Retinae were whole-mounted and stained for IB₄ followed by Alexafluor-488-streptavidin following excision from scleral/choroidal cups of non-diabetic or type-1 diabetic rats treated with SPHINX31 or control eye formulation buffer. Confocal microscopy was performed to obtain z-stacks of retinal vasculature and imported into Imaris software to obtain a 3-D rendering. **B:** Imaris filament tracer tool measured number of dendrite branches and determined no differences in response to diabetes or SPHINX31 compared to the non-diabetic group. **C:** Vascular diameter non-significantly increased in response to diabetes compared to non-diabetic rats. SPHINX31 somewhat blocked this increase (6.99 ± 0.28) but without statistical power. **D:** Diabetes appeared to increase retinal vascular volume compared to non-diabetic retinae. SPHINX31 reduced this increase but both of these changes were not to a statistically significant extent. NDb: $n=9$; Db+Veh: $n=8$; Db+X31: $n=9$. Error bars indicate mean + standard error. Data was analysed via a one-way analysis of variance with Tukey's post hoc.

Diabetes can trigger apoptosis of endothelial cells in the retina through expression of PKC- δ (Geraldes et al., 2009). Consequentially, acellular capillaries or ghost vessels can irreversibly form reducing perfusion across the retina, promoting retinal ischaemia (Yoon et al., 2016). To assess differential formation of acellular capillaries in my model, following termination of the *in vivo* study and ocular dissection, retinae were isolated from the eyecups and whole

mounted onto slides. Retinal sections were stained for nuclear marker, DAPI, endothelial cell marker, IB₄, and collagen IV to delineate the basement membrane. Sections were imaged using a Leica TCS SPE confocal microscope with a 20x objective to produce z-stacks. Image stacks were exported into FIJI for analysis and an acellular capillary was defined as a vessel with only collagen IV but without IB₄ staining (*highlighted by white arrows in Fig 5.3.3-3A*). Number of acellular capillaries were counted across the three central planes. Diabetes resulted in an increase in the formation of acellular capillaries which was ameliorated by a 28-day course of twice-daily 200µg/mL SPHINX31 topical administration (NDb+X31: 33.1±5.15; Db+Veh: 92.0±13.7; Db+X31: 48.4±8.08) (*Fig 5.3.3-3B*).

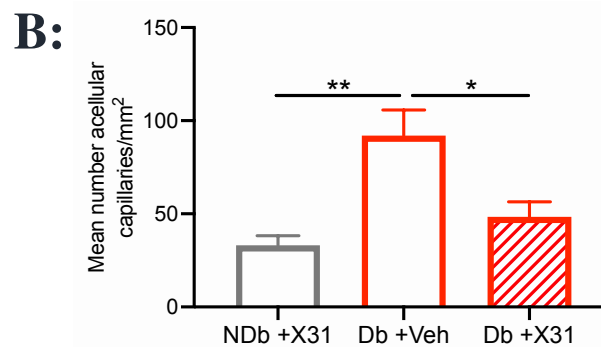
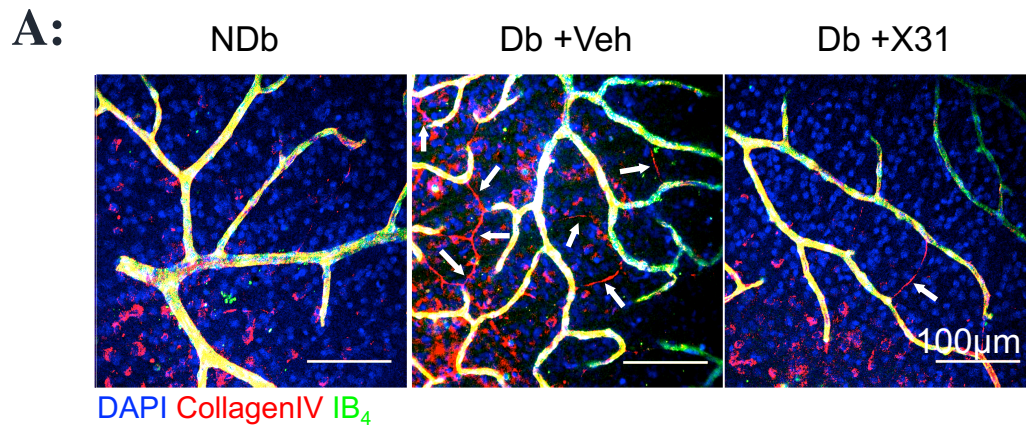


Figure 5.3.3-3: SPHINX31 inhibits diabetes induced increase in acellular capillary formation.

A: Norway Brown rats were given a single dose of streptozotocin (50mg/kg) to induce Type I diabetes alongside a non-diabetic saline control group. Rats were treated with twice-daily topical eyedrops of 200µg/mL SPHINX31 or control eye formulation buffer. Rats were enucleated at day 28 and whole retinas were mounted and stained with DAPI, IB₄ and collagenIV. The tissue was imaged using 20x objective. The number of capillaries positively stained for collagenIV but lacking IB₄ (white arrows) were counted across three planes **B:** Acellular capillaries expressed per mm³ increased in response to diabetes compared to non-diabetic retina. SPHINX31 blocked this diabetes-induced increase. ***p*<0.01, **p*<0.05. NDb: *n*=9; Db+Veh: *n*=8; Db+X31: *n*=9. Error bars indicate mean + standard error. Data was analysed via a one-way analysis of variance with Tukey's post hoc.

5.3.4 Effects of hyperglycaemia, VEGF-A_{165b} and SRPK1 inhibition on retinal endothelial cell permeability

Chapter 3 and 4 of this thesis has focused on the impact of diabetic conditions and SRPK1 inhibition on the oBRB, as RPEs produce a large quantity of VEGF-A in the eye. However, one of the primary factors contributing to the pathogenesis of DR is breakdown of the iBRB (Aiello et al., 1995). I had previously tried to isolate primary RECs from human donor eyes, but was

unable to yield a quantity to successfully perform permeability experiments. In addition, those that were isolated had very limited propagating potential and were contaminated with other cell types, despite use of CD31 beads to isolate. As such, I established a collaboration with Dr Heidrun Deißler of University of Ulm who has developed and characterised an immortalised bovine REC (iBREC) line. With the use of her protocols, to ensure non-differentiation of cells, the impact of glucose of iBREC monolayer permeability was determined by seeding iBRECs on a fibronectin coated xCelligence plate. Confluence of monolayers Cells were treated with 0-50mM D-glucose and impedance (cell index) was measured non-invasively using the xCelligence system over 72 hours. Cell index was normalised to the point after treatment addition and plotted over time (*Fig 5.3.4-1A*). The area under the curve, inversely proportional to permeability, reduced in response to increasing concentrations of glucose (*Fig 5.3.4-1B*). There appeared to be a negative trend in response to glucose concentration with cell index, thus suggesting that the higher the concentration of glucose, the lower the cell index, therefore the higher the permeability of the monolayer (*Fig 5.3.4-1C*). This experiment was important to determine the optimal concentration of glucose moving forward, which was concluded to be 30mM. Although this concentration did not increase permeability by the greatest extent out of those tested, cell morphology appeared to be healthier in this state (*not shown, as I was unable to capture images due to electrodes on plate*) and this concentration correlated with models used in published literature (Caprnda et al., 2017).

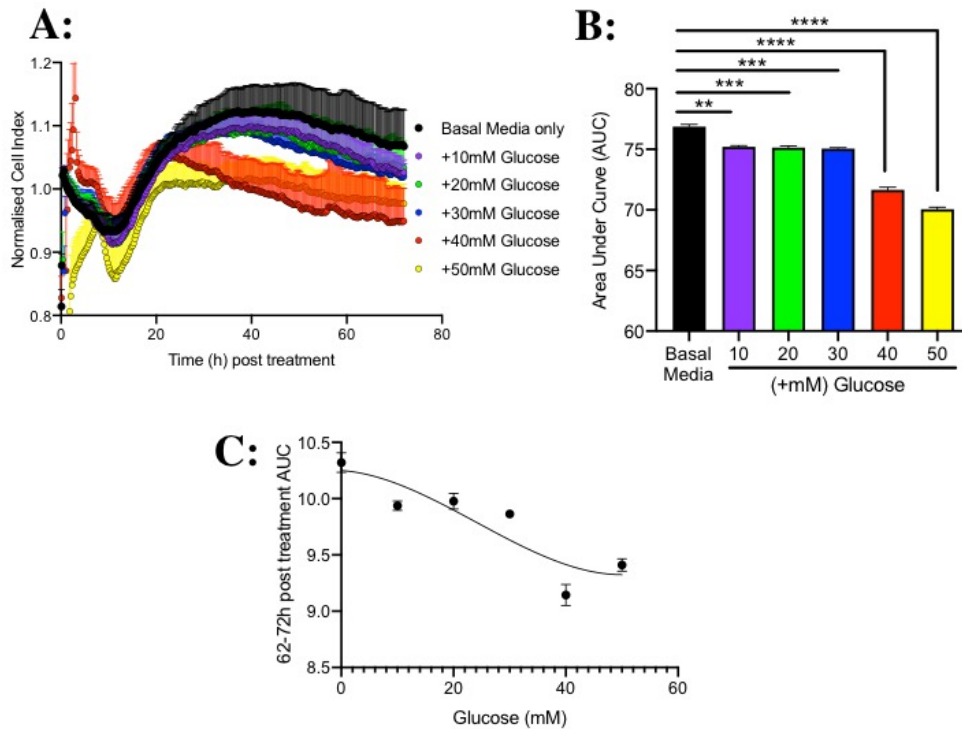


Figure 5.3.4-1: Permeability increases in response to glucose in a dose-dependent manner.

A: iBRECs were seeded onto fibronectin-coated xCelligence arrays, grown to confluence and treated with 0, 10, 20, 30, 40 or 50mM D-glucose. Impedance (cell index) measurements were taken over the course of 72h and normalised to cell index value after treatment addition. **B:** AUC decreased in response to 10mM glucose (75.21 ± 0.10), 20mM glucose (75.14 ± 0.15), 30mM glucose (75.06 ± 0.08), 40mM glucose (71.65 ± 0.22) and 50mM (70.06 ± 0.16) compared to basal media only (76.88 ± 0.17). **C:** Mean 62-72h AUC decreased in response to increasing concentrations of glucose; third order polynomial curve. ** $p < 0.01$, *** $p < 0.001$, **** $p < 0.0001$. Error bars of **A&B** indicate mean + standard error. Error bars of **C** mean \pm standard error. Data was analysed via a one-way analysis of variance with Bonferroni's post-hoc ($n=5$).

HG is known to induce an increase in permeability in RECs through a disruption of cell-type specific transmembrane proteins (Shin et al., 2014). To elucidate through which particular proteins iBREC monolayer permeability is increased in response to HG, iBRECs were grown to confluence on T75 flasks and treated with 30mM, 40mM and 50mM D-glucose. Cells were lysed, proteins separated by electrophoresis and transferred onto PVDF membranes. Blot were probed for membrane proteins implicated in REC barrier integrity: Claudin-1, Claudin-5 and ZO-1. In addition, actin expression was determined as a loading control (Fig 5.3.4-2A). Claudin-1 slightly decreased in response to increased glucose (Fig 5.3.4-2B) but not to a significant extent. However, as this experiment was

only an n=2, there may potentially be a significant difference if the n numbers were increased. 30mM and 40mM glucose but not 50mM glucose reduced expression of Claudin-5 (Fig 5.3.4-2C). Expression of ZO-1 did not change in response to differing glucose concentrations (Fig 5.3.4-2D). I observed that at 50mM glucose, expression of all assayed junctional proteins appeared to be somewhat increased. The changes observed in the junctional proteins, coupled with the results from figure 5.3.4-1 validated my decision to continue with 30mM glucose as the optimal glucose concentration for further experiments.

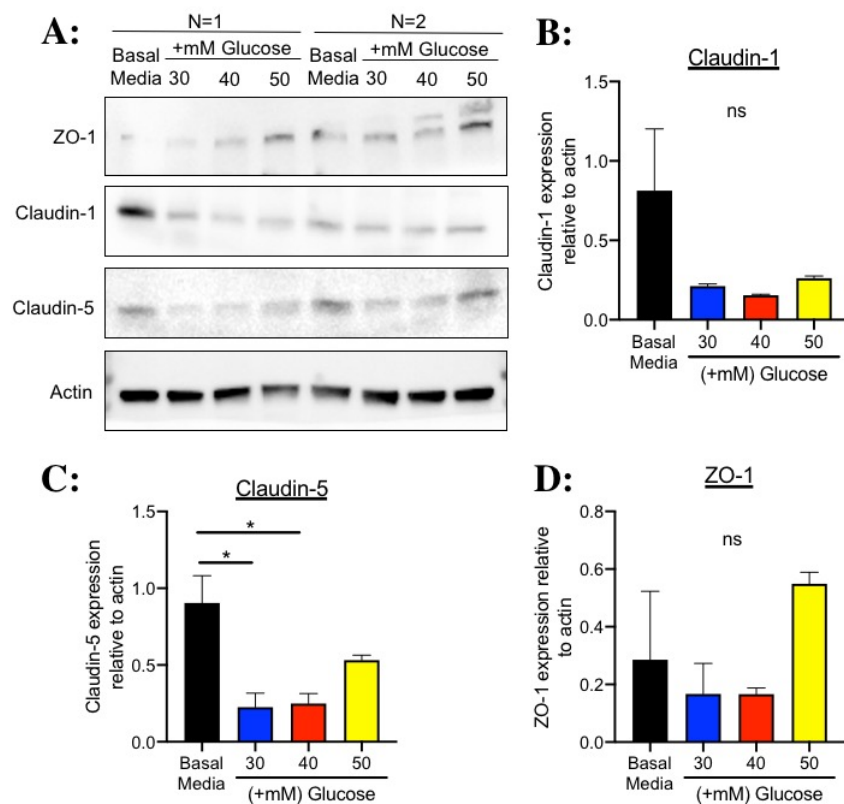


Figure 5.3.4-2: Claudin-5 expression is decreased in iBRECs exposed to 30mM and 40mM glucose.

A: T75s were coated with fibronectin were seeded with iBRECs, grown to confluence and treated with 0, 30, 40 or 50mM D-glucose for 3 days. Western blots were performed on cell lysates to assess for Claudin-1, ZO-1, Claudin-5 and actin expression **B:** Claudin-1 expressed relative to actin slightly decreased in response to 30mM (0.21 ± 0.014), 40mM (0.15 ± 0.0067) and 50mM glucose (0.26 ± 0.013) compared to basal media (0.81 ± 0.39). **C:** Claudin-5 expression significantly decreased in 30mM glucose (0.23 ± 0.092) and 40mM glucose (0.25 ± 0.065) but not 50mM glucose (0.53 ± 0.034) compared to basal media (0.93 ± 0.18). **D:** ZO-1 expression was not significantly changed from basal

media (0.29 ± 0.24) in 30mM (0.17 ± 0.11), 40mM (0.17 ± 0.021) or 50mM (0.55 ± 0.040). Error bars indicate mean + standard error ($n=2$).

Work in this thesis has established that inhibition of SRPK1 has protective effects against diabetic-insult in RPE monolayer of oBRB and in an *in vivo* model of DR. Previous results have shown that endothelial cells can produce VEGF-A, so if this was down to endothelial VEGF-A production, inhibition of SRPK1 would protect against HG-induced increase in permeability in iBRECs. To test this hypothesis, iBRECs were seeded on xCelligence arrays, incubated until confluent (confirmed by observing consistent cell index across 12h), and treated with or without 30mM D-glucose, in conjunction with 1% DMSO, 1 μ M or 3 μ M SPHINX31. Cell index was measured over 72h and plotted normalised prior to addition of treatment (Fig 5.3.4-3A). As in section 5.3.4-1, 30mM glucose induced a reduction in cell index. However 1 μ M and 3 μ M SPHINX31 also caused a statistically significant reduction in cell index in iBRECs exposed to both basal media and 30mM glucose (Fig 5.3.4-3B).

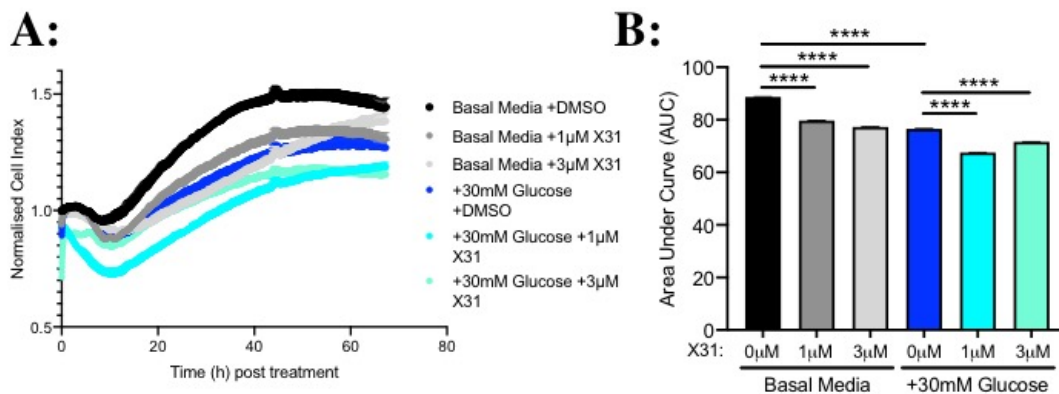


Figure 5.3.4-3: SPHINX31 induces a reduction in iBREC monolayer impedance in both basal media and HG conditions.

A: xCelligence arrays were coated with fibronectin and iBRECs were seeded, grown to confluence and treated with 0 or 30mM D-glucose in conjunction with 1% DMSO, 1 μ M or 3 μ M SPHINX31. Impedance (cell index) measurements were taken over the course of 72h and normalised to cell index value after treatment addition. **B:** AUC decreased in response to 1 μ M SPHINX31 (79.53 ± 0.09) and 3 μ M SPHINX31 (77.28 ± 0.08) in basal media group (88.72 ± 0.1). In addition, AUC reduced in response to 1 μ M SPHINX31 (67.51 ± 0.08) and 3 μ M SPHINX31 (71.6 ± 0.08) compared to 30mM glucose (76.56 ± 0.11). **** $p < 0.0001$. Error bars indicate mean + standard error. Data was analysed via a one-way analysis of variance with Bonferroni's post-hoc ($n=4$).

These results indicate that SPHINX31 was inducing an increase in iBREC monolayer permeability. However, whilst variances in impedance could be due to fluctuations in permeability, cell death can also cause large changes in impedance. In order to determine whether SPHINX31 affects permeability of iBREC monolayer, cells were grown to confluence in T75 flasks and treated with 30mM D-glucose, 30mM D-mannitol or basal media only. In addition cells were exposed to 1% DMSO or 1 μ M SPHINX31. 3 days after treatment administration, cells were lysed and assayed for ZO-1, Claudin-1, VE-Cadherin and actin expression (*Fig 5.3.4-4A*). Expression of tight junction protein ZO-1 was not significantly changed in response to osmotic (mannitol) or hyperglycaemic insult, nor SRPK1 inhibition (*Fig 5.3.4-4B*). Claudin-1 expression also did not significantly change in response to any treatment (*Fig 5.3.4-4C*). Adherens junction protein, VE-Cadherin, also does not significantly differ in response to 30mM mannitol, 30mM glucose nor 1 μ M SPHINX31. Thus suggesting that the SPHINX31-induced change in cell index (*Fig 5.3.4-3*) was not due to permeability shifts. However, it is important to consider when evaluating these results that they consist of a small n number (1% DMSO n=2; 1 μ M SPHINX31 n=1) and thus may not be representative of the true relationship and follow up work is required.

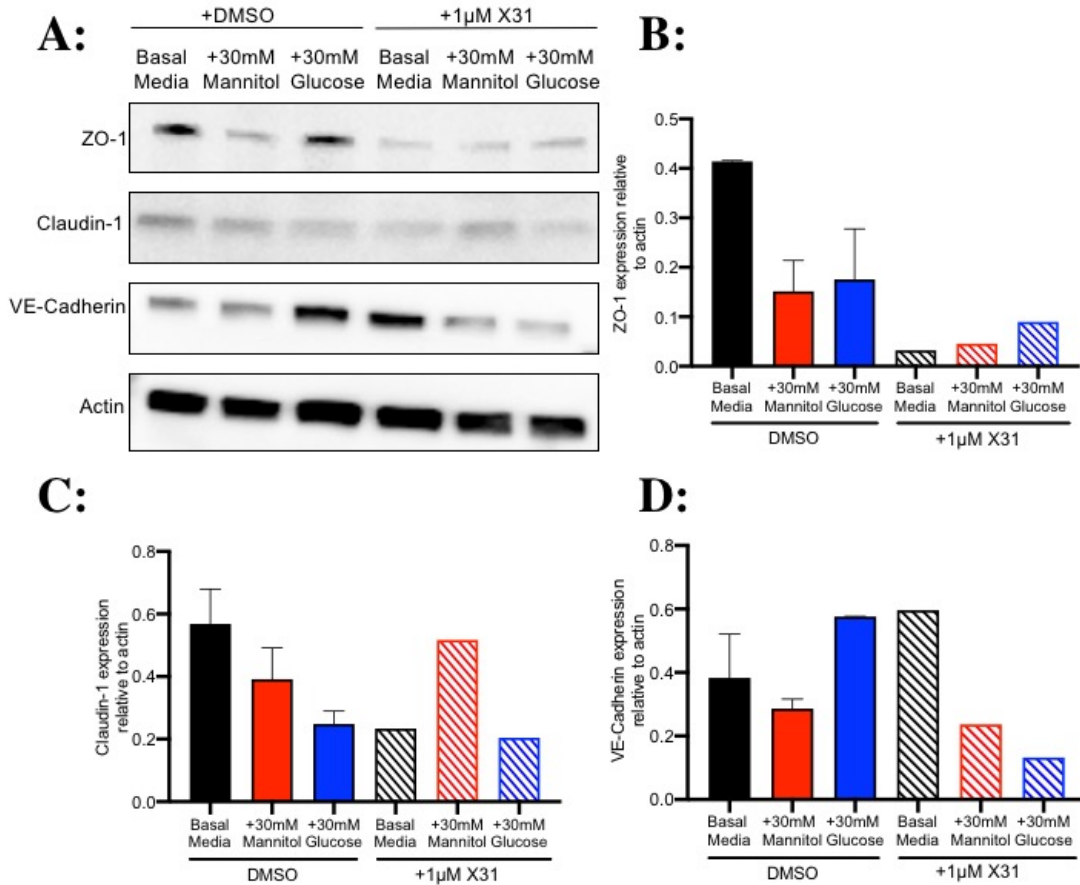


Figure 5.3.4-4: SRPK1 inhibition, osmotic and hyperglycaemic insult has no significant effect on ZO-1, Claudin-1 and VE-Cadherin in iBRECs.

A: Fibronectin coated T75s were seeded with iBRECs, grown to confluence and treated for 3 days with 0, 30mM D-mannitol or 30mM D-glucose in conjunction with 1% DMSO or 1μM SPHINX31. Western blots were performed on cell lysates to assess for Claudin-1, ZO-1, Claudin-5 and actin expression. **B:** ZO-1 expression did not significantly change in the 1% DMSO group (basal media: 0.414 ± 0.00 ; mannitol: 0.151 ± 0.06 ; glucose: 0.176 ± 0.10) nor the SPHINX31 group (basal media: 0.032; mannitol: 0.046; glucose: 0.09). **C:** Claudin-1 expressed relative to actin was not significantly changed in response to 1% DMSO 30mM mannitol (0.39 ± 0.01), 1% DMSO 30mM glucose (0.25 ± 0.04) compared to 1% DMSO basal media (0.57 ± 0.11). Nor was expression significantly altered in response to SPHINX31 (basal media: 0.233; mannitol: 0.517; glucose: 0.205). **D:** VE-Cadherin expression was not significantly altered in 1% DMSO (basal media: 0.383 ± 0.14 ; mannitol: 0.286 ± 0.03 ; glucose: 0.577 ± 0.0) or SPHINX31 (basal media: 0.596; mannitol: 0.237; glucose: 0.132). Error bars indicate mean + standard error. Data was analysed via a one-way analysis of variance with Dunnet's post-hoc (1% DMSO: $n=2$; 1μM SPHINX31: $n=1$).

These results suggest SPHINX31 has no effect on iBREC permeability, which indicate that the inhibition of SRPK1 that results in the protection against DR-

induced changes in permeability and vascular parameters *in vivo* is not an effect of SPHINX31 on the endothelial cells directly. iBRECs produce negligible amounts of endogenous VEGF-A, a concentration of which is unlikely to cause a disturbance in permeability (Deissler et al., 2011). However, substantial elevation of primary or immortalised BREC monolayer permeability is caused by exposure to exogenous VEGF-A_{165a} (Antonetti et al., 1999; Deissler et al., 2010; Harhaj et al., 2006). The impact of VEGF-A alternative isoforms on this cell line was therefore undertaken. Fibronectin-coated arrays were seeded with iBRECs. Impedance measurements were taken to confirm confluence and treated with either 30mM D-mannitol or 30mM D-glucose. In order to disrupt iBREC monolayer integrity, cells require exposure to a minimum of 25ng/mL recombinant VEGF-A_{165a} (Deissler et al., 2011), thus 25ng/mL VEGF-A_{165a} or above was used for this experiment. To elucidate the impact of VEGF-A_{165b} on VEGF-A_{165a}-induced barrier disruption, cells were also treated with 25ng/mL or 50ng/mL recombinant VEGF-A_{165b}. Cell index measurements were taken across 72h and plotted normalised to just prior to treatment addition (*Fig 5.3.4-5A*). Cell index values were normalised to 30mM mannitol (*Fig 5.3.4-5B*). Within the first 20h, there was a clear downward drift in those cells exposed to VEGF-A_{165a}, consistent which was what is seen in published literature (Deissler et al., 2008, 2010, 2011). 50ng/mL VEGF-A_{165a} exposure triggered a reduction in AUC compared to mannitol control (*Fig 5.3.4-5C*). 25ng/mL VEGF-A_{165b} by itself appeared to also induce a decrease in AUC, although to not the same extent as VEGF-A_{165a}. However, 25ng/mL VEGF-A_{165b} actually abrogated the disruption to monolayer layer induced by 50ng/mL VEGF-A_{165a} in NG conditions. Interestingly, equivalent concentrations of VEGF-A_{165a} and VEGF-A_{165b} completely blocked the reduction induced by VEGF-A_{165a}. To elucidate the impact of VEGF-A alternative isoforms on iBREC monolayer permeability, cell index values were normalised against 30mM glucose only (*Fig 5.3.4-5D*). Importantly, 30mM D-glucose reduced AUC compared to 30mM D-mannitol, thus confirming that glucose-induced changes are due to glycaemic stimulus and not osmotic shock. VEGF-A_{165a} in HG decreased AUC compared to NG, but not more so than HG alone. VEGF-A_{165b} (25ng/mL) alone did not change AUC compared to HG, even when cells were co-treated with VEGF-A_{165a}. Excitingly, both hyperglycaemic and VEGF-A_{165a} mediated disruption of iBREC

monolayer was ameliorated by exposure to 50ng/mL VEGF-A₁₆₅b (Fig 5.3.4-5E).

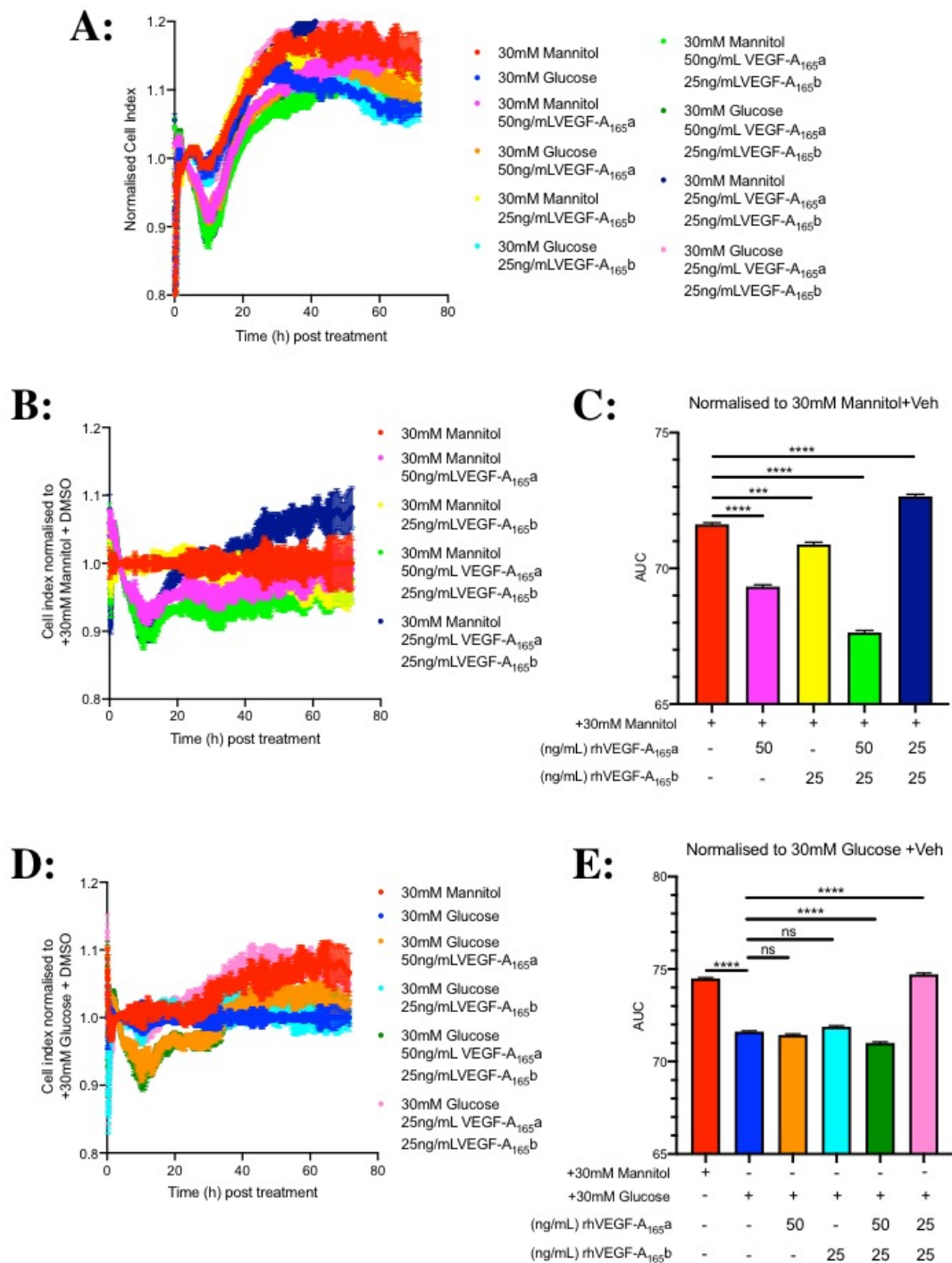


Figure 5.3.4-5: VEGF-A₁₆₅b ameliorates VEGF-A₁₆₅a-induced disruption in iBREC monolayer permeability in normo- and hyperglycaemia.

A: iBRECs were grown to confluence on fibronectin coated xCelligence arrays and treated with either 30mM D-mannitol or D-glucose. In addition, 25ng/mL or 50ng/mL recombinant VEGF-A₁₆₅a was administered with and without

25ng/mL VEGF-A_{165b}. Impedance (cell index) measurements were taken over the course of 72h and normalised to cell index value after treatment addition. **B**: Cell indexes normalised to 30mM mannitol. **C**: AUC decreased in response to rhVEGF-A_{165a} (69.33±0.07), rhVEGF-A_{165b} (70.88±0.08) and 50ng/mL rhVEGF-A_{165a} with 25ng/mL rhVEGF-A_{165b} (67.64±0.08) compared to mannitol only (71.62±0.06) whilst 25ng/mL rhVEGF-A_{165a} and rhVEGF-A_{165b} caused an increase in AUC (72.65±0.08). **D**: Cell index values normalised to 30mM glucose. **E**: Glucose induced a decrease in AUC (71.62±0.03) compared to mannitol only (74.48±0.05). rhVEGF-A_{165a} or rhVEGF-A_{165b} had no significant effect on AUC compared to glucose (71.44±0.05 and 71.38±0.06 respectively). 50ng/mL rhVEGF-A_{165a} with 25ng/mL rhVEGF-A_{165b} (71.01±0.05) triggered a decrease whilst 25ng/mL rhVEGF-A_{165a} and rhVEGF-A_{165b} caused an increase in AUC (74.71±0.07). ***p<0.001, ****p<0.0001, ns=not significant. Error bars of **C&E** indicate mean + standard error. Error bars of **A,B&D** mean ± standard error. Data was analysed via a one-way analysis of variance with Bonferroni's post-hoc (n=4).

5.4 Discussion

5.4.1 Retinal permeability can be deduced non-invasively through fundus fluorescein angiography

Evans blue (EB) dye perfusion assay is often remarked as the 'gold standard' in assessing permeability across the BRB. EB is a 961Da dye with a high affinity for albumin (66.5kDa), thereby becoming a high molecular weight tracer that remains predominately in the blood circulation. Disruption to barriers through pathologies such as DR will result in a flux of EB out of the circulation into surrounding tissues (Xu et al., 2001). Absorbance at 620nm can be assayed in these surrounding tissues in order to gain a measure of permeability (Uyama et al., 1988). However, this assay is not a true measure of permeability but rather solute flux and dye movement can be influenced by other factors, not only barrier properties. These include, but are not limited to: haemodynamic parameters; presence of EB dye in circulation un-bound to albumin (Moos & Møllgård, 1993); tissue clearance rates and EB dye binding to additional plasma and tissue proteins (Allen & Orahovats, 1950). Moreover, this technique is invasive and requires animals to be culled in order to gain measurements, thus cannot be paired, an issue especially apparent when monitoring permeability over a period of time. Each animal has particular biological variabilities, such as heart rate and blood pressure, which will impact EB dye flux regardless of treatment conditions, which must be taken into account when making conclusions from a time-course experiment (Saunders et al., 2015). Sodium fluorescein (Na-FI) is a small molecular weight tracer (376Da) commonly used for fundus fluorescein angiography (FFA); a clinical diagnostic procedure to visualise changes in retinal vasculature and neuronal tissue (Gass et al., 1967). The technique is non-invasive and latest advances in wide-field fluorescein angiography have allowed for the detection of subtle changes in the peripheral BRB (Shoughy et al., 2015). A mathematical formula based on Fick's Law coupled with FFA has been recently described to non-invasively quantify retinal permeability in a diabetic rat model (Allen et al., 2020). The technique involves intra-peritoneally injecting Na-FI into a rat and monitoring retinal perfusion using a Phoenix Micron IV fluorescent ophthalmoscope. Angiograms are analysed to determine mean fluorescence intensity in a retinal vessel and

nearby surrounding tissue. A mathematical variation of Fick's Law is used to determine retinal permeability from intensity gradients. As such, this offers a method to accurately and non-invasively monitor retinal permeability over time in the same animal (Allen et al., 2020). Moreover, in comparison with EB dye assay, this technique is more cost-effective, sensitive, less toxic and requires substantially less animals, in concordance with NC3Rs guidelines (NC3Rs, 2019).

Assessment of retinal permeability *in vivo*, be that by EB assay (Xu et al., 2001) or immunofluorescence (Scheppke et al., 2008), typically require sacrificing the animal and performing analysis on collected tissue. As such, monitoring permeability over time will require multiple animals with the resulting data unpaired. I used a novel non-invasive method of calculating retinal permeability that we have recently described in (Allen et al., 2020) to demonstrate that the STZ model of diabetes triggers an increase in retinal permeability trending on day 7 and significantly by day 14 and continues through to day 28 (Fig 5.3.1-2D). This corroborates with the published technique (Allen et al., 2020) and also where retinal permeability has been assessed through invasive measures (Ved et al., 2017; Xu et al., 2001). An important caveat of this model is it does not take into account the impact of blood pressure. As my study is a timecourse, and I normalise to day 0, biological variations of blood pressure between the animals should not influence the results. Retinal blood flow, venous diameter and velocity is not significantly changed in response to STZ after 4 or even 6 weeks, however systemic blood pressure is decreased after 4 weeks from 101 ± 18 mmHg to 79 ± 23 mmHg (Bunag et al., 1982). If the systemic blood pressure translates to the ocular vasculature, this may mean that our quantification of retinal permeability is actually an underestimate. Reduction in blood pressure will decrease the flux of molecules into the vessels, which according to Fick's Law should reduce permeability. There is currently no method to measure ocular blood pressure non-invasively, to do so would require sophisticated optical imaging techniques and tracers that were unavailable to me, but would have resulted in a more detailed understanding of permeability shifts. Despite this limitation, our model showed a characteristic

increase in retinal permeability in response to STZ-induced diabetes, and as such could be used for further experiments.

5.4.2 SRPK1 inhibition ameliorates DR-induced increase in retinal permeability in an *in vivo* model of Type-I diabetes

There are three primary routes of administration for ocular drugs: topical, periocular and systemic. Each route poses particular challenges, primarily due to the number of static and dynamic barriers the drugs will need to overcome to target a particular area of tissue. Whilst systemic drugs tend to be more patient compliant than the other routes, they have reduced bioavailability, could cause major side effects elsewhere in the body and need to cross both BRB and blood-aqueous barriers (Gaudana et al., 2010). Periocular routes include intravitreal injection, allow higher dosing to specific areas of the eye, in particular the posterior segment. However, as mentioned previously, this requires a trained professional, has low patient compliance and could lead to side effects that damage vision, such as haemorrhaging, endophthalmitis or even retinal detachment. Anti-VEGF-As could potentially pass into the systemic circulation through this route of administration, due to an impaired oBRB, they could be especially unfavourable in diabetic patients as it could exacerbate diabetic symptoms including hypertension, proteinuria and impaired wound healing (Simó & Hernández, 2008). Topical administration, primarily eyedrops, are typically employed to target the anterior segment of the eye due to the impermeability of the layers of cornea and the presence of efflux pumps limiting drug penetrance to posterior areas (Gaudana et al., 2010). However, this route is more patient compliant, non-invasive and will have negligible cross-over into the systemic circulation. As such, topical drug delivery to the eye is regarded by some as the 'holy grail' of ocular drug delivery. Despite success in pre-clinical studies, many candidate drugs fail to translate clinically (Rodrigues et al., 2018). Excitingly, a few groups have developed agents able to permeate to the back of the eye in animal models when delivered topically (Batson et al., 2017; de Cogan et al., 2017; Simó et al., 2019). With regards to SPHINX31, the SRPK1 inhibitor used throughout my study, approximately 24% of a 0.05 μ g dose to a mouse eye was measured in the retina 4 hours after dosing, and this remained fairly constant across 24 hours. At this dose, SPHINX31 was able to

reduce choroidal neovascularisation, highlighting its anti-angiogenic properties (Batson et al., 2017). Given its high specificity and potency for SRPK1, SPHINX31 offers potential as a therapeutic for DR, however its impact on retinal permeability remains to be elucidated.

Currently, the recommended treatment for PDR, aside from management of diabetes, is PRP (The Royal College of Ophthalmologists Diabetic Retinopathy Guidelines, 2012), a destructive method that results in the formation of scar tissue. Due to the pivotal role of VEGF-A in the pathogenesis of the disease, there have been a number of clinical trials aiming to repurpose anti-VEGF therapeutics commonly used to treat wet-AMD (Beaulieu et al., 2016; Bhavsar et al., 2013; Gross et al., 2018). There is also positivity surrounding use of anti-inflammatories, such as dexamethasone (Stewart et al., 2016) and fluocinolone, especially with regards to non-chemokine driven DMO (Boyer et al., 2014; Campochiaro et al., 2012). However, there are a large proportion of patients who are unresponsive to the various treatments currently on the market (Duh et al., 2017). In addition, routes of administration of these therapeutics are often unpleasant for the patient and require a clinical professional. Lack of responsiveness to anti-VEGF-As has been hypothesised to be due to the failure of these treatments to discriminate between alternative VEGF-A terminal exon 8 inclusions (Batson et al., 2017). This hypothesis, coupled with my data from Chapter 4 where I found inhibition of SRPK1 resulted in an amelioration of HG-induced changes in VEGF-A alternative isoform expression, led me to hypothesise that SPHINX31 could be an effective treatment in an *in vivo* model of DR.

Norway Browns are a highly pigmented strain, which have been commonly used to study vascular abnormalities in response to diabetes, including BRB breakdown (Schroder et al., 1991; Wanek et al., 2014). As such, use of these rats allows comparison with a large body of literature. Additionally, this strain developed sustained retinal vascular hyperpermeability across 16 weeks, compared to 3-10 days after diabetes onset before reversal in albino Sprague-Dawleys. This is potentially due to enhanced retinal VEGF mRNA and protein levels in Norway Brown compared to Sprague-Dawleys (Zhang et al., 2005).

As my study focuses on the impact of VEGF-A isoforms, this strain dependant elevated VEGF-A facilitates experimental manipulation. Albino rats are also described to have abnormal neural connections between the brain and eye, resulting in poor vision (Taylor et al., 1986). Norway Browns treated with STZ and insulin supplementation exhibited increased blood glucose concentrations three days after STZ injection (*Fig 5.3.1-1A*). It has been reported that HG can be spontaneously reversed in STZ models, however the diabetic cohort maintained HG across the 4 weeks. This cohort also had characteristic lower weights compared to the saline control group (*Fig 5.3.1-1B*). Interestingly, although the diabetic + vehicle group had statistically significantly lower weights than the non-diabetic group, the diabetic + SPHINX31 group just trended lower. As SPHINX31 was administered topically, and negligible amounts have been found in the systemic circulation, it is very unlikely that this is because SPHINX31 is affecting another organ. Contact time between the two groups were similar, as both groups received twice-daily eyedrops, were weighed almost daily, and underwent the same imaging procedures at the same frequency. One could speculate the weight difference is due to the SPHINX31 group having improved eyesight compared to diabetic animals treated with eye formulation control buffer, thus animals are more comfortable and more likely to eat and gain weight. However, behavioural studies would be required to confirm this. VEGF-A_{165b} expression was found to reduce in response to STZ-induced diabetes, consistent with published literature of the human diabetic vitreous (Jiang et al., 2020; Perrin et al., 2005). SPHINX31 ameliorated this decrease slightly, which may be significant had I increased n numbers, as topical SPHINX31 has been previously found to increase retinal VEGF-A_{165b} expression in mice (Batson et al., 2017) Gammons et. al., found that topical SPHINX31 did not alter expression of VEGF-A_{165b} in laser CNV model, and hypothesised that the reduction neovascularisation they observed was primarily due to decreased VEGF-A_{xxx}a expression (Gammons et al., 2013). However, they assessed VEGF-A_{165b} expression through western blot, rather than an ELISA, which is more sensitive and potentially able to identify smaller shifts in expression. Nevertheless, I would have also liked to assay the tissue for VEGF-A_{165a}, however due to poor protein yield I was unable to.

Perhaps the most significant finding of this thesis is that SPHINX31 blocked diabetes-induced increase in retinal permeability and capillary loss after 14 days over 28 days (*Fig 5.3.1-2D*). A pilot study found that SPHINX31 eyedrops induced protective effects against retinal permeability in STZ treated Norway-Browns after only 7 days (Allen et al., 2017). However, these rats were not supported with an insulin bolus, thus the diabetic-insult was harsher. In rats, morphological and functional studies suggest that STZ only models early DR phenotype (Lai & Lo, 2013). Supporting this, angiograms from STZ rats in my study did not show evidence of developing microaneurysms, the earliest clinical sign of retinopathy (*Fig 5.3.1-2A*). However, although microaneurysms have been detected in humans 4-7 years before clinical diabetes (Harris et al., 1992), in STZ rats microaneurysms are less likely to develop, with the earliest detection at 18 months if they maintain a persistent hyperglycaemia (Kato et al., 2003). Another SRPK1 inhibitor, SRPIN340 has also been suggested to be a potential therapeutic for neovascular eye diseases (Gammons et al., 2011). SRPIN340 is a SRPK1/2 inhibitor that has been shown to prevent VEGF-A_{165b} downregulation in response to IGF-1 stimulation in podocytes, which was confirmed through overexpression studies to be a SRPK1-mediated effect (Nowak et al., 2010). However, SPHINX31 is 50-fold more selective for SRPK1 over SRPK2, limiting the off-target effects. Especially important for my study; SPHINX31 is 50-fold more selective for SRPK1 over CLK1 and 100-fold against CLK4 (Batson et al., 2017), both these kinases have the capacity to phosphorylate SRSF6 promoting VEGF-A exon 8 distal splice site selection and VEGF-A_{165b} expression (Nowak et al., 2008). Thus inhibition of these kinases could reduce VEGF-A_{165b} levels and disrupt VEGF-A_{165b}:VEGF-A_{165a} ratio. Ved et al., found that administration of recombinant VEGF-A_{165b} prevented diabetes induced EB extravasation in the same animal model used in my study (Ved et al., 2017). This could explain the reduction in retinal permeability in response to SPHINX31, as inhibiting SRPK1 induces a switch in splicing that leads to increased exposure of VEGF-A_{165b} (*Fig 5.3.1-1C*) and protects against diabetic challenges to retinal permeability. Over recent years, there have been a number of candidate eye drops targeting ocular vasculature. Cyclosporine A eye drops reduce EB dye leakage in a Type-I allergic conjunctivitis mouse model (Shii et al., 2009). Peptidomimetic that selectively binds VEGFR1 and

NRP-1, Vasotide, inhibits pathological angiogenesis in a laser-induced monkey model of AMD (Sidman et al., 2015). PEDF bioactive peptide derivatives reduced BSA-FITC extravasation across the retina in a diabetic *Ins2^{Akita}* mouse (Liu et al., 2012). Despite the success of these pre-clinical studies, most fail at the clinical trial stage (Rodrigues et al., 2018).

5.4.3 STZ-induced increase in retinal thickening is localised to the RPE-Choroid layer and ameliorated by SPHINX31.

A clinical feature of DR that may occur is retinal thickening, which can occur due to vitreo-macular traction, intra-retinal cysts or oedema, glycation of the layers of nerve fibers and accumulation of sub-retinal fluid (Hee et al., 1998). These manifestations can be non-invasively monitored clinically with optical coherence tomography (OCT), a tool which revolutionised the identification of macular oedema. The operation is analogous to ultrasound imaging, except light is utilised rather than acoustic waves to provide highly detailed tomographic images (Chauhan & Marshall, 1999). Diabetes-associated issues in vision arise primarily due to DMO and monitoring retinal thickness may allow for early detection of DMO. Mean retinal thickness did increase in the diabetic cohort treated with control eye drops after 28 days, and there appeared to be some evidence of retinal separation from the choroid in four of the eight animals (*Fig 5.3.2-1*). Furthermore, this increase appeared to be localised specifically at the RPE and Bruch's membrane layer (*Fig 5.3.2-2*). Twice-daily topical administration of SPHINX31 blocked this increase. Increase in total retinal thickness corroborates with that seen in human eyes, patients with NPDR and PDR had greater macula thickness compared to normal eyes, although not to a statistically significant extent. However, when specifically measuring foveal thickness, they found statistically significant increases in thickness in diabetic patients (Sánchez-Tocino et al., 2002). Additionally, in Sprague-Dawley rats, total retinal thickness was increased in STZ treated male rats, when measured high resolution manganese-enhanced MRI (Berkowitz et al., 2007). The relationship between retinal thickness and visual acuity remains dubious, with some groups finding a correlation between retinal thickness and a decrease in visual acuity (Diabetic Retinopathy Clinical Research Network et al., 2007) and others finding a paradoxical increase in visual acuity (Sánchez-Tocino et al.,

2002). Despite this, evaluation of retinal thickness via OCT remains a valuable diagnostic tool, especially for DR, as changes, even subclinical, in retinal thickness can be indicative of disease progression or management (Virgili et al., 2011). To build upon this work further, I would have liked to localise where the thickness is with regards to the fovea. This could have been completed by obtaining 3D volumes rather than 2D scans and analysing spatially where increases in thickness are centralised.

5.4.4 STZ and SPHINX31 induces slight, but not significant changes in vessel parameters after 28-days

The Phoenix Micron IV was a useful tool for assessing retinal health, imaging retinal perfusion and guiding OCT imaging. However, the ophthalmoscope is limited in its resolution to 6 μ m for rats and has an imaging depth of 20 μ m. Thus, it is not possible from angiograms to deduce total vascular parameters, particularly of smaller capillaries. This was an important assessment to make, as our permeability quantification is based on a measurement of fluorescence intensity from tissue which may or may not contain capillaries below the detection limit of the Micron IV, and if this vascular network was amplified or reduced in response to diabetic insult, it could skew the data. In addition, evaluating vascular parameters offers insight to DR pathogenesis. Therefore, following termination of the eyedrop study, retinae were isolated from eyecups, whole-mounted and stained for IB4 as an endothelial marker. Both FIJI and Imaris tools were used to evaluate vascular properties. Diabetes appeared to induce a slight reduction in vessel density in the upper plexus of the retina which was unaffected by SRPK1 inhibition when evaluated by FIJI (*Fig 5.3.3-1B*). Vascular density within the lower plexus was unchanged in response to diabetic insult or SRPK1 treatment, and no significant differences with regards to vessel diameter was measured across both plexuses. However, this method of analysis is unable to accurately segment the middle plexus, which has been described to be distinctly affected in DR, with decreased parafoveal vascular density and flow index (Zhang et al., 2016). OCT angiography (OCTA), as the name suggests, combines angiography with OCT techniques to map retinal vasculature three-dimensionally and is able to segment the retinal vasculature to obtain an accurate image of the middle capillary plexus (Onishi et al., 2018).

A recent paper used swept-source OCT angiography to take multiple volume scans to obtain a highly detailed montage of the retinal vasculature across all three plexuses in healthy human eyes (Lavia et al., 2020). As of yet, they have not expanded their research to include diseased eyes, and their sample size was small (10 patients; mean age 31.8 ± 3.4 yrs), however this is a useful technique that could be exploited to further scrutinise total retinal vasculature. I used Imaris software to generate a 3D rendering of total IB₄ stained retinal vasculature from z-stacks and the filament tracer tool was repurposed to analyse vessel networks. In this way, I was able to analyse changes across all three plexuses, but was not able to segment them. Dendrite branches, a potential marker for neovascularisation (Geraldes et al., 2009), were unchanged in my model of diabetes or in response to SPHINX31 (*Fig 5.3.3-2B*). Unlike individual plexuses, vascular diameter and volume trended an increase in response to diabetes, and reduced due to topical SPHINX31 (*Fig 5.3.3-2C&D*). The fact that there were no significant changes in retinal vasculature was not surprising as my model is of a relatively short duration. Gross vascular remodelling in response to STZ-induced diabetes are observed 8 months after diabetic induction (Lai & Lo, 2013). Some groups use genetic models such as nonobese diabetic (NOD) mice which spontaneously develop type-I diabetes owing to a CD4⁺ and CD8⁺ responsive destruction of pancreatic β -cells. These mice have been described to have vascular abnormalities such as vasoconstriction and degeneration 4 months after hyperglycaemia onset (Shaw et al., 2006). The more popular Ins2^{Akita} mouse model, who carry a point mutation in insulin2 gene resulting in accumulation of the protein within pancreatic β -cells and ultimately cell death, are reported to display retinal vascular abnormalities with 26 weeks of hyperglycaemia (Wright et al., 2012). However, the primary focus of my study was permeability, and breakdown of BRB has been reported in this model after 2 weeks of hyperglycaemia (Rungger-Brändle et al., 2000; Zhang et al., 2008), justifying my decision to use this model.

5.4.5 SRPK1 inhibition protects against diabetes-induced acellular capillary formation

Loss of cellular components, pericytes and endothelial cells, are a characteristic early feature of DR. Due to the lack of primary human retinal samples from the primary stages of DR, the exact sequence with which the cells are lost remains debateable. However, animals models have established a pericyte dropout occurs before endothelial cell death leaving a basement membrane sleeve (Hammes et al., 2004). Collagen IV staining was used as a marker of basement membrane and IB₄ to stain endothelial cells. An acellular capillary was defined as one which contained basement membrane but no endothelial cells. STZ induced a significant increase in acellular capillary formation, which was blocked by SPHINX31 (*Fig 5.3.3-3B*). Administration of SPHINX31 increased VEGF-A_{165b} expression in this study (*Fig 5.3.1-1C*). VEGF-A_{165b} is a cytoprotective agent which is described to reduce cytotoxicity induced by Na butyrate and H₂O₂ in RPE. In the human umbilical vein endothelial cells, VEGF-A_{165b} was also found to be cytoprotective. Furthermore, exposure to a neutralising VEGF-A_{165b} antibody increasing cytotoxicity in both cell lines (Magnussen et al., 2010). As such, this offers an explanation for the reduction in acellular capillaries in the diabetic + SPHINX31 cohort, as the increased expression of VEGF-A_{165b} is protecting retinal endothelial cells from death in response to hyperglycaemic conditions. The formation of acellular capillaries after 28 days was surprising as acellular capillaries typically are not observed in this model until at least 8 months after onset (Duan et al., 2013; Lai & Lo, 2013). Elevated numbers of acellular capillaries were found in STZ-induced diabetic rats 6 months after diabetes induction, but not after 3 months in the same study (Luo et al., 2012). However, these studies assess acellular capillaries though trypsin digestion of the retina and haematoxylin and Periodic Acidic-Schiff stain. Basement membrane thickening especially through upregulated synthesis of collagen IV is an addition distinctive feature of early DR (Cai & Boulton, 2002), which may account for the increased collagen IV staining in diabetic rats. This could also suggest that SPHINX31 is protecting against increases in basement membrane. The number of acellular capillaries were not quantified at the

beginning of the study, which may exist in different numbers in different animals and could potentially skew the results. However, there is currently no robust method to non-invasively detect acellular capillaries, thus I was unable to make this assessment. Residual basement membrane tubes that have fused, shrunken or collapsed have been described in the retina (Archer et al., 1991). Pericytes survive within the walls of these tubes a while after loss of endothelial cells (Brown, 2010). Had I stained for pericytes, I would have been able to assess for presence of these string vessels.

5.4.6 VEGF-A_{165b} ameliorates VEGF-A_{165a}-induced disruption in iBREC monolayer permeability in normo- and hyperglycaemia

The previous chapters of this thesis have focused on the oBRB, and the impact of SRPK1 inhibition on the RPE monolayer of this barrier. However the increase in retinal vascular permeability in DR is a direct result of the breakdown of the iBRB (Klaassen et al., 2013). Thus, I aimed to generate an *in vitro* model of the iBRB, determine the impact of HG and assess the effects of SPHINX31. Initially, I trialled isolating primary RECs from human donor patient eyes by extracting retinae from posterior segments, collagenase treating the tissue and sorting the resultant lysate with CD31 magnetic beads to capture endothelial cells. This is a protocol that has been used successfully (Saker et al., 2014; Stewart et al., 2016), however I was unable to emulate their results. Cell yield was poor and failed to propagate, adhere to plates or survive for multiple passages. To solve this issue, I tried different sized magnetic beads to ensure the cells were not internalising them; different cell attachment factors with varying concentrations of fibronectin and reducing the wash steps. Due to rising costs and the timeframe of the study, I eventually decided to look for alternative cell lines that could match primary RECs. Dr Heidrun Deißler has established an immortalised bovine REC (iBREC) line displaying the distinct cobblestone morphology up to passage 90. iBRECs are sensitive to VEGF-A isoforms (Deissler et al., 2013; Deissler et al., 2005) and anti-VEGF-A therapeutics (Deissler et al., 2011, 2019). HG increased iBREC monolayer permeability in a dose dependent manner after three days exposure (*Fig 5.3.4-1C*). This corroborates with existing literature (El-Remessy et al., 2013; Eshaq & Harris,

2020; Jiao et al., 2019; Stewart et al., 2016). The optimal concentration moving forward for HG assay was determined to be 30mM D-glucose, despite the fact that 50mM D-glucose increased permeability to the highest extent. Cells exposed to 40mM and 50mM D-glucose appeared unhealthy, furthermore 50mM glucose causes glucose-induced toxicity resulting in cell death and expression of oxidative stress markers (Shokrzadeh et al., 2016). Effects of glucose on cell monolayer permeability has not been previously researched in this cell line. Although it has been found that HG in conjunction with TGF- β causes transdifferentiation into α -SMA expressing mesenchymal cells, contributing to DR pathogenesis (Deissler et al., 2006). Additionally, HG stimulates cell migration, regulated by tetraspanin CD9 (Kuhn et al., 2008). This increase in permeability appeared to be mediated through loss of Claudin-1 and Claudin-5, as the expression trended lower than in basal media alone (Fig 5.3.4-2). However this data is preliminary thus further work would be required to draw robust conclusions, although loss of Claudin-5 has previously been described in response to HG-insult (Stewart et al., 2016). Loss of PECAM-1 has also been implicated in HG-induced increase in REC permeability (Eshaq & Harris, 2020), as well as occludin and JAM-A (Stewart et al., 2016).

Chapter 4 describes how SPHINX31 can reduce RPE monolayer permeability in HG conditions, possibly mediated through a switch in VEGF-A splicing from VEGF-A_{165a} to VEGF-A_{165b} isoforms. Additionally retinal permeability in response to diabetic-insult is decreased in an *in vivo* model due to topical SPHINX31 (Fig 5.3.1-2) potentially through an increase in VEGF-A_{165b} (Fig 5.3.1-1). RECs are described to express VEGF-A (Aiello et al., 1995), which offers an explanation as to why iBREC permeability is increased in response to HG. As such, I hypothesised that SPHINX31 would protect against increases in iBREC permeability in HG conditions. However, this was not the case, and SPHINX31 actually slightly elevated monolayer permeability in both NG and HG (Fig 5.3.4-3). This was surprising as Wt1 induced activation of SRPK1 has previously been found to trigger angiogenic VEGF-A₁₆₄ expression in lung endothelial cells (Wagner et al., 2019). However, my measure of permeability is actually a measure of impedance, which can be impacted by cell proliferation, morphological changes and death as well as disruption to tight junctions. The

fact that SPHINX31 impacted cell index in NG conditions suggests that the disruption is not HG-mediated. iBRECs are sensitive to FBS concentration, and thus whilst measuring cell index, they are exposed to reduced serum media. SPHINX31 binds partially to FBS, and so the low concentration of FBS may expose cells to larger, potentially toxic concentrations of SPHINX31. VEGF-A expression in iBRECs is low (Deissler et al., 2011) and SRPK1 activity in these cells is not currently defined, so it is difficult to deduce what the impact of VEGF-A splicing would be, if at all.

Targeting endogenous VEGF-A did not appear to protect REC monolayer permeability in NG or HG. However, previous work from the Deißler group has discovered that iBRECs are sensitive to exogenous VEGF-A isoforms (Deissler et al., 2008, 2011, 2013). Recombinant VEGF-A_{165a} induced an increase in REC monolayer permeability in NG conditions, however the dual exposure to this isoform and HG did not increase permeability further than HG alone. This suggests that HG is disrupting REC monolayer through a pathway independent of VEGF-A expression. A number of non-VEGF-A dependent pathways have been implicated in REC monolayer permeability in diabetes, as it has been reported that diabetic eyes have increased aqueous levels of IL-6, IL-8, IP-10, TNF- α and MCP-1 alongside VEGF-A (Joussen et al., 2004; Koch et al., 1995; Lu et al., 1999; Roh et al., 2009; Yoshimura et al., 2009). Moreover, the co-transmitter, neuropeptide Y, has been found to inhibit VEGF-A induced increases in permeability in an *in vivo* diabetic model (Ou et al., 2020). Further work would be required to pinpoint through which inflammatory cytokine iBREC permeability is being increased in HG. Recombinant VEGF-A_{165b} alone also appeared to disrupt monolayer integrity in NG but induced no change in HG when compared to HG alone. Dual exposure to both VEGF-A isoforms again increased REC monolayer permeability when VEGF-A_{165a} concentration exceeded VEGF-A_{165b}. However, equimolar concentrations of VEGF-A alternative isoforms decreased permeability in NG and crucially protected against HG-induced barrier disruption (*Fig 5.3.4-5*) potentially because VEGF-A isoforms bind to VEGFR2 at a one-to-one ratio (Varey et al., 2008).

Chapter 6

Discussion

Diabetes-induced ocular complications, DR and DMO, remains the dominant cause of blindness in the western world across the working population, projected to rise as the obesity crisis continues. Current therapies are not effective in a subset of patients, thus necessitates the development of novel therapeutics. The present thesis explores the potential of manipulating VEGF-A alternative splicing to treat DR-induced pathologies. Additionally, this work highlights the impact of oBRB in DR progression and treatment. Furthermore, novel insights are gained in the activity and role of SRPK1 and associated proteins in RPE.

6.1 COVID-19 Impact Statement

The abrupt closure of the university in response to the COVID-19 pandemic has meant that some experiments I had planned to validate my results and further explore SRPK1 activity in RPE had to be terminated. In addition, due to the increased difficulty of transporting material during the COVID-19 pandemic, I have had to delay further work with our collaborative partner, Dr Heidrun Deißler, to increase the n number and build upon the research in RECs. These disruptions and delays were of particular significance as our lab group had moved buildings over November 2019 through to January 2020, thus I was unable to perform molecular biology experiments over this time. I will describe my planned experiments below.

6.2 SRPK1 and hyperglycaemia

The current literature surrounding SRPK1 in RPE is limited, especially with regards to hyperglycaemia. It is known that SRPK1 phosphorylates SRSF1 in activated RPE, inducing a translocation of the splicing factor to the nucleus, where it will promote proximal splice site selection of VEGF-A (Gammons et al., 2013). Previous published work in RPE has involved activating SRPK1 through EGF stimulation, however the present work in this thesis describes SRSF1 nuclear translocation as a result of HG- or Hx-insult highlighting its significance in DR. SRPK1 phosphorylates other splicing factors alongside SRSF1 and has additionally been implicated in mRNA maturation, chromatin reorganisation, cell cycle and p53 regulation and metabolic signalling in other cell types (Giannakouros et al., 2011). The complete downstream cascade associated

with SRPK1 activation is not fully elucidated as of yet, which could mean that my results of SRPK1 inhibition (Chapter 4 & 5) occurs in a process independent of the SRPK1-SRSF1 axis. Interestingly, the combination of HG and Hx does not activate SRPK1 when assessed through SRSF1 nuclear localisation (*Appendix D&E*) whilst each condition alone does, highlighting the necessity for further research in this area. RNA-seq analysis and subsequent validation of hits would confirm SRPK1 inhibition effects on permeability are due to increased distal splice selection of VEGF, as well as identify other potential DR biomarkers. Whilst this experiment would be interesting, I believe the ECIS data where α VEGF-A_{165b} neutralises the effects of SPHINX31 (Chapter 4) is sufficient evidence that increased VEGF-A_{165b} expression has a dominant role. Long non-coding RNA MALAT1 binds and regulates the phosphorylation of SRSF1, and also directly binds to SRPK1 (Hu et al., 2016). MALAT1 expression is increased in Hx cells (Liu et al., 2019) and HG cells. Interestingly, MALAT1 depletion also up-regulates VEGF-A_{165b} expression (Yang et al., 2018). This could point to an intermediary step between SRPK1 and SRSF1 where MALAT1 is involved. However, my direct measurement of SRPK1 activity via a nano-BRET: based on SRPK1 proximity with its cognate splicing factor, SRPK1 was described for the first time to activate in response to HG (Chapter 3). However, this requires repeating in Hx to determine whether increased SRSF1 nuclear localisation occurs as a direct affect of SRPK1. Although I hypothesised that SRPK1:SRSF1 complexes are more concentrated in the nucleus as a result of HG-insult, I believe the transfection efficiency would need to be improved and further repeats performed before concluding this. Furthermore, the addition of a positive control, a construct expressing both Nanoluc® and Halotag® moieties alongside would help optimise the imaging parameters and validate my results. In addition, longer term imaging could be performed on euglycemic RPE dosed with D-glucose, to determine the time it takes for the translocation to occur.

PKC is known to activate SRPK1 in IGF-1 stimulated cells (Harper & Bates, 2008). Furthermore, HG activates PKC in RPE, resulting in an upregulation in VEGF (Poulaki et al., 2002). However, RPE exposure to 35mM glucose resulted in a decrease in expression of IGF-1 (Kang et al., 2018), thus is not

the pathway associated with PKC activation in HG. In diabetes, PKC activation is a result of oxidative stress (Konishi et al., 1997), and DAG production (Nishikawa et al., 2000). I believe this is the first time that PKC activation in HG RPE has been reported to activate SRPK1 and induce nuclear localisation of SRSF1 (Chapter 4). Furthermore, this activation appeared to be specific to PKC γ , PKC δ or potentially PKC ϵ isoforms and not PKC- α , - β 1 or - β 2. Expression of the former three isoforms has been attributed to DAG as they contain DAG-binding C1B domains, however PKC δ and PKC ϵ are potentially more sensitive to DAG concentration as their C1B domains have a 100-fold higher affinity for DAG than conventional isoforms (Wu-Zhang & Newton, 2013). Additionally, intravitreal VEGF injection in rats results in activation of PKC δ . With regards to PKC γ , it has also been reported to be activated in hyperglycaemia (Idris et al., 2001). The literature surrounding PKC isoform specificity in SRPK1 activation is lacking, and I believe that my experiments are the first to describe this notion. However, I am cautious to draw conclusions as I think these studies could have been built upon with PKC isoform-specific silencing RNAs to pinpoint which isoforms are involved. Additionally, an immunoprecipitation against SRPK1 and SRSF1 probed for PKC isoforms would determine whether PKC is acting directly on SRPK1 and SRSF1, or if there are intermediary components.

6.3 Dual effects of hypoxia and hyperglycaemia on RPEs

Hyperglycaemia coupled with hypoxia produced different results to each condition alone (*See Appendix*). The nuclear localisation of SRSF1 did not increase in these conditions, and actually appeared to be below that of basal level (*Appendix D&E*). There was a lot of discussion about the necessity of subjecting the cells to both hyperglycaemia and hypoxia, as this may not actually occur in DR due to the dropping off and occlusion of capillaries reducing tissue perfusion and thus exposure to glucose in the blood. However, cells may exhibit an epigenetic memory of hyperglycaemia even after they lose exposure to high glucose, so may actually be both hyperglycaemia and hypoxic at the same time. On the other hand, diffusion of both glucose and oxygen across retinal tissue has been found to be different in animal models and human

diabetic retina compared to healthy controls, which may refute the possibility of hypoxic and hyperglycaemic areas (Tang et al., 2000, Wangsa-Wirawan and Linsenmeier, 2003). Nevertheless, the result is interesting, as the two conditions appeared to cancel each other out, whereas we hypothesised the effects seen in hyperglycaemia would be aggregated in hypoxia, due to an increased expression of glucose transporters such as GLUT-1 (Ozaki et al., 1999). Lafosse *et. al.* reported similar findings in dermal fibroblasts exposed to the same conditions. The results are likely due to changes in cellular metabolism, however further work is required. Expression of VEGF-A_{165a} is increased under oxidative stress with glucose, but not to a significant amount like that which is seen in each condition separately (*Appendix A*). This is likely due to the lack of nuclear SRSF1 localisation, but VEGF is still upregulated, suggesting other mechanisms in play. VEGF-A_{165b} reduces compared to normoglycemia in hyperglycaemic plus hypoxic conditions, but not significantly, and when expressed as a ratio over VEGF-A_{165a}, the decrease is the same as with each condition alone (*Appendix B-C*). ZO-1 staining reduces to the same extent as seen in hypoxia alone (*Appendix F&G*). In addition, the peak number and thus number of gaps in the tight junction also decreases to the same extent as hypoxia. In order to target the research of this thesis, at this point it was decided that we would no longer explore the dual effects of hyperglycaemia plus hypoxia, thus I removed it from the primary thesis data.

6.4 Targeting the outer BRB for DR therapy

DR manifestation and progression is attributed to breakdown of BRB. However, the majority of work in this field has been focused on the impact of the iBRB. This is especially apparent in my review of the literature, where a lot of publications use 'BRB' to describe the iBRB, neglecting to consider the oBRB completely. The contribution and importance of oBRB in DR pathogenesis, especially with regards to DME is now beginning to be understood over recent years. Perhaps the reason as to why the oBRB has been overlooked is due to issues generating an *in vitro* model. I describe in the discussion of chapter 3 the difficulties in establishing a representative model of the RPE monolayer, and conclude that primary cells are beneficial over ARPE-19s to assess oBRB integrity and VEGF-A expression. I think it is a fair interpretation that the

increase in retinal permeability as determined by FFA is predominately a result of iBRB breakdown. The imaging depth of the ophthalmoscope is not sufficient to visualise down to the RPE layer. However, this does not mean the oBRB is not involved in the increase in retinal permeability. The increase in retinal thickness is due to breakdown of both BRBs and fluid leakage (Xia & Rizzolo, 2017). The choroidal circulation makes up 80% of the total retinal circulation and RPE are continually exposed to this. As such, one could speculate that high blood glucose will affect RPE more than REC, due to their increased exposure. Furthermore, choroidal endothelial cell-cell junctions are disrupted in response to HG (Saker et al., 2014), exacerbating choroidal leakiness in already fenestrated vessels. In healthy eyes, VEGF-A is secreted dominantly from the apical side of RPE, but also through the basal lamina, to the choroidal vasculature. Diabetes results in a reversal of this, and the basal lamina becomes the dominant site for VEGF-A secretion, which could impact the choroidal circulation (Kannan et al., 2006). This leads me to speculate that SPHINX31 treatment on RPE would result in an increase in VEGF-A_{165b} secretion from the basal lamina and thus into the choroidal circulation. Further, this could be assessed by culturing RPE on transwells, treating with SPHINX31 and measuring VEGF-A isoform expression in the upper and lower chambers.

The results from ECIS were promising, as it suggested inhibition of SRPK1 protects against HG-induced increase in permeability (Chapter 4). However, this method of determining permeability is limited in that impedance fluctuations are additionally caused by cell death, changes in cell morphology and proliferation. RPE cells are polarised and in healthy monolayers carry a trans-epithelial potential of difference of 3.5mV. As such, they give rise to high trans-epithelial resistance values to preserve the ionic gradient (Cao et al., 2018). This was reflected in the high impedance values observed and maintained for several hours as the cells appeared to be a confluent monolayer. Thus, I would assume that the impedance was reflective of permeability shifts and not cell proliferation or death, which would have resulted in large dips in the trace. Furthermore, any changes in cell morphology would have been observed through the associated immunofluorescent experiments (Chapter 3 & 4). Notably, despite the report from ibidi (the company supplying the ECIS

system) that measurement of impedance at low or high frequencies would differentiate between paracellular and transcellular flow respectively, in practice I observed no differences across frequencies. A particular caveat of this technique is the lack of an anterior chamber allow solute flux across. Whilst measuring solute flux with a tracer compound could potentially disrupt barrier integrity and the transport process, resistance measurements taken using chopstick electrodes in a chamber above and below cells grown on a semi-permeable membrane would have potentially been more representative of the oBRB *in vivo*. However, ECIS is more sensitive than the chopstick method and the data achieved from the ZO-1 immunofluorescence corroborates with the ECIS results, thus giving me confidence in the results. Additionally, due to the use of a primary cell line with more biological variability than an immortalised line, I repeated the ECIS experiments ~ 6 times, and consistently found the same result, validating my observations.

Disruption of the oBRB has been implicated in oedema formation in diabetic eyes (Xia & Rizzolo, 2017). As rats do not possess a macula, they are limited in their ability to accurately model DMO formation. However, characteristic early DMO features such as retinal thickening and altered RPE fluid transport has been independently observed in my model 4 weeks post-STZ administration (Desjardins et al., 2016), and therefore this model, although not perfect, does allow for some assessment of DMO. Furthermore, the largest DMO patient cohort are classified as having diffusible DMO: localised thickening of the ONL, which again has been previously modelled in rats (Xu et al., 2011). OCT is a powerful tool, able to produce high resolution images of the retinal layers, allowing for the non-invasive assessment of oedema formation. Despite the benefits associated with this technique, it is limited in addressing RPE health. Spectral-domain OCT, a more sensitive approach than OCT, observes particular RPE phenotypes such as atrophy and disassociation (Curcio et al., 2017), however I do not believe improved sensitivity would offer any benefit answering the questions posed in this thesis. On the other hand, there has been development in a technique combining OCT with fluorescence molecular imaging, using a dye with a far-red emission spectrum, Cy5 (Yuan et al., 2010). This exploits the OCT capability to capture infrared light. Further work in this

technique would allow observations to be made of solute flux across RPE in response to SPHINX31, however this would take some time to develop and confirm robustness of analysis. The majority of my results from OCT scans are quantitative, based on measurements made of the retinal layers, rather than qualitative observations made from the scans. Perhaps with clinical assessments from a clinical advisor, I would have gained to deeper insight into retinal health in my model. I had attempted to determine changes to visual function in response to SPHINX31 in this model, by performing electroretinograms. Unfortunately, I was unsuccessful in this technique, due to equipment malfunctions and the timings, however as DR can result in blindness I believe this would have been a useful assessment to make. However, SPHINX31 has previously been reported in healthy mice to not change electroretinograms compared to untreated animals, which leads me to assume that SPHINX31 should not have a detrimental effect on visual function in my DR model (Batson et al., 2017). Additionally, I could have performed visual behavioural studies, such as the startle reflex, orientation, maze or optokinetic test, to determine changes in visual function.

I am hesitant to interpret that a 4-week model of type-I diabetes to predict gross changes to retinal vasculature, despite the trends observed (Chapter 5). The literature describes detectable blood vessel changes 8-months after STZ-injection, thus my model appears to be too short (Lai & Lo, 2013). As the focus of this PhD was permeability and not neovascularisation, I deem termination of the study at 4-weeks to be the correct decision, as BRB breakdown occurs at the 2 weeks after diabetes onset (Rungger-Brändle et al., 2000; Zhang et al., 2008), and after four weeks I was able to move my focus to other permeability associated research areas rather than prolonging the study unnecessarily. However, the trends do offer promise that SPHINX31 would be impactful against retinopathy induced vascular remodelling. The data offered from the iBREC study: exogenous VEGF-A_{165b} protecting against HG-induced permeability, supports this hypothesis as well as the literature (Gammons et al., 2013a; Gammons et al., 2013b). Further work in a longer term model would confirm these thoughts.

6.5 SPHINX31 mechanism of action

Recombinant VEGF-A_{165b} is a promising candidate for the treatment DR, as it has proven benefit, reducing permeability in an *in vivo* DR model and *in vitro* RPE (Ved et al., 2017). However, the half-life is smaller than the current gold standard anti-angiogenic drugs in use whilst the route of administration is the same. Thus, this would necessitate intravitreal injections more frequently than a four-week period, increasing the risk of inflammatory associated effects. Use of SPHINX31 may be advantageous as it is able to reprogram cell expression of a factor promoting DR progression to a protective expression profile. Thus, the VEGF-A_{165b} concentration in the retina will be generated 'in house' so to speak and not from an external source, coupled with a decrease in pro-angiogenic VEGF-A expression. Furthermore, as previously stated, the SPHINX31 route of administration is far more compliant than recombinant VEGF-A_{165b} and associated with less side effects. Although eye-drops would need to be given more frequently than injectables due to decreased permeance and increased clearance, I still believe the benefits of the topical route outweigh the drawbacks, as patients would prefer an eyedrop over an injection.

SPHINX31 has excellent potency for SRPK1 and of the published SRPK1 inhibitors, has the highest specificity for SRPK1. However, it also binds to SRPK2 and CLK-1 at 50-fold less affinity than SRPK1 with an enzyme IC₅₀ of 128nM and 191nM respectively. As such, SRPK2 and CLK-1 could be partially inhibited by SPHINX31 when used at 3µM. SRPK2 is associated with phosphorylation of SRSF2 and not SRSF1 (Wang et al., 1998). However CLK-1 hyperphosphorylates SRSF1 to induce its release from the nuclear speckles (Aubol et al., 2016). Therefore, its inhibition could potentially explain why HG-induced release of SRSF1 from nuclear speckles is ameliorated by SPHINX31 (Chapter 4).

That SPHINX31 did not offer any protective benefit to iBREC permeability (Chapter 5) was intuitively disappointing, as the breakdown of the iBRB is primarily responsible for the vasculopathies associated with the diabetic retina. This suggests that in diabetes, SPHINX31 permeates through the retina to act on RPE cells, triggering a switch in splicing from VEGF-A_{165a} to VEGF-A_{165b}.

Heightened exogenous expression of VEGF-A_{165b} over VEGF-A_{165a} could act upon RECs of the retinal vasculature to protect against disruption to tight junction complexes and thus increase in vascular permeability (Jiang et al., 2020; Ved et al., 2017). This idea is supported from a co-culture of ARPE-19s and RECs, where VEGF expression in ARPE-19 was silenced through interfering RNA resulting in a reduction in REC proliferation (Ma et al., 2011). This highlights the capabilities of RPE to influence REC behavior. I had also aimed to confirm this hypothesis by treating iBRECs with media collected from RPE exposed to HG and SPHINX31, as well as increasing the n number for the current experiments performed for the iBRECs. Furthermore, I would have liked to perform co-culture experiments with iBRECs and another cell type that produces large quantities of VEGF-A, Müller cells. Additionally, the protective effect that SPHINX31 offered against increased retinal thickness in diabetic rats suggests that SPHINX31 does reach and affect RPE function when administered as an eyedrop, especially as I observed evidence of RPE-choroidal separation and probable oedema in diabetic rats untreated with SPHINX31 but not in the SPHINX31 cohort. This notion is supported by topical application of SRPK1 inhibitors reducing choroidal neovascularisation in laser-induced choroidal lesions (Gammons et al., 2013).

A consistent finding throughout this thesis was that VEGF-A_{165b} expression was changed relative to VEGF-A_{165a}, but unchanged when measured directly in RPE (Chapter 3 and 4), corroborating with published findings (Gammons et al., 2013). Whilst the literature agrees that activation of the SRPK1:SRSF1 axis results in proximal splice site selection, this does not necessarily mean that SRPK1 inhibition will induce distal splice site selection. In fact, SRSF6 has been associated with distal splice selection (Nowak et al., 2010). Thus SPHINX31 may be working through impeding proximal splice site selection. However, this effect may be RPE-specific as retinal tissue isolated from SPHINX31-treated diabetic Norway-Browns exhibited increased VEGF-A_{165b} expression (Chapter 5). Challenging this result, Nowak et al., found that VEGF-A_{165b} expression did not change in response to SRPK1 inhibition in laser-induced CNV mouse retinae (Gammons et al., 2013). Retinal tissue includes other VEGF-A secreting cells as well as RPE, including pericytes, astrocytes, Müller cells. The impact

of SPHINX31 has as of yet to be elucidated in these cell types but may offer explanation. However, an important caveat to consider when interpreting results from the VEGF-A isoform ELISA is the α -VEGF-A_{165a} antibody used also binds to VEGF-A_{121a}. VEGF-A₁₂₁ has been detected in human and rat retinae and makes up 24% of the total VEGF-A secretion from RPE (Gerhardinger et al., 1998; Saint-Geniez et al., 2006). VEGF-A₁₂₁ has lower mitogenic potential compared to VEGF-A_{165a}, due to a lower affinity for VEGFR2, thus the phenotypes reported in DR are more likely due to VEGF-A_{165a} expression. Moreover, VEGF-A₁₂₁ is associated with the maintenance of homeostasis of retinal neurones and vessels rather than in a pathological context (Nishijima et al., 2007). Western blots probed with α -VEGF-A_{165a} of RPE lysates treated with SPHINX31 related SRPK1 inhibitors (allowing separation of the isoforms) found significant differences in VEGF-A_{165a} and not VEGF-A₁₂₁ expression (*correspondence with Dr Elizabeth Stewart*).

6.6 Summary

The results from this present thesis highlight the potential of SPHINX31 as a novel treatment for DR and DMO. Through experiments performed, I conclude that SPHINX31 is permeating to the back of the eye and acting upon the RPE cells to increase VEGF-A_{165b} expression relative to VEGF-A_{165a}. VEGF-A_{165b} acts in both an autocrine and paracrine fashion, protecting against DR-induced disruptions to tight-junctions in RPE and REC respectively. The schematic below summarises these ideas, and describes the proposed pathways associated with SRPK1 in DR relevant to this thesis.

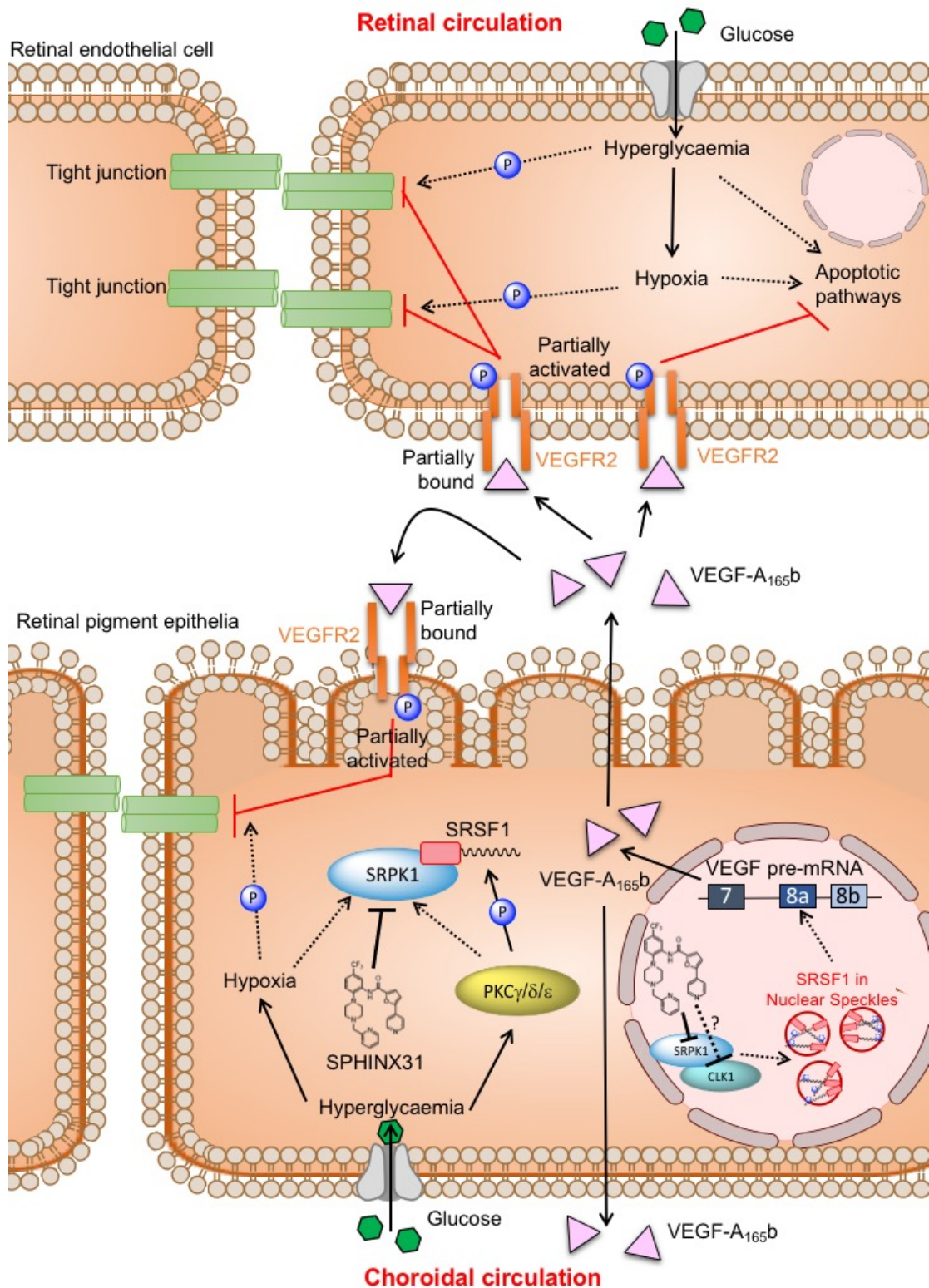


Figure 6: Schematic of proposed mechanism for SPHINX3 in diabetic retinopathy

Increased blood-glucose results in hyperglycemic RPE and REC. Hyperglycaemia activates PKC $\gamma/\delta/\epsilon$ isoforms which in turn activate SRPK1 in RPE. In addition, hyperglycaemia-induced hypoxia also activates SRPK1.

Activation of SRPK1 hypophosphorylates SRSF1, causing a translocation to the nucleus where it accumulates within the nuclear speckles. PKC $\gamma/\delta/\epsilon$ isoforms appear to also induce the nuclear translocation of SRSF1 independently of SRPK1. SRPK1 complexing with CLK-1 in the nucleus hyperphosphorylates SRSF1 inducing its release from the nuclear speckles, where it is able to bind to VEGF pre-mRNA promoting proximal splice site selection and the expression of pro-angiogenic and pro-permeable VEGF-A_{xxx α} isoforms. These isoforms act on VEGFR2, causing a dimerisation and phosphorylation of the receptor to activate downstream pathways resulting in the phosphorylation tight junctions proteins and disrupt the complex, increasing outer blood retinal barrier permeability. In a similar way, hyperglycaemia can result in hypoxia in RECs, triggering expression of VEGF-A_{xxx α} isoforms, activation of VEGFR2, phosphorylation of tight junction proteins and breakdown of the inner blood retinal barrier. Additionally prolonged hyperglycaemia can induce apoptosis of RECs resulting in formation of acellular capillaries. SPHINX31 acts upon RPE to inhibit the activation of SRPK1. Thus the kinase is no longer able to phosphorylate SRSF1 and remains complexed with it in the cytoplasm. Within the nucleus, SPHINX31 inhibits SRPK1 and potentially CLK-1 to block the release of SRSF1 from nuclear speckles. Consequentially, SRSF1 is unable to promote proximal splice site selection and RPE express larger quantities of alternative VEGF isoform VEGF-A_{165b}. This isoform acts in an autocrine manner, binding to VEGFR2 resulting in a partial, transient VEGFR2 phosphorylation. This prevents phosphorylation of tight junction proteins and protects against hyperglycaemia and hypoxia induced breakdown of the outer blood retinal barrier. VEGF-A_{165b} additionally acts in a paracrine manner, on RECs, also binding to VEGFR2 but not activating it. This protects against increases in inner blood retinal barrier permeability and appears to protect against cell death. Dotted arrows = pathways that would be activated if not for SRPK1 inhibition. Black inhibition arrows = inhibition via SPHINX31. Black inhibition dotted arrows = hypothesised inhibition via SPHINX31. Red inhibition arrows = actions caused by VEGF-A_{165b}.

REFERENCES

Abcouwer, S. F. (2013). Angiogenic Factors and Cytokines in Diabetic Retinopathy. *Journal of Clinical & Cellular Immunology*, Suppl 1(11), 1. <https://doi.org/10.4172/2155-9899>

Ablonczy, Z., Dahrouj, M., Tang, P. H., Liu, Y., Sambamurti, K., Marmorstein, A. D., & Crosson, C. E. (2011). Human retinal pigment epithelium cells as functional models for the RPE in vivo. *Investigative Ophthalmology & Visual Science*, 52(12), 8614–8620. <https://doi.org/10.1167/iovs.11-8021>

Adamis, A. P., Shima, D. T., Yeo, K. T., Yeo, T. K., Brown, L. F., Berse, B., Damore, P. A., & Folkman, J. (1993). Synthesis and Secretion of Vascular Permeability Factor/Vascular Endothelial Growth Factor by Human Retinal Pigment Epithelial Cells. *Biochemical and Biophysical Research Communications*, 193(2), 631–638. <https://doi.org/10.1006/bbrc.1993.1671>

Aiello, L P, Avery, R. L., Arrigg, P. G., Keyt, B. A., Jampel, H. D., Shah, S. T., Pasquale, L. R., Thieme, H., Iwamoto, M. A., & Park, J. E. (1995). Vascular Endothelial Growth Factor In Ocular Fluid of Patients with Diabetic Retinopathy and Other Retinal Disorders. *Retina*. <https://doi.org/10.1097/00006982-199515020-00026>

Aiello, L P, Northrup, J. M., Keyt, B. A., Takagi, H., & Iwamoto, M. A. (1995). Hypoxic regulation of vascular endothelial growth factor in retinal cells. *Archives of Ophthalmology*, 113(12), 1538–1544. <https://doi.org/10.1001/archopht.1995.01100120068012>

Aiello, Lloyd Paul. (2002). The potential role of PKC β in diabetic retinopathy and macular edema. *Survey of Ophthalmology*. [https://doi.org/10.1016/S0039-6257\(02\)00391-0](https://doi.org/10.1016/S0039-6257(02)00391-0)

Allen, C., Horton, K., Malhi, N., Batson, J., & Bates, D. (2017). The SRPK1 inhibitor SPHINX31 prevents increased retinal permeability in a rodent model of diabetes. *Acta Ophthalmologica*, 95. <https://doi.org/10.1111/j.1755-3768.2017.0F066>

Allen, C. L., Malhi, N. K., Whatmore, J. D., Bates, D. O., & Arkill, K. P. (2020). Non-invasive measurement of retinal permeability in a diabetic rat model. *Microcirculation*, micc.12623. <https://doi.org/10.1111/micc.12623>

Allen, T. H., & Orahovats, P. D. (1950). COMBINATION OF TOLUIDINE DYE ISOMERS WITH PLASMA ALBUMIN. *American Journal of Physiology-Legacy Content*, 161(3), 473–482. <https://doi.org/10.1152/ajplegacy.1950.161.3.473>

Amin, E. M., Oltean, S., Hua, J., Gammons, M. V. R., Hamdollah-Zadeh, M., Welsh, G. I., Cheung, M. K., Ni, L., Kase, S., Rennel, E. S., Symonds, K. E., Nowak, D. G., Royer-Pokora, B., Saleem, M. A., Hagiwara, M., Schumacher, V. A., Harper, S. J., Hinton, D. R., Bates, D. O., & Lodomery, M. R. (2011). WT1 Mutants Reveal SRPK1 to Be a Downstream Angiogenesis Target by Altering VEGF Splicing. *Cancer Cell*, 20(6), 768–780. <https://doi.org/10.1016/j.ccr.2011.10.016>

Amoaku, W. M., Ghanchi, F., Bailey, C., Banerjee, S., Banerjee, S., Downey, L., Gale, R., Hamilton, R., Khunti, K., Posner, E., Quhill, F., Robinson, S., Setty, R., Sim, D., Varma, D., & Mehta, H. (2020). Diabetic retinopathy and diabetic macular oedema pathways and management: UK Consensus Working Group. *Eye*, 34(S1), 1–51. <https://doi.org/10.1038/s41433-020-0961-6>

Anderson, R. E., Rapp, L. M., & Wiegand, R. D. (1984). Lipid peroxidation and retinal degeneration. *Current Eye Research*, 3(1), 223–227. <https://doi.org/10.3109/02713688408997203>

Antonetti, D A, Barber, A. J., Hollinger, L. A., Wolpert, E. B., & Gardner, T. W. (1999). Vascular endothelial growth factor induces rapid phosphorylation of tight junction proteins occludin and zonula occluden 1. A potential mechanism for vascular permeability in diabetic retinopathy and tumors. *The Journal of Biological Chemistry*, 274(33), 23463–23467. <https://doi.org/10.1074/JBC.274.33.23463>

Antonetti, David A., Klein, R., & Gardner, T. W. (2012). Diabetic Retinopathy. *New England Journal of Medicine*, 366(13), 1227–1239. <https://doi.org/10.1056/NEJMra1005073>

Applied BioPhysics | Quantifying Cell Behavior. (2017). <http://www.biophysics.com/ecis-theory.php>

Archer, D. B., Amoaku, W. M. K., & Gardiner, T. A. (1991). Radiation retinopathy-clinical, histopathological, ultrastructural and experimental correlations. *Eye (Basingstoke)*. <https://doi.org/10.1038/eye.1991.39>

Atkinson, M. A. (2014). Pancreatic biopsies in type 1 diabetes: Revisiting the myth of Pandora's box. In *Diabetologia*. <https://doi.org/10.1007/s00125-013-3159-7>

Aubol, B. E., Plocinik, R. M., Hagopian, J. C., Ma, C.-T., McGlone, M. L., Bandyopadhyay, R., Fu, X.-D., & Adams, J. A. (2013). Partitioning RS domain phosphorylation in an SR protein through the CLK and SRPK protein kinases. *Journal of Molecular Biology*, 425(16), 2894–2909. <https://doi.org/10.1016/j.jmb.2013.05.013>

Aubol, B. E., Wu, G., Keshwani, M. M., Movassat, M., Fattet, L., Hertel, K. J., Fu, X.-D., & Adams, J. A. (2016). Release of SR Proteins from CLK1 by SRPK1: A Symbiotic Kinase System for Phosphorylation Control of Pre-mRNA Splicing. *Molecular Cell*, 63(2), 218–228. <https://doi.org/10.1016/j.molcel.2016.05.034>

Bates, D. O. (2010). Vascular endothelial growth factors and vascular permeability. *Cardiovascular Research*, 87(2), 262–271. <https://doi.org/10.1093/cvr/cvq105>

Bates, D. O., Cui, T.-G., Doughty, J. M., Winkler, M., Sugiono, M., Shields, J. D., Peat, D., Gillatt, D., & Harper, S. J. (2002). VEGF165b, an inhibitory splice variant of vascular endothelial growth factor, is down-regulated in renal cell

carcinoma. *Cancer Research*, 62(14), 4123–4131.
<https://doi.org/10.1038/35025220>

Batson, J., Toop, H. D., Redondo, C., Babaei-Jadidi, R., Chaikuad, A., Wearmouth, S. F., Gibbons, B., Allen, C., Tallant, C., Zhang, J., Du, C., Hancox, J. C., Hawtrey, T., da Rocha, J., Griffith, R., Knapp, S., Bates, D. O., & Morris, J. C. (2017). Development of Potent, Selective SRPK1 Inhibitors as Potential Topical Therapeutics for Neovascular Eye Disease. *ACS Chemical Biology*, 12(3), 825–832. <https://doi.org/10.1021/acscchembio.6b01048>

Beatch, M., Jesaitis, L. A., Gallin, W. J., Goodenough, D. A., & Stevenson, B. R. (1996). The tight junction protein ZO-2 contains three PDZ (PSD-95/Discs-Large/ZO-1) domains and an alternatively spliced region. *The Journal of Biological Chemistry*, 271(42), 25723–25726.
<http://www.ncbi.nlm.nih.gov/pubmed/8824195>

Beaulieu, W. T., Bressler, N. M., Melia, M., Owsley, C., Mein, C. E., Gross, J. G., Jampol, L. M., & Glassman, A. R. (2016). Panretinal Photocoagulation Versus Ranibizumab for Proliferative Diabetic Retinopathy: Patient-Centered Outcomes From a Randomized Clinical Trial. *American Journal of Ophthalmology*. <https://doi.org/10.1016/j.ajo.2016.08.008>

Benson, K., Cramer, S., & Galla, H. J. (2013). Impedance-based cell monitoring: Barrier properties and beyond. In *Fluids and Barriers of the CNS* (Vol. 10, Issue 1). <https://doi.org/10.1186/2045-8118-10-5>

Berkowitz, B. A., Roberts, R., Stemmler, A., Luan, H., & Gadianu, M. (2007). Impaired Apparent Ion Demand in Experimental Diabetic Retinopathy: Correction by Lipoic Acid. *Investigative Ophthalmology & Visual Science*, 48(10), 4753. <https://doi.org/10.1167/iovs.07-0433>

Bettinger, T., Carlisle, R. C., Read, M. L., Ogris, M., & Seymour, L. W. (2001). Peptide-mediated RNA delivery: A novel approach for enhanced transfection of primary and post-mitotic cells. *Nucleic Acids Research*. <https://doi.org/10.1093/nar/29.18.3882>

Bhavsar, A. R., Torres, K., Beck, R. W., Bressler, N. M., Ferris, F. L., Friedman, S. M., Glassman, A. R., Maturi, R. K., Melia, M., Singer, M. A., & Stockdale, C. R. (2013). Randomized clinical trial evaluating intravitreal ranibizumab or saline for vitreous hemorrhage from proliferative diabetic retinopathy. *JAMA Ophthalmology*. <https://doi.org/10.1001/jamaophthalmol.2013.2015>

Bills, V., Salmon, A., Harper, S., Overton, T., Neal, C., Jeffery, B., Soothill, P., & Bates, D. (2011). Impaired vascular permeability regulation caused by the VEGF165b splice variant in pre-eclampsia. *BJOG: An International Journal of Obstetrics & Gynaecology*, 118(10), 1253–1261.
<https://doi.org/10.1111/j.1471-0528.2011.02925.x>

Biselli-Chicote, P. M., Biselli, J. M., Cunha, B. R., Castro, R., Maniglia, J. V., Neto, D. de S., Tajara, E. H., Góis Filho, J. F. de, Fukuyama, E. E., Pavarino, É. C., & Goloni-Bertollo, E. M. (2017). Overexpression of Antiangiogenic

Vascular Endothelial Growth Factor Isoform and Splicing Regulatory Factors in Oral, Laryngeal and Pharyngeal Squamous Cell Carcinomas. *Asian Pacific Journal of Cancer Prevention: APJCP*, 18(8), 2171–2177. <https://doi.org/10.22034/APJCP.2017.18.8.2171>

Blair, N. P., Tso, M. O. M., & Dodge, J. T. (1984). Pathologic studies on the blood-retinal barrier in the spontaneously diabetic BB rat. *Investigative Ophthalmology and Visual Science*.

Bolinger, M. T., & Antonetti, D. A. (2016). Moving past anti-VEGF: Novel therapies for treating diabetic retinopathy. In *International Journal of Molecular Sciences* (Vol. 17, Issue 9). <https://doi.org/10.3390/ijms17091498>

Bowler, E., Porazinski, S., Uzor, S., Thibault, P., Durand, M., Lapointe, E., Rouschop, K. M. A., Hancock, J., Wilson, I., & Ladomery, M. (2018). Hypoxia leads to significant changes in alternative splicing and elevated expression of CLK splice factor kinases in PC3 prostate cancer cells. *BMC Cancer*, 18(1), 355. <https://doi.org/10.1186/s12885-018-4227-7>

Boyer, D. S., Yoon, Y. H., Belfort, R., Bandello, F., Maturi, R. K., Augustin, A. J., Li, X. Y., Cui, H., Hashad, Y., & Whitcup, S. M. (2014). Three-year, randomized, sham-controlled trial of dexamethasone intravitreal implant in patients with diabetic macular edema. *Ophthalmology*. <https://doi.org/10.1016/j.ophtha.2014.04.024>

Brown, W. R. (2010). A review of string vessels or collapsed, empty basement membrane tubes. *Journal of Alzheimer's Disease: JAD*, 21(3), 725–739. <https://doi.org/10.3233/JAD-2010-100219>

Brownlee, M. (2001). Biochemistry and molecular cell biology of diabetic complications. *Nature*, 414(6865), 813–820. <https://doi.org/10.1038/414813a>

Brownlee, M. (2005). The pathobiology of diabetic complications: A unifying mechanism. *Diabetes*. <https://doi.org/10.2337/diabetes.54.6.1615>

Bunag, R. D., Tomita, T., & Sasaki, S. (1982). Streptozotocin diabetic rats are hypertensive despite reduced hypothalamic responsiveness. *Hypertension*. <https://doi.org/10.1161/01.HYP.4.4.556>

Cai, J., & Boulton, M. (2002). The pathogenesis of diabetic retinopathy: old concepts and new questions. *Eye*, 16(3), 242–260. <https://doi.org/10.1038/sj.eye.6700133>

Caldwell, R. B., Bartoli, M., Behzadian, M. A., El-Remessy, A. E. B., Al-Shabraway, M., Platt, D. H., & Caldwell, R. W. (2003). Vascular endothelial growth factor and diabetic retinopathy: pathophysiological mechanisms and treatment perspectives. *Diabetes/Metabolism Research and Reviews*, 19(6), 442–455. <https://doi.org/10.1002/dmrr.415>

Campochiaro, P. A., Aiello, L. P., & Rosenfeld, P. J. (2016). Anti-Vascular Endothelial Growth Factor Agents in the Treatment of Retinal Disease.

Campochiaro, P. A., Brown, D. M., Pearson, A., Chen, S., Boyer, D., Ruiz-Moreno, J., Garretson, B., Gupta, A., Hariprasad, S. M., Bailey, C., Reichel, E., Soubrane, G., Kapik, B., Billman, K., Kane, F. E., & Green, K. (2012). Sustained delivery fluocinolone acetonide vitreous inserts provide benefit for at least 3 years in patients with diabetic macular edema. *Ophthalmology*. <https://doi.org/10.1016/j.ophtha.2012.04.030>

Cao, L., Liu, J., Pu, J., Milne, G., Chen, M., Xu, H., Shipley, A., Forrester, J. v, McCaig, C. D., & Lois, N. (2018). Polarized retinal pigment epithelium generates electrical signals that diminish with age and regulate retinal pathology. *Journal of Cellular and Molecular Medicine*, 22(11), 5552–5564. <https://doi.org/10.1111/jcmm.13829>

Caprnda, M., Kubatka, P., Saxena, S., Valaskova, J., Stefanickova, J., Kobyljak, N., Zulli, A., & Kruzliak, P. (2017). The Impact of Hyperglycemia on VEGF Secretion in Retinal Endothelial Cells. *Folia Medica I Folia Medica*, 5959(22), 183–189. <https://doi.org/10.1515/folmed-2017-0029>

Cébe Suarez, S., Pieren, M., Cariolato, L., Arn, S., Hoffmann, U., Bogucki, A., Manlius, C., Wood, J., & Ballmer-Hofer, K. (2006). A VEGF-A splice variant defective for heparan sulfate and neuropilin-1 binding shows attenuated signaling through VEGFR-2. *Cellular and Molecular Life Sciences*, 63(17), 2067–2077. <https://doi.org/10.1007/s00018-006-6254-9>

Chauhan, D. S., & Marshall, J. (1999). The interpretation of optical coherence tomography images of the retina. *Investigative Ophthalmology and Visual Science*.

Chen, X. L., Nam, J. O., Jean, C., Lawson, C., Walsh, C. T., Goka, E., Lim, S. T., Tomar, A., Tancioni, I., Uryu, S., Guan, J. L., Acevedo, L. M., Weis, S. M., Cheresh, D. A., & Schlaepfer, D. D. (2012). VEGF-Induced Vascular Permeability Is Mediated by FAK. *Developmental Cell*, 22(1), 146–157. <https://doi.org/10.1016/j.devcel.2011.11.002>

Cheung, N., Mitchell, P., & Wong, T. Y. (2010). Diabetic retinopathy. *The Lancet*, 376(9735), 124–136. [https://doi.org/10.1016/S0140-6736\(09\)62124-3](https://doi.org/10.1016/S0140-6736(09)62124-3)

Choi, Y. K., Kim, J. H., Kim, W. J., Lee, H. Y., Park, J. A., Lee, S.-W., Yoon, D.-K., Kim, H. H., Chung, H., Yu, Y. S., & Kim, K.-W. (2007). AKAP12 Regulates Human Blood-Retinal Barrier Formation by Downregulation of Hypoxia-Inducible Factor-1. *Journal of Neuroscience*, 27(16), 4472–4481. <https://doi.org/10.1523/JNEUROSCI.5368-06.2007>

Colwill, K., Pawson, T., Andrews, B., Prasad, J., Manley, J. L., Bell, J. C., & Duncan, P. I. (1996). The Clk/Sty protein kinase phosphorylates SR splicing factors and regulates their intranuclear distribution. *The EMBO Journal*, 15(2), 265–275. <https://doi.org/10.1002/j.1460-2075.1996.tb00357.x>

- Corada, M., Zanetta, L., Orsenigo, F., Breviario, F., Lampugnani, M. G., Bernasconi, S., Liao, F., Hicklin, D. J., Bohlen, P., & Dejana, E. (2002). A monoclonal antibody to vascular endothelial-cadherin inhibits tumor angiogenesis without side effects on endothelial permeability. *Blood*, 100(3), 905–911. <https://doi.org/10.1182/blood.V100.3.905>
- Coucha, M., Elshaer, S. L., Eldahshan, W. S., Mysona, B. A., & El-Remessy, A. B. (2015). Molecular Mechanisms of Diabetic Retinopathy: Potential Therapeutic Targets. *Middle East African Journal of Ophthalmology*, 22(2), 135. <https://doi.org/10.4103/0974-9233.154386>
- Coughlin, B. A., Feenstra, D. J., & Mohr, S. (2017). Müller cells and diabetic retinopathy. *Vision research*, 139, 93–100. <https://doi.org/10.1016/j.visres.2017.03.013>
- Crane, I. J., Wallace, C. A., Mckillop-Smith, S., & Forrester, J. v. (2000). Control of chemokine production at the blood-retina barrier. *Immunology*. <https://doi.org/10.1046/j.0019-2805.2000.01105.x>
- Crawford, T., Alfaro III, D., Kerrison, J., & Jablon, E. (2009). Diabetic Retinopathy and Angiogenesis. *Current Diabetes Reviews*, 5(1), 8–13. <https://doi.org/10.2174/157339909787314149>
- Cunha-Vaz, José. (1979). The blood-ocular barriers. In *Survey of Ophthalmology*. [https://doi.org/10.1016/0039-6257\(79\)90158-9](https://doi.org/10.1016/0039-6257(79)90158-9)
- Cunha-Vaz, Jose, & Maurice, D. (1969). Fluorescein dynamics in the eye. *Documenta Ophthalmologica*. <https://doi.org/10.1007/BF00943962>
- Curcio, C. A., Zanzottera, E. C., Ach, T., Balaratnasingam, C., & Freund, K. B. (2017). Activated Retinal Pigment Epithelium, an Optical Coherence Tomography Biomarker for Progression in Age-Related Macular Degeneration. *Investigative Ophthalmology & Visual Science*, 58(6), BIO211–BIO226. <https://doi.org/10.1167/iovs.17-21872>
- Curtis, T. M., Gardiner, T. A., & Stitt, A. W. (2009). Microvascular lesions of diabetic retinopathy: clues towards understanding pathogenesis? *Eye*, 23(7), 1496–1508. <https://doi.org/10.1038/eye.2009.108>
- Cutler, R. G. (2005). Oxidative stress profiling: Part I. Its potential importance in the optimization of human health. *Annals of the New York Academy of Sciences*. <https://doi.org/10.1196/annals.1323.027>
- das Evcimen, N., & King, G. L. (2007). The role of protein kinase C activation and the vascular complications of diabetes. *Pharmacological Research*, 55(6), 498–510. <https://doi.org/10.1016/J.PHRS.2007.04.016>
- Das, S., Anczuków, O., Akerman, M., & Krainer, A. R. (2012). Oncogenic Splicing Factor SRSF1 Is a Critical Transcriptional Target of MYC. *Cell Reports*, 1(2), 110–117. <https://doi.org/10.1016/j.celrep.2011.12.001>

- de Cogan, F., Hill, L. J., Lynch, A., Morgan-Warren, P. J., Lechner, J., Berwick, M. R., Peacock, A. F. A., Chen, M., Scott, R. A. H., Xu, H., & Logan, A. (2017). Topical Delivery of Anti-VEGF Drugs to the Ocular Posterior Segment Using Cell-Penetrating Peptides. *Investigative Ophthalmology & Visual Science*, 58(5), 2578. <https://doi.org/10.1167/iovs.16-20072>
- Decanini, A., Karunadharm, P. R., Nordgaard, C. L., Feng, X., Olsen, T. W., & Ferrington, D. A. (2008). Human retinal pigment epithelium proteome changes in early diabetes. *Diabetologia*, 51(6), 1051–1061. <https://doi.org/10.1007/s00125-008-0991-2>
- DeFronzo, R. A., Ferrannini, E., Groop, L., Henry, R. R., Herman, W. H., Holst, J. J., Hu, F. B., Kahn, C. R., Raz, I., Shulman, G. I., Simonson, D. C., Testa, M. A., & Weiss, R. (2015). Type 2 diabetes mellitus. *Nature Reviews Disease Primers*, 1. <https://doi.org/10.1038/nrdp.2015.19>
- Deissler, H., Deissler, H., Lang, S., & Lang, G. E. (2008). VEGF-induced effects on proliferation, migration and tight junctions are restored by ranibizumab (Lucentis) in microvascular retinal endothelial cells. *British Journal of Ophthalmology*. <https://doi.org/10.1136/bjo.2007.135640>
- Deissler, H. L., Deissler, H., & Lang, G. E. (2010). Inhibition of protein kinase C is not sufficient to prevent or reverse effects of VEGF165 on claudin-1 and permeability in microvascular retinal endothelial cells. *Investigative Ophthalmology and Visual Science*. <https://doi.org/10.1167/iovs.09-3917>
- Deissler, H. L., Deissler, H., & Lang, G. E. (2011). Inhibition of vascular endothelial growth factor (VEGF) is sufficient to completely restore barrier malfunction induced by growth factors in microvascular retinal endothelial cells. *British Journal of Ophthalmology*. <https://doi.org/10.1136/bjo.2010.192229>
- Deissler, H. L., Deissler, H., Lang, G. K., & Lang, G. E. (2013). VEGF but not PIGF disturbs the barrier of retinal endothelial cells. *Experimental Eye Research*. <https://doi.org/10.1016/j.exer.2013.07.018>
- Deissler, H. L., Lang, G. K., & Lang, G. E. (2019). Fate of the Fc fusion protein aflibercept in retinal endothelial cells: competition of recycling and degradation. *Graefe's Archive for Clinical and Experimental Ophthalmology = Albrecht von Graefes Archiv Fur Klinische Und Experimentelle Ophthalmologie*, 257(1), 83–94. <https://doi.org/10.1007/s00417-018-4166-7>
- Deissler, Heidrun, Deissler, H., Lang, G. K., & Lang, G. E. (2005). Generation and characterization of iBREC: novel hTERT-immortalized bovine retinal endothelial cells. *International Journal of Molecular Medicine*. <https://doi.org/10.3892/ijmm.16.1.65>
- Deissler, Heidrun, Deissler, H., Lang, G. K., & Lang, G. E. (2006). TGFbeta induces transdifferentiation of iBREC to alphaSMA-expressing cells. *International Journal of Molecular Medicine*.

Dejana, E. (2004). Endothelial cell–cell junctions: happy together. *Nature Reviews Molecular Cell Biology*, 5(4), 261–270. <https://doi.org/10.1038/nrm1357>

Desjardins, D. M., Yates, P. W., Dahrouj, M., Liu, Y., Crosson, C. E., & Ablonczy, Z. (2016). Progressive Early Breakdown of Retinal Pigment Epithelium Function in Hyperglycemic Rats. *Investigative Ophthalmology & Visual Science*, 57(6), 2706. <https://doi.org/10.1167/IOVS.15-18397>

Devendra, D., Liu, E., & Eisenbarth, G. S. (2004). Clinical review Type 1 diabetes: recent developments. *British Medical Journal*. <https://doi.org/10.1136/bmj.328.7442.750>

Diabetic Retinopathy Clinical Research Network, Browning, D. J., Glassman, A. R., Aiello, L. P., Beck, R. W., Brown, D. M., Fong, D. S., Bressler, N. M., Danis, R. P., Kinyoun, J. L., Nguyen, Q. D., Bhavsar, A. R., Gottlieb, J., Pieramici, D. J., Rauser, M. E., Apte, R. S., Lim, J. I., & Miskala, P. H. (2007). Relationship between Optical Coherence Tomography–Measured Central Retinal Thickness and Visual Acuity in Diabetic Macular Edema. *Ophthalmology*, 114(3), 525–536. <https://doi.org/10.1016/j.ophtha.2006.06.052>

Dolgin, E. (2017). The most popular genes in the human genome. *Nature*, 551(7681), 427–431. <https://doi.org/10.1038/d41586-017-07291-9>

Donath, M. Y., & Shoelson, S. E. (2011). Type 2 diabetes as an inflammatory disease. In *Nature Reviews Immunology*. <https://doi.org/10.1038/nri2925>

Dong, N., Li, X., Xiao, L., Yu, W., Wang, B., & Chu, L. (2012). Upregulation of retinal neuronal MCP-1 in the rodent model of diabetic retinopathy and its function in vitro. *Investigative Ophthalmology and Visual Science*. <https://doi.org/10.1167/iovs.12-9446>

Donnelly, R., Idris, I., & Forrester, J. v. (2004). Protein kinase C inhibition and diabetic retinopathy: a shot in the dark at translational research. *The British Journal of Ophthalmology*, 88(1), 145. <https://doi.org/10.1136/BJO.88.1.145>

Duan, H., Huang, J., Li, W., & Tang, M. (2013). Protective Effects of Fufang Xueshuantong on Diabetic Retinopathy in Rats. *Evidence-Based Complementary and Alternative Medicine*, 2013, 1–9. <https://doi.org/10.1155/2013/408268>

Duh, E. J., Sun, J. K., & Stitt, A. W. (2017). Diabetic retinopathy: current understanding, mechanisms, and treatment strategies. *JCI Insight*, 2(14). <https://doi.org/10.1172/jci.insight.93751>

Duke-Elder, S. (1956). Biochemistry of the Eye. In *Bmj* (Vol. 2, Issue 4989). <https://doi.org/10.1136/bmj.2.4989.405>

Eichler W, Yafai Y, Keller T, Wiedemann P, Reichenbach A (2004). PEDF derived from glial Müller cells: a possible regulator of retinal angiogenesis. *Exp Cell Res*, 299(1):68-78.

Eliceiri, B. P., Paul, R., Schwartzberg, P. L., Hood, J. D., Leng, J., & Cheresh, D. A. (1999). Selective requirement for Src kinases during VEGF-induced angiogenesis and vascular permeability. *Molecular Cell*, 4(6), 915–924. [https://doi.org/10.1016/S1097-2765\(00\)80221-X](https://doi.org/10.1016/S1097-2765(00)80221-X)

El-Remessy, A. B., Franklin, T., Ghaley, N., Yang, J., Brands, M. W., Caldwell, R. B., & Behzadian, M. A. (2013). Diabetes-induced superoxide anion and breakdown of the blood-retinal barrier: role of the VEGF/uPAR pathway. *PLoS One*, 8(8), e71868. <https://doi.org/10.1371/journal.pone.0071868>

Engerman, R., Bloodworth, J. M. B., & Nelson, S. (1977). Relationship of Microvascular Disease in Diabetes to Metabolic Control. *Diabetes*, 26(8), 760–769. <https://doi.org/10.2337/diab.26.8.760>

Engerman, R. L., & Kern, T. S. (1984). Experimental galactosemia produces diabetic-like retinopathy. *Diabetes*. <https://doi.org/10.2337/diabetes.33.1.97>

Eshaq, R. S., & Harris, N. R. (2020). Hyperglycemia-induced ubiquitination and degradation of β -catenin with the loss of platelet endothelial cell adhesion molecule-1 in retinal endothelial cells. *Microcirculation*, 27(2). <https://doi.org/10.1111/micc.12596>

Ezzati, M. (2016). Worldwide trends in diabetes since 1980: A pooled analysis of 751 population-based studies with 4??4 million participants. *The Lancet*, 387(10027), 1513–1530. [https://doi.org/10.1016/S0140-6736\(16\)00618-8](https://doi.org/10.1016/S0140-6736(16)00618-8)

Farnoodian, M., Halbach, C., Slinger, C., Pattnaik, B. R., Sorenson, C. M., & Sheibani, N. (2016). High glucose promotes the migration of retinal pigment epithelial cells through increased oxidative stress and PEDF expression. *American Journal of Physiology. Cell Physiology*, 311(3), C418-36. <https://doi.org/10.1152/ajpcell.00001.2016>

Ferguson, F. M., & Gray, N. S. (2018). Kinase inhibitors: the road ahead. *Nature Reviews Drug Discovery*, 17(5), 353–377. <https://doi.org/10.1038/nrd.2018.21>

Ferrara, N., & Henzel, W. J. (1989). Pituitary follicular cells secrete a novel heparin-binding growth factor specific for vascular endothelial cells. *Biochemical and Biophysical Research Communications*, 161(2), 851–858. [https://doi.org/10.1016/0006-291x\(89\)92678-8](https://doi.org/10.1016/0006-291x(89)92678-8)

Ferrara, Napoleone, Gerber, H. P., & LeCouter, J. (2003). The biology of VEGF and its receptors. In *Nature Medicine* (Vol. 9, Issue 6, pp. 669–676). <https://doi.org/10.1038/nm0603-669>

Flaxman SR, Bourne RRA, Resnikoff S, Ackland P, Braithwaite T, Cicinelli MV, Das A, Jonas JB, Keeffe J, Kempen JH, Leasher J, Limburg H, Naidoo K, Pesudovs K, Silvester A, Stevens GA, Tahhan N, Wong TY, Taylor HR, Vision Loss Expert Group of the Global Burden of Disease Study. Global causes of blindness and distance vision impairment 1990-2020: a systematic review and meta-analysis. *Lancet Glob Health*. 2017 Dec; 5(12):e1221-e1234

Ford, K. M., Saint-Geniez, M., Walshe, T., Zahr, A., & D'Amore, P. A. (2011). Expression and Role of VEGF in the Adult Retinal Pigment Epithelium. *Investigative Ophthalmology & Visual Science*, 52(13), 9478. <https://doi.org/10.1167/iovs.11-8353>

Fukuhara, T., Hosoya, T., Shimizu, S., Sumi, K., Oshiro, T., Yoshinaka, Y., Suzuki, M., Yamamoto, N., Herzenberg, L. A., Herzenberg, L. A., & Hagiwara, M. (2006). Utilization of host SR protein kinases and RNA-splicing machinery during viral replication. *Proceedings of the National Academy of Sciences of the United States of America*. <https://doi.org/10.1073/pnas.0604616103>

G. Obrosova, I., & F. Kador, P. (2011). Aldose Reductase / Polyol Inhibitors for Diabetic Retinopathy. *Current Pharmaceutical Biotechnology*. <https://doi.org/10.2174/138920111794480642>

Gammons, M. V. R., Dick, A. D., Harper, S. J., & Bates, D. O. (2013). SRPK1 inhibition modulates VEGF splicing to reduce pathological neovascularization in a rat model of retinopathy of prematurity. *Investigative Ophthalmology and Visual Science*, 54(8), 5797–5806. <https://doi.org/10.1167/iovs.13-11634>

Gammons, M v, Lucas, R., Dean, R., Coupland, S. E., Oltean, S., & Bates, D. O. (2014). Targeting SRPK1 to control VEGF-mediated tumour angiogenesis in metastatic melanoma. *British Journal of Cancer*, 111(3), 477–485. <https://doi.org/10.1038/bjc.2014.342>

Gammons, Melissa v., Fedorov, O., Ivison, D., Du, C., Clark, T., Hopkins, C., Hagiwara, M., Dick, A. D., Cox, R., Harper, S. J., Hancox, J. C., Knapp, S., & Bates, D. O. (2013). Topical antiangiogenic SRPK1 inhibitors reduce choroidal neovascularization in rodent models of exudative AMD. *Investigative Ophthalmology and Visual Science*, 54(9), 6052–6062. <https://doi.org/10.1167/iovs.13-12422>

Gammons, Melissa v., Hagiwara, M., Dick, A. D., & Bates, D. O. (2011). SRPK1/2 Inhibition, By SRPIN340, As A Novel Therapeutic To Control VEGF Mediated Choroidal Neovascularisation. *Investigative Ophthalmology & Visual Science*, 52(14), 5928–5928. <https://iovs.arvojournals.org/article.aspx?articleid=2358379>

Ganta, V. C., Choi, M., Kutateladze, A., & Annex, B. H. (2017). VEGF 165 b Modulates Endothelial VEGFR1-STAT3 Signaling Pathway and Angiogenesis in Human and Experimental Peripheral Arterial Disease. *Circulation Research*, 120(2), 282–295. <https://doi.org/10.1161/CIRCRESAHA.116.309516>

Gardner, T. W., Abcouwer, S. F., Barber, A. J., & Jackson, G. R. (2011). An integrated approach to diabetic retinopathy research. *Archives of Ophthalmology* (Chicago, Ill. : 1960). <https://doi.org/10.1001/archophthalmol.2010.362>

Gass, J. D. M., Sever, R. J., Sparks, D., & Goren, J. (1967). A Combined Technique of Fluorescein Funduscopy and Angiography of the Eye. *Archives*

of Ophthalmology, 78(4), 455–461.
<https://doi.org/10.1001/archopht.1967.00980030457009>

Gaudana, R., Ananthula, H. K., Parenky, A., & Mitra, A. K. (2010). Ocular Drug Delivery. *The AAPS Journal*, 12(3), 348. <https://doi.org/10.1208/S12248-010-9183-3>

Geraldes, P., Hiraoka-Yamamoto, J., Matsumoto, M., Clermont, A., Leitges, M., Marette, A., Aiello, L. P., Kern, T. S., & King, G. L. (2009). Activation of PKC- δ and SHP-1 by hyperglycemia causes vascular cell apoptosis and diabetic retinopathy. *Nature Medicine*, 15(11), 1298–1306. <https://doi.org/10.1038/nm.2052>

Gerber, H. P., Condorelli, F., Park, J., & Ferrara, N. (1997). Differential transcriptional regulation of the two vascular endothelial growth factor receptor genes. Flt-1, but not Flk-1/KDR, is up-regulated by hypoxia. *The Journal of Biological Chemistry*, 272(38), 23659–23667. <https://doi.org/10.1074/jbc.272.38.23659>

Gerhardinger, C., Brown, L. F., Roy, S., Mizutani, M., Zucker, C. L., & Lorenzi, M. (1998). Expression of vascular endothelial growth factor in the human retina and in nonproliferative diabetic retinopathy. *The American Journal of Pathology*, 152(6), 1453–1462. <http://www.ncbi.nlm.nih.gov/pubmed/9626050>

Ghasemi Falavarjani, K., & Nguyen, Q. D. (2013). Adverse events and complications associated with intravitreal injection of anti-VEGF agents: a review of literature. *Eye*, 27(7), 787–794. <https://doi.org/10.1038/eye.2013.107>

Giannakouros, T., Nikolakaki, E., Mylonis, I., & Georgatsou, E. (2011). Serine-arginine protein kinases: a small protein kinase family with a large cellular presence. *FEBS Journal*, 278(4), 570–586. <https://doi.org/10.1111/j.1742-4658.2010.07987.x>

Gillies, M. C., Su, T., Stayt, J., Simpson, J. M., Naidoo, D., & Salonikas, C. (1997). Effect of high glucose on permeability of retinal capillary endothelium in vitro. *Investigative Ophthalmology and Visual Science*.

Gologorsky, D., Thanos, A., & Vavvas, D. (2012). Therapeutic interventions against inflammatory and angiogenic mediators in proliferative diabetic retinopathy. *Mediators of Inflammation*, 2012, 629452. <https://doi.org/10.1155/2012/629452>

Gonçalves, V., Henriques, A. F. A., Henriques, A., Pereira, J. F. S., Pereira, J., Neves Costa, A., Moyer, M. P., Moita, L. F., Gama-Carvalho, M., Matos, P., & Jordan, P. (2014). Phosphorylation of SRSF1 by SRPK1 regulates alternative splicing of tumor-related Rac1b in colorectal cells. *RNA (New York, N.Y.)*, 20(4), 474–482. <https://doi.org/10.1261/rna.041376.113>

Gonçalves, V., & Jordan, P. (2015). Posttranscriptional regulation of splicing factor SRSF1 and its role in cancer cell biology. In *BioMed Research International* (Vol. 2015). <https://doi.org/10.1155/2015/287048>

Grimes, P. A., & Laties, A. M. (1980). Early morphological alteration of the pigment epithelium in streptozotocin-induced diabetes: Increased surface area of the basal cell membrane. *Experimental Eye Research*, 30(6), 631–639. [https://doi.org/10.1016/0014-4835\(80\)90062-7](https://doi.org/10.1016/0014-4835(80)90062-7)

Gross, J. G., Glassman, A. R., Liu, D., Sun, J. K., Antoszyk, A. N., Baker, C. W., Bressler, N. M., Elman, M. J., Ferris, F. L., Gardner, T. W., Jampol, L. M., Martin, D. F., Melia, M., Stockdale, C. R., & Beck, R. W. (2018). Five-Year Outcomes of Panretinal Photocoagulation vs Intravitreal Ranibizumab for Proliferative Diabetic Retinopathy: A Randomized Clinical Trial. *JAMA Ophthalmology*. <https://doi.org/10.1001/jamaophthalmol.2018.3255>

Gui, J.-F., Lane, W. S., & Fu, X.-D. (1994). A serine kinase regulates intracellular localization of splicing factors in the cell cycle. *Nature*, 369(6482), 678–682. <https://doi.org/10.1038/369678a0>

Gupta, N. (2013). Diabetic Retinopathy and VEGF. *The Open Ophthalmology Journal*. <https://doi.org/10.2174/1874364101307010004>

Gurel, Z., Sieg, K. M., Shallow, K. D., Sorenson, C. M., & Sheibani, N. (2013). Retinal O-linked N-acetylglucosamine protein modifications: implications for postnatal retinal vascularization and the pathogenesis of diabetic retinopathy. *Molecular Vision*, 19, 1047. <https://www.ncbi.nlm.nih.gov/pmc/articles/PMC3668662/>

Gurel, Z., Zaro, B. W., Pratt, M. R., & Sheibani, N. (2014). Identification of O-GlcNAc Modification Targets in Mouse Retinal Pericytes: Implication of p53 in Pathogenesis of Diabetic Retinopathy. *PLoS ONE*, 9(5). <https://doi.org/10.1371/JOURNAL.PONE.0095561>

Hall, L. L., Smith, K. P., Byron, M., & Lawrence, J. B. (2006). Molecular anatomy of a speckle. *The Anatomical Record. Part A, Discoveries in Molecular, Cellular, and Evolutionary Biology*, 288(7), 664–675. <https://doi.org/10.1002/ar.a.20336>

Hammes, H. P., Alt, A., Niwa, T., Clausen, J. T., Bretzel, R. G., Brownlee, M., & Schleicher, E. D. (1999). Differential accumulation of advanced glycation end products in the course of diabetic retinopathy. *Diabetologia*. <https://doi.org/10.1007/s001250051221>

Hammes, Hans Peter, Lin, J., Wagner, P., Feng, Y., vom Hagen, F., Krzizok, T., Renner, O., Breier, G., Brownlee, M., & Deutsch, U. (2004). Angiopoietin-2 Causes Pericyte Dropout in the Normal Retina: Evidence for Involvement in Diabetic Retinopathy. *Diabetes*. <https://doi.org/10.2337/diabetes.53.4.1104>

Harhaj, N. S., & Antonetti, D. A. (2004). Regulation of tight junctions and loss of barrier function in pathophysiology. *The International Journal of Biochemistry & Cell Biology*, 36(7), 1206–1237. <https://doi.org/10.1016/j.biocel.2003.08.007>

Harhaj, N. S., Felinski, E. A., Wolpert, E. B., Sundstrom, J. M., Gardner, T. W., & Antonetti, D. A. (2006). VEGF activation of protein kinase C stimulates occludin phosphorylation and contributes to endothelial permeability.

Harper, S. J., & Bates, D. O. (2008). VEGF-A splicing: the key to anti-angiogenic therapeutics? *Nature Reviews. Cancer*, 8(11), 880–887. <https://doi.org/10.1038/nrc2505>

He, J., Wang, H., Liu, Y., Li, W., Kim, D., & Huang, H. (2015). Blockade of vascular endothelial growth factor receptor 1 prevents inflammation and vascular leakage in diabetic retinopathy. *Journal of Ophthalmology*, 2015. <https://doi.org/10.1155/2015/605946>

Hee, M. R., Puliafito, C. A., Duker, J. S., Reichel, E., Coker, J. G., Wilkins, J. R., Schuman, J. S., Swanson, E. A., & Fujimoto, J. G. (1998). Topography of diabetic macular edema with optical coherence tomography. *Ophthalmology*. [https://doi.org/10.1016/S0161-6420\(98\)93601-6](https://doi.org/10.1016/S0161-6420(98)93601-6)

Hosoya, K., & Tachikawa, M. (2013). *The Inner Blood-Retinal Barrier* (pp. 85–104). Springer, New York, NY. https://doi.org/10.1007/978-1-4614-4711-5_4

Hu, D. L., Yu, Y. X., Liang, R., Zhou, S. Y., Duan, S. L., Jiang, Z. Y., Meng, C. Y., Jiang, W., Wang, H., Sun, Y. X., & Fang, L. S. (2019). Regulation of hypoxia inducible factor-1 α on permeability of vascular endothelial cells and the mechanism. *Chinese Journal of Burns*, 35(3), 209–217. <https://doi.org/10.3760/cma.j.issn.1009-2587.2019.03.009>

Hu, Z.-Y., Wang, X.-Y., Guo, W.-B., Xie, L.-Y., Huang, Y.-Q., Liu, Y.-P., Xiao, L.-W., Li, S.-N., Zhu, H.-F., Li, Z.-G., & Kan, H. (2016). Long non-coding RNA MALAT1 increases AKAP-9 expression by promoting SRPK1-catalyzed SRSF1 phosphorylation in colorectal cancer cells. *Oncotarget*, 7(10), 11733–11743. <https://doi.org/10.18632/oncotarget.7367>

Hua, J., Spee, C., Kase, S., Rennel, E. S., Magnussen, A. L., Qiu, Y., Varey, A., Dhayade, S., Churchill, A. J., Harper, S. J., Bates, D. O., & Hinton, D. R. (2010). Recombinant human vegf165b inhibits experimental choroidal neovascularization. *Investigative Ophthalmology and Visual Science*, 51(8), 4282–4288. <https://doi.org/10.1167/iovs.09-4360>

Idris, I., Gray, S., & Donnelly, R. (2001). Protein kinase C activation: isozyme-specific effects on metabolism and cardiovascular complications in diabetes. *Diabetologia*, 44(6), 659–673. <https://doi.org/10.1007/s001250051675>

Itoh, M., Furuse, M., Morita, K., Kubota, K., Saitou, M., & Tsukita, S. (1999). Direct binding of three tight junction-associated MAGUKs, ZO-1, ZO-2, and ZO-3, with the COOH termini of claudins. *The Journal of Cell Biology*, 147(6), 1351–1363. <http://www.ncbi.nlm.nih.gov/pubmed/10601346>

Jiang, F., Chong, L., Du, S., Duan, Y., Wang, Y., Wang, J., Chen, S., & He, T. (2020). Decreased Ratio of VEGF165b/VEGF in Aqueous Humor Predicts Progression of Diabetic Retinopathy. *Ophthalmic Research*. <https://doi.org/10.1159/000508250>

- Jiao, W., Ji, J.-F., Xu, W., Bu, W., Zheng, Y., Ma, A., Zhao, B., & Fan, Q. (2019). Distinct downstream signaling and the roles of VEGF and PlGF in high glucose-mediated injuries of human retinal endothelial cells in culture. *Scientific Reports*, 9(1), 15339. <https://doi.org/10.1038/s41598-019-51603-0>
- Joussen, A. M., Poulaki, V., Le, M. L., Koizumi, K., Esser, C., Janicki, H., Schraermeyer, U., Kociok, N., Fauser, S., Kirchhof, B., Kern, T. S., & Adamis, A. P. (2004). A central role for inflammation in the pathogenesis of diabetic retinopathy. *The FASEB Journal*. <https://doi.org/10.1096/fj.03-1476fje>
- Junod, A., Lambert, A. E., Orci, L., Pictet, R., Gonet, A. E., & Renold, A. E. (1967). Studies of the Diabetogenic Action of Streptozotocin. *Proceedings of the Society for Experimental Biology and Medicine*. <https://doi.org/10.3181/00379727-126-32401>
- Kador, P. F., Akagi, Y., Takahashi, Y., Ikebe, H., Wyman, M., & Kinoshita, J. H. (1990). Prevention of Retinal Vessel Changes Associated With Diabetic Retinopathy in Galactose-Fed Dogs by Aldose Reductase Inhibitors. *Archives of Ophthalmology*. <https://doi.org/10.1001/archopht.1990.01070110117035>
- Kaiser, N., Sasson, S., Feener, E. P., Boukobza-Vardi, N., Higashi, S., Moller, D. E., Davidheiser, S., Przybylski, R. J., & King, G. L. (1993). Differential Regulation of Glucose Transport and Transporters by Glucose in Vascular Endothelial and Smooth Muscle Cells. *Diabetes*, 42(1), 80–89. <https://doi.org/10.2337/DIAB.42.1.80>
- Kandarakis, S. A., Piperi, C., Topouzis, F., & Papavassiliou, A. G. (2014). Emerging role of advanced glycation-end products (AGEs) in the pathobiology of eye diseases. In *Progress in Retinal and Eye Research*. <https://doi.org/10.1016/j.preteyeres.2014.05.002>
- Kaneto, H., Suzuma, K., Sharma, A., Bonner-Weir, S., King, G. L., & Weir, G. C. (2002). Involvement of Protein Kinase C β 2 in c-myc Induction by High Glucose in Pancreatic β -Cells. *Journal of Biological Chemistry*, 277(5), 3680–3685. <https://doi.org/10.1074/JBC.M109647200>
- Kang, M.-K., Lee, E.-J., Kim, Y.-H., Kim, D. Y., Oh, H., Kim, S.-I., & Kang, Y.-H. (2018). Chrysin Ameliorates Malfunction of Retinoid Visual Cycle through Blocking Activation of AGE-RAGE-ER Stress in Glucose-Stimulated Retinal Pigment Epithelial Cells and Diabetic Eyes. *Nutrients*, 10(8). <https://doi.org/10.3390/nu10081046>
- Kannan, R., Zhang, N., Sreekumar, P. G., Spee, C. K., Rodriguez, A., Barron, E., & Hinton, D. R. (2006). Stimulation of apical and basolateral VEGF-A and VEGF-C secretion by oxidative stress in polarized retinal pigment epithelial cells. *Molecular Vision*, 12, 1649–1659. <http://www.ncbi.nlm.nih.gov/pubmed/17200665>
- Kataoka, N., Bachorik, J. L., & Dreyfuss, G. (1999). Transportin-SR, a nuclear import receptor for SR proteins. *Journal of Cell Biology*, 145(6), 1145–1152. <https://doi.org/10.1083/jcb.145.6.1145>

Katsuno, T., Umeda, K., Matsui, T., Hata, M., Tamura, A., Itoh, M., Takeuchi, K., Fujimori, T., Nabeshima, Y., Noda, T., Tsukita, S., & Tsukita, S. (2008). Deficiency of zonula occludens-1 causes embryonic lethal phenotype associated with defected yolk sac angiogenesis and apoptosis of embryonic cells. *Molecular Biology of the Cell*, 19(6), 2465–2475. <https://doi.org/10.1091/mbc.E07-12-1215>

Kato, N., Yashima, S., Suzuki, T., Nakayama, Y., Jomori, T. (2003) Long-term treatment with fidarestat suppresses the development of diabetic retinopathy in STZ-induced diabetic rats. *Journal of Diabetes and its Complications*, 17(6), 374-379. [https://doi.org/10.1016/S1056-8727\(02\)00193-9](https://doi.org/10.1016/S1056-8727(02)00193-9)

Kawamura, H., Li, X., Harper, S. J., Bates, D. O., & Claesson-Welsh, L. (2008). Vascular endothelial growth factor (VEGF)-A165b is a weak in vitro agonist for VEGF receptor-2 due to lack of coreceptor binding and deficient regulation of kinase activity. *Cancer Research*, 68(12), 4683–4692. <https://doi.org/10.1158/0008-5472.CAN-07-6577>

Kern, T. S., Du, Y., Miller, C. M., Hatala, D. A., & Levin, L. A. (2010). Overexpression of Bcl-2 in vascular endothelium inhibits the microvascular lesions of diabetic retinopathy. *American Journal of Pathology*, 176(5), 2550–2558. <https://doi.org/10.2353/ajpath.2010.091062>

Kim, B.-S., Chen, J., Weinstein, T., Noiri, E., & Goligorsky, M. S. (2002). VEGF expression in hypoxia and hyperglycemia: reciprocal effect on branching angiogenesis in epithelial-endothelial co-cultures. *Journal of the American Society of Nephrology: JASN*, 13(8), 2027–2036. <http://www.ncbi.nlm.nih.gov/pubmed/12138133>

Kim, C.-H., Kim, Y.-D., Choi, E.-K., Kim, H.-R., Na, B.-R., Im, S.-H., & Jun, C.-D. (2016). Nuclear Speckle-related Protein 70 Binds to Serine/Arginine-rich Splicing Factors 1 and 2 via an Arginine/Serine-like Region and Counteracts Their Alternative Splicing Activity. *The Journal of Biological Chemistry*, 291(12), 6169–6181. <https://doi.org/10.1074/jbc.M115.689414>

Kim, Dong-il, Park, M., Lim, S., Choi, J., Kim, J., Han, H., Kundu, T. K., Park, J., Yoon, K., Park, S., Park, J., Heo, Y., & Park, S. (2014). High-glucose-induced CARM1 expression regulates apoptosis of human retinal pigment epithelial cells via histone 3 arginine 17 dimethylation: Role in diabetic retinopathy. *Archives of Biochemistry and Biophysics*, 560, 36–43. <https://doi.org/10.1016/J.ABB.2014.07.021>

Kim, Dong il, Lim, S. K., Park, M. J., Han, H. J., Kim, G. Y., & Park, S. H. (2007). The involvement of phosphatidylinositol 3-kinase /Akt signaling in high glucose-induced downregulation of GLUT-1 expression in ARPE cells. *Life Sciences*, 80(7), 626–632. <https://doi.org/10.1016/j.lfs.2006.10.026>

Kim, J.-H., Kim, J. H., Jun, H.-O., Yu, Y. S., & Kim, K.-W. (2010). Inhibition of protein kinase C delta attenuates blood-retinal barrier breakdown in diabetic retinopathy. *The American Journal of Pathology*, 176(3), 1517–1524. <https://doi.org/10.2353/ajpath.2010.090398>

Kim †, C.-H., Kim, Y.-D., Choi †, E.-K., Kim †, H.-R., Na †, B.-R., Im, S.-H., & Jun †, C.-D. (2016). NSrp70 Impedes SRSF1 and SRSF2 Splicing Activity-1-Nuclear Speckle-related Protein 70 Binds to Serine/Arginine-Rich Splicing Factor-1 and-2 Via an Arginine/Serine-Like Region and Counteracts Their Alternative Splicing Activity. <https://doi.org/10.1074/jbc.M115.689414>

Kinoshita, J. H. (1990). A thirty year journey in the polyol pathway. *Experimental Eye Research*, 50(6), 567–573. [https://doi.org/10.1016/0014-4835\(90\)90096-D](https://doi.org/10.1016/0014-4835(90)90096-D)

Klaassen, I., van Noorden, C. J. F., & Schlingemann, R. O. (2013). Molecular basis of the inner blood-retinal barrier and its breakdown in diabetic macular edema and other pathological conditions. *Progress in Retinal and Eye Research*, 34, 19–48. <https://doi.org/10.1016/J.PRETEYERES.2013.02.001>

Klein, B. E. K. (2007). Overview of epidemiologic studies of diabetic retinopathy. *Ophthalmic Epidemiology*, 14(4), 179–183. <https://doi.org/10.1080/09286580701396720>

Koch, A. E., Halloran, M. M., Haskell, C. J., Shah, M. R., & Polverini, P. J. (1995). Angiogenesis mediated by soluble forms of E-selectin and vascular cell adhesion molecule-1. *Nature*. <https://doi.org/10.1038/376517a0>

Konishi, H., Tanaka, M., Takemura, Y., Matsuzaki, H., Ono, Y., Kikkawa, U., & Nishizuka, Y. (1997). Activation of protein kinase C by tyrosine phosphorylation in response to H₂O₂. *Proceedings of the National Academy of Sciences of the United States of America*, 94(21), 11233–11237. <https://doi.org/10.1073/pnas.94.21.11233>

Kowluru, R. A., & Chan, P.-S. (2007). Oxidative Stress and Diabetic Retinopathy. *Experimental Diabetes Research*, 2007. <https://doi.org/10.1155/2007/43603>

Koya, D., & King, G. L. (1998). Protein kinase C activation and the development of diabetic complications. *Diabetes*, 47(6), 859–866. <https://doi.org/10.1055/s-0031-1280517>

Kozak, I., & Luttrull, J. K. (2015). Modern retinal laser therapy. In *Saudi Journal of Ophthalmology* (Vol. 29, Issue 2, pp. 137–146). <https://doi.org/10.1016/j.sjopt.2014.09.001>

Kuhn E.-M., Deissler, H., Lang, G. E., & Deissler, H. L. (2008). CD9 is Important for Migration of Retinal Endothelial Cells - A Novel Target for Therapeutic Intervention? *Investigative Ophthalmology & Visual Science*, 49(13), 5884–5884. <https://iovs.arvojournals.org/article.aspx?articleid=2381265>

Lafosse, A., Dufey, C., Beauloye, C., Horman, S., and Dufrane, D. (2016). Impact of hyperglycemia and low oxygen tension on adipose-derived stem cells compared with dermal fibroblasts and keratinocytes: Importance for wound healing in type 2 diabetes. *PLoS One*, 11(12).

Lai, A. K. W., & Lo, A. C. Y. (2013). Animal models of diabetic retinopathy: summary and comparison. *Journal of Diabetes Research*, 2013, 106594. <https://doi.org/10.1155/2013/106594>

Lavia, C., Mecê, P., Nassisi, M., Bonnin, S., Marie-Louise, J., Couturier, A., Erginay, A., Tadayoni, R., & Gaudric, A. (2020). Retinal Capillary Plexus Pattern and Density from Fovea to Periphery Measured in Healthy Eyes with Swept-Source Optical Coherence Tomography Angiography. *Scientific Reports*, 10(1), 1474. <https://doi.org/10.1038/s41598-020-58359-y>

Liew G, Wong VW, Ho IV. Mini Review: Changes in the Incidence of and Progression to Proliferative and Sight-Threatening Diabetic Retinopathy Over the Last 30 Years. *Ophthalmic Epidemiol*. 2017 Apr; 24(2):73-80.

Liu, H., Zhang, Z., Xiong, W., Zhang, L., Du, Y., Liu, Y., & Xiong, X. (2019). Long non-coding RNA MALAT1 mediates hypoxia-induced pro-survival autophagy of endometrial stromal cells in endometriosis. *Journal of Cellular and Molecular Medicine*, 23(1), 439–452. <https://doi.org/10.1111/jcmm.13947>

Liu, Y., Leo, L. F., McGregor, C., Grivitchvili, A., Barnstable, C. J., & Tombran-Tink, J. (2012). Pigment Epithelium-Derived Factor (PEDF) Peptide Eye Drops Reduce Inflammation, Cell Death and Vascular Leakage in Diabetic Retinopathy in Ins2Akita Mice. *Molecular Medicine*, 18(10), 1387–1401. <https://doi.org/10.2119/molmed.2012.00008>

Lu, M., Perez, V. L., Ma, N., Miyamoto, K., Peng, H. B., Liao, J. K., & Adamis, A. P. (1999). VEGF increases retinal vascular ICAM-1 expression in vivo. *Investigative Ophthalmology and Visual Science*.

Luippold, G., Bedenik, J., Voigt, A., & Grempler, R. (2016). Short- and Longterm Glycemic Control of Streptozotocin-Induced Diabetic Rats Using Different Insulin Preparations. *PLOS ONE*, 11(6), e0156346. <https://doi.org/10.1371/journal.pone.0156346>

Luo, D., Fan, Y., & Xu, X. (2012). The effects of aminoguanidine on retinopathy in STZ-induced diabetic rats. *Bioorganic & Medicinal Chemistry Letters*, 22(13), 4386–4390. <https://doi.org/10.1016/J.BMCL.2012.04.130>

Alice Ly, Peter Yee, Kirstan A. Vessey, Joanna A. Phipps, Andrew I. Jobling, Erica L. Fletcher; Early Inner Retinal Astrocyte Dysfunction during Diabetes and Development of Hypoxia, Retinal Stress, and Neuronal Functional Loss. (2011). *Invest. Ophthalmol. Vis. Sci*, 52(13), 9316-9326. doi: <https://doi.org/10.1167/iovs.11-7879>.

Ma, C.-T., Hagopian, J. C., Ghosh, G., Fu, X.-D., & Adams, J. A. (2009). Regiospecific Phosphorylation Control of the SR Protein ASF/SF2 by SRPK1. *Journal of Molecular Biology*, 390(4), 618–634. <https://doi.org/10.1016/j.jmb.2009.05.060>

Ma, J., Shen, Z., Zhang, Q., Zhu, T., & Yao, K. (2011). The Effect of siRNA-VEGF on the Growth of REC in Retinal Pigment Epithelial Cell and Retinal

Endothelial Cell Co-Culture System. *Eye Science*, 26(2).
<https://doi.org/10.3969/J.ISSN.1000-4432.2011.02.015>

Magnussen, A. L., Rennel, E. S., Hua, J., Bevan, H. S., Beazley Long, N., Lehrling, C., Gammons, M., Floege, J., Harper, S. J., Agostini, H. T., Bates, D. O., & Churchill, A. J. (2010). VEGF-A165b is cytoprotective and antiangiogenic in the retina. *Investigative Ophthalmology & Visual Science*, 51(8), 4273–4281.
<https://doi.org/10.1167/iovs.09-4296>

Malecaze, F., Clamens, S., Simorre-Pinatel, V., Mathis, A., Chollet, P., Favard, C., Bayard, F., & Plouet, J. (1994). Detection of Vascular Endothelial Growth Factor Messenger RNA and Vascular Endothelial Growth Factor-like Activity in Proliferative Diabetic Retinopathy. *Archives of Ophthalmology*, 112(11), 1476.
<https://doi.org/10.1001/archophth.1994.01090230090028>

Mandarino, L. J. (1992). Current hypotheses for the biochemical basis of diabetic retinopathy. *Diabetes Care*, 15(12), 1892–1901.
<http://www.ncbi.nlm.nih.gov/pubmed/1464244>

Manetti, M., Guiducci, S., Romano, E., Ceccarelli, C., Bellando-Randone, S., Conforti, M. L., Ibba-Manneschi, L., & Matucci-Cerinic, M. (2011). Overexpression of VEGF165b, an inhibitory splice variant of vascular endothelial growth factor, leads to insufficient angiogenesis in patients with systemic sclerosis. *Circulation Research*, 109(3), e14-26.
<https://doi.org/10.1161/CIRCRESAHA.111.242057>

Marneros, A. G., Fan, J., Yokoyama, Y., Gerber, H. P., Ferrara, N., Crouch, R. K., & Olsen, B. R. (2005). Vascular endothelial growth factor expression in the retinal pigment epithelium is essential for choriocapillaris development and visual function. *The American Journal of Pathology*, 167(5), 1451–1459.
[https://doi.org/10.1016/S0002-9440\(10\)61231-X](https://doi.org/10.1016/S0002-9440(10)61231-X)

Marshall, G., Garg, S. K., Jackson, W. E., Holmes, D. L., & Chase, H. P. (1993). Factors influencing the onset and progression of diabetic retinopathy in subjects with insulin-dependent diabetes mellitus. *Ophthalmology*, 100(8), 1133–1139. [https://doi.org/10.1016/S0161-6420\(13\)31517-6](https://doi.org/10.1016/S0161-6420(13)31517-6)

Maury, B., Gonçalves, C., Tresset, G., Zeghal, M., Cheradame, H., Guégan, P., Pichon, C., & Midoux, P. (2014). Influence of pDNA availability on transfection efficiency of polyplexes in non-proliferative cells. *Biomaterials*.
<https://doi.org/10.1016/j.biomaterials.2014.04.007>

Mavrou, A., Brakspear, K., Hamdollah-Zadeh, M., Damodaran, G., Babaei-Jadidi, R., Oxley, J., Gillatt, D. A., Ladomery, M. R., Harper, S. J., Bates, D. O., & Oltean, S. (2015). Serine–arginine protein kinase 1 (SRPK1) inhibition as a potential novel targeted therapeutic strategy in prostate cancer. *Oncogene*, 34(33), 4311–4319. <https://doi.org/10.1038/onc.2014.360>

Michaelson, I. C. (1948). The mode of development of the vascular system of the retina, with some observations on their significance in certain retinal diseases. *Trans Ophthalmol Soc UK*, 68, 137–180.

Moos, T., & Møllgård, K. (1993). Cerebrovascular permeability to azo dyes and plasma proteins in rodents of different ages. *Neuropathology and Applied Neurobiology*, 19(2), 120–127. <https://doi.org/10.1111/j.1365-2990.1993.tb00416.x>

Morimoto, Y. (1998). Estimation of the branching number of the blood vessel system. *Physics Letters A*, 242(4–5), 285–289. [https://doi.org/10.1016/S0375-9601\(98\)00186-8](https://doi.org/10.1016/S0375-9601(98)00186-8)

Morooka, S., Hoshina, M., Kii, I., Okabe, T., Kojima, H., Inoue, N., Okuno, Y., Denawa, M., Yoshida, S., Fukuhara, J., Ninomiya, K., Ikura, T., Furuya, T., Nagano, T., Noda, K., Ishida, S., Hosoya, T., Ito, N., Yoshimura, N., & Hagiwara, M. (2015). Identification of a dual inhibitor of SRPK1 and CK2 that attenuates pathological angiogenesis of macular degeneration in mice. *Molecular Pharmacology*. <https://doi.org/10.1124/mol.114.097345>

Naro, C., & Sette, C. (2013). Phosphorylation-mediated regulation of alternative splicing in cancer. *International Journal of Cell Biology*, 2013, 151839. <https://doi.org/10.1155/2013/151839>

Nathan, D M, Genuth, S., Lachin, J., Cleary, P., Crofford, O., Davis, M., Rand, L., & Siebert, C. (1993). The Effect of Intensive Treatment of Diabetes on the Development and Progression of Long-Term Complications in Insulin-Dependent Diabetes Mellitus. *New England Journal of Medicine*, 329(14), 977–986. <https://doi.org/10.1056/NEJM199309303291401>

Nathan, David M, & DCCT/EDIC Research Group, for the D. R. (2014). The diabetes control and complications trial/epidemiology of diabetes interventions and complications study at 30 years: overview. *Diabetes Care*, 37(1), 9–16. <https://doi.org/10.2337/dc13-2112>

NC3Rs. (2019). Responsibility in the use of animals in bioscience research: expectations of the major research councils and charitable funding bodies. London: NC3Rs.

Nentwich, M. M. (2015). Diabetic retinopathy - ocular complications of diabetes mellitus. *World Journal of Diabetes*. <https://doi.org/10.4239/wjd.v6.i3.489>

Newman, D. K. (2010). Surgical management of the late complications of proliferative diabetic retinopathy. *Eye*. <https://doi.org/10.1038/eye.2009.325>

Nishijima, K., Ng, Y. S., Zhong, L., Bradley, J., Schubert, W., Jo, N., Akita, J., Samuelsson, S. J., Robinson, G. S., Adamis, A. P., & Shima, D. T. (2007). Vascular endothelial growth factor-A is a survival factor for retinal neurons and a critical neuroprotectant during the adaptive response to ischemic injury. *American Journal of Pathology*. <https://doi.org/10.2353/ajpath.2007.061237>

Nishikawa, T., Edelstein, D., Du, X. L., Yamagishi, S., Matsumura, T., Kaneda, Y., Yorek, M. A., Beebe, D., Oates, P. J., Hammes, H.-P., Giardino, I., & Brownlee, M. (2000). Normalizing mitochondrial superoxide production blocks

three pathways of hyperglycaemic damage. *Nature*, 404(6779), 787–790. <https://doi.org/10.1038/35008121>

Nowak, D. G., Woolard, J., Amin, E. M., Konopatskaya, O., Saleem, M. A., Churchill, A. J., Lodomery, M. R., Harper, S. J., & Bates, D. O. (2008). Expression of pro- and anti-angiogenic isoforms of VEGF is differentially regulated by splicing and growth factors. *Journal of Cell Science*, 121(20), 3487–3495. <https://doi.org/10.1242/jcs.016410>

Nowak, Dawid G, Amin, E. M., Rennel, E. S., Hoareau-Aveilla, C., Gammons, M., Damodoran, G., Hagiwara, M., Harper, S. J., Woolard, J., Lodomery, M. R., & Bates, D. O. (2010). Regulation of vascular endothelial growth factor (VEGF) splicing from pro-angiogenic to anti-angiogenic isoforms: a novel therapeutic strategy for angiogenesis. *The Journal of Biological Chemistry*, 285(8), 5532–5540. <https://doi.org/10.1074/jbc.M109.074930>

Nurözler Tabakçı, B., & Ünlü, N. (2017). Corticosteroid Treatment in Diabetic Macular Edema. *Turkish Journal of Ophthalmology*, 47(3), 156–160. <https://doi.org/10.4274/tjo.56338>

Olivares, A. M., Althoff, K., Chen, G. F., Wu, S., Morrisson, M. A., DeAngelis, M. M., & Haider, N. (2017). Animal Models of Diabetic Retinopathy. *Current Diabetes Reports*, 17(10), 93. <https://doi.org/10.1007/s11892-017-0913-0>

Omri, S., Behar-Cohen, F., Rothschild, P.-R., Gélizé, E., Jonet, L., Jeanny, J. C., Omri, B., & Crisanti, P. (2013). PKC ζ Mediates Breakdown of Outer Blood-Retinal Barriers in Diabetic Retinopathy. *PLoS ONE*, 8(11), e81600. <https://doi.org/10.1371/journal.pone.0081600>

Onishi, A. C., Nesper, P. L., Roberts, P. K., Moharram, G. A., Chai, H., Liu, L., Jampol, L. M., & Fawzi, A. A. (2018). Importance of Considering the Middle Capillary Plexus on OCT Angiography in Diabetic Retinopathy. *Investigative Ophthalmology & Visual Science*, 59(5), 2167. <https://doi.org/10.1167/IOVS.17-23304>

Ou, K., Copland, D. A., Theodoropoulou, S., Mertsch, S., Li, Y., Liu, J., Schrader, S., Liu, L., & Dick, A. D. (2020). Treatment of diabetic retinopathy through neuropeptide Y-mediated enhancement of neurovascular microenvironment. *J Cell Mol Med*, 00, 1–13. <https://doi.org/10.1111/jcmm.15016>

Ouellette, M. M., McDaniel, L. D., Wright, W. E., Shay, J. W., & Schultz, R. A. (2000). The establishment of telomerase-immortalized cell lines representing human chromosome instability syndromes. *Human Molecular Genetics*, 9(3), 403–411. <https://doi.org/10.1093/hmg/9.3.403>

Ozaki, H., Yu, A. Y., Della, N., Ozaki, K., Luna, J. D., Yamada, H., Hackett, S. F., Okamoto, N., Zack, D. J., Semenza, G. L., & Campochiaro, P. A. (1999). Hypoxia inducible factor-1 α is increased in ischemic retina: temporal and spatial correlation with VEGF expression. *Investigative Ophthalmology & Visual Science*, 40(1), 182–189. <http://www.ncbi.nlm.nih.gov/pubmed/9888442>

Parekh, D. B., Ziegler, W., & Parker, P. J. (2000). NEW EMBO MEMBER'S REVIEWS: Multiple pathways control protein kinase C phosphorylation. *The EMBO Journal*, 19(4), 496. <https://doi.org/10.1093/EMBOJ/19.4.496>

Pedram, A., Razandi, M., & Levin, E. R. (2002). Deciphering vascular endothelial cell growth factor/vascular permeability factor signaling to vascular permeability. Inhibition by atrial natriuretic peptide. *The Journal of Biological Chemistry*, 277(46), 44385–44398. <https://doi.org/10.1074/jbc.M202391200>

Perrin, R. M., Konopatskaya, O., Qiu, Y., Harper, S., Bates, D. O., & Churchill, A. J. (2005). Diabetic retinopathy is associated with a switch in splicing from anti- to pro-angiogenic isoforms of vascular endothelial growth factor. *Diabetologia*, 48(11), 2422–2427. <https://doi.org/10.1007/s00125-005-1951-8>

Ponnalagu, M., Subramani, M., Jayadev, C., Shetty, R., & Das, D. (2017). Retinal pigment epithelium-secretome: A diabetic retinopathy perspective. *Cytokine*, 95, 126–135. <https://doi.org/10.1016/J.CYTO.2017.02.013>

Poulaki, V., Qin, W., Jousen, A. M., Hurlbut, P., Wiegand, S. J., Rudge, J., Yancopoulos, G. D., & Adamis, A. P. (2002). Acute intensive insulin therapy exacerbates diabetic blood-retinal barrier breakdown via hypoxia-inducible factor-1 α and VEGF. *Journal of Clinical Investigation*, 109(6), 805–815. <https://doi.org/10.1172/JCI13776>

Rahman, A., Anwar, K. N., & Malik, A. B. (2000). Protein kinase C- ζ mediates TNF- α -induced ICAM-1 gene transcription in endothelial cells. *American Journal of Physiology-Cell Physiology*, 279(4), C906–C914. <https://doi.org/10.1152/ajpcell.2000.279.4.C906>

Rajalakshmi, R., Prathiba, V., & Mohan, V. (2016). Does tight control of systemic factors help in the management of diabetic retinopathy? *Indian Journal of Ophthalmology*, 64(1), 62–68. <https://doi.org/10.4103/0301-4738.178146>

Rennel, E. S., Varey, A. H. R., Churchill, A. J., Wheatley, E. R., Stewart, L., Mather, S., Bates, D. O., & Harper, S. J. (2009). VEGF(121)b, a new member of the VEGF(xxx)b family of VEGF-A splice isoforms, inhibits neovascularisation and tumour growth in vivo. *British Journal of Cancer*, 101(7), 1183–1193. <https://doi.org/10.1038/sj.bjc.6605249>

Robison, W. G., Kador, P. F., & Kinoshita, J. H. (1985). Early Retinal Microangiopathy: Prevention with Aldose Reductase Inhibitors. *Diabetic Medicine*. <https://doi.org/10.1111/j.1464-5491.1985.tb00635.x>

Rodrigues, G. A., Lutz, D., Shen, J., Yuan, X., Shen, H., Cunningham, J., & Rivers, H. M. (2018). Topical Drug Delivery to the Posterior Segment of the Eye: Addressing the Challenge of Preclinical to Clinical Translation. *Pharmaceutical Research*, 35(12). <https://doi.org/10.1007/S11095-018-2519-X>

Roh, M. I., Kim, H. S., Song, J. H., Lim, J. B., & Kwon, O. W. (2009). Effect of Intravitreal Bevacizumab Injection on Aqueous Humor Cytokine Levels in

Clinically Significant Macular Edema. Ophthalmology.
<https://doi.org/10.1016/j.ophtha.2008.09.036>

Rossi, F., Labourier, E., Forné, T., Divita, G., Derancourt, J., Riou, J. F., Antoine, E., Cathala, G., Brunel, C., & Tazi, J. (1996). Specific phosphorylation of SR proteins by mammalian DNA topoisomerase I. *Nature*, 381(6577), 80–82. <https://doi.org/10.1038/381080a0>

Royle, P., Mistry, H., Auguste, P., Shyangdan, D., Freeman, K., Lois, N., & Waugh, N. (2015). HEALTH TECHNOLOGY ASSESSMENT Pan-retinal photocoagulation and other forms of laser treatment and drug therapies for non-proliferative diabetic retinopathy: systematic review and economic evaluation. 19(51). <https://doi.org/10.3310/hta19510>

Rungger-Brändle, E., Dosso, A. A., & Leuenberger, P. M. (2000). Glial reactivity, an early feature of diabetic retinopathy. *Investigative Ophthalmology and Visual Science*.

Rydén, L., Grant, P. J., Anker, S. D., Berne, C., Cosentino, F., Danchin, N., Deaton, C., Escaned, J., Hammes, H. P., Huikuri, H., Marre, M., Marx, N., Mellbin, L., Ostergren, J., Patrono, C., Seferovic, P., Uva, M. S., Taskinen, M. R., Tendera, M., ... Xuereb, R. G. (2013). ESC guidelines on diabetes, pre-diabetes, and cardiovascular diseases developed in collaboration with the EASD. *European Heart Journal*. <https://doi.org/10.1093/eurheartj/eh108>

Saint-Geniez, M., Maldonado, A. E., & D'Amore, P. A. (2006). VEGF expression and receptor activation in the choroid during development and in the adult. *Investigative Ophthalmology and Visual Science*. <https://doi.org/10.1167/iovs.05-1229>

Saker, S., Stewart, E. A., Browning, A. C., Allen, C. L., & Amoaku, W. M. (2014). The effect of hyperglycaemia on permeability and the expression of junctional complex molecules in human retinal and choroidal endothelial cells. *Experimental Eye Research*, 121, 161–167. <https://doi.org/10.1016/J.EXER.2014.02.016>

Samuel, W., Jaworski, C., Postnikova, O. A., Kutty, R. K., Duncan, T., Tan, L. X., Poliakov, E., Lakkaraju, A., & Redmond, T. M. (2017). Appropriately differentiated ARPE-19 cells regain phenotype and gene expression profiles similar to those of native RPE cells. *Molecular Vision*, 23, 60–89. <http://www.ncbi.nlm.nih.gov/pubmed/28356702>

Sánchez-Tocino, H., Alvarez-Vidal, A., Maldonado, M. J., Moreno-Montañés, J., & García-Layana, A. (2002). Retinal thickness study with optical coherence tomography in patients with diabetes. *Investigative Ophthalmology and Visual Science*.

Saunders, N. R., Dziegielewska, K. M., Møllgård, K., & Habgood, M. D. (2015). Markers for blood-brain barrier integrity: how appropriate is Evans blue in the twenty-first century and what are the alternatives? *Frontiers in Neuroscience*, 9. <https://doi.org/10.3389/FNINS.2015.00385>

Scheppke, L., Aguilar, E., Gariano, R. F., Jacobson, R., Hood, J., Doukas, J., Cao, J., Noronha, G., Yee, S., Weis, S., Martin, M. B., Soll, R., Cheresch, D. A., & Friedlander, M. (2008). Retinal vascular permeability suppression by topical application of a novel VEGFR2/Src kinase inhibitor in mice and rabbits. *The Journal of Clinical Investigation*, 118(6), 2337–2346. <https://doi.org/10.1172/JCI33361>

Schroder, S., Palinski, W., & Schmid-Schonbein, G. W. (1991). Activated monocytes and granulocytes, capillary nonperfusion, and neovascularization in diabetic retinopathy. *American Journal of Pathology*.

Scoles, D., Sulai, Y. N., Dubra, A., Marlhens, 8 F, Bareil, C., Griffoin, J. M., Zrenner, E., Amalric, P., Eliaou, C., Liu, S. Y., Harris, E., Redmond, T. M., Arnaud, B., Claustres, M., Hamel, C. P., Greenstein, 9 V C, Duncker, T., Holopigian, K., Carr, R. E., ... Carroll, J. (1997). In vivo dark-field imaging of the retinal pigment epithelium cell mosaic " Mutations in RPE65 cause Leber's congenital amaurosis. *Nat. Genet. R. Wayne, Light and Video Microscopy*. <https://doi.org/10.1364/BOE.4.001710>

Shakib, M., & Cunha-Vaz, J. G. (1966). Studies on the permeability of the blood-retinal barrier: IV. Junctional complexes of the retinal vessels and their role in the permeability of the blood-retinal barrier. *Experimental Eye Research*, 5(3), 229-IN16. [https://doi.org/10.1016/S0014-4835\(66\)80011-8](https://doi.org/10.1016/S0014-4835(66)80011-8)

Shanmugam, N., Reddy, M. A., Guha, M., & Natarajan, R. (2003). High glucose-induced expression of proinflammatory cytokine and chemokine genes in monocytic cells. *Diabetes*, 52(5), 1256–1264. <https://doi.org/10.2337/diabetes.52.5.1256>

Shaw, S. G., Boden, J. P., Biecker, E., Reichen, J., & Rothen, B. (2006). Endothelin antagonism prevents diabetic retinopathy in NOD mice: A potential role of the angiogenic factor adrenomedullin. *Experimental Biology and Medicine*. <https://doi.org/10.3181/00379727-232-2311101>

Shiba, T., Inoguchi, T., Sportsman, J. R., Heath, W. F., Bursell, S., & King, G. L. (1993). Correlation of diacylglycerol level and protein kinase C activity in rat retina to retinal circulation. *The American Journal of Physiology*, 265(5 Pt 1), E783-93. <https://doi.org/10.1152/ajpendo.1993.265.5.E783>

Shih, S. C., Ju, M., Liu, N., & Smith, L. E. H. (2003). Selective stimulation of VEGFR-1 prevents oxygen-induced retinal vascular degeneration in retinopathy of prematurity. *Journal of Clinical Investigation*, 112(1), 50–57. <https://doi.org/10.1172/JCI200317808>

Shii, D., Oda, T., Shinomiya, K., Katsuta, O., & Nakamura, M. (2009). Cyclosporine A Eye Drops Inhibit the Early-Phase Reaction in a Type-I Allergic Conjunctivitis Model in Mice. *Journal of Ocular Pharmacology and Therapeutics*, 25(4), 321–328. <https://doi.org/10.1089/jop.2009.0009>

Shin, E. S., Sorenson, C. M., & Sheibani, N. (2014). Diabetes and Retinal Vascular Dysfunction. *Journal of Ophthalmic & Vision Research*, 9(3), 362. <https://doi.org/10.4103/2008-322X.143378>

Shokrzadeh, M., Abdi, H., Asadollah-Pour, A., & Shaki, F. (2016). Nanoceria Attenuated High Glucose-Induced Oxidative Damage in HepG2 Cells. *Cell Journal (Yakhteh)*, 18(1), 97. <https://doi.org/10.22074/CELLJ.2016.3992>

Shoughy, S. S., Arevalo, J. F., & Kozak, I. (2015). Update on wide- and ultra-widefield retinal imaging. *Indian Journal of Ophthalmology*, 63(7), 575–581. <https://doi.org/10.4103/0301-4738.167122>

Sidman, R. L., Li, J., Lawrence, M., Hu, W., Musso, G. F., Giordano, R. J., Cardó-Vila, M., Pasqualini, R., & Arap, W. (2015). The peptidomimetic Vasotide targets two retinal VEGF receptors and reduces pathological angiogenesis in murine and nonhuman primate models of retinal disease. *Science Translational Medicine*, 7(309), 309ra165. <https://doi.org/10.1126/scitranslmed.aac4882>

Simó, R., & Hernández, C. (2008). Intravitreal anti-VEGF for diabetic retinopathy: hopes and fears for a new therapeutic strategy. *Diabetologia*, 51(9), 1574–1580. <https://doi.org/10.1007/s00125-008-0989-9>

Simó, Rafael, Hernández, C., Porta, M., Bandello, F., Grauslund, J., Harding, S. P., Aldington, S. J., Egan, C., Frydkjaer-Olsen, U., García-Arumí, J., Gibson, J., Lang, G. E., Lattanzio, R., Massin, P., Midea, E., Ponsati, B., Ribeiro, L., Scanlon, P., Lobo, C., ... Cunha-Vaz, J. (2019). Effects of Topically Administered Neuroprotective Drugs in Early Stages of Diabetic Retinopathy: Results of the EUROCONDOR Clinical Trial. *Diabetes*, 68(2), 457–463. <https://doi.org/10.2337/DB18-0682>

Simó, Rafael, Villarreal, M., Corraliza, L., Hernández, C., & Garcia-Ramírez, M. (2010). The retinal pigment epithelium: Something more than a constituent of the blood-retinal barrier-implications for the pathogenesis of diabetic retinopathy. In *Journal of Biomedicine and Biotechnology*. <https://doi.org/10.1155/2010/190724>

Sinnakannu, J. R., Lee, K. L., Cheng, S., Li, J., Yu, M., Tan, S. P., Ong, C. C. H., Li, H., Than, H., Anczuków-Camarda, O., Krainer, A. R., Roca, X., Rozen, S. G., Iqbal, J., Yang, H., Chuah, C., & Ong, S. T. (2020). SRSF1 mediates cytokine-induced impaired imatinib sensitivity in chronic myeloid leukemia. *Leukemia*, 1–12. <https://doi.org/10.1038/s41375-020-0732-1>

Sivaprasad, S., & Pearce, E. (2018). The unmet need for better risk stratification of non-proliferative diabetic retinopathy. *Diabetic Medicine*, 36(4), dme.13868. <https://doi.org/10.1111/dme.13868>

Sivaprasad, Sobha, Gupta, B., Crosby-Nwaobi, R., & Evans, J. (2012). Prevalence of Diabetic Retinopathy in Various Ethnic Groups: A Worldwide Perspective. *Survey of Ophthalmology*, 57(4), 347–370. <https://doi.org/10.1016/j.survophthal.2012.01.004>

Stern, J., & Temple, S. (2015). Retinal pigment epithelial cell proliferation. *Experimental Biology and Medicine*. <https://doi.org/10.1177/1535370215587530>

Stevenson, B. R., Siliciano, J. D., Mooseker, M. S., & Goodenough, D. A. (1986). Identification of ZO-1: a high molecular weight polypeptide associated with the tight junction (zonula occludens) in a variety of epithelia. *The Journal of Cell Biology*, 103(3), 755–766. <http://www.ncbi.nlm.nih.gov/pubmed/3528172>

Stewart, E. A., Saker, S., & Amoaku, W. M. (2016). Dexamethasone reverses the effects of high glucose on human retinal endothelial cell permeability and proliferation in vitro. *Experimental Eye Research*, 151, 75–81. <https://doi.org/10.1016/J.EXER.2016.08.005>

Stewart, M. W. (2012). Aflibercept (VEGF Trap-eye): the newest anti-VEGF drug. *The British Journal of Ophthalmology*, 96(9), 1157–1158. <https://doi.org/10.1136/bjophthalmol-2011-300654>

Stitt, A. W., Curtis, T. M., Chen, M., Medina, R. J., McKay, G. J., Jenkins, A., Gardiner, T. A., Lyons, T. J., Hammes, H.-P., Simó, R., & Lois, N. (2016). The progress in understanding and treatment of diabetic retinopathy. *Progress in Retinal and Eye Research*, 51, 156–186. <https://doi.org/10.1016/j.preteyeres.2015.08.001>

Strauss, O. (2005). The Retinal Pigment Epithelium in Visual Function. *Physiological Reviews*, 85(3), 845–881. <https://doi.org/10.1152/physrev.00021.2004>

Székelyhidi, Z., Pató, J., Wáczeck, F., Bánhegyi, P., Hegymegi-Barakonyi, B., Eros, D., Mészáros, G., Hollósy, F., Hafenbradl, D., Obert, S., Klebl, B., Kéri, G., & Orfi, L. (2005). Synthesis of selective SRPK-1 inhibitors: Novel tricyclic quinoxaline derivatives. *Bioorganic and Medicinal Chemistry Letters*. <https://doi.org/10.1016/j.bmcl.2005.04.064>

Szkudelski, T. (2001). The mechanism of alloxan and streptozotocin action in B cells of the rat pancreas. In *Physiological Research*.

Tang, J., Zhu, X., Lust, W., Kern, T. S. (2000). Retina accumulates more glucose than does the embryologically similar cerebral cortex in diabetic rats. *Diabetologia* 43, 1417–1423. <https://doi.org/10.1007/s001250051548>

Taylor, A. M., Jeffery, G., & Lieberman, A. R. (1986). Subcortical afferent and efferent connections of the superior colliculus in the rat and comparisons between albino and pigmented strains. *Experimental Brain Research*. <https://doi.org/10.1007/BF00237409>

The Diabetic Retinopathy Study Research Group. (1981). Photocoagulation treatment of proliferative diabetic retinopathy. Clinical application of Diabetic Retinopathy Study (DRS) findings, DRS Report Number 8. *Ophthalmology*, 88(7), 583–600. <http://www.ncbi.nlm.nih.gov/pubmed/7196564>

The Royal College of Ophthalmologists Diabetic Retinopathy Guidelines. (2012). www.rcophth.ac.uk

Tian, J., Ishibashi, K., & Handa, J. T. (2004). The expression of native and cultured RPE grown on different matrices. *Physiological Genomics*, 17(2), 170–182. <https://doi.org/10.1152/physiolgenomics.00179.2003>

Toda, N., & Nakanishi-Toda, M. (2007). Nitric oxide: Ocular blood flow, glaucoma, and diabetic retinopathy. *Progress in Retinal and Eye Research*, 26(3), 205–238. <https://doi.org/10.1016/J.PRETEYERES.2007.01.004>

Tripathi, V., Song, D. Y., Zong, X., Shevtsov, S. P., Hearn, S., Fu, X.-D., Dundr, M., & Prasanth, K. v. (2012). SRSF1 regulates the assembly of pre-mRNA processing factors in nuclear speckles. *Molecular Biology of the Cell*, 23(18), 3694–3706. <https://doi.org/10.1091/mbc.E12-03-0206>

Twyffels, L., Gueydan, C., & Kruijs, V. (2011). Shuttling SR proteins: more than splicing factors. *FEBS Journal*, 278(18), 3246–3255. <https://doi.org/10.1111/j.1742-4658.2011.08274.x>

Unemori, E. N., Ferrara, N., Bauer, E. a, & Amento, E. P. (1992). Vascular endothelial growth factor induces interstitial collagenase expression in human endothelial cells. *Journal of Cellular Physiology*, 153, 557–562. <https://doi.org/10.1002/jcp.1041530317>

Uyama, O., Okamura, N., Yanase, M., Narita, M., Kawabata, K., & Sugita, M. (1988). Quantitative Evaluation of Vascular Permeability in the Gerbil Brain after Transient Ischemia Using Evans Blue Fluorescence. *Journal of Cerebral Blood Flow & Metabolism*, 8(2), 282–284. <https://doi.org/10.1038/jcbfm.1988.59>

van Itallie, C. M., Fanning, A. S., Bridges, A., & Anderson, J. M. (2009). ZO-1 Stabilizes the Tight Junction Solute Barrier through Coupling to the Perijunctional Cytoskeleton. *Molecular Biology of the Cell*, 20(17), 3930–3940. <https://doi.org/10.1091/mbc.E09-04-0320>

van Itallie, Christina M., & Anderson, J. M. (2006). CLAUDINS AND EPITHELIAL PARACELLULAR TRANSPORT. *Annual Review of Physiology*, 68(1), 403–429. <https://doi.org/10.1146/annurev.physiol.68.040104.131404>

Varey, A. H. R., Rennel, E. S., Qiu, Y., Bevan, H. S., Perrin, R. M., Raffy, S., Dixon, A. R., Paraskeva, C., Zaccheo, O., Hassan, A. B., Harper, S. J., & Bates, D. O. (2008). VEGF165b, an antiangiogenic VEGF-A isoform, binds and inhibits bevacizumab treatment in experimental colorectal carcinoma: Balance of pro- and antiangiogenic VEGF-A isoforms has implications for therapy. *British Journal of Cancer*, 98(8), 1366–1379. <https://doi.org/10.1038/sj.bjc.6604308>

Ved, N., Hulse, R. P., Bestall, S. M., Donaldson, L. F., Bainbridge, J. W., & Bates, D. (2017). Vascular endothelial growth factor-A_b ameliorates outer-retinal barrier and vascular

dysfunction in the diabetic retina. *Clinical Science*.
<http://www.clinsci.org/content/early/2017/03/24/CS20170102.abstract>

Villarroel, M., García-Ramírez, M., Corraliza, L., Hernández, C., & Simó, R. (2009). Effects of high glucose concentration on the barrier function and the expression of tight junction proteins in human retinal pigment epithelial cells. *Experimental Eye Research*, 89(6), 913–920.
<https://doi.org/10.1016/J.EXER.2009.07.017>

Virgili, G., Menchini, F., Murro, V., Peluso, E., Rosa, F., & Casazza, G. (2011). Optical coherence tomography (OCT) for detection of macular oedema in patients with diabetic retinopathy. In G. Virgili (Ed.), *Cochrane Database of Systematic Reviews* (Issue 7). John Wiley & Sons, Ltd.
<https://doi.org/10.1002/14651858.CD008081.pub2>

Vitale, S., Maguire, M. G., Murphy, R. P., Hiner, C. J., Rourke, L., Sackett, C., & Patz, A. (1995). Clinically Significant Macular Edema in Type I Diabetes: Incidence and Risk Factors. *Ophthalmology*. [https://doi.org/10.1016/S0161-6420\(95\)30894-9](https://doi.org/10.1016/S0161-6420(95)30894-9)

Vlassara, H., & Uribarri, J. (2014). Advanced glycation end products (AGE) and diabetes: Cause, effect, or both? *Current Diabetes Reports*, 14(1).
<https://doi.org/10.1007/s11892-013-0453-1>

Voukkalis, N., Koutroumani, M., Zarkadas, C., Nikolakaki, E., Vlassi, M., & Giannakouros, T. (2016). SRPK1 and Akt Protein Kinases Phosphorylate the RS Domain of Lamin B Receptor with Distinct Specificity: A Combined Biochemical and In Silico Approach. *PLOS ONE*, 11(4), e0154198.
<https://doi.org/10.1371/journal.pone.0154198>

Wagner, K.-D., el Maï, M., Lodomery, M., Belali, T., Leccia, N., Michiels, J.-F., & Wagner, N. (2019). Altered VEGF Splicing Isoform Balance in Tumor Endothelium Involves Activation of Splicing Factors Srpk1 and Srsf1 by the Wilms' Tumor Suppressor Wt1. *Cells*, 8(1).
<https://doi.org/10.3390/cells8010041>

Walter, A., Chaikuad, A., Helmer, R., Loaëc, N., Preu, L., Ott, I., Knapp, S., Meijer, L., & Kunick, C. (2018). Molecular structures of cdc2-like kinases in complex with a new inhibitor chemotype. *PLoS ONE*, 13(5).
<https://doi.org/10.1371/JOURNAL.PONE.0196761>

Wanek, J., Teng, P., Blair, N. P., & Shahidi, M. (2014). Inner Retinal Oxygen Delivery and Metabolism in Streptozotocin Diabetic Rats. *Investigative Ophthalmology & Visual Science*, 55(3), 1588.
<https://doi.org/10.1167/IOVS.13-13537>

Wang, H. Y., Lin, W., Dyck, J. A., Yeakley, J. M., Songyang, Z., Cantley, L. C., & Fu, X. D. (1998). SRPK2: a differentially expressed SR protein-specific kinase involved in mediating the interaction and localization of pre-mRNA splicing factors in mammalian cells. *The Journal of Cell Biology*, 140(4), 737–750. <http://www.ncbi.nlm.nih.gov/pubmed/9472028>

Wang, Jian, Wu, H.-F., Shen, W., Xu, D.-Y., Ruan, T.-Y., Tao, G.-Q., & Lu, P. (2016). SRPK2 promotes the growth and migration of the colon cancer cells. *Gene*, 586(1). <https://doi.org/10.1016/j.gene.2016.03.051>

Wang, Juanjuan, Xu, E., Elliott, M. H., Zhu, M., & Le, Y. Z. (2010). Müller cell-derived VEGF is essential for diabetes-induced retinal inflammation and vascular leakage. *Diabetes*. <https://doi.org/10.2337/db09-1420>

Wang, Y. L., Hui, Y. N., Guo, B., & Ma, J. X. (2007). Strengthening tight junctions of retinal microvascular endothelial cells by pericytes under normoxia and hypoxia involving angiopoietin-1 signal way. *Eye*, 21(12), 1501–1510. <https://doi.org/10.1038/sj.eye.6702716>

Wang-Fischer, Y., & Garyantes, T. (2018). Improving the Reliability and Utility of Streptozotocin-Induced Rat Diabetic Model. *Journal of Diabetes Research*, 2018, 8054073. <https://doi.org/10.1155/2018/8054073>

Wangsa-Wirawan ND, Linsenmeier RA. (2003). Retinal Oxygen: Fundamental and Clinical Aspects. *Arch Ophthalmol*. 121(4). 547–557. doi:10.1001/archophth.121.4.547

Wegener, J., Keese, C. R., & Giaever, I. (2000). Electric cell-substrate impedance sensing (ECIS) as a noninvasive means to monitor the kinetics of cell spreading to artificial surfaces. *Experimental Cell Research*, 259(1), 158–166. <https://doi.org/10.1006/excr.2000.4919>

Weinberger, D., Fink-Cohen, S., Gatton, D. D., Priel, E., & Yassur, Y. (1995). Non-retinovascular leakage in diabetic maculopathy. *The British Journal of Ophthalmology*, 79(8), 728–731. <https://doi.org/10.1136/bjo.79.8.728>

Weis, S. M., & Cheresh, D. A. (2005). Pathophysiological consequences of VEGF-induced vascular permeability. *Nature*, 437, 497. <http://dx.doi.org/10.1038/nature03987>

Wenick, A. S., & Bressler, N. M. (2012). Diabetic macular edema: current and emerging therapies. *Middle East African Journal of Ophthalmology*, 19(1), 4–12. <https://doi.org/10.4103/0974-9233.92110>

Williams, B., Gallacher, B., Patel, H., & Orme, C. (1997). Glucose-induced protein kinase C activation regulates vascular permeability factor mRNA expression and peptide production by human vascular smooth muscle cells in vitro. *Diabetes*, 46(9), 1497–1503. <https://doi.org/10.2337/diab.46.9.1497>

Williamson, J. R., Chang, K., Frangos, M., Hasan, K. S., Ido, Y., Kawamura, T., Nyengaard, J. R., van den Enden, M., Kilo, C., & Tilton, R. G. (1993). Hyperglycemic pseudohypoxia and diabetic complications. In *Diabetes* (Vol. 42, Issue 6, pp. 801–813). <https://doi.org/10.2337/diab.42.6.801>

Winkler BS, Arnold MJ, Brassell MA, Puro DG. (2000). Energy metabolism in human retinal Müller cells. *Invest Ophthalmol Vis Sci*, 41(10), 3183-90.

Wong, Tien Y., Cheung, C. M. G., Larsen, M., Sharma, S., & Simó, R. (2016). Diabetic retinopathy. *Nature Reviews Disease Primers*, 2, 16012. <https://doi.org/10.1038/nrdp.2016.12>

Wong, Tien Yin. (2011). Retinal Vessel Diameter as a Clinical Predictor of Diabetic Retinopathy Progression. *Archives of Ophthalmology*, 129(1), 95. <https://doi.org/10.1001/archophthalmol.2010.347>

Wright, W. S., Singh Yadav, A., McElhatten, R. M., & Harris, N. R. (2012). Retinal blood flow abnormalities following six months of hyperglycemia in the Ins2(Akita) mouse. *Experimental Eye Research*. <https://doi.org/10.1016/j.exer.2012.03.003>

Wu-Zhang, A. X., & Newton, A. C. (2013). Protein Kinase C Pharmacology: Refining the Toolbox. *The Biochemical Journal*, 452(2), 195. <https://doi.org/10.1042/BJ20130220>

Xia, P., Jirousek, M. R., & King, G. L. (1996). Characterization of vascular endothelial growth factor's effect on the activation of protein kinase C, its isoforms, and endothelial cell growth. *J Clin Invest*, 98(9), 2018–2026. <https://doi.org/10.1172/JCI119006>

Xia, T., & Rizzolo, L. J. (2017). Effects of diabetic retinopathy on the barrier functions of the retinal pigment epithelium. *Vision Research*, 139, 72–81. <https://doi.org/10.1016/J.VISRES.2017.02.006>

Xu, H., Czerwinski, P., Hortmann, M., Sohn, H.-Y., Förstermann, U., & Li, H. (2008). Protein kinase C alpha promotes angiogenic activity of human endothelial cells via induction of vascular endothelial growth factor. *Cardiovascular Research*, 78(2), 349–355. <https://doi.org/10.1093/cvr/cvm085>

Xu, H.-Z., & Le, Y.-Z. (2011). Significance of Outer Blood–Retina Barrier Breakdown in Diabetes and Ischemia. *Investigative Ophthalmology & Visual Science*, 52(5), 2160. <https://doi.org/10.1167/iovs.10-6518>

Xu, H.-Z., Song, Z., Fu, S., Zhu, M., & Le, Y.-Z. (2011). RPE barrier breakdown in diabetic retinopathy: seeing is believing. *Journal of Ocular Biology, Diseases, and Informatics*, 4(1–2), 83–92. <https://doi.org/10.1007/s12177-011-9068-4>

Xu, Q., Qaum, T., & Adamis, A. P. (2001). Sensitive blood-retinal barrier breakdown quantitation using Evans blue. *Investigative Ophthalmology and Visual Science*.

Yang, C., Kelaini, S., Caines, R., & Margariti, A. (2018). RBPs Play Important Roles in Vascular Endothelial Dysfunction Under Diabetic Conditions. *Frontiers in Physiology*, 9. <https://doi.org/10.3389/FPHYS.2018.01310>

Yang, J., Välineva, T., Hong, J., Bu, T., Yao, Z., Jensen, O. N., Frilander, M. J., & Silvennoinen, O. (2007). Transcriptional co-activator protein p100 interacts with snRNP proteins and facilitates the assembly of the spliceosome. *Nucleic Acids Research*, 35(13), 4485–4494. <https://doi.org/10.1093/nar/gkm470>

Yokouchi, H., Eto, K., Nishimura, W., Takeda, N., Kaburagi, Y., Yamamoto, S., & Yasuda, K. (2013). Angiopoietin-like protein 4 (ANGPTL4) is induced by high glucose in retinal pigment epithelial cells and exhibits potent angiogenic activity on retinal endothelial cells. *Acta Ophthalmologica*, 91(4). <https://doi.org/10.1111/aos.12097>

Yoon, C., Kim, D., Kim, S., Park, G. bin, Hur, D. Y., Yang, J. W., Park, S. G., & Kim, Y. S. (2014). MiR-9 regulates the post-transcriptional level of VEGF165a by targeting SRPK-1 in ARPE-19 cells. *Graefe's Archive for Clinical and Experimental Ophthalmology*, 252(9), 1369–1376. <https://doi.org/10.1007/s00417-014-2698-z>

Yoon, C.-H., Choi, Y.-E., Cha, Y. R., Koh, S.-J., Choi, J., Kim, T.-W., Woo, S. J., Park, Y.-B., Chae, I.-H., & Kim, H.-S. (2016). Diabetes-Induced Jagged1 Overexpression in Endothelial Cells Causes Retinal Capillary Regression in a Murine Model of Diabetes Mellitus. *Circulation*, 134(3), 233–247. <https://doi.org/10.1161/CIRCULATIONAHA.116.014411>

Yoshimura, T., Sonoda, K. H., Sugahara, M., Mochizuki, Y., Enaida, H., Oshima, Y., Ueno, A., Hata, Y., Yoshida, H., & Ishibashi, T. (2009). Comprehensive analysis of inflammatory immune mediators in vitreoretinal diseases. *PLoS ONE*. <https://doi.org/10.1371/journal.pone.0008158>

Young, R. W., & Bok, D. (1969). Participation of the retinal pigment epithelium in the rod outer segment renewal process. *The Journal of Cell Biology*. <https://doi.org/10.1083/jcb.42.2.392>

Young, T. A., Wang, H., Munk, S., Hammoudi, D. S., Young, D. S., Mandelcorn, M. S., & Whiteside, C. I. (2005). Vascular endothelial growth factor expression and secretion by retinal pigment epithelial cells in high glucose and hypoxia is protein kinase C-dependent. *Experimental Eye Research*, 80(5), 651–662. <https://doi.org/10.1016/J.EXER.2004.11.015>

Yuan, S., Roney, C. A., Wierwille, J., Chen, C.-W., Xu, B., Griffiths, G., Jiang, J., Ma, H., Cable, A., Summers, R. M., & Chen, Y. (2010). Co-registered optical coherence tomography and fluorescence molecular imaging for simultaneous morphological and molecular imaging. *Physics in Medicine and Biology*, 55(1), 191–206. <https://doi.org/10.1088/0031-9155/55/1/011>

Zhang, J., Wu, Y., Jin, Y., Ji, F., Sinclair, S. H., Luo, Y., Xu, G., Lu, L., Dai, W., Yanoff, M., Li, W., & Xu, G.-T. (2008). Intravitreal Injection of Erythropoietin Protects both Retinal Vascular and Neuronal Cells in Early Diabetes. *Investigative Ophthalmology & Visual Science*, 49(2), 732. <https://doi.org/10.1167/iovs.07-0721>

Zhang, M., Hwang, T. S., Dongye, C., Wilson, D. J., Huang, D., & Jia, Y. (2016). Automated quantification of nonperfusion in three retinal plexuses using projection-resolved optical coherence tomography angiography in diabetic retinopathy. *Investigative Ophthalmology and Visual Science*. <https://doi.org/10.1167/iovs.16-19776>

Zhang, S. X., Ma, J. X., Sima, J., Chen, Y., Hu, M. S., Otlecz, A., & Lambrou, G. N. (2005). Genetic difference in susceptibility to the blood-retina barrier breakdown in diabetes and oxygen-induced retinopathy. *American Journal of Pathology*. [https://doi.org/10.1016/S0002-9440\(10\)62255-9](https://doi.org/10.1016/S0002-9440(10)62255-9)

Zhong, X. Y., Ding, J. H., Adams, J. A., Ghosh, G., & Fu, X. D. (2009). Regulation of SR protein phosphorylation and alternative splicing by modulating kinetic interactions of SRPK1 with molecular chaperones. *Genes and Development*. <https://doi.org/10.1101/gad.1752109>

Zhou, Z., Qiu, J., Liu, W., Zhou, Y., Plocinik, R. M., Li, H., Hu, Q., Ghosh, G., Adams, J. A., Rosenfeld, M. G., & Fu, X.-D. (2012). The Akt-SRPK-SR axis constitutes a major pathway in transducing EGF signaling to regulate alternative splicing in the nucleus. *Molecular Cell*, 47(3), 422–433. <https://doi.org/10.1016/j.molcel.2012.05.014>

Zvereva, M. I., Shcherbakova, D. M., & Dontsova, O. A. (2010). Telomerase: Structure, functions, and activity regulation. *Biochemistry (Moscow)*, 75(13), 1563–1583. <https://doi.org/10.1134/S0006297910130055>

Appendix

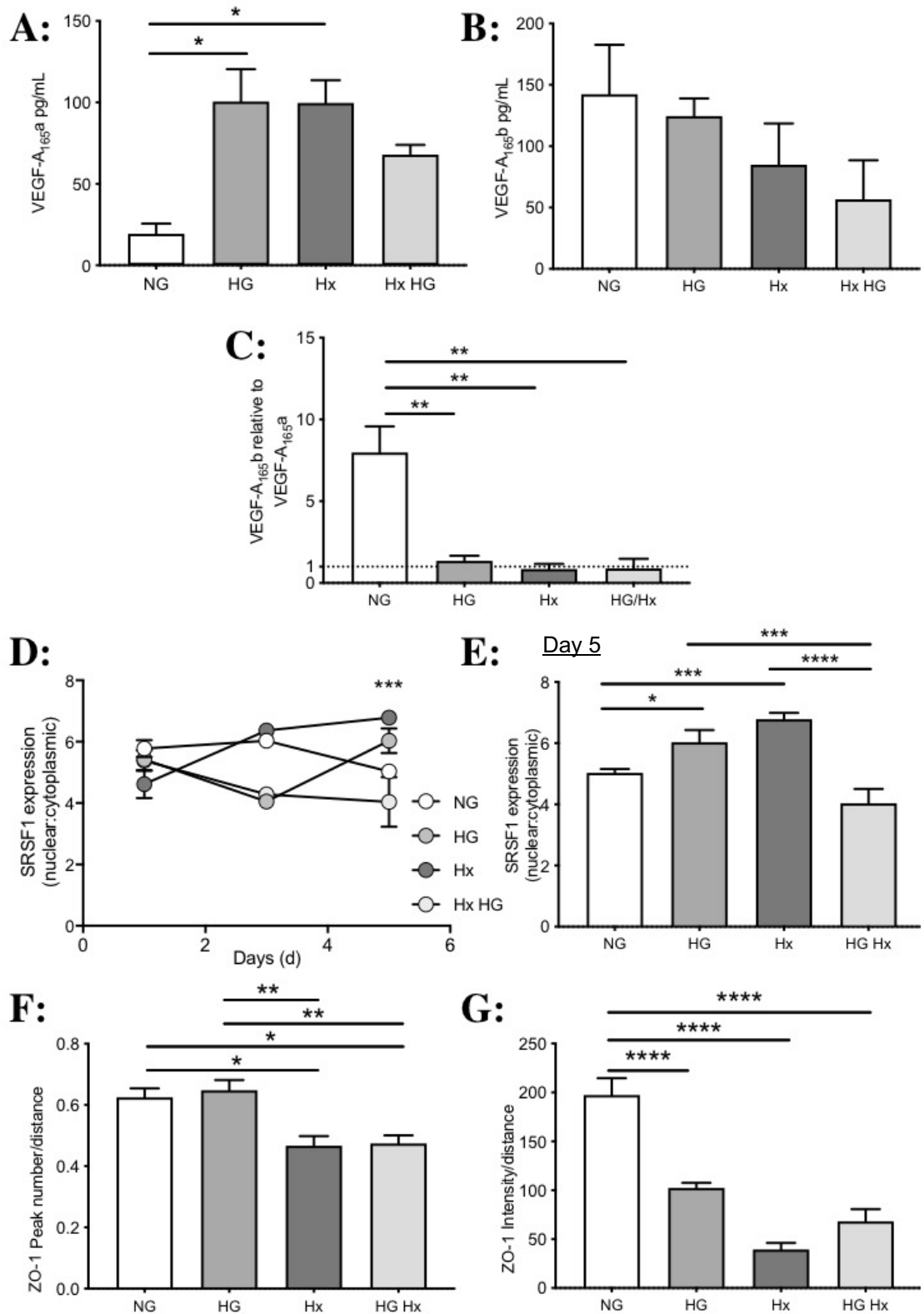


Figure 8: The impact of hyperglycaemia coupled with hypoxia on hprPE VEGF-A alternative isoform expression, SRSF1 localisation and ZO-1 barrier localisation

A: Hyperglycaemia (HG) and hypoxia (Hx) alone increase VEGF-A_{165a} isoform expression compared to normoglycemia (NG). When conditions are coupled (HG Hx), VEGF-A_{165a} also increases, although not to the same extent as each condition alone. **B:** HG Hx decreases VEGF-A_{165b} expression compared to further than HG or Hx alone, but not statistically significantly lower than NG. **C:** The ratio of VEGF-A_{165b} to VEGF-A_{165a} expression is significantly reduced ($p < 0.01$) in response to HG and Hx and HG Hx. **D:** SRSF1 localisation expressed as a ratio of nuclear to cytoplasmic over a 5 day timecourse. **E:** Day 5 nuclear SRSF1 expression increased in response to prolonged HG or Hx exposure compared to NG. HG Hx caused a reduction in nuclear SRSF1 expression. **F:** Peak number/distance of ZO-1 expression reduced in response to Hx alone and HG Hx but not HG. **G:** Intensity/distance of expression reduced in response to HG, Hx and also in HG Hx compared to NG. Error bars indicate mean + standard error except for **D** where is indicates mean \pm standard error. Statistical analysis for all except **D** performed using a one-way analysis of variance with Bonferonni post-hoc. Two way analysis of variance with Bonferonni post-hoc performed for **D**. * $p < 0.05$, ** $p < 0.01$, *** $p < 0.001$, **** $p < 0.0001$ ($n=3$).